EVIDÊNCIAS EXPERIMENTAIS DE UM SISTEMA MAGNÉTICO MULTIFÁSICO EM PEQUENOS AGREGADOS DE HIDROXISULFATO FÉRRICO

KALIL SKEFF NETO

- TESE DE DOUTORADO -

CENTRO BRASILEIRO DE PESQUISAS FISICAS - CBPF

RIO DE JANEIRO

1984

Dedico este trabalho a

Jens M. Knudsen e

Paulo C. de Morais

AGRADECIMENTOS:

- Agradeço ao Prof. Jacques A. Danon por todo o incentivo, colaboração e interesse que tem sempre dispensado ao grupo de Mössbauer da Universidade de Brasília e, sobretudo, pela amizade e orientação que recebi no desenvolver da minha formação científica.

- Ao Prof. Paulo C. de Morais pela convivência, dedicação e colaboração ao longo deste trabalho.

- À minha família pelo esforço e incentivo que nunca faltaram.

- À todos os funcionários da UnB, que direta ou indiretamente me ajudaram.

Este trabalho foi fruto da amizade e dedicação de meus alunos.

RESUMO:

Apresentam-se resultados experimentais que sugerem fortemente a presença de um sistema magnético multifásico (ferrimagnetismo, antiferromagnetismo e superparamagnetismo) em pequenos aglomerados de $FeOHSO_4$. Distribuições de temperaturas características decorrem naturalmente de distribuições nos diâmetros dos clusters. Tais distribuições de temperaturas parecem ser fortemente dependentes dos diâmetros dos clusters. Independente do tipo de ordem magnética, i.e., independente da faixa de temperatura e campo externo utilizados, os resultados experimentais sugerem que a lei de potência $\beta = 1/3$ parece ser a mais correta.

ABSTRACT

Experimental results that suggest the presence of a multiphase magnetic system (ferrimagnetic, antiferromagnetic, superparamagnetic) in fine particles of $FeOHSO_4$, are presented. Characteristic temperature distributions follow from the presence of particle-size distritions. Such characteristic temperature distribution appear to be strongly dependent from the particle-size distribution. The experimental data suggest that the $\beta = 1/3$ power-law may be correct, independent of both enternal field and temperature, in the range of our experiments.

I N D I C E

1.1 - INTRODUÇÃO

O estudo das propriedades magnéticas e estruturais de materiais em estados superparamagnéticos, é não só de interesse teórico mas também de interesse prático. Os estudos experimentais realizados neste campo (antes da descoberta do efeito Mössbauer) por métodos clássicos, ~~onde~~ de o tempo de observação é caracteristicamente elevado, não poderiam contribuir para o entendimento dos aspectos dinâmicos das interações magnéticas (onde ~~se exige~~ é encontrado um tempo de observação muito pequeno). É compreensível portanto, que só após o aparecimento da Ressonância Gama Nuclear (NGR), tenha sido possível estudar detalhes da estrutura magnética de "partículas" ultrafinas.

Superparamagnetismo foi observado pela primeira vez, por Elmore (1938), em uma suspensão coloidal de "cluster" de Fe_3O_4 |01|. Além do termo superparamagnetismo, outros também são utilizados: "magnetismo aparente", "paramagnetismo coletivo" e "quase-paramagnetismo" |02|.

O conceito de superparamagnetismo foi proposto originalmente por Néel, para explicar a possibilidade de flutuações térmicas em "clusters" ferromagnéticos |03|. Superparamagnetismo tem sido observado, não só em "clusters" com ordenamento ferromagnético |04|, mas também em "clusters" cujo ordenamento interno é antiferromagnético |05| ou ferrimagnético |06|.

É importante notar que não faremos uma distinção rígida entre os termos "clusters" e "partícula", embora alguns autores o façam |07|. Para estes, o termo partícula implica na

existência de uma entidade física com contorno bem definido, enquanto o termo "cluster" poderia significar até mesmo uma região com alta densidade de ordenamento, em relação à vizinhança e com dimensões na faixa de (10 - 150) Å de raio.

Em um sistema superparamagnético, a energia térmica é suficiente para equilibrar a magnetização de um conjunto de "clusters", durante um tempo que é pequeno, comparado com aquele do experimento. Admitindo que cada "cluster" tenha um momento magnético efetivo μ, é possível tratar o sistema com o modelo de paramagnetismo, tomando $J \to \infty$ na função de Brillouin. Existe, entretanto, uma diferença fundamental; o momento magnético μ é muito maior que o de um paramagneto comum, isto é, êle está associado a um "cluster" que pode conter mais de 10^5 átomos acoplados magneticamente |08|.

Experimentalmente, o efeito de superparamagnetismo é inequivocamente comprovado, quando a magnetização M é plotada versus H/T. A superposição das curvas de M versus H/T, tomadas a diferentes temperaturas, é a indicação primária da presença de superparamagnetismo (Fig. 1.1).

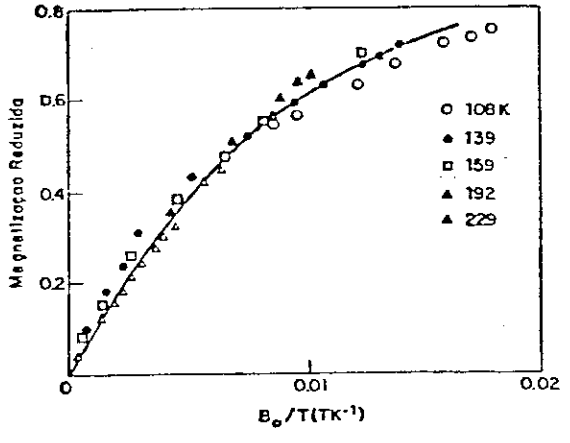

Fig. 1.1 - Comportamento superparamagnético. Magnetização reduzida versus B_o/T para diferentes temperaturas (J. Crangle in "The Magnetic Properties of Solids", Edward Arnold, 1977).

Um segundo critério, é a ausência do efeito de histerese, que caracteriza os sistemas ferromagnéticos. Então de uma maneira bastante simplificada, é possível imaginar um sistema superparamagnético, como sendo intermediário entre um paramagnético puro e um ferromagnético puro (Fig. 1.2) |07|.

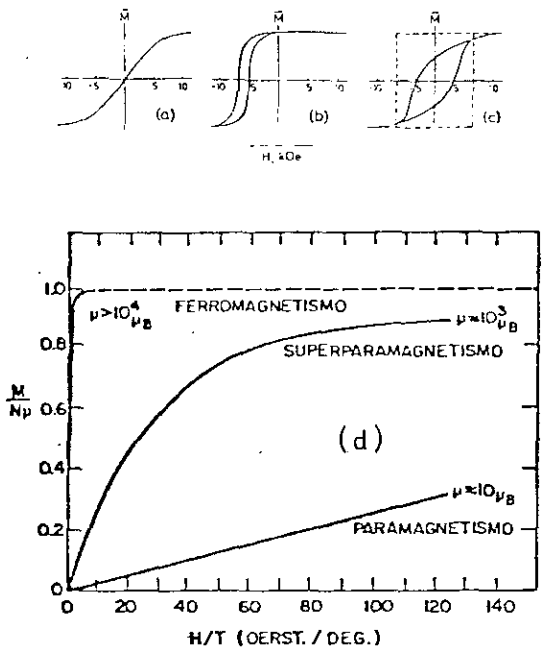

Fig. 1.2 - Curvas características de histerese: (a) superparamagnetismo; (b) anisotropia de exchange; (c) conjuntos de partículas com magnetização termicamente estável, aleatória (curva solida) alinhada (curva tracejada); (d) gráfico da magnetização relativa, M/Nμ, como função da razão entre o campo e a temperatura, H/T.

Com o auxílio de um computador, é possível ajustar os dados experimentais de M versus H/T, à equação de Langevin, para obter o momento magnético efetivo dos "clusters" (μ) e o número de "clusters" por unidade de volume (N). Assim, a magnetização de saturação pode ser obtida, já que $M_s = \mu N$ |09|.

A interação magnética, que desdobra as linhas do espectro Mössbauer é uma fonte de informações sobre o comportamento do vetor $\vec{H}_{eff}$. Em materiais magneticamente ordenados, $\vec{H}_{eff}$ é colinear com o vetor $\vec{M}$, e, consequentemente, usando o efeito Mössbauer para estudar o vetor $\vec{H}_{eff}$, podemos obter dire

tamente informações sobre a dinâmica do vetor $\vec{M}$ |10|

Desprezando as interações hiperfinas, tais como a interação do momento de quadrupolo nuclear com o gradiente de campo elétrico, a presença de cations de Fe^{III}, em sítios diferentes ou a presença simultânea de cations de Fe^{II} e Fe^{III}, o espectro Mössbauer, de um sistema paramagnético, normalmente consiste de uma única linha |11|. Por outro lado, os sistemas magneticamente ordenados ou aqueles com valores elevados do tempo de relaxação (em relação à frequência de Larmor), apresentam espectros Mössbauer, com mais de uma linha |12|.

É importante notar que os espectros Mössbauer de sistemas superparamagnéticos apresentam o mesmo aspecto geral daqueles associados a sistemas paramagnéticos. Existe, ainda, uma correlação muito forte entre a dimensão dos "clusters", forma de linha e tempo de relaxação |07|.

Uma consequência do modelo de Néel, para o superparamagnetismo, é a dependência do tempo de relaxação τ dos momentos magnéticos atômicos dos átomos no interior de um "cluster" com o volume V e com a temperatura T :

$$\tau = \tau_o \exp \frac{KV}{KT} \quad , \qquad 1.1$$

onde K é a constante de anisotropia. Um decréscimo de τ (causado por diminuição de V ou aumento de T), produz um alargamento das linhas Mössbauer em um espectro hiperfino e um decréscimo do campo $\vec{H}_{eff}$ no núcleo Mössbauer. Este comportamento é ob

servado na maioria dos experimentos, envolvendo partículas ultrafinas de materiais ferro - e ferrimagnéticos. Entretanto a forma dos espectros, em função da temperatura ou do volume das partículas, é bastante diferente daquele previsto pela equação acima, quando se trata de partículas ultrafinas com ordenamento antiferromagnético, e podem ser entendidas, admitindo a existência de um certo volume crítico V_{cr} e uma temperatura crítica T_{cr} |05, 13 e 14|.

A existência de um diâmetro crítico, para o qual a magnetização seria máxima, é discutida por Luborsky |15|. E em seu trabalho Luborsky, relaciona a dependência da força coerciva em função do diâmetro das partículas para vários materiais (Fig. 1.3).

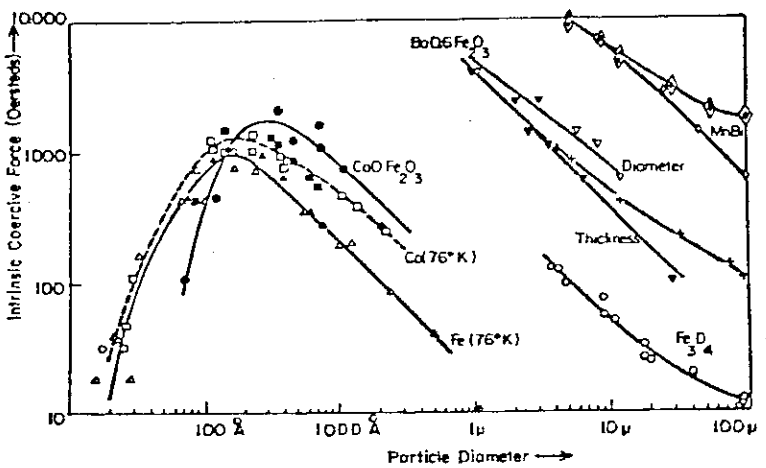

Fig. 1.3 - Força cerciva versus diâmetro para vários materiais |15|

Por outro lado podemos associar a força coerciva H_c com o campo interno no núcleo Mössbuaer H_o através de

$$H_c = cte \cdot H_o^2 \quad , \qquad 1.2$$

onde cte., depende das características geométricas da partícula |16|.

A relação de Bean-Livingston :

$$H_c = \frac{2K\!\!\!/V}{\mu} \left[1 - \left(\frac{T}{T_B}\right)^{1/2} \right] \qquad 1.3$$

possibilita determinar a região de temperatura onde o material apresenta propriedades superparamagnéticas. Na relação anterior, T_B é a temperatura de bloqueio definida como a temperatura na qual o tempo de relaxação de um dado "cluster" é $\sim 10^2$ seg. A temperatura T_B da uma visão grosseira da dimensão máxima a partir da qual a "partícula" cai na região superparamagnética. Assim, para $T > T_B$ um conjunto idêntico de "partículas" apresenta $H_c = 0$ para $H_{eff} = 0$. Devido à dificuldade em preparar experimentalmente um conjunto de partículas, com uma distribuição estreita de diâmetro o que se apresenta é uma distribuição de temperatura T_B. |17|

O aumento da intensidade das linhas paramagnéticas e a diminuição da intensidade das linhas magnéticas no espectro Mössbauer é interpretado em termos da diminuição da fração de átomos magneticamente ordenados e do aumento da fração de átomos magneticamente desordenados à medida em que alteramos a temperatura ou a distribuição do diâmetro das partículas que compõem a amostra.

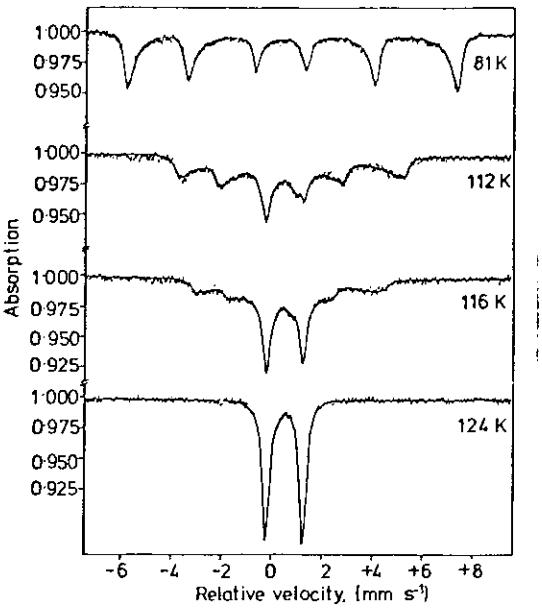

Fig. 1.4 - Espectros Mössbauer de "particulas" finas em várias temperaturas |26|

Medindo-se as áreas, sob o espectro de absorção, obtem-se a fração, superparamagnética na amostra a varias temperaturas. A diferenciação desta curva resulta na distribuição volumétrica das partículas na amostra. Esta distribuição concorda perfeitamente com aquela determinada por microscopia eletrônica |18|.

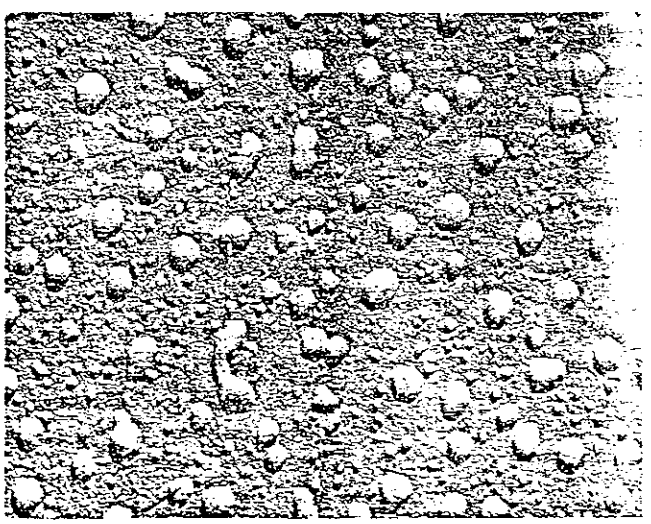

Fig. 1.5 - Microscopia Eletrônica de um superparamagneto.

Aproveitando o fato de que os espectros Mössbauer são altamente sensíveis à relação IKV/KT e considerando o caráter cooperativo das interações ferro - e antiferromagnéticas, devemos esperar que os espectros Mössbauer forneçam campos hiperfinos e temperaturas de transições magnéticas diferentes para amostras com diferentes amostragens de granulação. Dentro desta idéia, buscamos criar diferentes distribuições de "partículas" para um mesmo material, utilizando hidratações e desidratações sucessivas.

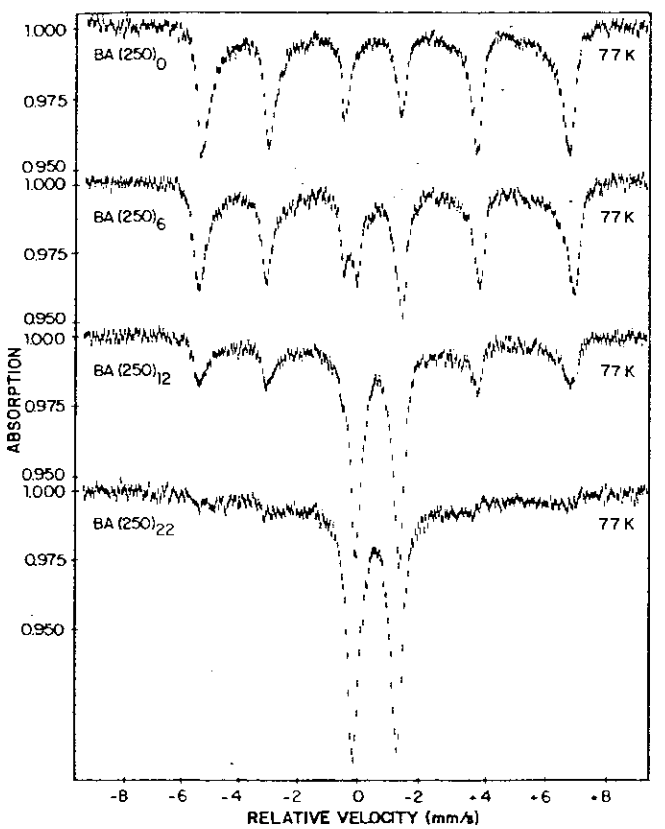

Fig. 1.6 - Espectros Mössbauer (77 K), para diferentes distribuições volumétrica das partículas |27|

O processo de hidratação e desidratação do material $FeOHSO_4$ é reversível e em relação à composição química o composto permanece quimicamente inalterado após uma sequência de hidratações e desidratações. Por outro lado, os pro

cessos de hidratação e desidratação alteram a distribuição de granulação do material, produzindo diferentes amostragens de "partículas". Tais "partículas" apresentam propriedades físicas diferentes quando comparadas às propriedades do material "bulk". Algumas destas propriedades têm sido estudadas utilizando-se a Espectroscopia Mössbauer e Ressonância Paramagnética Eletrônica (ver anexos, A, C e D).

I.2 - MODELOS PARA SUPERPARAMAGNETISMO

O primeiro modelo de superparamagnetismo aparece em 1949, com a publicação do artigo "Influence des fluctuations thermiques sur l'aimantation de grains ferromagnetiques très fins", publicado por Néel [03]. Segundo Néel, um grão ferromagnético, tendo a forma de um elipsóide de revolução de eixo A, volume V e suficientemente pequeno para constituir um domínio elementar, possui um momento magnético $\mu = VM$, onde M é o valor da magnetização. Sendo θ o ângulo entre $\vec{\mu}$ e o eixo A, a energia do grão, na ausência de campo externo, é da forma $E = 1/2\ \mu\ h\ \sin^2\theta$, onde h é uma constante positiva dependente da anisotropia de forma e da anisotropia magnetocristalina do grão. Néel frisou que as flutuações térmicas deveriam provocar um tipo de movimento Browniano em torno da direção da magnetização e mostrou que, na ausência de campo externo, a probabilidade de encontrar $\vec{\mu}$ entre θ e $\theta + d\theta$ é dada por:

$$2\bar{\omega}(\theta) = \frac{\mu\ h}{K\ T} \exp\left\{ - \frac{\mu\ h\ \sin^2\theta}{2\ K\ T} \right\} \sin\theta \quad . \qquad 1.4$$

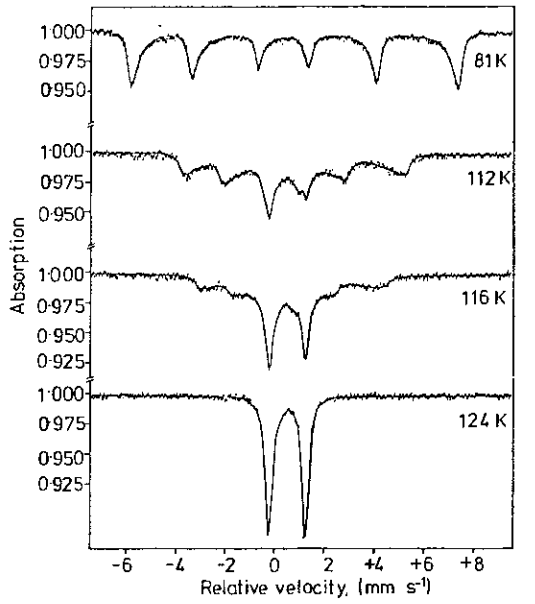

Fig. 1.4 - Espectros Mössbauer de "particulas" finas em várias temperaturas |26|

Medindo-se as áreas, sob o espectro de absorção, obtem-se a fração, superparamagnética na amostra a varias temperaturas. A diferenciação desta curva resulta na distribuição volumétrica das partículas na amostra. Esta distribuição concorda perfeitamente com aquela determinada por microscopia eletrônica |18|.

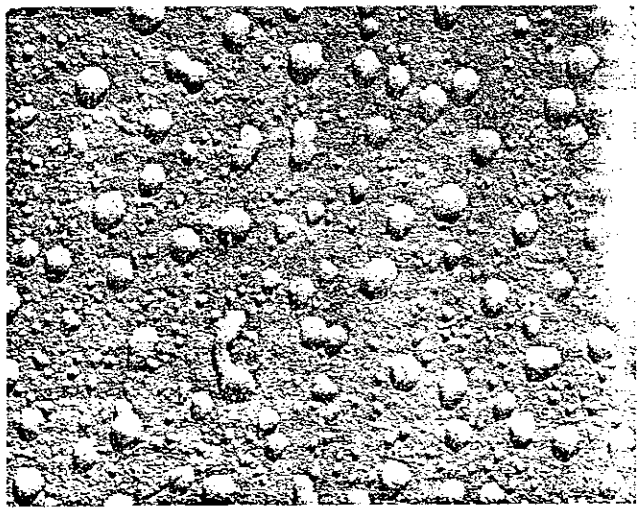

Fig. 1.5 - Microscopia Eletrônica de um superparamagneto.

Aproveitando o fato de que os espectros Mössbauer são altamente sensíveis à relação IKV/KT e considerando o caráter cooperativo das interações ferro - e antiferromagnéticas, devemos esperar que os espectros Mössbauer forneçam campos hiperfinos e temperaturas de transições magnéticas diferentes para amostras com diferentes amostragens de granulação. Dentro desta idéia, buscamos criar diferentes distribuições de "partículas" para um mesmo material, utilizando hidratações e desidratações sucessivas.

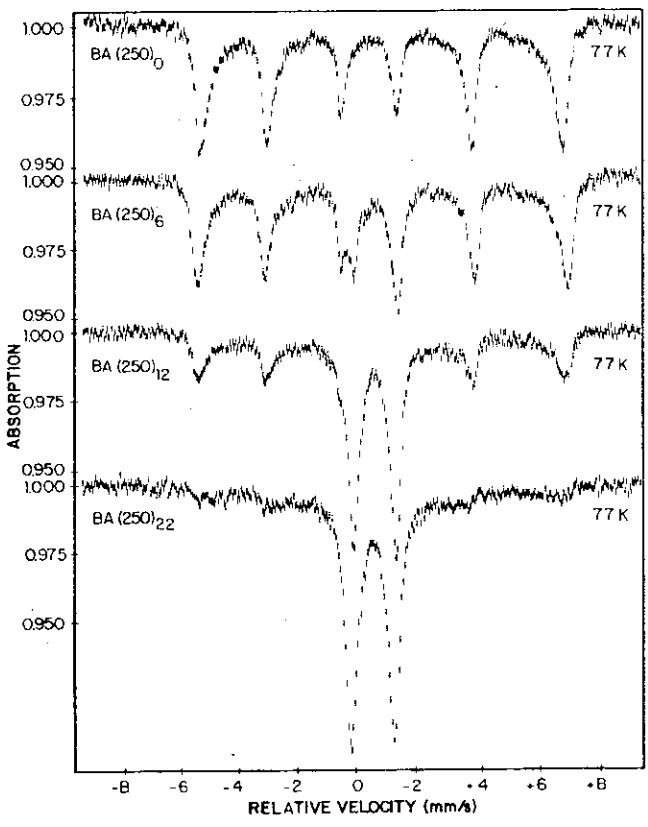

Fig. 1.6 - Espectros Mössbauer (77 K), para diferentes distribuições volumétrica das partículas |27|

O processo de hidratação e desidratação do material $FeOHSO_4$ é reversível e em relação à composição química o composto permanece quimicamente inalterado após uma sequência de hidratações e desidratações. Por outro lado, os pro

cessos de hidratação e desidratação alteram a distribuição de granulação do material, produzindo diferentes amostragens de "partículas". Tais "partículas" apresentam propriedades físicas diferentes quando comparadas às propriedades do material "bulk". Algumas destas propriedades têm sido estudadas utilizando-se a Espectroscopia Mössbauer e Ressonância Paramagnética Eletrônica (ver anexos, A, C e D).

I.2 - MODELOS PARA SUPERPARAMAGNETISMO

O primeiro modelo de superparamagnetismo aparece em 1949, com a publicação do artigo "Influence des fluctuations thermiques sur l'aimantation de grains ferromagnetiques très fins", publicado por Néel |03|. Segundo Néel, um grão ferromagnético, tendo a forma de um elipsóide de revolução de eixo A, volume V e suficientemente pequeno para constituir um domínio elementar, possui um momento magnético $\mu = VM$, onde M é o valor da magnetização. Sendo θ o ângulo entre $\vec{\mu}$ e o eixo A, a energia do grão, na ausência de campo externo, é da forma $E = 1/2\ \mu\ h\ \sin^2\theta$, onde h é uma constante positiva dependente da anisotropia de forma e da anisotropia magnetocristalina do grão. Néel frisou que as flutuações térmicas deveriam provocar um tipo de movimento Browniano em torno da direção da magnetização e mostrou que, na ausência de campo externo, a probabilidade de encontrar $\vec{\mu}$ entre θ e $\theta + d\theta$ é dada por:

$$2\bar{\omega}(\theta) = \frac{\mu\ h}{K\ T} \exp\left\{ - \frac{\mu\ h\ \sin^2\theta}{2\ K\ T} \right\} \sin\theta \quad . \qquad 1.4$$

Se considerarmos um conjunto de partículas idênticas (clusters), mutuamente independente, com N partículas por unidade de volume e cada uma com momento magnético $\vec{\mu} = V\vec{M}$, podemos tomar $S = \infty$ (número quântico total, pois $\mu >> \mu_B$) e tratar o problema classicamente. Desta forma, na presença de campo externo $\vec{H}$, o valor de equilíbrio da magnetização $\vec{M}$ paralela à direção do campo é |02|:

$$M = N \mu 2\pi Z^{-1} \int_0^{\pi} \cos\theta \sin\theta \exp(-E/KV)\, d\theta \quad , \qquad 1.5$$

Com :

$$Z = 2\pi \int_0^{\pi} \sin\theta \exp(-E/KT)\, d\theta \quad , \qquad 1.6$$

$$E = KV \sin^2\theta - \mu H \cos\theta \qquad 1.7$$

onde K é a constante de anisotropia. Para valores de KV, tais que $KV/KT << 1$, temos:

$$M = N \mu \left| \coth(\mu H/KT) - KT/\mu H \right| . \qquad 1.8$$

Podem-se fazer, ainda, aproximações :

$$M \simeq N \mu^2 H/3\,KT \quad , \quad \mu H/KT << 1 \, , \qquad 1.9$$

$$M \simeq N \mu (1 - KT/\mu H) \; ; \quad \mu H/KT >> 1 \; . \qquad 1.10$$

As equações anteriores são formalmente idênticas

ãs correspondentes equações do paramagnetismo clássico de Langevin (1905). A diferença é que $\vec{\mu}$, o momento magnético da partícula (cluster), pode incluir até 10^5 átomos. É justamente por esta razão que o fenômeno foi chamado superparamagnetismo.

Quando se aplica um campo externo $\vec{H}$ a um conjunto de tais "partículas" e, em seguida, o mesmo é removido, a magnetização remanescente cai, de acordo com a expressão:

$$M_r = M \exp(-t/\tau) \quad , \qquad 1.11$$

onde τ é o tempo de relaxação do processo dado por:

$$\frac{1}{\tau} = f = f_o \exp(-IKV/KT) \quad , \qquad 1.12$$

onde o fator f_o é da ordem de 10^9 seg^{-1} |08|.

O modelo proposto por Néel não leva em conta a interação cluster - cluster. No modelo de Néel, a barreira de energia que a partícula deve vencer é apenas IKV (caso de $\vec{H} = 0$). Mesmo assim, foi possível explicar uma série de observações experimentais, em termos qualitativos. Um melhoramento do modelo seria considerar a interação inter-cluster e verificar em que condições ela seria significativa.

Suzdalev e Colaboradores (1973) utilizaram uma expressão semi-empírica para descrever o tempo de relaxação do momento magnético de uma partícula:

$$\tau = \tau_o \exp\left(\frac{\mathbb{K} V}{K T} + \frac{\alpha \mu^2/d^3}{K T} + \frac{\beta \mu H}{K T}\right) \qquad 1.13$$

$$\tau_o = \frac{2 \pi \hbar a^3}{\eta^2 \mu_B^2} \qquad 1.14$$

onde:

$\mathbb{K}$: Constante de anisotropia magnética,

V : Volume da partícula,

μ : Momento magnético de uma partícula,

d : Diâmetro da partícula,

H : Campo magnético externo,

α : Constante de interação de dipolo magnético entre partículas,

β : Constante de interação entre o momento magnético do cluster e o campo externo,

a : Distância inter-cluster,

η : Número de magnetons de Bohr por partícula.

A expressão anterior leva em conta a barreira de energia potencial ($\mathbb{K}$ V), a interação partícula - partícula ($\alpha\mu^2/d^3$) e a interação com o campo magnético externo ($\beta\mu H$). Utilizando a expressão proposta, é possível fazer uma estimativa dos valores de $\mathbb{K}$ V, α, β e μ, que caracterizam as propriedades magnéticas de uma partícula, a partir dos espectros Mössbauer (na faixa de 10^{-10} seg $< \tau < 10^{-7}$ seg). As medidas foram realizadas utilizando partículas ultrafinas de ferro com diâmetros médios de 105 Å, 115 Å, 140 Å, 165 Å e 230 Å. O valor da anisotropia magnética permanece praticamente constante na faixa

de 300 K - 850 K para uma determinada amostra enquanto que o seu valor decresce, com o aumento das dimensões das partículas. Os valores de α, para partículas com diâmetros médios de 115 Å e 165 Å, foram de 0,2 e 0,1 respectivamente. O valor de β foi de 0,1 para a amostra, contendo partículas com diâmetro médio de 115 Å, em um campo externo de 3 K Oe |19|.

Avraamov e colaboradores (1975) propuseram-se a desenvolver uma teoria que explicasse a magnetização de um superparamagneto, em função da temperatura, dentro de uma faixa bem ampla de temperaturas. Para temperaturas $T << Tc$ o modelo de Langevin descreve adequadamente a dependência da magnetização, em relação ao campo e à temperatura. Entretanto, à medida que T se aproxima de Tc, a dependência experimental da magnetização por unidade de massa $\sigma(T)$ difere fortemente da equação de Langevin. A proposição de Avraamov e colaboradores é considerar a dependência de $\mu(T, H)$, ainda dentro do modelo molecular:

$$\mu\ (T,\ H) = \mu_0\ B_s \left[\frac{2\ \mu_B\ S\ H_{eff}}{K\ T} \right] \qquad 1.15$$

Na expressão anterior H_{eff} é o campo molecular efetivo, agindo sobre os átomos com spin S:

$$H_{eff} = \alpha M + \frac{\sigma}{M} H \quad , \qquad 1.16$$

onde :

μ = momento magnético de uma partícula de massa m

μ_0 = momento magnético na saturação

B_s = função de Brillouin para spin "S"

μ_B = magneton de Bohr

α = constante de interação dos spins em uma partícula superparamagnética

M = magnetização

σ = magnetização por unidade de massa

H = campo magnético sobre a amostra.

Considerando a função de Brillouin para S = 1/2, e que neste caso $\alpha = K\ Tc/\mu_B\ M_o$, onde Tc é a temperatura de Curie e $M_o = \mu_o/m = \sigma\ (T = 0K)$, obtém-se um sistema de equações que, resolvido graficamente, possibilita o conhecimento de $\sigma\ (T)$ para um dado campo H ou então o conhecimento de (H), para uma dada temperatura;

$$\frac{\sigma}{M_o} = \frac{M}{M_o}\ L\left(\frac{\mu_o\ H}{K\ T}\ \frac{M}{M_o}\right)\ , \qquad 1.17$$

$$\frac{\sigma}{M_o} = \frac{M}{M_o}\ \frac{K\ Tc}{\mu_B\ H_a}\left[\frac{1}{2}\ \frac{T}{T_c}\ \ell n\ \frac{1 + M/M_o}{1 - M/M_o} - \frac{M}{M_o}\right]\ . \qquad 1.18$$

A proposta acima foi testada para a liga Y_u NDK 38 T 8 ($\mu_o = 3.23 \times 10^{-8}$ emu e Tc = 385 K) |20|.

Morup e Topsoe (1976) apresentaram um modelo simples para explicar a diminuição do desdobramento magnético hiperfino, de amostras constituídas de pequenas partículas

(~ 100 Å de diâmetro), em relação ao desdobramento magnético de monocristais. O efeito é significativo, a temperaturas abaixo de bloqueio do superparamagneto. O modelo se baseia em oscilações da magnetização, em torno de um mínimo de energia. No caso da relaxação superparamagnética convencional, se a barreira de energia de anisotropia (KV), é comparável ou menor que a energia térmica (KT), a magnetização pode alternar entre dois mínimos de energia ($\phi = 0$ e $\phi = \pi$). Entretanto, para temperaturas em que KV >> KT, o vetor magnetização é considerado fixo em $\phi = 0$ ou $\phi = \pi$. Morup e Topsoe propuseram que, mesmo nestas condições (KV >> KT), existe uma probabilidade do vetor magnetização estar entre ϕ e $\phi + d\phi$, em relação a $\phi = 0$, dada por

$$P(\phi)\, d\phi = \exp\left| - E/KT \right| \sin\phi \, d\phi / \int_0^{\pi/2} \exp\left| - E/KT \right| \sin\phi \, d\phi \qquad 1.19$$

onde;

$$E = - KV \cos^2\phi \quad . \qquad 1.20$$

A magnetização média é dada por;

$$M(T) = M_0(T) \langle \cos\phi \rangle \qquad 1.21$$

onde $M_0(T)$ é a magnetização do monocristal, à temperatura T e $\langle \cos\phi \rangle_T$ a média térmica de $\cos\phi$. O cálculo de $\langle \cos\phi \rangle_T$ para KT << KV leva a:

$$\langle \cos\phi \rangle_T = \frac{\int_0^{\pi/2} \exp |E/KT| \cos\phi \sin\phi \, d\phi}{\int_0^{\pi/2} \exp |E/KT| \sin\phi \, d\phi} \equiv (1 - KT/2KV) \, . \qquad 1.22$$

Consequentemente, o desdobramento magnético em um espectro Mössbauer deverá ser proporcional à magnetização média M(T). Assim, o desdobramento magnético no espectro de pequenas partículas deverá ser reduzido pelo fator (1 - KT/2 K V) relativo ao desdobramento encontrado para o monocristal. É importante notar que, se a amostra contém uma distribuição alargada de partículas,as linhas Mössbauer correspondentes às partículas com diferentes diâmetros não deverão ser deslocadas numa mesma proporção. Isto significa que o espectro da amostra deverá ser alargado e necessariamente, assimétrico |21|.

Tsuei e colaboradores (1968) analisaram a dependência da magnetização de um ferromagneto amorfo com a temperatura. O sistema utilizado foi a liga $Fe_{80}\ P_{12,5}\ C_{7,5}$ que apresentou espectros Mössbauer com linhas alargadas. O alargamento das linhas Mössbauer foi atribuído a dois fatores: (1) aos efeitos de relaxação eletrônica e (2) à existência de uma distribuição de campo hiperfino no núcleo do Fe^{57}. Segundo Tsuei e colaboradores não foi possível obter um bom ajuste dos espectros Mössbauer, à temperatura ambiente, baseando-se em uma distribuição Lorentziana para o campo hiperfino P(H) |22|. Sharon e Tsuei (1972) e Tsuei e Lilienthal (1976) voltaram ao problema de ajustar o espectro Mössbauer de um ferromagneto amorfo em termos de uma distribuição de campo hiperfino. O sistema utilizado foi uma liga de Fe - Pd - P obti

da por resfriamento rápido a partir da fase líquida. O argumento para a análise, em termos da distribuição do campo hiperfino, está no fato de que em um material amorfo há uma variedade local de campo hiperfino e deslocamento isomérico. Daí a necessidade de se discutir tais parâmetros em cima de bases estatísticas. Assim, os espectros Mössbauer da liga $Fe_x\ Pd_{80-x}\ P_{20}$ ($13 < x < 44$) foram ajustados em termos de uma distribuição de campos hiperfinos P(H), um deslocamento isomérico de linha Γ. Para obter a forma da distribuição de campo hiperfino P(H), foi considerado o modelo onde o campo hiperfino em um dado sítio de Fe^{57} fosse função do número de vizinhos de fósforo mais próximos. No ajuste dos dados por métodos numéricos, a fórmula empírica que ajustou melhor foi uma contribuição de Lorentz e Gauss

$$P(H) = \begin{cases} \dfrac{1}{\left[(H - H_0)^2 + \frac{1}{4}\Gamma_0^2\right]} & ; \quad 0 \leq H \leq H_0 \qquad 1.23 \\ \exp\left[(H - H_0)^2 / 2\,\Gamma_1^2\right] & H > H_0 \qquad 1.24 \end{cases}$$

como condição de contorno as duas expressões de P(H) igualam-se em $H = H_0$ e P(H) é normalizada por

$$\int_0^\infty P(H)\, dH = 1 \quad . \qquad 1.25$$

Para calcular P(H) admite-se que H(T)/H(0) varia com a temperatura de acordo com

$$\frac{H_o\ (T)}{H_o\ (0)} = \frac{M\ (T)}{M\ (0)} = B_S \left[\frac{S}{S+1} \frac{M\ (T)\ /\ M\ (0)}{T\ /\ T_c} \right] \qquad 1.26$$

onde B_S é a função de Brillouin para spins S |23 e 24|.

No anexo A-3, analisamos as propriedades magnéticas de "microcristais" de FeOH SO_4, baseando-se no modelo para ligas ferromagnéticas randomicamente diluídas. A variação do campo interno com a temperatura, para os espectros Mössbauer a várias temperaturas, é descrita em termos de uma função de distribuição de campo hiperfino P (H). O melhor ajuste para os resultados experimentais foi obtido usando uma distribuição Lorentziana assimétrica para P (H):

$$P\ (H) = \begin{cases} A \left[(H - H_0)^2 + (\Gamma_1/2)^2 \right]^{-1} \ ; \ 0 < H < H_0 & 1.27 \\ B \left[(H - H_0)^2 + (\Gamma_2/2)^2 \right]^{-1} \ ; \ H > H_0 & 1.28 \end{cases}$$

onde as constantes A e B são determinadas por:

$$\int_0^\infty P\ (H)\ dH = 1 \quad . \qquad 1.29$$

O modelo proposto admite que em torno de cada átomo de Fe^{57} exista z vizinhos mais próximos nos quais a magnetização é determinada pela concentração local de átomos de Fe e pela temperatura. Admite-se que somente os átomos magnéticos interagem entre si

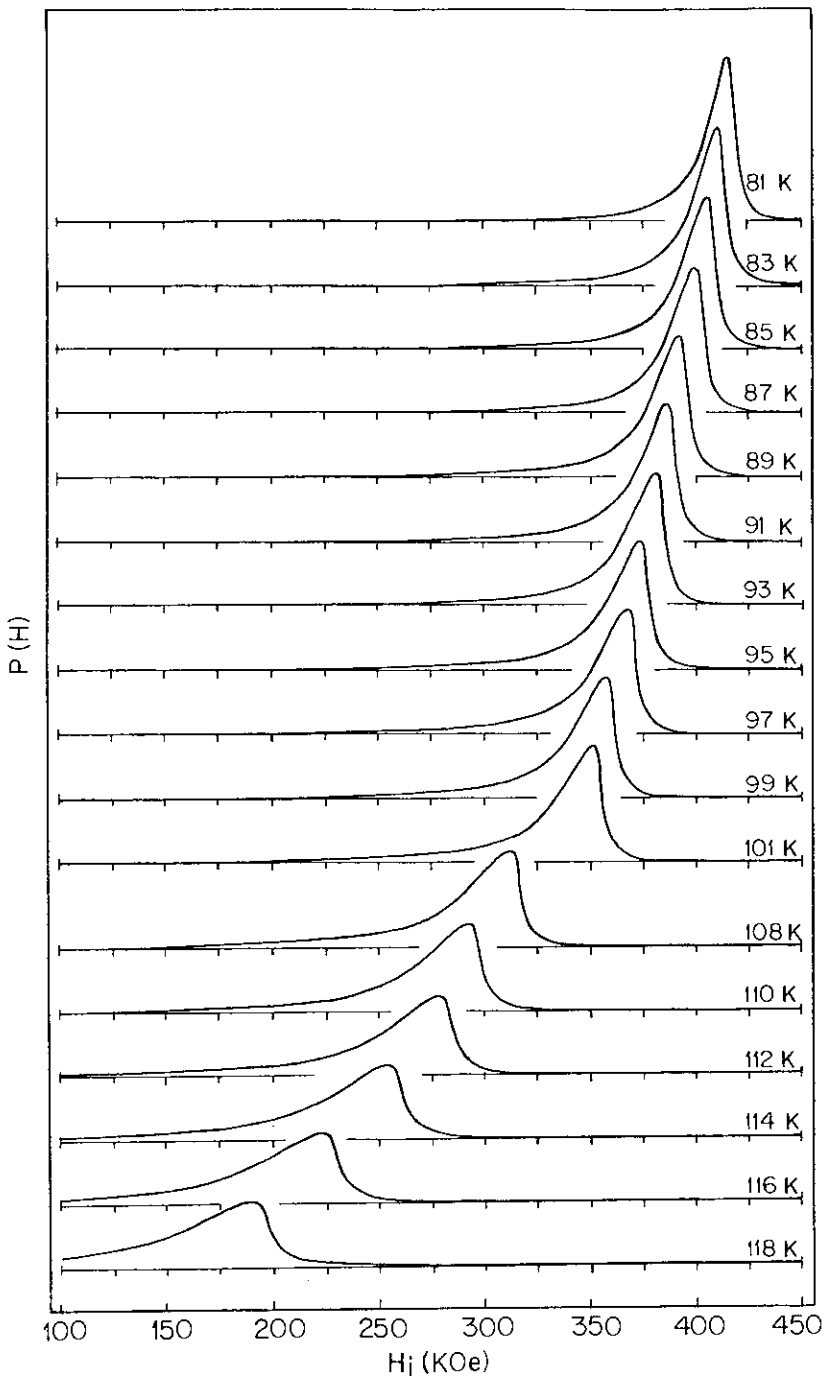

Fig. 1.7 - Distribuição de campo hiperfino P(H) em função da temperatura [25]

através de um campo molecular que é proporcional à temperatura de magnetização dos átomos vizinhos. Admite-se ainda que a intensidade das linhas paramagnéticas que surgem com o aumento da temperatura seja proporcional ao número de átomos de Fe paramagnéticos. Isto conduz a uma densidade magnética como função da temperatura m(T) :

$$m(T) = \lambda \left[1 - I_p (T) / I_p (124\ K) \right] . \qquad 1.30$$

onde λ é uma constante menor que a unidade e 124 K é a temperatura em que o sistema FeOH SO_4 considerado está totalmente desmagnetizado. Admitiu-se a aproximação de um sistema magnético randômico dentro do modelo molecular, para S = 1/2, e usou-se a expressão para a magnetização por átomo como sendo

$$\frac{1}{2} - M = \sum_{\nu=0}^{z} \frac{z! \left[m(T)\right]^{\nu} \left[1 - m(T)\right]^{z-\nu}}{(z - \nu)!\ \nu! \left[\exp \frac{2MJ\nu}{kT} + 1\right]} \qquad 1.31$$

onde J representa a energia interação entre os centros magnéticos mais próximos e m(T) é agora uma função da temperatura. A função m(T) foi determinada impondo a condição de que $(2M)^3$, obtido a partir da expressão anterior, ajustava adequadamente os valores experimentais de H_0^3. A expressão para $I_p(T)/I_p$ (124 K) foi ajustada por

$$\lambda\, I_p(T)/I_p\,(124\ K) = \begin{cases} \dfrac{\tan^{-1}\ \dfrac{2(T - T_0)}{\Gamma_1} + \tan^{-1}\ \left(\dfrac{2T_0}{\Gamma_1}\right)}{\tan^{-1}\ \left(\dfrac{2T_0}{\Gamma_1}\right) + \dfrac{\Gamma\ \sqrt{2\pi}}{\Gamma_1}}\ \lambda\ ;\ 0<T<T_0, \\ \qquad\qquad 1.32 \\ \lambda - \dfrac{2\sqrt{2\pi}\ \Gamma_0 \left[1 - \mathrm{erf}\ \left(\dfrac{T - T_0}{\Gamma_0\ \sqrt{2\pi}}\right)\right]}{\Gamma_1 \left[\tan^{-1}\left(\dfrac{2\ T_0}{\Gamma_1}\right) + \dfrac{\Gamma_0\ \sqrt{2\pi}}{\Gamma_1}\right]}\ \lambda\ ;\ T > T_0\ , \\ \qquad\qquad 1.33 \end{cases}$$

com $T_0 = 0{,}88$, $\Gamma_0 = 0{,}051$ e $\Gamma_1 = 0{,}074$. Fisicamente a existência de $m(T)$, dada por

$$T = T_c\ m(T)\ , \qquad 1.34$$

foi associada ao fato de que o sistema consiste de uma distribuição de partículas $P(V)$. implicando em uma distribuição de temperatura $P(T)$ dada por

$$P(T) = \begin{cases} A \left[(T - T_0)^2 + (\Gamma_1/2)^2 \right]^{-1}\ ;\ 0 < T < T_0 \qquad 1.35 \\ \dfrac{A}{(\Gamma_1/2)^2}\ \exp\left[- (T - T_0)^2 / 2\sigma^2 \right]\ ;\ T > T_0 \\ \qquad\qquad 1.36 \end{cases}$$

onde $T_0 = 116{,}7$ K, $\Gamma_1 = 9{,}8$ K, $\sigma = 2{,}9$ K e A é a constante de normalização [25].

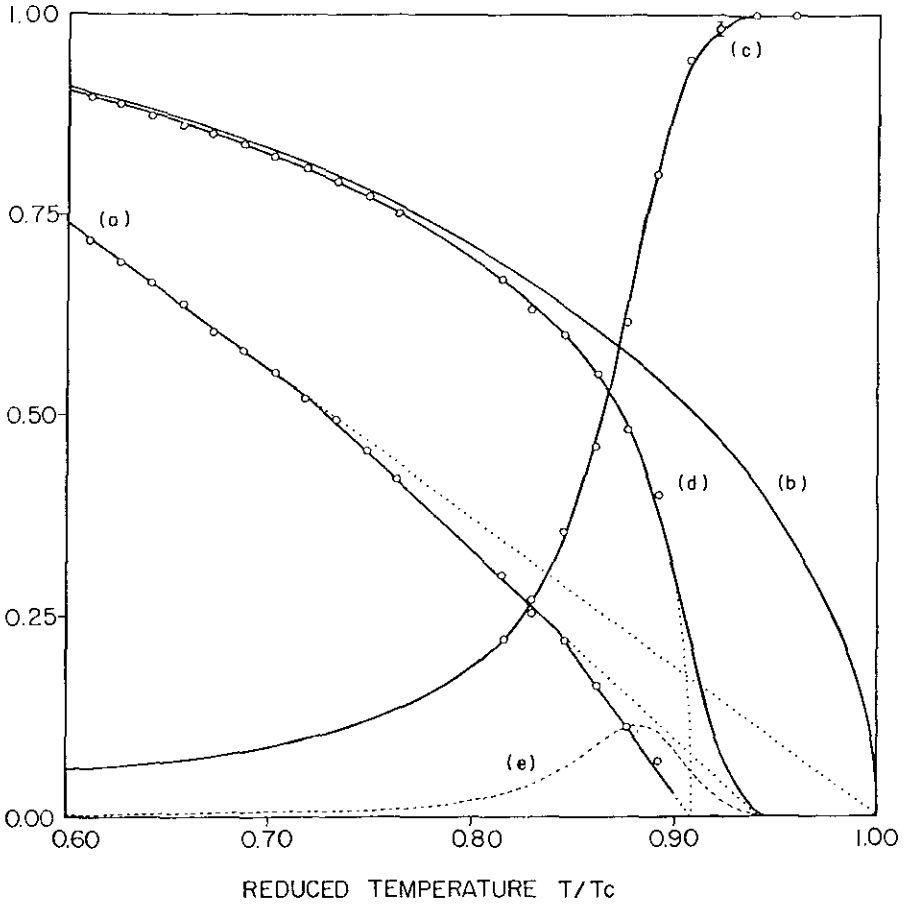

Fig. 1.8 - Dependência de (a) $|H(T)/H(0)|^3$, (b) e (d) $H(T)/H(0)$, (c) $m_p(T)$, (e) $P(T)$ versus T/T_c |25|

No anexo A-4, interpretamos o comportamento magnético de "microcristais", utilizando o modelo molecular, para mostrar que a distribuição de volume das "partículas" é fortemente responsável por suas propriedades magnéticas. O alargamento das linhas Mössbauer foi interpretado em termos de uma distribuição de campo hiperfino P (H), que é, por sua vez, causado por uma distribuição de volume P (V). O trabalho propõe uma distribuição Lorentziana para P (V)

$$P(V) = \frac{B}{(V - V_0)^2 + (\Gamma/2)^2} \qquad 1.37$$

onde V_0 é o volume mais provável e Γ a largura da distribuição. Os valores ajustados de V_0 e Γ, para uma amostra de $FeOHSO_4$, foram respectivamente 0.52×10^{-18} cm^3 (d = 100 Å) e 4.19×10^{-12} cm^3 (Γ = 20 Å). A magnetização da amostra foi calculada segundo a expressão

$$M = \int_0^{\infty} P\,(V)\, M\,(V)\, dV \quad , \qquad 1.38$$

onde M (V) é obtida pelo modelo molecular para S = 1/2

$$M\,(V) = \frac{1}{2} \tanh \left[\beta\,(J_z + KV)\, M\,(V)/2 \right] \quad , \qquad 1.39$$

onde $\beta = (k\,T)^{-1}$. Com a expansão da expressão de M (V) no limite de M (V) → 0, a temperatura de transição T_c (V) fica dada por

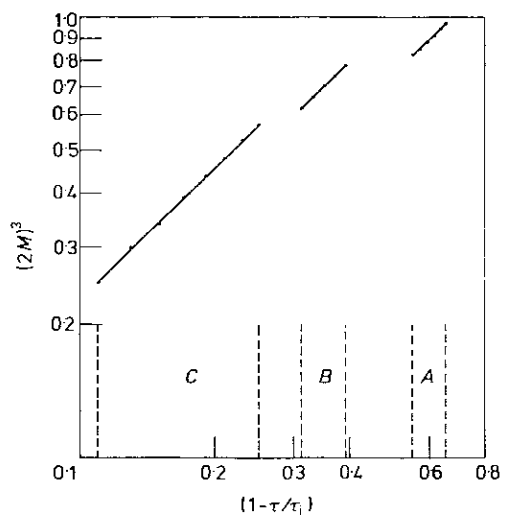

Fig. 1.9 - Dependência de $(2M)^3$ versus $(1 - \tau/\tau_i)$, para diferentes valores de temperatura críticas, τ_i |26|

$$k\,T_c\,(V) = (J_z + \mathbb{K}V)/4 \quad . \qquad 1.40$$

A equação anterior fornece a temperatura de transição T_c para um grão de volume V. Assim a distribuição de volume P (V) implica em uma distribuição de temperaturas críticas P (T_c). Os resultados experimentais foram ajustados para a curva de $(2M)^3$ versus temperatura reduzida, ao longo de três trechos distintos. Estes trechos foram ajustados por retas, indicando que M (T) obedece à lei de potência para 1/3. A presença dos três trechos foi interpretada dentro da idéia de que as "partículas" maiores demoram mais a se desordenar |26|.

No anexo A-5, buscamos um tratamento mais elaborado da interpretação das propriedades magnéticas de amostras policristalinas de $FeOHSO_4 \cdot xH_2O$. No anexo A-3 e A-4 consideramos a existência de uma única distribuição de "Clusters" e conseqüentemente uma única distribuição de temperatura críticas. Agora levaremos em conta a existência de mais de uma distribuição de "partículas" e conseqüentemente mais de uma distribuição de temperaturas críticas. Além de conseguirmos um melhor ajuste para os resultados experimentais, teremos ainda uma correlação entre as propriedades magnéticas do material e o fenômeno de ordem e desordem a curta e longa distância |27|.

Para ajustar o campo interno (H_0), admitimos que

$$\frac{M(T)}{M(o)} = \frac{H_0(T)}{H_0(o)} = D\left(1 - \frac{T}{T_c}\right)^{\beta} \qquad 1.41$$

e utilizamos a expressão

$$\frac{1}{2} - M = \sum_{\nu=0}^{z} \frac{z! m^{\nu} (1 - m)^{z-\nu}}{\nu\,(z - \nu)!\,\{\exp(\beta \mu + 2 M J \nu) + 1\}} , \quad 1.42$$

levando em conta a dependência da densidade de átomos magneticamente ordenados como função da temperatura

$$m(T) = \lambda \left[1 - \sum_{j=1}^{2} \alpha_i \frac{I_p^i(T)}{I_p(T')} \right] \quad 1.43$$

onde λ representa a densidade de átomos magneticamente ordenados próximos a zero Kelvin e α é dado, no nosso caso, por

$$\sum_i \alpha_i = \alpha_1 + \alpha_2 = 1 , \quad 1.44$$

onde α_1 e α_2 representam as frações de átomos de Fe contidas nas partículas com diâmetros médios em torno de d_1 e d_2, respectivamente. $I_p(T')$ é a intensidade das linhas paramagnéticas a uma temperatura T e $I_p(T')$ é a intensidade das linhas paramagnéticas onde a intensidade das linhas magnéticas é considerada nula. Isto ocorre à temperatura T'.

Nos ajustes do campo interno (H_0), o valor de β e D encontrados é, dentro do êrro experimental, iguais a $\beta = 1/3$ e $D = 1.22$. O valor para $\beta = 1/3$ foi ajustado para todas as amostras independentemente dos trechos considerados. A expressão para $I_p^i(T)/I_p(T')$ foi ajustada por

$$I_p^i(T)/I_p(T') = \begin{cases} \dfrac{\tan^{-1}\dfrac{2(T-T_{0i})}{\Gamma_{1i}} + \tan^{-1}\left(\dfrac{2\,T_{0i}}{\Gamma_{1i}}\right)}{\tan^{-1}\left(\dfrac{2\,T_{0i}}{\Gamma_{1i}}\right) + \dfrac{\Gamma_{01}\sqrt{2\pi}}{\Gamma_{1i}}}, & 0<T<T_{0i} \\ 1 - \dfrac{2\sqrt{2\pi}\,\Gamma_{0i}\left|1 - \operatorname{erf}\left(\dfrac{T - T_{0i}}{\Gamma_{01}\sqrt{2\pi}}\right)\right|}{\Gamma_{1i}\left[\tan^{-1}\left(\dfrac{2\,T_{0i}}{\Gamma_{1i}}\right) + \dfrac{\Gamma_{0i}\sqrt{2\pi}}{\Gamma_{1i}}\right]}, & T > T_{0i} \end{cases} . \qquad (1.45)$$

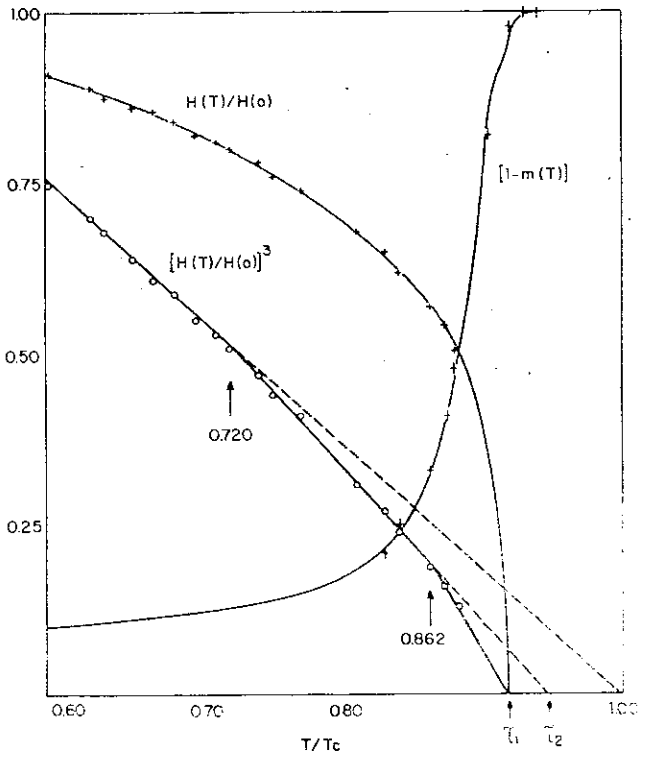

Fig. 1.10 - Dependência de $H(T)/H(0)$, $|H(T)/H(0)|^3$, $m_p(T)$ versus T/T_c. O ajuste teórico corresponde as linhas cheias e os pontos marcados correspondem aos resultados experimentais |27|

Tendo em vista a existência de uma distribuição de campo hiperfino P(H) e a presença de um desordenamento por trechos devido a diferentes classes de partículas, a distribuição de temperatura segue a expressão

$$P(T) = \frac{dm(T)}{dT} = \frac{d}{dT} \sum_i \alpha_i \, I_p^i(T)/I_p(\theta) \qquad 1.46$$

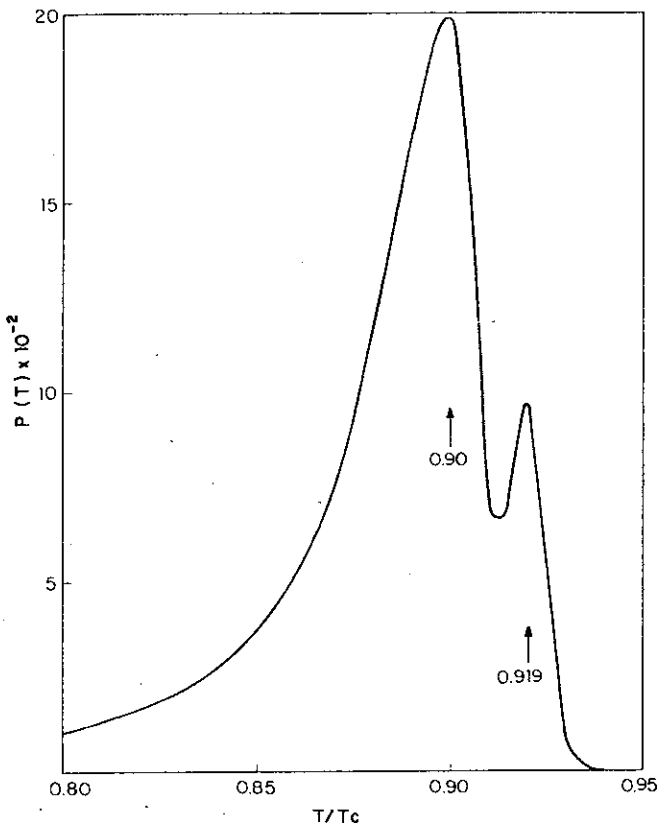

Fig. 1.11 - Distribuição de temperaturas críticas versus T/T_c |27|

S . M. Bhagat e colaboradores (1981) utilizaram uma expressão empírica para descrever o alargamento da linha de Ressonância Paramagnética (Γ) em função da temperatura dada por:

$$\Gamma = \Gamma_o + \Gamma_1 + \exp - \left(\frac{T}{T_o}\right) \qquad 1.47$$

onde Γ_1 e T_o são parâmetros empíricos associados com o "congelamento" dos spins e Γ_o é a largura de linha a uma temperatura elevada comparada com T_o (28).

No anexo A-6 apresentamos um modelo para explicar o alargamento das linhas de Ressonância Paramagnética Eletrô

nica (EPR) em função da temperatura, para uma amostra contendo partículas finas de hidroxisulfato de ferro-III. |29|. Tal modelo tem sido utilizado para explicar algumas propriedades de vidros de spin (ver anexo C-1) |30|.

Para explicar o alargamento da linha de EPR foi utilizado o modelo de um ferromagneto diluido constituido por um "cluster" infinito de spins coexistindo com uma distribuição de "clusters" finitos com dimensões centradas em torno de valores médios. Dentro deste modelo consideramos as ondas de spins geradas nos cluster infinito e seu acoplamento com os clusters finitos, através de um mecanismo de relaxação, induzido pelo campo de microondas.

O efeito da interação entre os "clusters" finitos e as ondas de spins é provocar nestas um decaimento ($\Omega(\omega)$). Este decaimento é associado ao alargamento da linha de ressonância $\delta\Gamma = \delta\Omega(\omega)/\hbar\gamma$. Considerando o fato de termos uma distribuição nas dimensões dos "clusters" finitos e uma distribuição de barreiras de energias para os "clusters" dentro de um potencial duplo e assimétrico, calculamos o valor médio de $\delta\Gamma(\omega)$ e obtemos $\Delta\Gamma$ como função de T dada por :

$$\Delta\Gamma_j(\omega) = \frac{\pi S N^i D^2}{h N_o v_o^i} \exp - \left(\frac{T}{T_f}\right) \qquad 1.48$$

S = spin no cluster infinito

N^i = número de clusters finitos com diâmatros centrados em torno do valor médio α_i

D = constante de acoplamento para interação anisotrópica

γ = razão giromagnética

N_o = número de spins no cluster infinito

v_o^i = energia de ativação associada aos clusters finitos com diâmetros centrados em torno de d_i

ω = freqüência da radiação de excitação

T_f = temperatura freezing

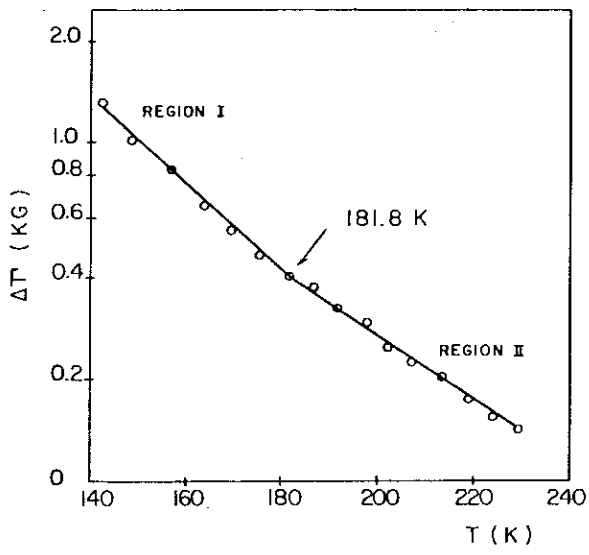

Fig. 1.12 - Dependência do alargamento da linha de EPR em função da temperatura |29|

No anexo C-2, o alargamento das linhas Mössbauer em função da temperatura foi explicado utilizando o modelo de relaxação clássico de Debye para um sistema do tipo citado anteriormente (anexo A-6). Assumimos que o canal de relaxação é através do momento magnético (μ) dos clusters finitos. Admitindo uma distribuição de barreiras de energia através da mesma função utilizada no modelo anterior e tomando os valores medios para o alargamento da linha Mössbauer obtemos $\Delta\Gamma$ como função de T dada por :

$$\Delta\Gamma\ (T) = \Gamma'\ \left(\frac{T}{\Theta}\right)\ \exp\ \left(\frac{T}{\Theta}\right) \qquad 1.49$$

onde Γ' e Θ são parâmetros empíricos. O significado físico de Θ é que a temperaturas $T > \Theta$ o momento dos "clusters" funcionam como um canal de relaxação do sistema [31].

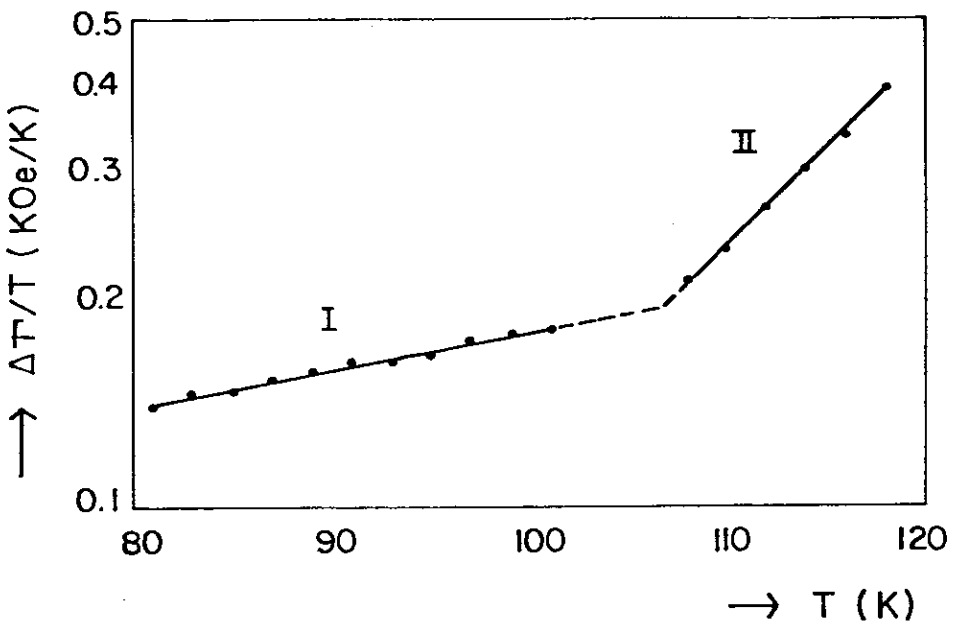

Fig. 1.13 - Dependência da razão $\Delta\Gamma/T$ versus T

1.3 - PREPARAÇÃO DO MATERIAL $FeOHSO_4 . xH_2O$ E RESULTADOS OBTIDOS

O material que nós utilizamos, de fórmula molecular $FeOHSO_4$ (hidroxisulfato de ferro-III) pode ser obtido através de uma série de reações de decomposição térmica a partir do $FeSO_4 . 7H_2O$.

A investigação de alguns produtos da decomposição térmica do composto $FeSO_4.7H_2O$, através da técnica Mössbauer, tem sido realizada por vários estudiosos.

Vértes e colaboradores (1970), investigaram misturas dos produtos da decomposição térmica, e observaram que um destes produtos, à temperatura ambiente, possui um deslocamento isomérico (δ), correspondente a Fe(III) iônico |32 e 33|.

Gallagher e colaboradores (1970), também estudaram a decomposição térmica dos sulfetos de Fe(II). Utilizaram análise térmica diferencial, análise de gás e termo-gravimetria. Os espectros Mössbauer indicam a presença de vários produtos da decomposição térmica. Um destes produtos possui um desdobramento quadrupolar ΔE_Q = 1.40 mm/seg., a 317°C e um deslocamento isomérico correspondente a Fe(III) iônico |34|.

No anexo A-1. mostramos que aquecendo amostras de $FeSO_4.xH_2O$, um novo composto é formado e seu espectro Mössbauer possui duas linhas bem resolvidas correspondentes a um desdobramento quadrupolar ΔE_Q = 1,45 ± 0.02 mm/seg.; à temperatura ambiente |35|. No anexo A-2, mostramos também, que este composto (chamaremos de composto - A) de fórmula molecular $FeOHSO_4$, é magneticamente ordenado, à temperatura do nitrogênio líquido. Este composto (A) em uma atmosfera saturada com vapor d'água transforma-se em um outro composto (chamaremos de composto - B) de fórmula molecular $FeOHSO_4.2H_2O$, e apresenta à temperatura ambiente, um espectro Mössbauer com um desdobramento quadrupolar ΔE_Q = 0.97 ± 0.02 mm/seg. Este composto

- B, não possui desdobramento magnético à temperatura de nitrogênio líquido [36].

Os absorvedores Mössbauer (ver anexo E - parte 2) foram preparados aquecendo-se o composto $FeSO_4.7H_2O$ analiticamente puro.

Para fazer o estudo de decomposição térmica, procedemos de maneira convencional. Analisamos os produtos de decomposição térmica, utilizando as técnicas:Mössbauer, Infravermelho, Raios-X, Microscopia Eletrônica, Ressonância Paramagnética Eletrônica, Magnetômetro, Fotoacústica, Termo-gravimétrica e Termo-diferencial. [ver anexos A, B, C, D e E].

Os produtos da decomposição térmica, foram inicialmente selecionados a partir da análise termo-diferencial (Fig. 1.14, pág. 50). Os espectros Mössbauer destes produtos apresentam, como nas ref. 32, 33, e 34, misturas de vários materiais (Fig. 1.15 - pág. 51).

Utilizando-se a análise termo-gravimétrica, para estudar a perda de peso em função da temperatura (Fig. 1.16 e 1.18 - pág. 52, 53), e os espectros infravermelho dos produtos desta análise (Fig. 1.17 e 1.19 - pág. 52 e 53), constatou-se que a saída d'água nos compostos de sulfato de ferro hepta, tetra e monohidratado é lenta e pode ser confirmada através da evolução dos parâmetros Mössbauer (Fig. 1.21 - pág. 54) [36].

Expondo o composto A, à temperatura ambiente e em uma atmosfera saturada d'água, após duas semanas, aproximadamente, um novo espectro é observado (Fig. 1.22 - pág. 55). Es

te composto - B, quando aquecido a 110°C, por alguns dias, apresenta o mesmo espectro Mössbauer e infravermelho do composto - A. No espectro infravermelho (Fig. 1.23 - pág. 55) o composto - A apresenta uma absorção próxima a 3.500 cm^{-1} bastante estreita e um pouco acima da absorção que ocorre no espectro correspondente ao composto - B. O composto - B apresenta uma absorção alargada em torno de 3.500 cm^{-1} e uma outra em torno de 1.650 cm^{-1}. A banda do SO_4^{2-} é característica em ambos |27, 36 e 37|.

Durante o processo de hidratação do composto - A, acompanhado através da espectroscopia Mössbauer, infravermelho e raios-X (Fig. 1.24, 1.25 e 1.26 - pág. 56, 56, e 52), de dois em dois dias, retiramos uma porção do material exposto à umidade e reaquecemos a 200°C por 200 horas. Com este procedimento voltamos quimicamente ao composto - A. A reversibilidade do processo de hidratação foi acompanhada por espectroscopia Mössbauer, infravermelho e raios-X. Os espectros Mössbauer apresentaram os mesmos parâmetros, à temperatura ambiente, ΔE_Q = 1,45 mm/seg e δ_{Fe} = 0.44 mm/seg. Os espectros de infravermelho e raios-X, também apresentaram os mesmos espectros (298 K) do composto - A. Os espectros Mössbauer (Fig. 1.27 - pág. 57) à temperatura do nitrogênio líquido, desta seqüência de amostras ($FeOHSO_4$), mostram claramente uma variação de granulação nas diferentes amostras, onde o efeito de superparamagnetismo é evidente. Este processo de alteração na granulação da amostra $FeOHSO_4$ ao longo do tratamento descrito, pode ser visto pela dependência do campo interno (H_0), nos espectros Mössbauer em função dos dias de hidratação, co-

mo mostra a Fig. 1.28 - pág. . |27|.

Podemos comparar a evolução do caráter superparamagnético em relação ao caráter ferromagnético, ao longo do processo:

$$A \rightarrow x\ A + (1 - x)\ B \rightarrow A\ ,$$

através das intensidades das linhas magnéticas e paramagnéticas dos espectros Mössbauer (Fig. 1.27 - pág.), como mostra a Fig. 1.29 - pág. . Uma comprovação direta da presença de distribuição de granulação foi obtida por microscopia eletrônica, como mostra a fotografia da Fig. 1.32 - pág. . A fotografia da Fig. 1.30b - pág. 59 , mostra o material, antes de ser aquecido, isto é, parcialmente hidratado |27, 37|.

O diagrama de distribuição do diâmetro das partículas (Fig. 1.31 - pág. 59), correspondente a um dos materiais preparado a 250°C, pode ser comparado com o diagrama (Fig. 1.32 - pág. 60), de um outro material - A, preparado a 300°C.

Os espectros Mössbauer correspondentes ao material - A, preparado a 300°C, obtidos a várias temperaturas (Fig. 1.33 - pág. 60), a T = 112 K apresenta uma figura de seis linhas com boa resolução, um razoável alargamento das linhas internas e a presença das linhas paramagnéticas que aumentam de intensidade com o aumento da temperatura. Tais características sugerem que existe uma distribuição de campo hiperfino $P(H_0)$ |25|.

Utilizaremos a partir de agora, uma nova notação

para caracterizar os materiais: A e B ($FeOHSO_4 . xH_2O$), ao longo do processo de preparação :

$$FeSO_4 . H_2O \xrightarrow[\Delta t]{T} A\ (T)$$

hidratação : $A\ (T) \longrightarrow AB\ (T)_d \longrightarrow B\ (T)$

reaquecimento : $B\ (T) \longrightarrow BA\ (T)^j_d \longrightarrow A\ (T)^j_d$

onde T = temperatura a qual o material foi preparado

d = dias de hidratação

j = temperatura a qual o material foi reaquecido.

Três conjuntos de amostras de $FeOHSO_4$ com diferentes amostragens de granulação foram estudadas por espectroscopia Mössbauer, a diferentes temperaturas. As amostras utilizadas, correspondem aquelas com zero, quatro e seis dias de hidratação e posterior aquecimento, a 200°C, e que foram inicialmente preparadas a 250°C. Os espectros Mössbauer correspondente as amostras $BA\ (250)^{200}_0$, $BA\ (250)^{200}_4$ e mostrados nas Figs. 1.34 e 1.35 - pág. 61 e 61 apresentam as mesmas características gerais daquelas discutidas para a material A(300). O surgimento das linhas paramagnéticas se dão, porém, a diferentes temperaturas (Fig. 1.36 - pág. 62) e os diagramas H_o^3 versus T mostram trechos retilíneos com diferentes inclinações, porém, curvadas em sentidos opostos ao gráfico correspondente ao material A (300) |27|.

O desdobramento quadrupolar (ΔE_Q), em função da temperatura (Fig. 1.37 - pág. 62), também foi acpmpanhado desde o surgimento das linhas paramagnéticas até a temperatura de 209 K, para o material BA $(250)_o$.

Os espectros de Ressonância Paramagnética Eletrônica correspondentes ao material A(250), a várias temperaturas (Fig. 1.38 - pág. 63), apresentam um alargamento assimétrico, característico de uma distribuição de campo hiperfino P (H). Estes espectros apresentam também um alargamento na linha de ressonância (Fig. 1.39 - pág. 63), à temperaturas $T<T_c$ |29|. O material A(300), apresenta as mesmas características gerais do material A (250), o gráfico $\Delta\Gamma_i$ versus T (Fig. 1.40 - pág. 64), mostram trechos característicos a T_B^i como função do volume dos "clusters" e da temperatura |38|.

O comportamento da largura de linha ($\Delta\Gamma/T$ versus T) dos espectros Mössbauer (Fig. 1.42 - pág. 65), apresentam trechos lineares também característicos relacionados à distribuição de volume e a sua natureza superparamagnética |31|.

No anexo C - 5, apresentamos um novo tipo de magnetômetro |39|. Este magnetômetro foi utilizado para estudar o comportamento da magnetização (M), em função do campo (H) e da temperatura (ver anexo D - 2). Os gráficos M (H,T), material A (300), mostram (Fig. 1.44 - pág. 66) também, as fases de alto e baixo ordenamento, devido ao carater superparamagnético da amostra A (300). Os diagramas M^3 versus T (Fig. 1.47 pág. 68) mostram trechos lineares com diferentes inclinações características de interações a curta e a longa distância |40|.

No anexo B - 3 apresentamos um novo tipo de célula fotoacústica |41|. Esta célula foi utilizada para estudar o comportamento do calor específico como função da temperatura. O gráfico do sinal fotoacústico, em função da temperatura, para o material A(300), mostra (Fig. 1.45 - pág. 67) também trechos lineares com diferentes inclinações (ver anexo D - 4). O gráfico $1/_{ST}{}^2$ versus T^2 mostram (Fig. 1.46 - pág. 67) picos característicos a ordem e a desordem magnética na amostra, constituída de "partículas" finas do material $FeOHSO_4$ |42|.

1.4 - DISCUSSÕES

A análise de perda de peso e termo-diferencial em função da temperatura em atmosfera oxidante, por exemplo ar, nos possibilita propor um esquema para a decomposição térmica de $FeSO_4 \cdot 7H_2O$:

% MASSA					T(°C)	t(min)
100,0				$FeSO_4 \cdot 7H_2O$	25	0
				$\downarrow -H_2O$		
81,37	$FeSO_4 \cdot 7H_2O$	+		$FeSO_4 \cdot 4H_2O$	144	
				$\downarrow -H_2O$		
62,93	$FeSO_4 \cdot 4H_2O$	+		$FeSO_4H_2O$	172	25
				$\downarrow -H_2O + O_2$		
62,90	$FeSO_4H_2O$	+		A	195	30
				$\downarrow$		
61,20				A	195	780

composto-B é $FeOHSO_4.2H_2O$. A fórmula empírica para o composto-A pode ser $FeOHSO_4$ ou $FeOHSO_4H_2O$.

Gallagher e col., (ref. 34), propuseram o seguinte esquema em atmosferas não oxidantes

$$FeSO_4H_2O \xrightarrow{(200 - 300)^oC} FeSO_4 + H_2O$$

$$2\ FeSO_4 \xrightarrow{(475 - 575)^oC} Fe_2O_2SO_4 + SO_2$$

$$Fe_2O_2SO_4 \xrightarrow{(550 - 675)^oC} Fe_2O_3 + SO_3$$

A decomposição no ar, na região de $(150 - 500)^oC$:

$$2\ FeSO_4H_2O + \tfrac{1}{2}\ O_2 \longrightarrow 2\ FeOHSO_4 + H_2O$$

$$2\ FeOHSO_4 \longrightarrow Fe_2O(SO_4)_2 + H_2O$$

e

$$2\ FeSO_4H_2O \longrightarrow 2\ Fe_2SO_4 + H_2O$$

$$2\ FeSO_4 + \tfrac{1}{2}\ O_2 \longrightarrow Fe_2O(SO_4)_2$$

A Fig. 123 mostra o espectro infravermelho dos compostos $FeSO_4.7H_2O$, A e B. A absorção na região de 1100 cm^{-1} foi atribuída ao modo ν^3 de vibração do ion SO_4^{--}. Quando a simetria do ion sulfato é Td, o modo é degenerado, como no caso do $FeSO_4.7H_2O$. Quando a simetria do ion sulfato é C_{3v}, isto é quando um dos oxigênios está ligado ao metal a degenerescência é levantada. Esse é o caso no composto-A.

O composto B mostrou desdobramento adicional da absorção infravermelho do ion sulfato quando comparado com o

composto-A, que pode indicar que em último caso alguns dos íons SO_4^{2-} estão ligados via dois oxigênios ao ferro.

O espectro infravermelho do $FeSO_4.7H_2O$ e do composto B mostra absorção devido a HOH em 1650 cm^{-1} e uma ampla absorção em torno de 3450 cm^{-1}. Essas informações indicam a presença de água. Contudo o composto A mostra uma absorção muito ligeira em 1650 cm^{-1} e a absorção OH^- próxima de 3500 cm^{-1} é abrupta e aparece a uma freqüência ligeiramente mais alta do que nos dois outros espectros infravermelhos. Essas informações sugerem que o composto-A não contêm água, mas contêm OH^-.

Um estudo dos parâmetros Mössbauer da Fig. 1.21 e uma comparação com os resultados obtidos na termo-gravimetria juntamente com os espectros de infravermelho, nos possibilita propor um esquema para a decomposição térmica do sulfato de ferro monohidratado.

A decomposição em atmosferas não oxidantes, (por exemplo N_2) é :

$$FeSO_4.H_2O \xrightarrow[\text{por 40 horas}]{200^oC} FeSO_4 + H_2O$$

A decomposição em atmosferas oxidantes, (por exemplo ar) é significantemente diferente :

$$FeSO_4.H_2O + \frac{1}{2}\,O_2 \xrightarrow[\Delta t = (12\ ;\ 6)\ \text{horas}]{T = (220\ ;\ 230)^oC} FeOHSO_4 + H_2O$$

onde Δt é o tempo gasto para acumular o espectro Mössbauer (veja Fig. 1.21)

Uma proposta para a estrutura do $FeOHSO_4$ é aquela que corresponde a um dímero de fórmula estrutural plana como a que mostramos abaixo :

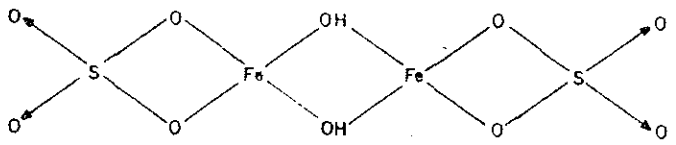

O valor elevado do desdobramento quadrupolar (ΔEq = 1.45 mm/seg.) do composto $FeOHSO_4$, em relação a compostos de Fe^{III} em alto spin, pode ser associado à estrutura dímera proposta anteriormente. Nesta estrutura, o anel de quatro membros, mostrado abaixo, não é coplanar, o que leva o sítio do Fe a fugir bastante

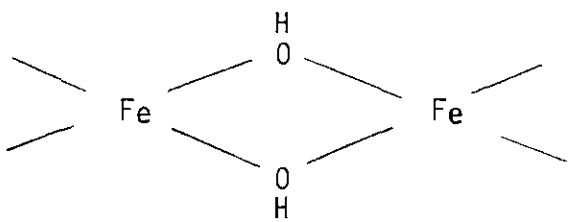

de uma simetria octaédrica, conduzindo a um valor elevado do desdobramento quadrupolar |27|. A afirmação de que temos no $FeOHSO_4$, o Fe^{III} em alto spin é apoiada pela dependência do desdobramento quadrupolar com a temperatura (veja Fig. 1.37). O desdobramento quadrupolar permanece praticamente constante dentro do intervalo de temperatura considerado.

Embora um ciclo de hidratação e desidratação não altere quimicamente o composto - A, modifica profundamente suas propriedades magnéticas. Isto é evidenciado pelos espectros Mössbauer a nitrogênio líquido (Fig. 1.27). Os resultados de microscopia eletrônica mostram que após um ciclo de hidratação / desidratação ocorre uma modificação acentuada na granulação do material (Fig. 1.30). O resultado final pode ser um acréscimo bem como um decréscimo no diâmetro médio dos grãos. Se a desidratação é suficientemente lenta ocorre um acréscimo no diâmetro médio dos grãos e se, por outro lado, a desidratação não for suficientemente lenta pode ocorrer fraturas nos grãos, o que levaria até mesmo a uma redução no diâmetro médio dos grãos. Assim quem domina o processo de crescimento dos grãos é a hidratação. Isto pode ocorrer por dois mecanismos; difusão e fase líquida. A difusão é caracterizada por um movimento simultâneo de átomos (moléculas) e vacâncias na interface entre dois grão [37]. A sinterização em fase líquida é caracterizada por uma transferência de massa entre superfícies de alta (aquelas com pequeno raio de curvatura convexa) e baixa (aquelas com pequeno raio de curvatura côncava) energia. Em comum, os dois mecanismos envolvem transporte de massa seguido por um processo de recristalização. A presença da recristalização é bem sugerida nos espectros de raios-x, pela presença de linhas alargadas (Fig. 1.26).

A análise dos espectros Mössbauer (N_2L) da série BA $(250)_d$ mostra a presença de um diâmetro crítico D_c associado ao valor máximo do campo interno (Fig. 28). Para grãos de

$FeOHSO_4$ este diâmetro é seguramente acima de 100 Å e abaixo de 1000 Å. Sendo assim, o comportamento magnético da amostra A(300), com uma distribuição cunhada em torno de dois diâmetros médios (d_1 = 50 Å e d_2 = 110 Å) deve ser analisado levando em consideração sua topografia. Este deve ser o caso ao se analisar a transição de fase magnética tomando o campo interno como parâmetro de ordem da transição. É natural esperar não uma temperatura crítica mas sim uma distribuição bimodal de temperaturas críticas. As larguras da distribuição de temperaturas críticas deverão ser coerentes com as larguras da própria distribuição de diâmetro das partículas. As posições dos máximos da distribuição de temperaturas críticas deverão refletir o fato de que as partículas com diâmetros centrados em torno de 50 Å devem ter uma ordem magnética menor que as partículas com diâmetros centrados em torno de 110 Å. Estes fatos são evidentes após uma análise das figuras (Fig. 1.32 e 1.43). Igualmente importantes são os pontos de inflexão que aparecem nos diagramas de $\left[H_0(T) / H_0(D) \right]^3$ x T (Fig. 1.36). Eles refletem mudanças na ordem magnética dos componentes do sistema. Tais pontos indicam as regiões em que cada componente da distribuição bimodal pode ser analisado sob o ponto de vista de ordem a curta e longa distância. Finalmente, independente da ordem magnética associada a cada componente da distribuição bimodal e independente da faixa de temperatura considerada, a lei de potência é $\beta = 1/3$.

Os espectros Mössbauer da amostra A(300) (Fig. 1.33), apresentam linhas assimétricamente alargadas. Basicamente são

duas as origens; distribuição de campo hiperfino e fenômenos de relaxação. É possível analisar o alargamento relacionado à transição $|\ 1/2 > \rightarrow |\ 3/2 >$ através de um modelo de relaxação. O canal de relaxação é o momento magnético dos grãos, através de uma dinâmica envolvendo um potencial duplo e assimétrico. O momento magnético associado ao cluster funciona como canal de relaxação acima de uma temperatura Θ, relacionada à barreira de energia do potencial. O modelo utilizado admite um sistema de dois níveis com um mecanismo de relaxação do tipo de Debye |31|. A presença de uma distribuição de diâmetros sugere uma distribuição de energias de ativação. Utiliza-se então uma distribuição exponencial de energias de ativação para se calcular o valor médio do alargamento da linha Mössbauer ($\Delta\Gamma$). A temperatura abaixo de 106 K o comportamento de $\Delta\Gamma$ x T é dominado pela relaxação associada as partículas com diâmetros centrados em torno de 110 Å. Acima de 106 K o comportamento é dominado pela outra componente da distribuição bimodal |27 e 31|. O gráfico $\Delta\Gamma/T$ x T da figura 1.42 mostra uma inflexão em 106 K. A extrapolação do primeiro trecho ($T < 106$ K) do diagrama $\Delta\Gamma/T$ x T mostra que a linha Mössbauer será simétrica em 17.1K. Assim o diagrama $\Delta\Gamma/T$ x T ($0K < T < 130K$) deverá mostrar duas inflexões; 17.1 K e 106 K. Estes pontos refletem uma correlação muito forte entre a temperatura de transição da amostra (τ) e a temperatura de transição do composto $FeOHSO_4$ a campo zero (T_c). No anexo D - 1 mostramos que $\tau = \lambda \sum_i \alpha_i T_c$. Isto nos dá duas contribuições para o decréscimo da temperatura de transição ; $\delta_i = \lambda \alpha_i T_c$ ($i = 1, 2$). Tomando os valores λ, α_i ($i = 1, 2$) e T_c temos $\delta_i = 103.5$ K e $\delta_2 = 17.7$ K |43|.

Medidas de magnetização versus temperatura tomadas a diferentes valores de campo magnético externo contribuiram para oferecer uma visão mais detalhada do comportamento magnético da amostra A(300)|40|. As medidas foram realizadas com um magnetômetro de amostra vibrante (MVSM) |39|. A Figura 1.50 mostra claramente a presença de ordem magnética a curta e longa distância. Entretanto uma visão mais detalhada é obtida supondo que a lei de potência seja $\beta = 1/3$ em toda faixa de temperatura, independente do ordenamento magnético do sistema. Os dados de M^3 x T são mostrados na Fig. 1.45. Admitimos que os pontos de inflexão representam mudanças de ordenamento magnético. Isto nos possibilitou levantar um diagrama de fases para a amostra A(300) na faixa de temperaturas considerada (Fig. 1.51). Independente do campo magnético utilizado (veja Fig. 1.47) o diagrama M^3 x T apresenta inflexões em 111 K e 165 K. Estas temperaturas foram interpretadas como temperaturas mais provāveis de ativação do equilíbrio ferri / antiferromagnético nos "clusters" com $d_1 = 50$ Å ($T_A^1 = 111$ K) e $d_2 = 110$ Å ($T_A^2 = 165$ K). Observamos que o material A(300) apresenta um comportamento essencialmente ferrimagnético abaixo de 111 K. Admitimos que a energia térmica média associada a este processo de ativação ($k\,T_A^i$) é proporcional ã energia de "exchange" média (J^i). Assim devemos ter $J^1/J^2 \simeq T_A^1 / T_A^2 \simeq 0.673$. As medidas Mössbauer mostram que o campo interno (H_0) deve ser proporcional ã raiz quadrada do diâmetro médio dos "clusters" para diâmetros menores, que o valor crítico. Admindo que o campo interno seja proporcional ã energia de exchange, devemos esperar que

$J^1 / J^2 = (d_1 / d_2)^{1/2} \simeq 0.674$. Um segundo conjunto de pontos de inflexão, ao longo da linha D D' (Fig. 1.45), está relacionado à temperatura de bloqueio dos clusters. As temperaturas acima da linha D D' os clusters com diâmetros centrados em torno de $d_1 = 50$ Å passam para uma fase essencialmente superparamagnética (veja Fig. 1.51). A temperatura em que isto ocorre é a temperatura de bloqueio T_B . Sua relação com o campo externo é dada por

$$25\ K\ T_B \simeq 2\ K\ V + \beta\ \mu\ H_{ext}. \qquad 1.50$$

Ajustando os dados experimentais (linha D D') à equação anterior obtemos $\mu^1 = 1.01 \times 10^3\ \mu_B$, $T_B^1\ (H_{ext} = 0) = 117.5$ K e $K^1 = 3.1 \times 10^5\ j/m^3$. Observamos que $T_B^1\ (H_{ext} = 0)$ é próximo ao valor mais provável da temperatura de transição ($T_{01} = 118.5$ K) associada à distribuição de temperaturas críticas para os "clusters" com diâmetros em torno de $d_1 = 50$ Å [27].

Medidas de calor específico, utilizando uma célula fotoacústica, confirmam as interpretações relativas ao comportamento magnético multifásico da amostra A(300). O diagrama de $C/T \times T^2$ é mostrado na Fig. 1.46. Como seria de se esperar a Fig. 1.46 não mostra um pico acentuado. Na realidade as medidas de calor específico mostram vários picos sobressaindo de um envoltório alargado e bimodal. Os picos que sobressaem do envoltório representam temperaturas características da amostra A(300) obtidas utilizando-se muitas vezes técnicas diferentes (Mössbauer, EPR e magnetização).

As medidas da largura de linha de EPR indicam que o $FeOHSO_4$ deve apresentar uma fase de vidro de spin. A partir do alargamento da linha de ressonância é possível prever as temperaturas "freezing" para as partículas que compõem a distribuição bimodal na amostra A(300). O diagrama $\Delta\Gamma$ x T (Fig. 1. 40) mostra também a presença de inflexões. Estas certamente associadas às mudanças de ordenamento magnético no material |38|. Finalmente, baseando-se em recente experimentos realizados com outros sistemas (pseudobrokita e dados da literatura) é razoável sugerir que as temperaturas "freezing" devam ser obtidas, via medidas de EPR, em uma faixa de temperaturas em que o sistema seja essencialmente paramagnético, i.e., próximo de T_c.

1.5 - CONCLUSÕES

Resultados experimentais obtidos por medidas de Mössbauer, EPR, magnetização e fotoacústica indicam que o $FeOHSO_4$ apresenta um comportamento magnético multifásico entre as temperaturas de nitrogênio líquido e ambiente. Fases superparamagnéticas bem como equilíbrios ferri / antiferro são profundamente dependentes das características topográficas da amostra utilizada. Presença de distribuições multimodais de diâmetros de partículas devem ser considerados na determinação de distribuições de temperaturas características. Não se pode portanto esperar que modelos teóricos simples (por exemplo aqueles baseados em um único tipo de interação) sejam capazes de descrever o comportamento magnético de amostras de $FeOHSO_4$,

contendo distribuições de partículas, dentro de uma faixa ampla de temperatura. Entretanto qualquer proposta deve levar em conta um fato relevante : os resultados experimentais mostram que a lei de potência 1/3 é mantida dentro da faixa de temperatura e campos externo utilizados. Mais recentemente esta hipótese tornou-se fundamental na interpretação dos dados de magnetização.

1.6 - PROPOSTAS DE EXPERIÊNCIAS FUTURAS

O comportamento magnético multifásico observado em pequenos aglomerados de $FeOHSO_4$ a temperaturas acima de 77 K (N_2L) sugere novas experiências:

(1) Mössbauer a partir de hélio líquido; análise do comportamento do campo interno e da largura de linha.

(2) Ressonância paramagnética eletrônica em banda-Q a partir de nitrogênio líquido; análise da largura de linha e campo de ressonância.

(3) Susceptibilidade AC a partir de hélio líquido a diferentes frequências; análise da dependência do pico de susceptibilidade ($T = T_f$) com a freqüência e a comprovação da lei de Curie ou Curie - Weiss acima de T_f.

(4) Ressonância magnética nuclear do próton a partir de nitrogênio líquido, análise da conformação do anel $Fe(OH)_2Fe$.

(5) Calor específico via efeito fotoacústico (veja anexo-B),

a partir de hélio líquido; análise das contribuições eletrônica e de rede associadas aos processos de transições magnéticas | e |.

(6) Efeito fotoacústico de partículas finas de $FeOHSO_4$ dissolvidas em matrizes dielétricas (resinas acrílicas); análise da curva de absorção (deslocamento e alargamento) em função do comprimento de onda, temperatura, concentração e granulação.

Experiências recentes utilizando um magnetômetro de amostra vibrante (pequenas oscilações) | |, análise do comportamento do sinal fotoacústico na região de microondas | |, e medidas de calor específico via efeito fotoacústico | |, sugerem sua utilização em ligas metálicas amorfizadas ($Fe_x Si_{1-x}$, $Fe_x Au_{1-x}$, $Fe_x Ti_{1-x}$, etc.):

(1) Medidas de magnetização (usando MVSM) em função da temperatura e campo externo; análise do comportamento magnético das ligas metálicas com diferentes proporções e diferentes tratamentos térmicos.

(2) Comportamento do sinal fotoacústico (região de M.O.) em função de freqüência de modulação, temperatura e campo externo (Ressonância Ferromagnética | e |); análise de efeitos de superfície causados por diferentes tratamentos térmicos.

(3) Medidas de calor específico via efeito fotoacústico; estudo das contribuições eletrônica e de rede em transições de fase magnética.

(4) Efeito fotoacústico em partículas finas de metais e ligas dissolvidas em matrizes dielétricas; análise das curvas de absorção na região do visível e ultravioleta.

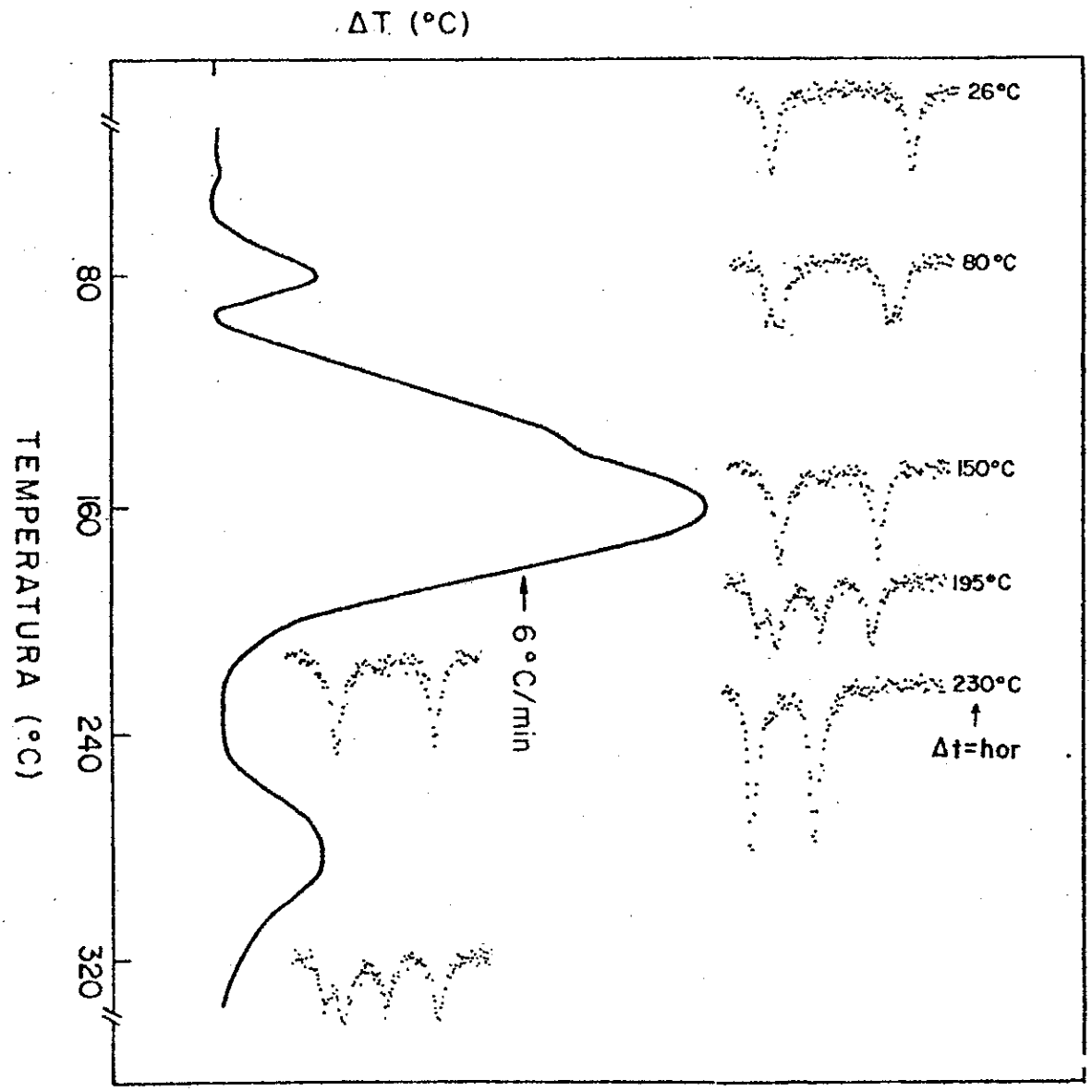

Fig. 1.14 - Análise termo-diferencial e espectros Mössbauer no ar, do composto $FeSO_4 \cdot 7H_2O$

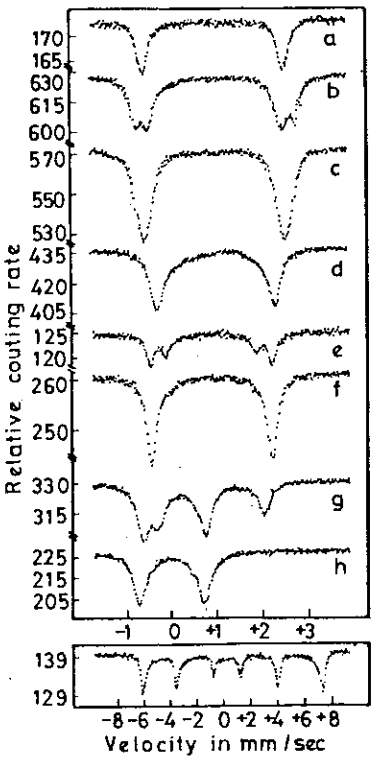

Fig. 1.15 - Espectros Mössbauer: (a) $FeSO_4.7H_2O$ a 25 °C; (b) $FeSO_4.7H_2O$ preparado a 52 °C em solução aquosa, espectro a 25 °C; (c) $FeSO_4.7H_2O$ preparado a 60 °C em solução aquosa, espectro a 25 °C; (d) $FeSO_4.7H_2O$ preparado a 70 °C em solução aquosa, espectro a 25 °C; (e) produto de (d) aquecido em atmosfera de N_2 a 180 °C, espectro a 25 °C; (f) produto de (e) aquecido em atmosfera de N_2 a 200 °C, espectro a 25 °C; (g) $FeSO_4.7H_2O$ preparado no ar a 180 °C, espectro a 25 °C; (h) produto de (g) aquecido a 220 °C, espectro a 220 °C; (i) espectro de (h) a 80 °K [35]

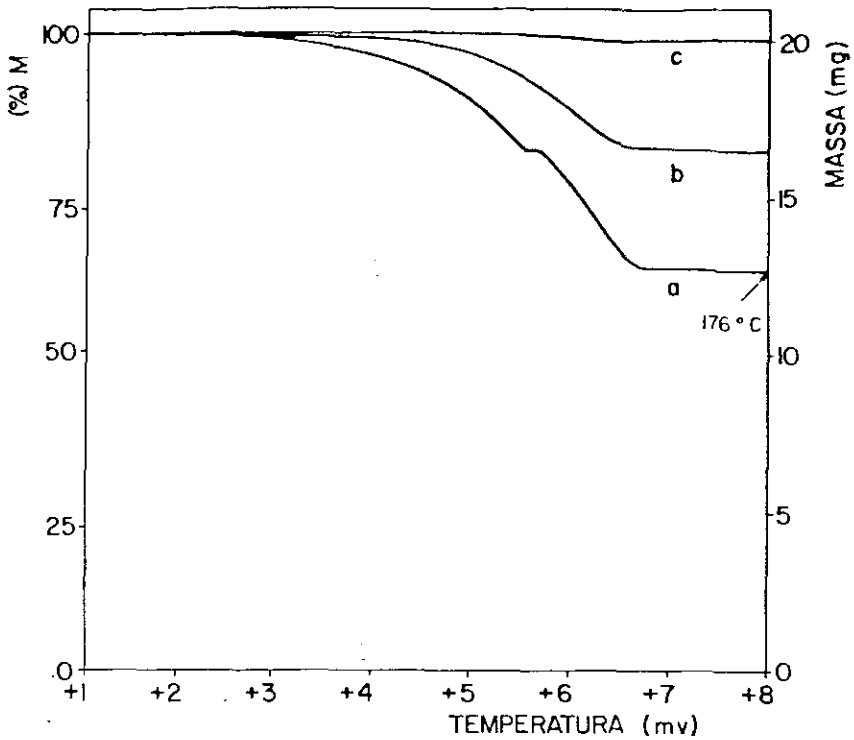

Fig. 1.16 - perda de peso em função da temperatura: (a) $FeSO_4.7H_2O$, (b) $FeSO_4.4H_2O$, (c) $FeSO_4.H_2O$

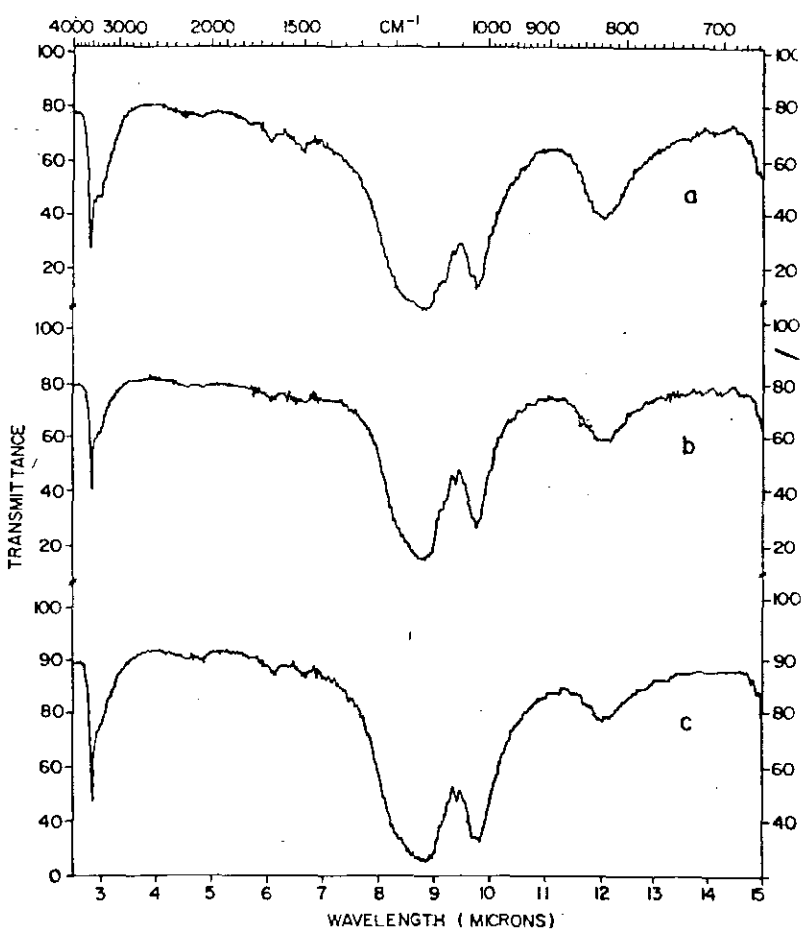

Fig. 1.17 - Espectros infravermelho dos produtos da análise da figura - 1.16: (a) produto da análise da fig. 1.16a, (b) produto da análise da fig. 1.16b, (c) produto da análise da fig. 1.16c.

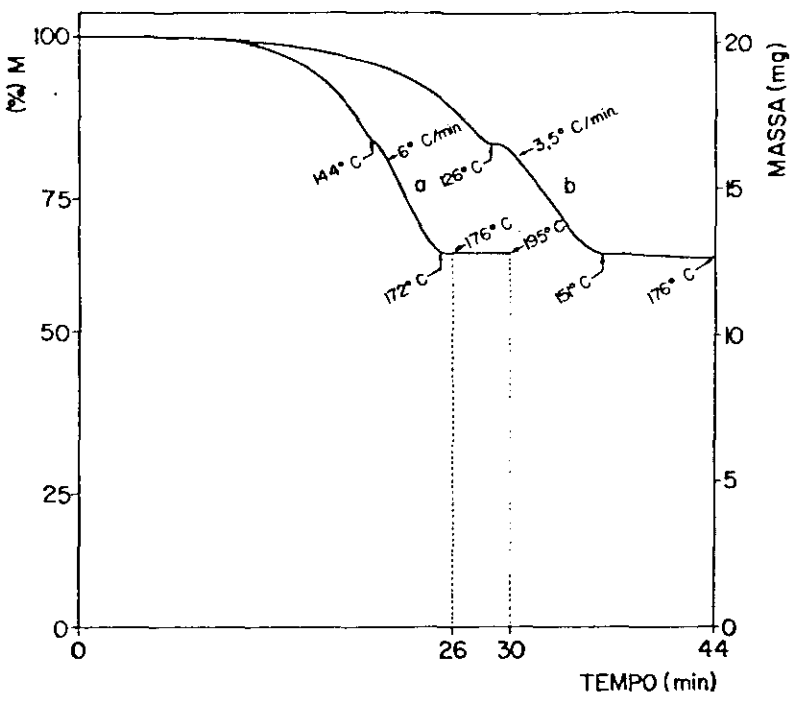

Fig. 1.18 - perda de peso em função da temperatura e do tempo: (a) 6 °C/min, (b) 3.5 °C/min. para o composto $FeSO_4.7H_2O$.

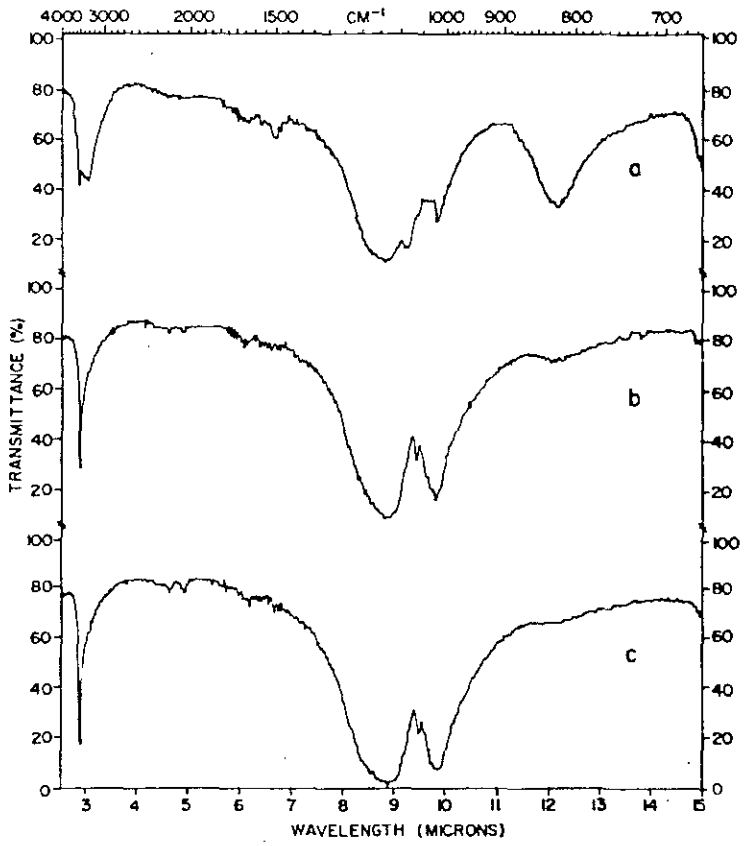

Fig. 1.19 - Espectros infravermelho dos produtos da análise da Fig. 1.18a: (a) produto da análise da fig. 1.18a; (b) produto de 1.18a aquecido a 195 °C no ar durante 300 min, (c) produto 1.18a aquecido a 195 °C no ar durante 780 min.

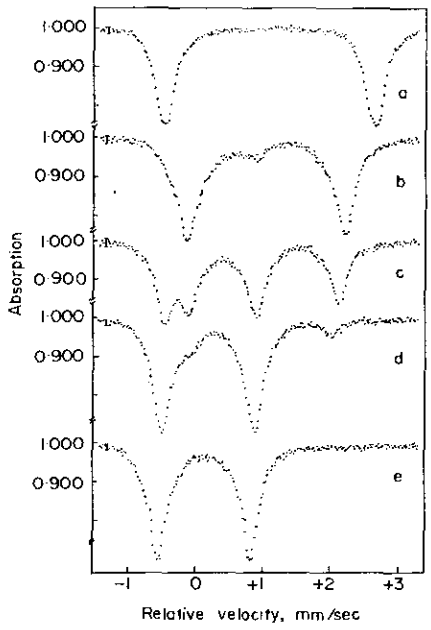

Fig. 1. Mössbauer spectra of: (a) $FeSO_4.H_2O$ at 300 K; (b) Sample (a) heated in air at 378 K for 12 hr Spectra at 378 K; (c) Sample (b) heated in air at 413 K for 12 hr spectra at 413 K in air; (d) Sample (c) heated in air at 453 K for 12 hr spectra at 453 K; (e) Sample (d) heated in air at 593 K for 12 hr spectra at 593 K.

Fig. 1.20 - Espectros Mössbauer: (a) $FeSO_4.7H_2O$ a 25 °C; (b) $FeSO_4.7H_2O$ aquecido no ar a 105 °C, espectro a 105 °C por 12 horas; (c) produto de (b) aquecido no ar a 140 °C por 12 horas; (d) produto de (c) aquecido no ar a 180 °C, espectro a 180 °C por 12 horas; (e) produto de (d) aquecido no ar a 300 °C, espectro a 300 °C por 12 horas.

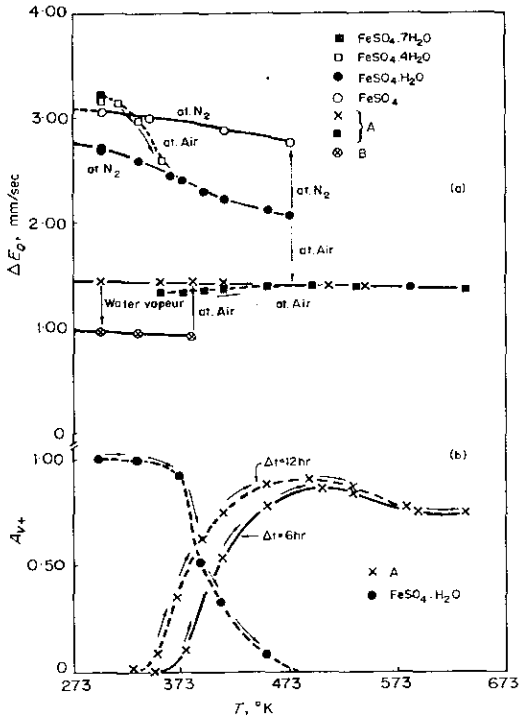

Fig. 6. Temperature dependence of Q.S. of various thermal decomposition products of $FeSO_4.7H_2O$. Temperature dependence of positive peak area (A_{v+}).

Fig. 1.21 - (a) Dependência do desdobramento quadrupolar com a temperatura dos produtos da decomposição térmica do composto $FeSO_4.7H_2O$. (b) Dependência em percentagem das áreas das linhas do espectro Mössbauer com a temperatura.

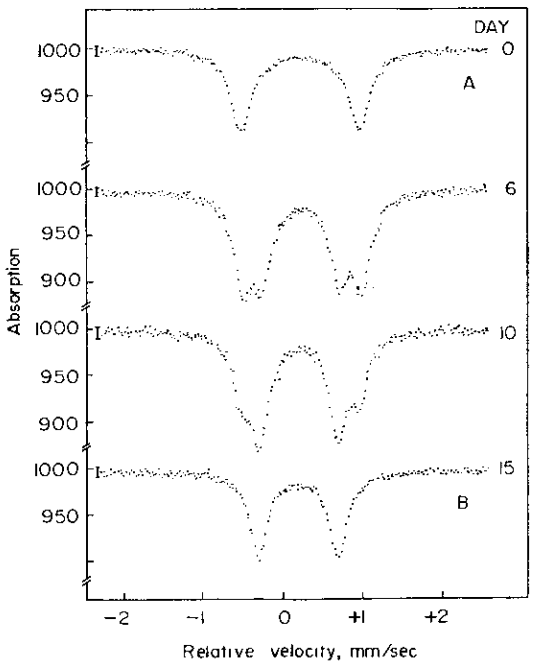

Fig. 2. Mössbauer spectras of sample A exposed to saturated aqueous vapourous atmosphere as a function of days.

Fig. 1.22 - Espectros Mössbaur à temperatura ambiente do composto - A exposto a uma atmosfera saturada d'água por 15 dias (composto - B).

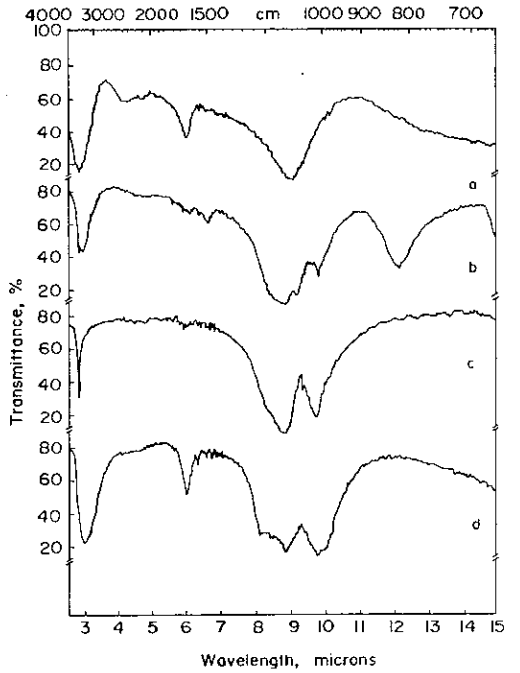

Fig. 3. I.R. spectras of (a) $FcSO_4.7H_2O$, (b) impure A, (c) pure A and (d) pure B.

Fig. 1.23 - Espectro Infravermelho de (a) $FeSO_4.7H_2O$; (b) composto - A com impurezas; (c) composto - A puro; (d) composto - B puro.

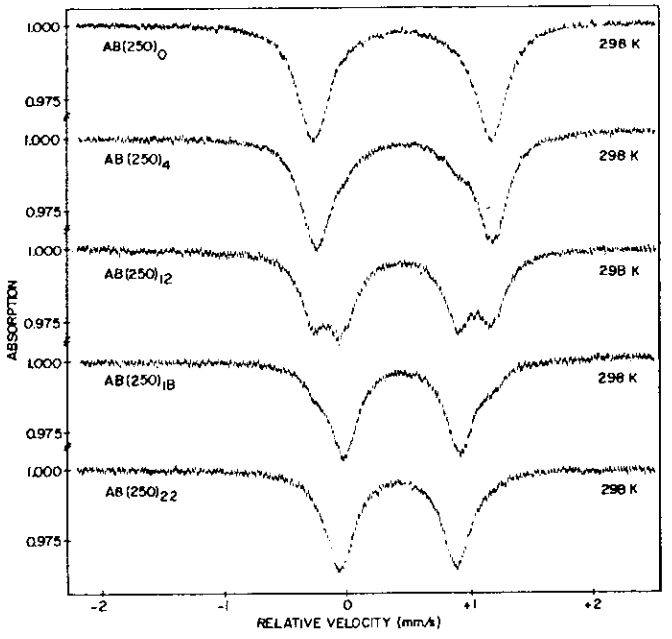

Fig. 1. Mössbauer spectra of AB(250)$_d$, at room temperature, after $d = 0$, 4, 12, 18 and 22 days of hydration.

Fig. 1.24 - Espectros MÖssbauer à temperatura ambiente do composto - A (exposto a uma atmosfera saturada d'água) após 0, 4, 12, 18 e 22 dias de hidratação respectivamente |27|

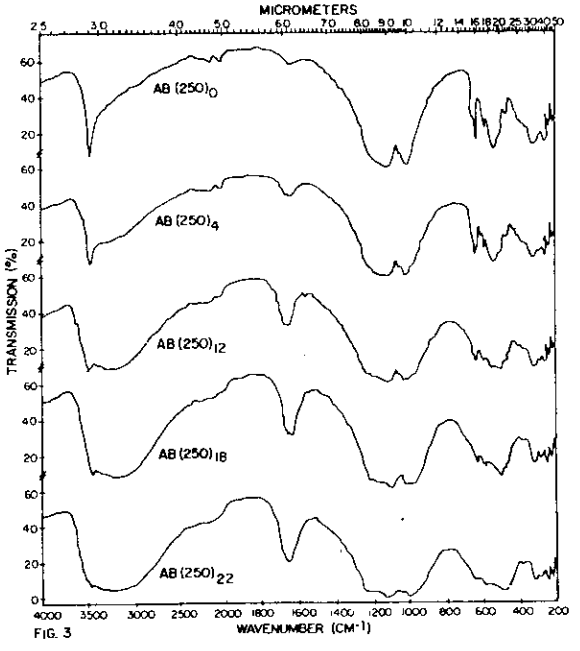

Fig. 3. IR spectra of AB(250)$_d$, at room temperature, after $d = 0$, 4, 12, 18 and 22 days of hydration.

Fig. 1.25 - Espectros de Infravermelho do composto - A após 0, 4, 12, 18, e 22 dias de hidratação respectivamente |27|

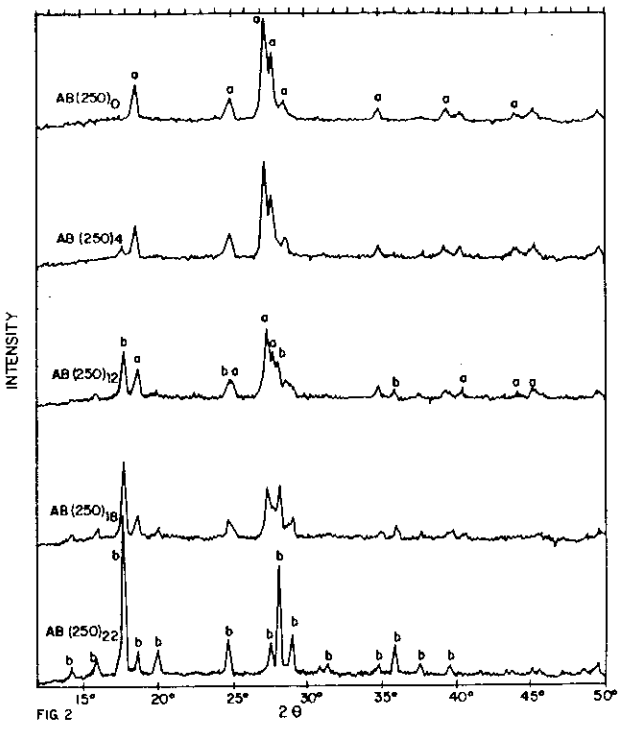

Fig. 2. X-Ray diffraction patterns of $AB(250)_d$, at room temperature, *a* denotes the diffraction peak related to $Fe(OH)SO_4$ and *b* denotes the diffraction peak related to $Fe(OH)SO_4(H_2O)_2$.

Fig. 1.26 - Espectros de Raio-X do composto A após 0, 4, 12, e 22 dias de hidratação respectivamente |27|

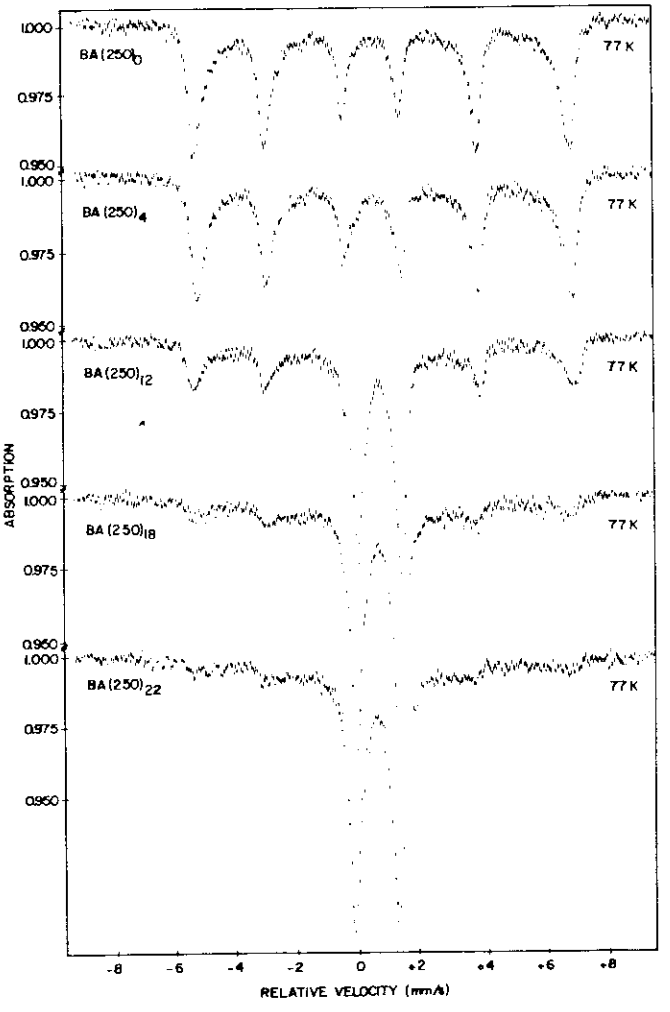

Fig. 1.27 - Espectros Mössbauer à temperatura do nitrogênio líquido do composto - A aquecido a 200 °C após 0, 4, 12, 18 e 22 dias de hidratação respectivamente |27|

Fig. 4. Mössbauer spectra of $BA(250)_d$, at 77 K, for $d = 0$, 4, 12, 18 and 22.

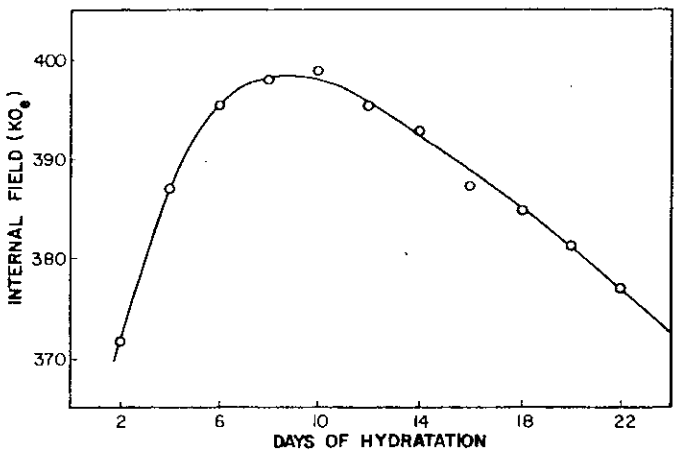

FIG. 7. Magnetic internal field behavior as the days of hydration for B A(250)$_d$ sample ($d = 2, 4, 6, 8, 10, 12, 14, 16, 18, 20, 22$).

Fig. 1.28 - Variação do campo interno para amostras de $FeOHSO_4$ aquecida a 200 °C após diferentes dias de hidratação |27|

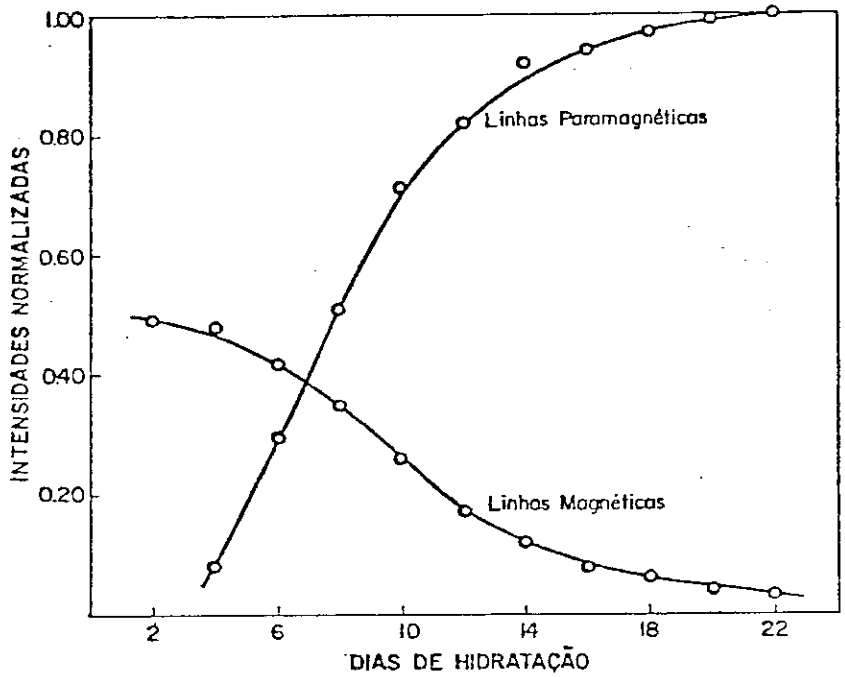

Fig. 1.29 - Comparação da evolução do caráter superparamagnético em relação ao caráter magnético para amostras de $FeOHSO_4$ aquecidas a 200 °C após diferentes dias de hidratação.

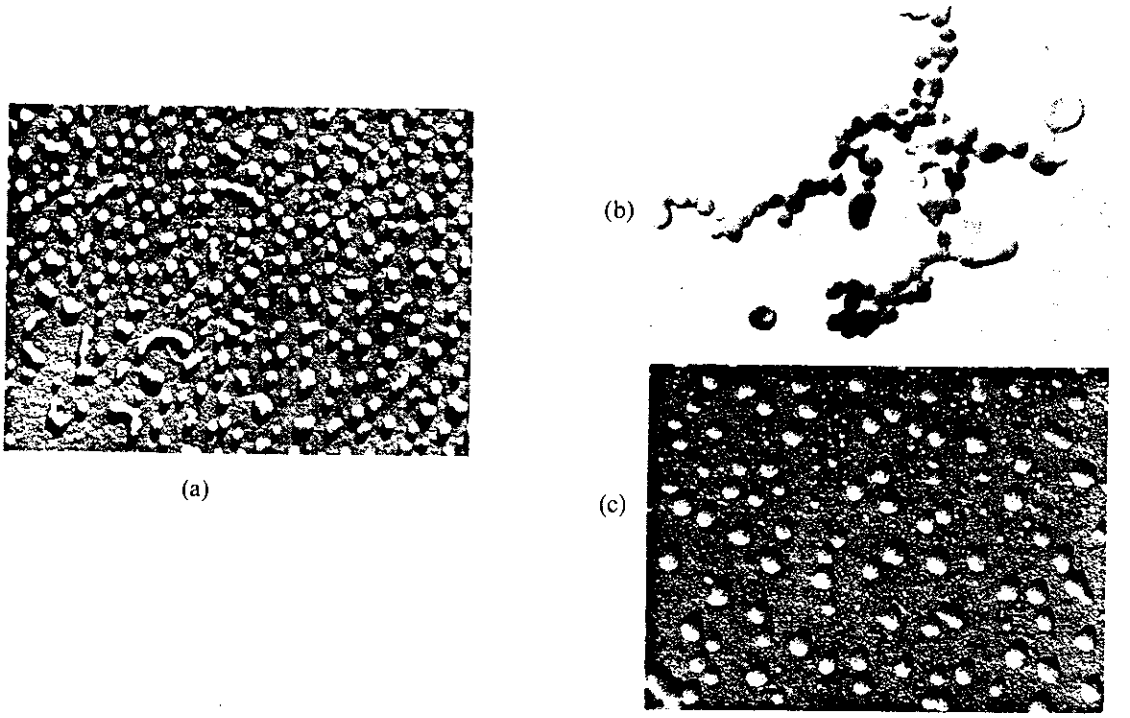

Fig. 5. Electron microscopy patterns. (a) $AB(250)_0$ sample (44.000x). (b) $AB(250)_4$ sample (113.000x). (c) $BA(250)_4$ sample (44.000x).

Fig. 1.30 - Microscopia Eletrônica: (a) amostra $AB(250)_0$, (b) amostra $AB(250)_4$ e (c) amostra $BA(250)_4$ |37|

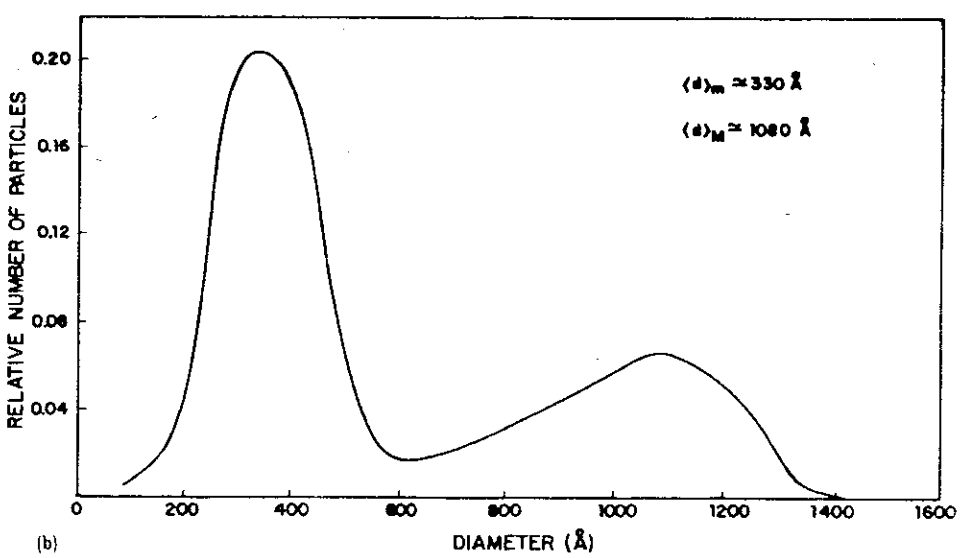

Fig. 1.31 - Diagrama de distribuição do diâmetro das partículas correspondente ao composto - A(250) |27|.

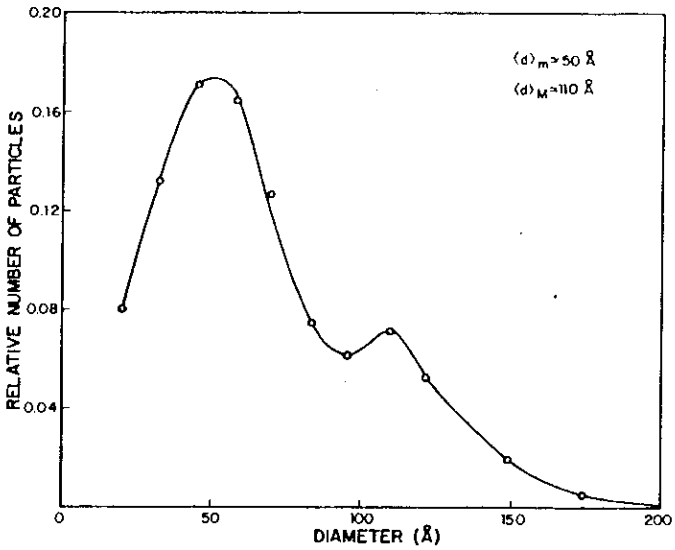

FIG. 6. Particle size distribution for A(300) sample obtained by electron microscropy.

Fig. 1.32 - Diagrama de distribuição do diâmetro das partículas correspondentes ao composto - A(300) |27|

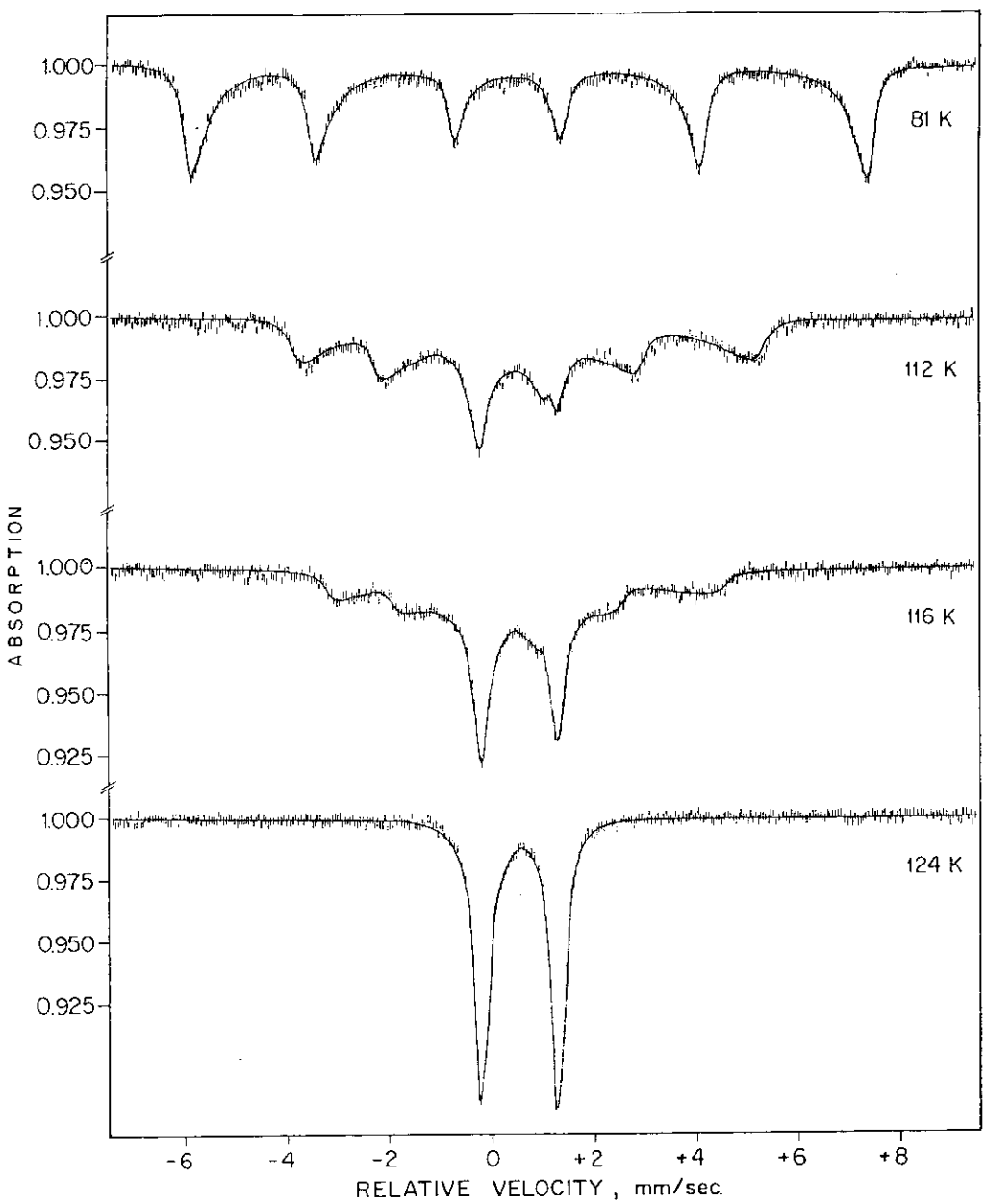

Fig. 1.33 - Espectros Mössbauer do composto - A a diferentes temperaturas |27|

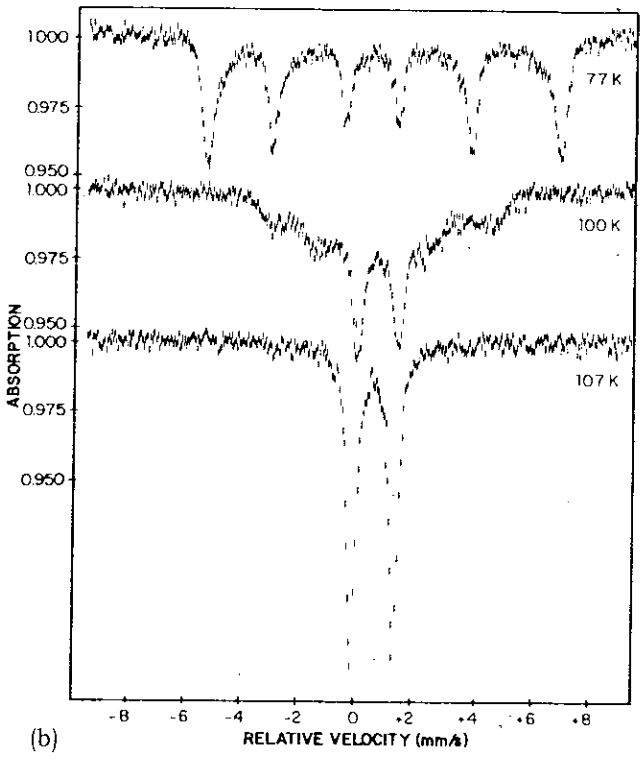

Fig. 1.34 - Espectros MÖssbauer do composto - $BA(250)_2$ a diferentes temperaturas |27|.

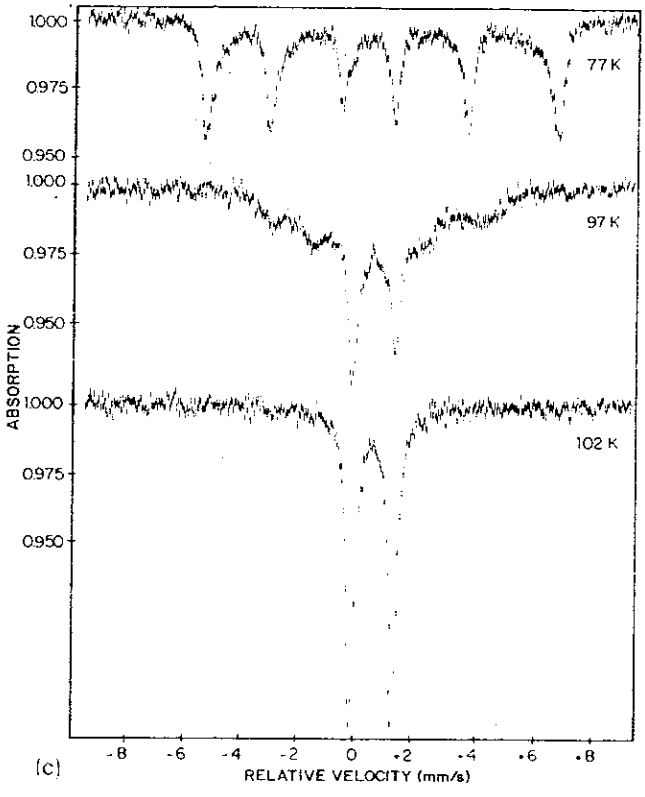

Fig. 1.35 - Espectros MÖssbauer do composto - $BA(250)_4$ a diferentes temperaturas |27|

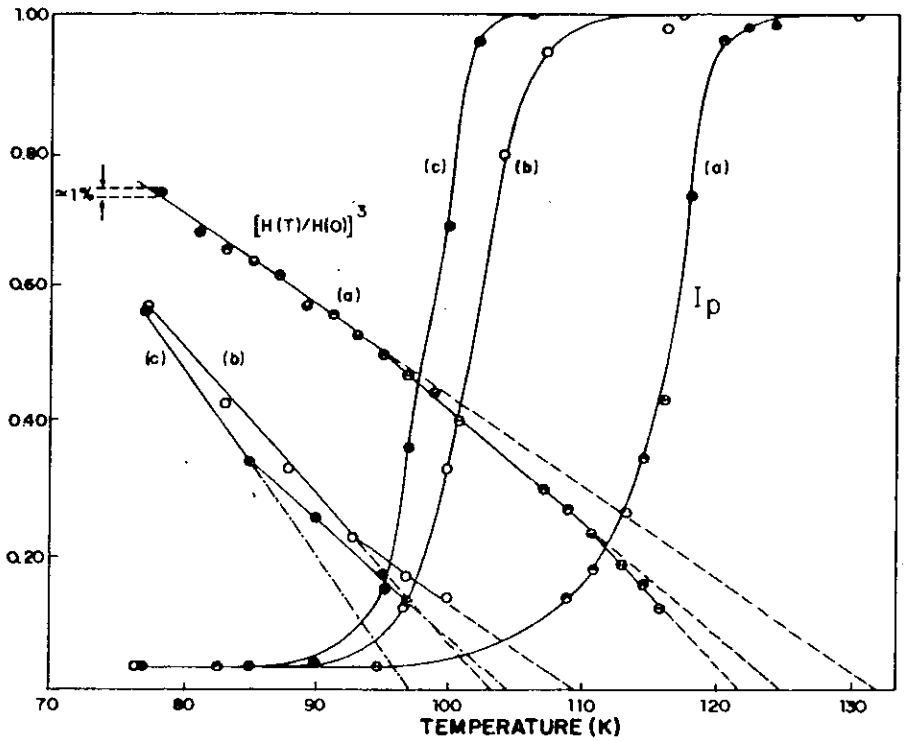

FIG. 8. Experimental values of $[H_0(T)/H_0(0)]^3$ and paramagnetic intensity lines (I_p) as a function of temperature for (a) A(300), (b) B A$(250)_2$, and B A$(250)_4$ samples.

Fig. 1.36 - Comportamento do campo interno $|H(T)/H(0)|^3$ e intensidade das linhas paramagnética: (a) material A(300), (b) material $BA(250)_2$ e (c) material $BA(250)_4$ |27|

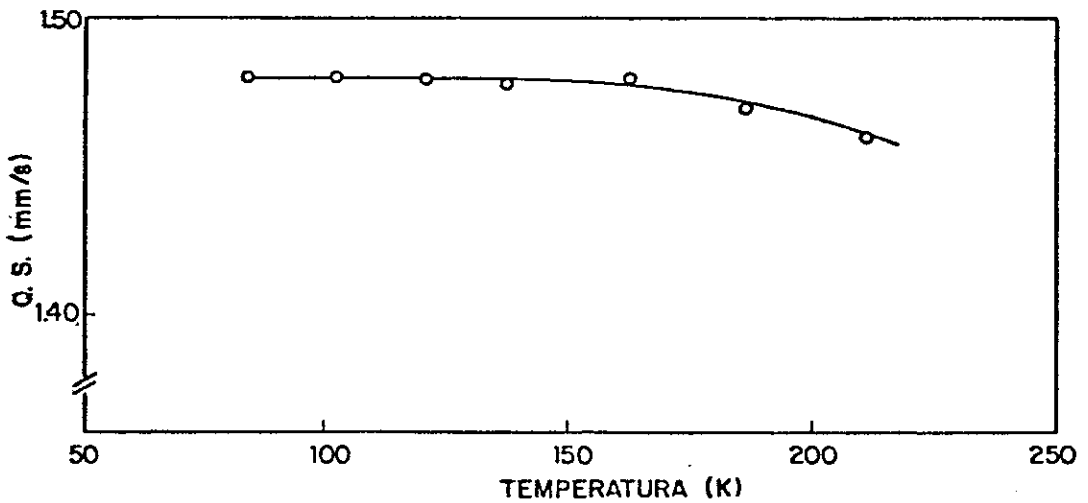

Fig. 1.37 - Dependência do desdobramento quadrupolar do $FeOHSO_4$ em função da temperatura.

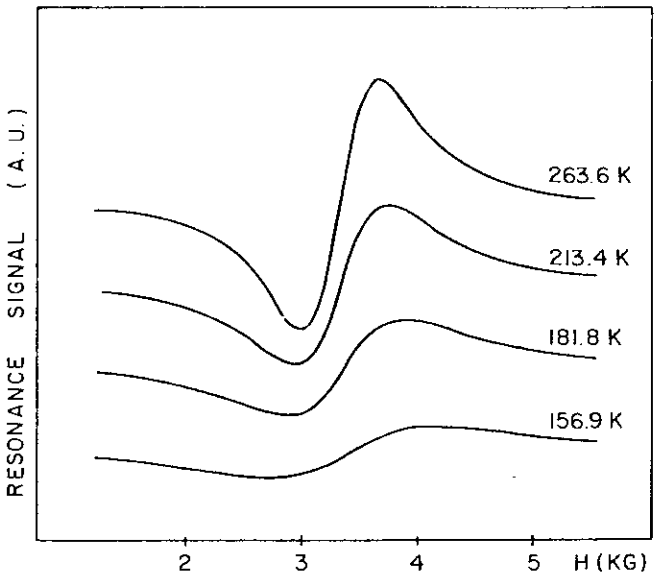

FIG. 1. Resonance signals, i.e., field derivatives of the absorptive component of the microwave susceptibility at some different temperatures. Sample A (250).

Fig. 1.38 - Espectros de EPR do composto A(250) a diferentes temperatura |29|

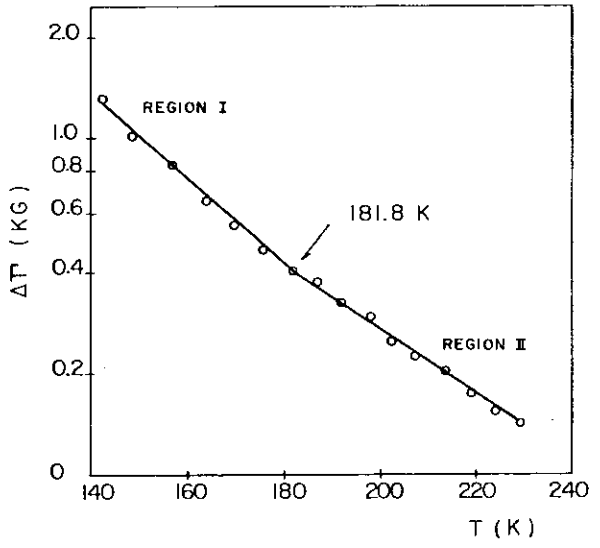

FIG. 2. Temperature dependence of the EPR linewidth of superparamagnetic A (250) particles. Note the logarithmic vertical scale.

Fig. 1.39 - Dependência do alargamento da linha de EPR em função da temperatura para o composto - A(250) |29|

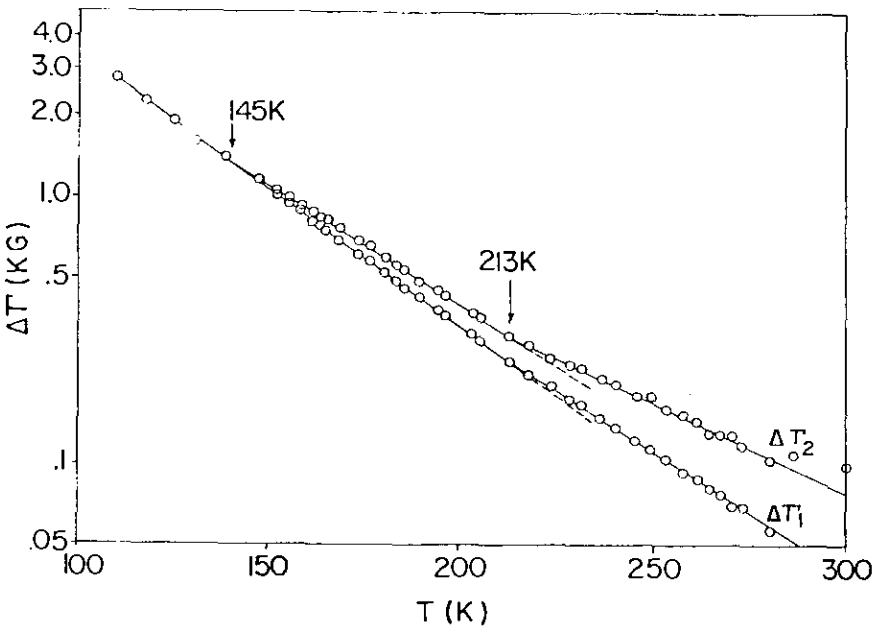

Fig. 1.40 - Dependência do alargamento da linha de EPR em função da temperatura para o composto - A(250) |38|

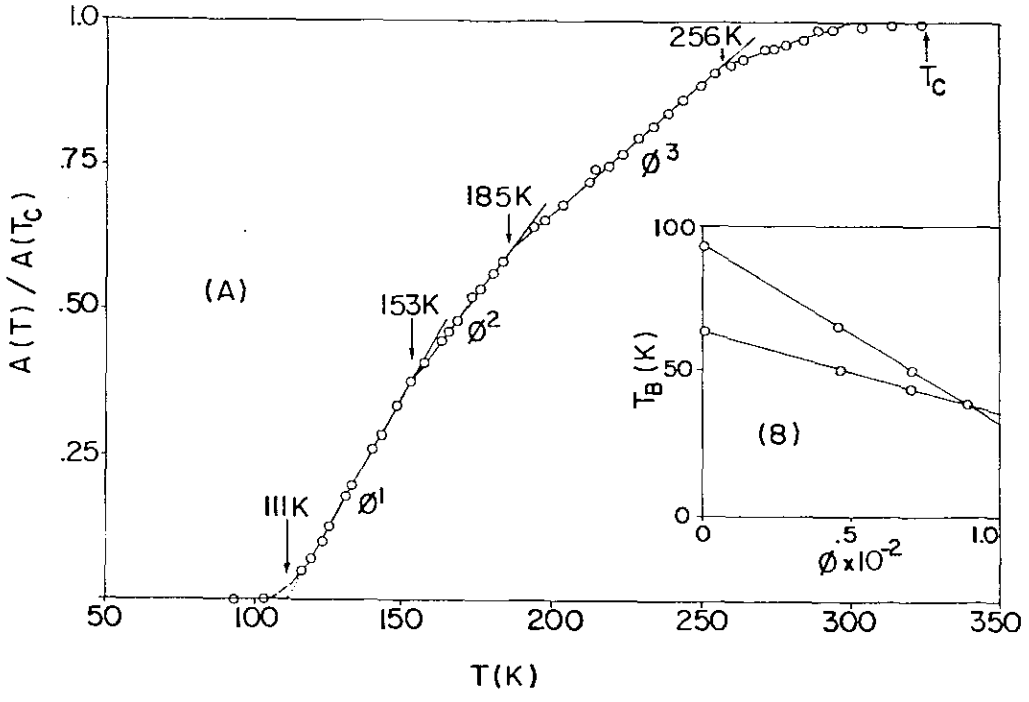

Fig. 1.41 - (a) Dependência da área dos espectros de EPR com a temperatura para o composto - A(300), (b) dependência da temperatura "freezing" T_B versus $\phi = \Delta A/\Delta T$ |38|

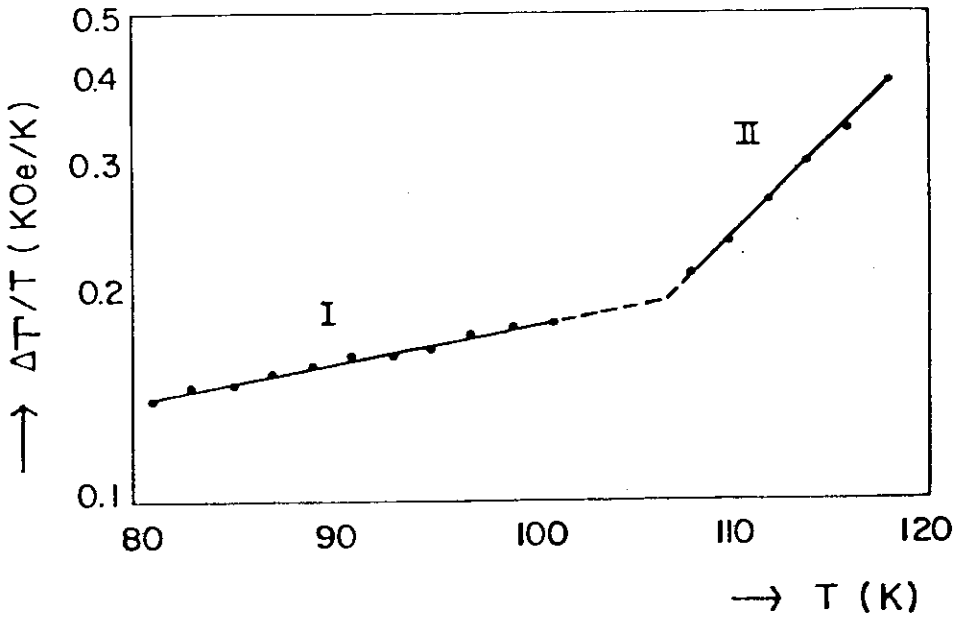

Fig. 1.42 - Dependência da largura de linha Mössbauer com a temperatura [31]

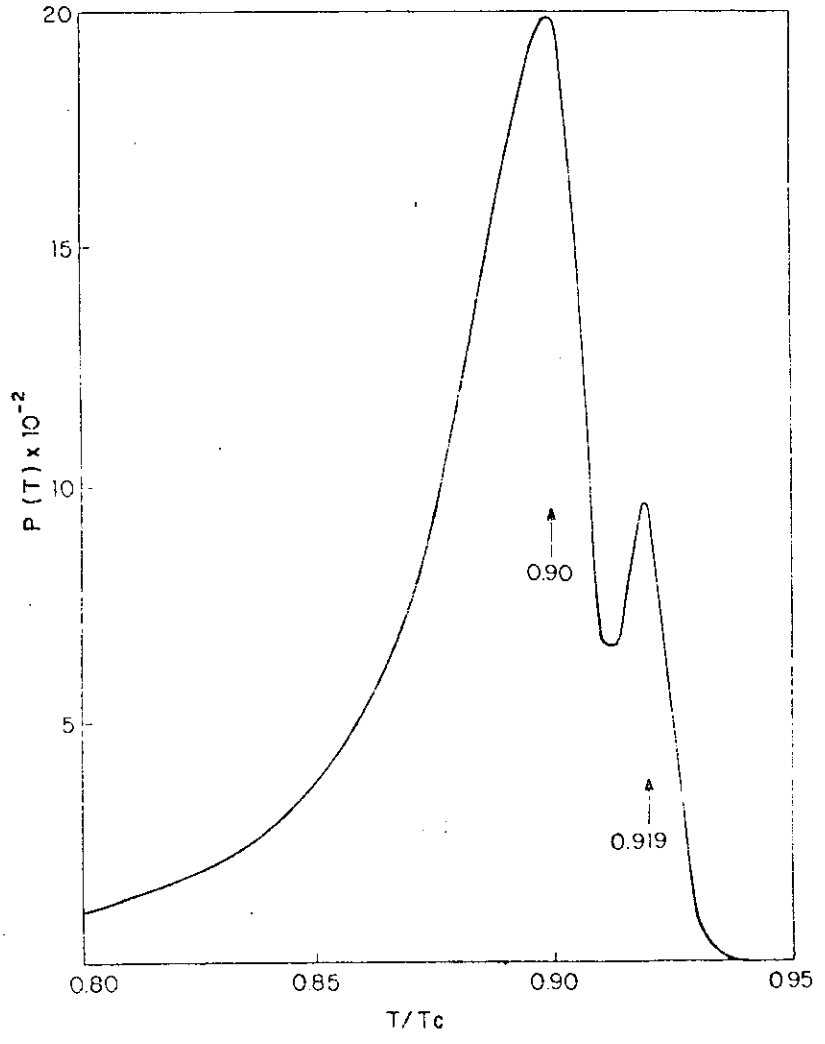

Fig. 1.43 - Distribuição de temperaturas críticas versus T/T_c

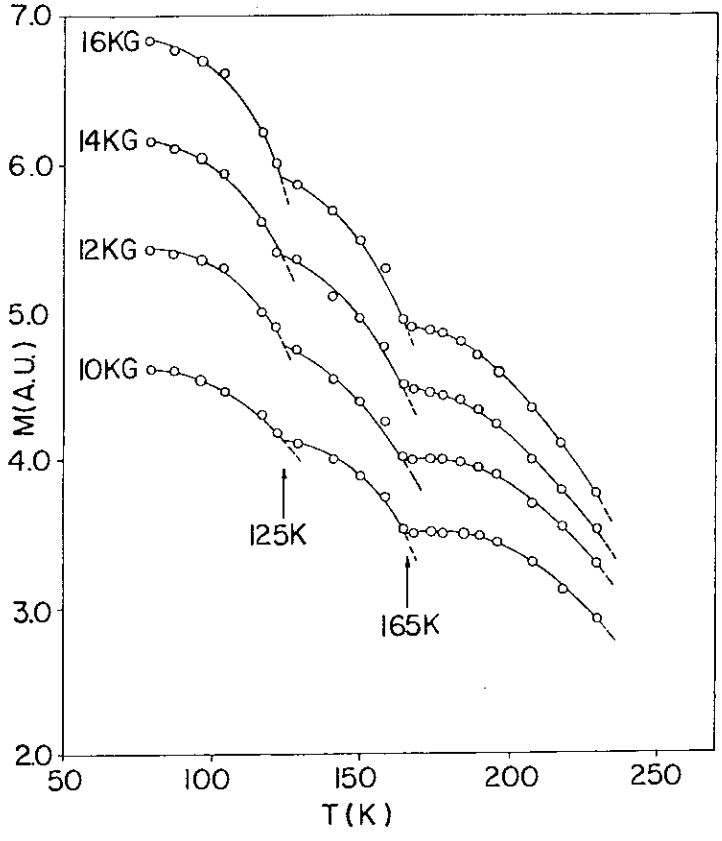

Fig. 1.44 - Dependência da magnetização do composto - A com a temperatura para 10, 12, 14 e 16 KG |40|

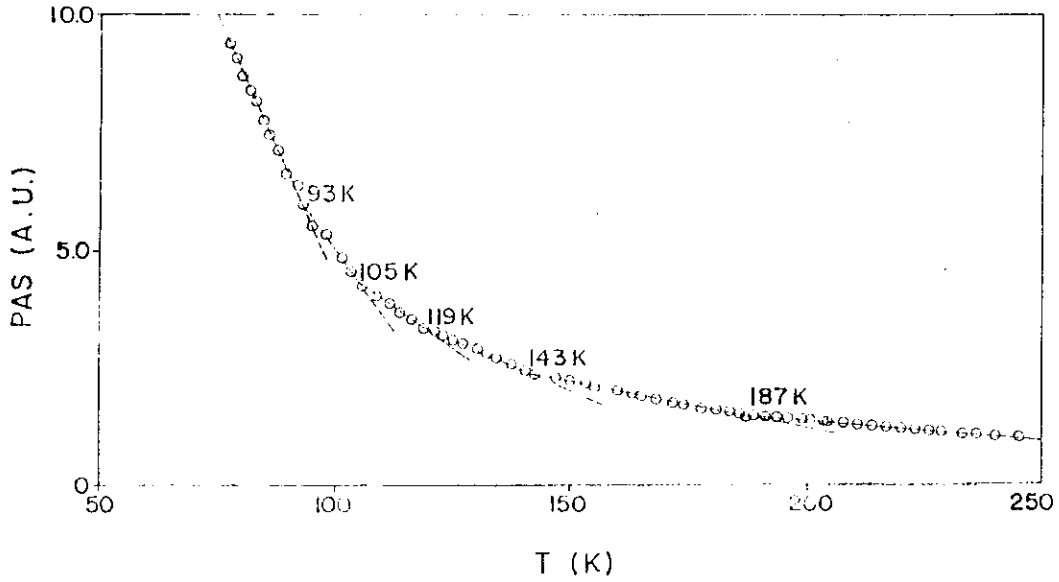

Fig. 1.45 - Dependência do sinal fotoacústico do composto - A com a temperatura |42|

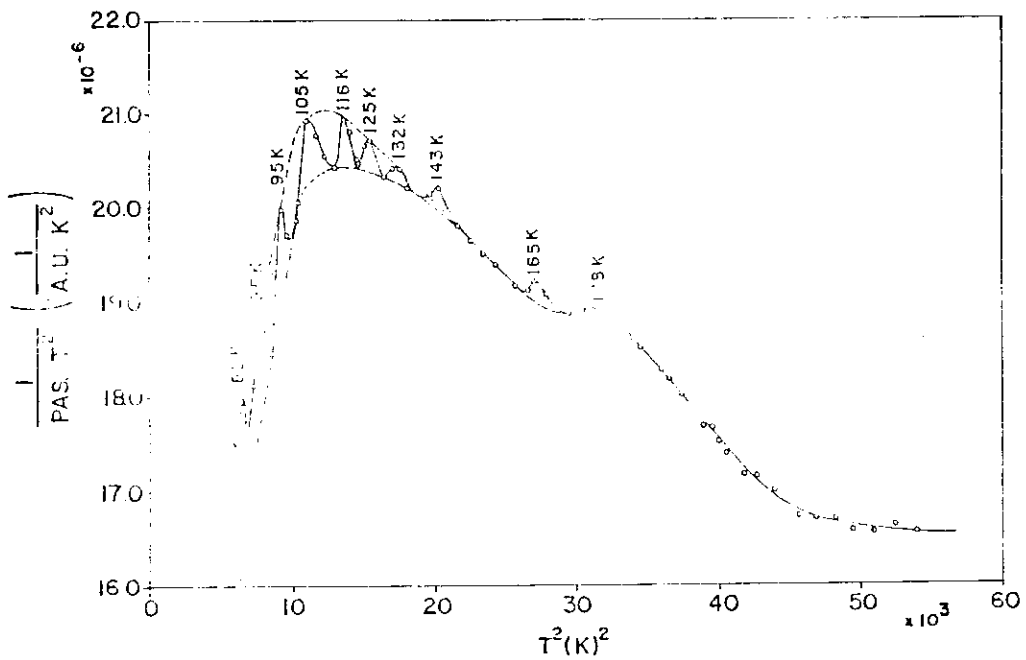

Fig. 1.46 - Diagrama $PAS^{-1} \cdot T^{-2}$ ou $C \cdot T^{-1}$ versus T^2 para o composto - A(300) |42|

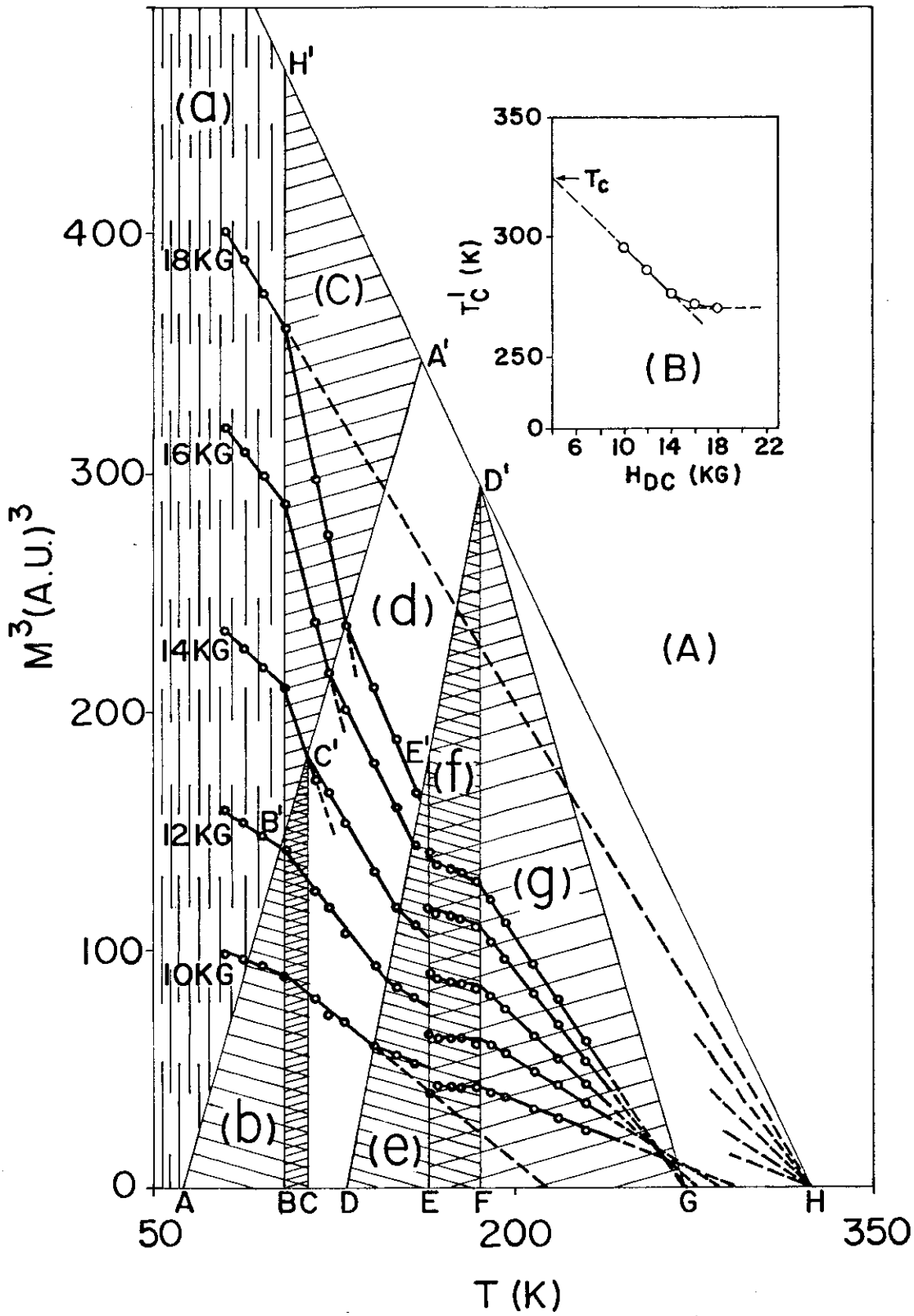

Fig. 1.47 - Diagrama M^3 do composto - A em função da temperatura para 10, 12, 14. 16 e 18 KG |40|

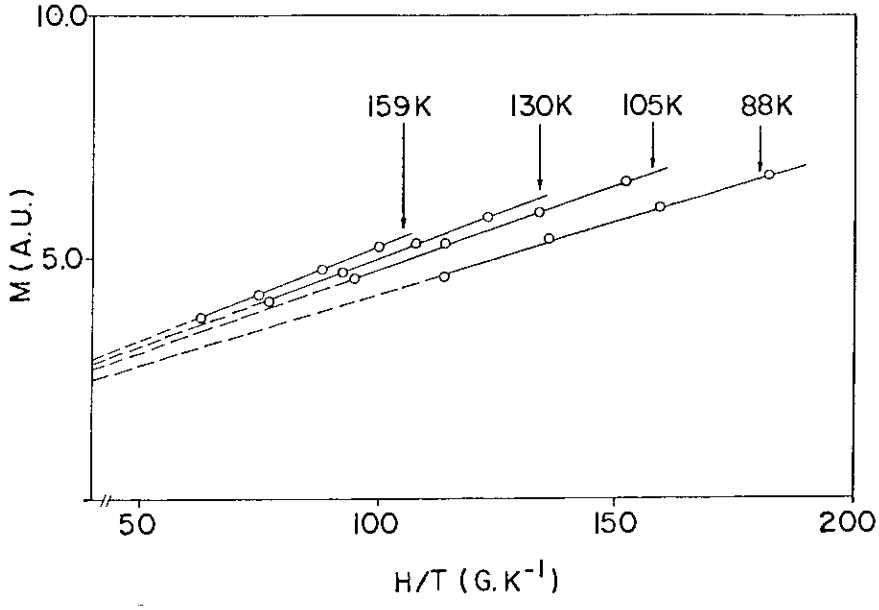

Fig. 1.48 - Diagrama M versus HT^{-1} para o composto A(300) |40|

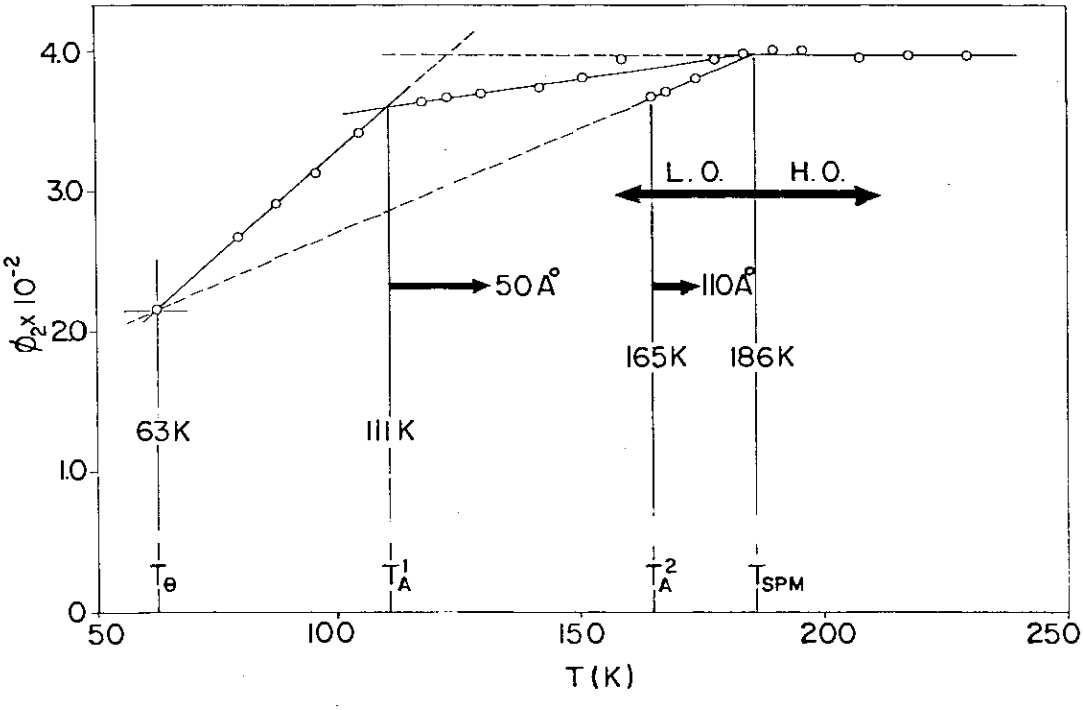

Fig. 1.49 - Diagrama $\phi_2 = M/HT^{-1}$ versus T para o composto A(300) |40|

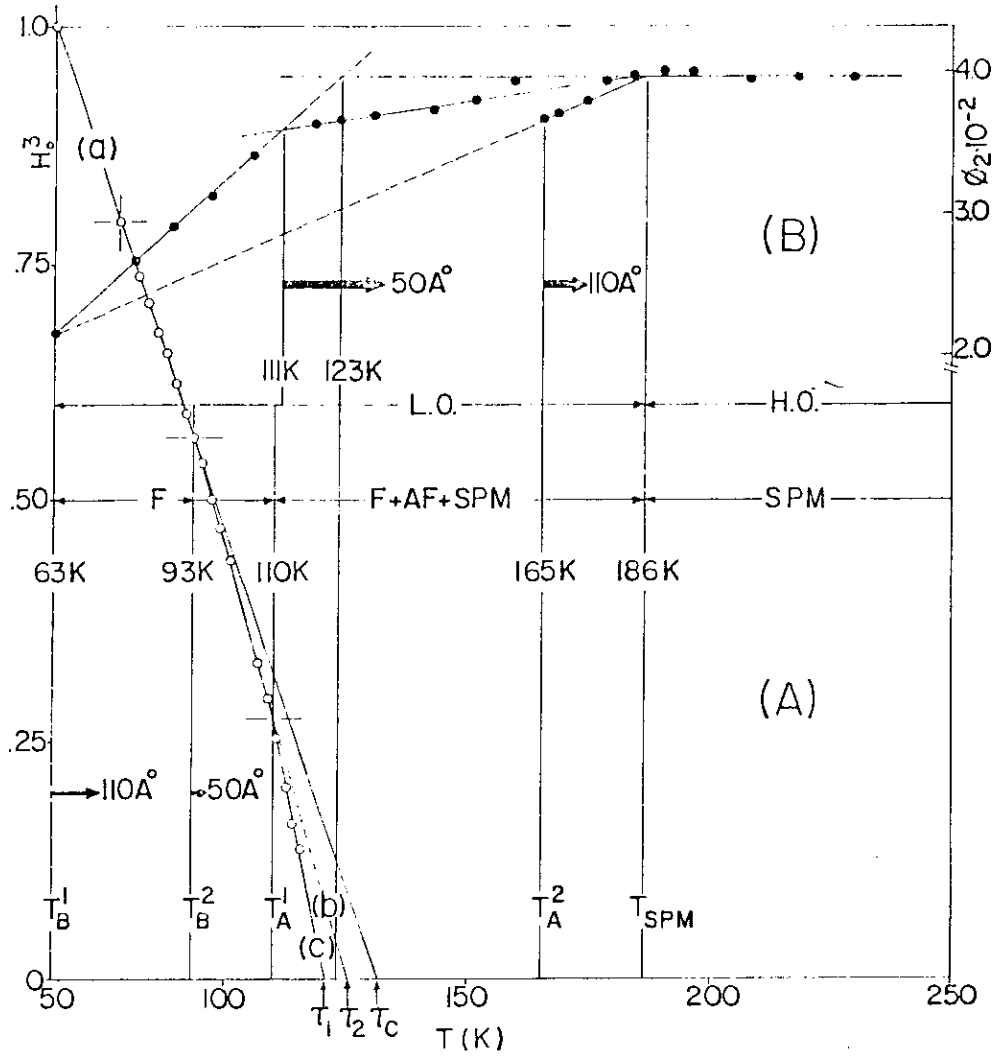

Fig. 1.50 - (a) Diagrama do campo interno H_o^3 versus T, (b) Diagrama $\phi_2 = M/HT^{-1}$ versus T para o composto A(300)

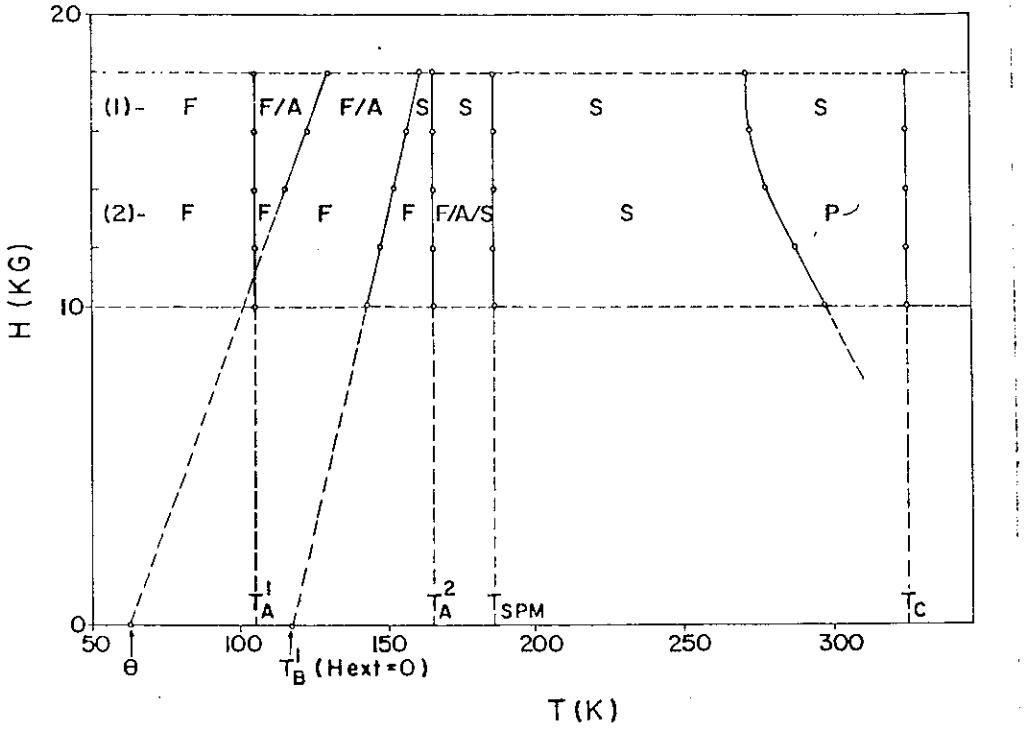

Fig. 1.51 - Diagrama de fase, H versus T para o composto - A(300) |40|

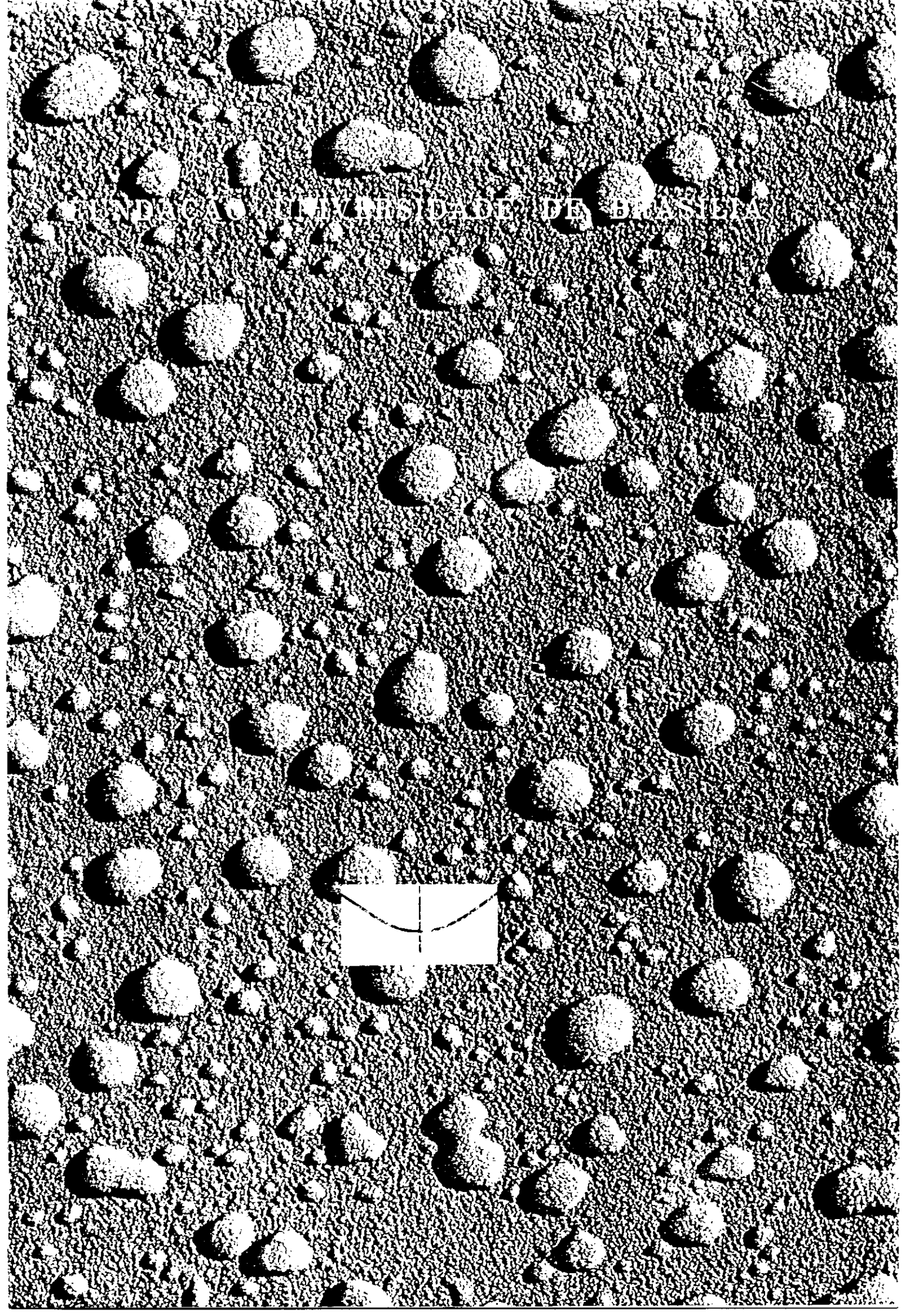

A N E X O A - 1

RADIOCHEM.RADIOANAL.LETTERS 15/6/357-362/1973/

MÖSSBAUER STUDIES IN FERROUS SULPHATE MONOHYDRATE*

K.Skeff Neto, V.K.Garg

Department of Physics, University of Brasilia
Brasilia, Brazil

Received 15 October 1973
Accepted 25 October 1973

Ferrous sulphate monohydrate has been studied as a function of temperature. It was also heated in different atmospheres to study by Mössbauer resonance. The sign of the efg has been concluded to be positive, analogous to other iron sulphates.

Szomolnokite grows in prismatic monoclinic[1] crystals with four molecules per unit cell. The Fe^{2+} is surrounded by a distorted octahedron of four O^{2-} from SO_4^{2-} and two O^{2-} from H_2O.

The Mössbauer spectra were recorded in the standared transmission geometry with a constant acceleration doppler velocity transducer, ^{57}Co in Cu with an initial activity of 5 mCi and Ar - CH_4 filled proportional counter. The thickness of the absorber was of the order of 150 mg/cm^2. Analytically pure $FeSO_4.7H_2O$ was used for our studies. $FeSO_4.4H_2O$ was grown from aquous solution of $FeSO_4.7H_2O$ at a constant temperature $\pm$ 0.25^oC within the range 54^oC - 64^oC. Repeated crystallisation of various temperatures was studied for Mössbauer parameters. Sample

* Partially supported by BNDE, Brasil.
In partial fulfilment of M.S. degree of K.S.N.

obtained from aqueous solution at 52°C gave an unresolved four line spectra.

Ferrous sulphate monohydrate was obtained from the aqueous solution of $FeSO_4.4H_2O$ or $FeSO_4.7H_2O$ at 78°C. The temperature dependence of ΔEQ for $FeSO_4.H_2O$ in the atmosphere of nitrogen is depicted in Fig.1. The temperature dependence is significant and at 473°K the $FeSO_4.H_2O$ converts to $FeSO_4$. Alternately

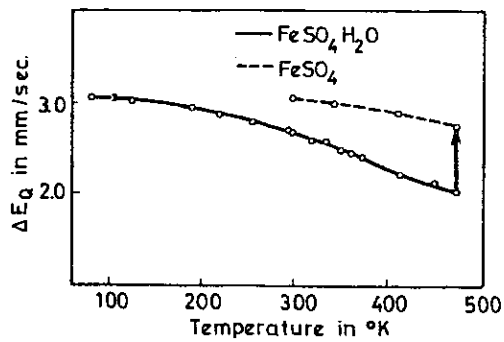

Fig.1. Temperature dependence of ΔE_Q of $FeSO_4.H_2O$ and conversion of $FeSO_4$

$FeSO_4.H_2O$ was obtained from $FeSO_4.7H_2O$ or $FeSO_4.4H_2O$ kept at room temperature in vacuum for a few days. The compound slowly looses water to give $FeSO_4.H_2O$ which was confirmed by chemical analysis and reported[2] Mössbauer parameters. On the basis of ΔEQ it is concluded that distortion in octahedron around Fe^{2+} is less for $FeSO_4.H_2O$ as compared to the distortion around Fe^{2+} in $FeSO_4.7H_2O$ and $FeSO_4.4H_2O$.

The lattice contribution to the observed Mössbauer quadrupole splitting has been estimated[3] for $FeSO_4.7H_2O$ by carrying out direct lattice sum calculations on a point change model and the contribution has been shown to be nearly 2 % of the

experimental value of the splitting being +ve for one site and negative for the other site. Assuming an analogous situation to hold in the case of $FeSO_4.H_2O$ this indicates a negligible contribution of the lattice charges and mixing of electronic configurations to the efg. The ground state configuration for iron $3d^6$ in $FeSO_4.4H_2O$ molecule is $d_\varepsilon^4\, d_\gamma^2$, the five electron in the $d_\varepsilon^3 d_\gamma^2$ constituting a ferric-like core and the sixth electron being in the d_{xy} state. With the increase of temperature the sixth electron outside the spherical distribution of charge will partly populate the $/d_{xz}, d_{yz}/$ level; the population in d_γ levels will remain unchanged since these are much higher in energy. The population density n_{xy}, n_{xy} and n_{xz} at room temperature is estimated as follows

Johnson[4] et al assumed the field gradient in $FeSiF_6.6H_2O$ to be due to a single electron in d_z^2 i.e. $n_z^2 = 1$ comparing the experimentally observed values of ΔEQ of $FeSO_4.H_2O$ with those of $FeSiF_6.6H_2O$, the population densities are,

$$\frac{\text{Splitting of } FeSO_4.H_2O}{\text{Low temp. splitting of } FeSiF_6.6H_2O} = n_{xy} - \frac{1}{2}\,/n_{yz} + n_{xz}/$$

$$\frac{2.7}{3.7} = 1 - \frac{3}{2}\,/n_{yz} + n_{xz}\,/$$

$$\text{Thus } n_{xy} = 0.819,\ n_{xz} + n_{yz} = 0.181.$$

The direct comparison was preferred to the analysis of quadrupole splitting in the reverse that went into obtaining Q from the splitting in $FeSiF_6.6H_2O$, since it avoids the uncertainities in the value of Q, the covalency parameter and

TABLE 1

Compound	Temp ^{o}K	δ/Cu	ΔE_Q	EFG Sign	Ref.
$FeSO_4.7H_2O$	298	+0.984	3.204	+ve	5
	5		3.350		11
$FeSO_4.4H_2O$	298			+ve	6
$FeSO_4.H_2O$	298	+1.032	2.688	+ve concluded	
	80	+1.064	3.068		
$FeSO_4$	298	+1.032	3.072	+ve	7
	5		3.650		11
$Fe_2O/SO_4/_2$	298	+0.192	1.445		
	373	0.156	1.416		
	423	0.120	1.392		
	473	0.084	1.368		

that of function F. In absence of any reported MO calculations no comparison with the theoretical values of population densities is possible.

The sign of efg for listed Fe/II/ sulphates /Table 1/ has been reported[5-9] as positive. Assuming an analogous situation a positive efg is concluded for $FeSO_4.H_2O$ and probably the direction of maximum field gradient lies parallel to the shortes Fe-O distance. The peak area ratio of polycrystalline sample is ~1 indicating that Goldanskii effect is not significant.

On heating $FeSO_4.H_2O$ at 200°C in nitrogen atmosphere a mixture of $FeSO_4.H_2O$ and $FeSO_4$ resulted first. Prolonged heating resulted in pure $FeSO_4$. When $FeSO_4.H_2O$ was heated in air upto

180°C a mixture of compounds was obtained whose Mössbauer parameters corresponds to $FeSO_4.H_2O$ and $Fe_2O/SO_4/_2$. For $Fe_2O/SO_4/_2$ the internal magnetic field Hi at 80°K is 418 ± 8 Koe compared to the reported value of 373 Koe at liquid air temperature. Prolonged heating resulted in pure $Fe_2O/SO_4/_2$.

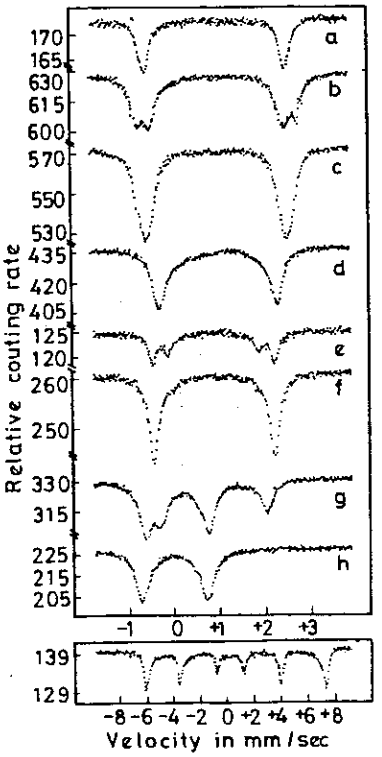

Fig.2. Mössbauer spectra
a/ Absorber $FeSO_4.7H_2O$ spectra at room temperature
b/ Absorber from aqueous solution of /a/ at 52°C, spectra at room temperature
c/ Absorber from aqueous solution of /a/ at 60°C, spectra at room temperature
d/ /a/ Kept at 70°C for 6 hours, spectra at room temperature
e/ /d/ heated in N_2 atmosphere at 180°C and spectra at 180°C
f/ /e/ heated at 200°C and spectra at 200°C
g/ /a/ heated in air upto 180°C and spectra at 180°C
h/ /g/ heated at 220°C in air and spectra at 220°C
i/ Spectra of /h/ at 90°K

Thermal decomposition studies of iron/II/ sulphates have been reported by many workers[1-9]. In absence of any phase diagram it will be interesting to study the metastable states in $FeSO_4.nH_2O$ as reported for $FeCl_2.nH_2O$[10].

*

The authors are thankful to Dr. Deo Raj and Dr. P.G.David for some discussions.

REFERENCES

1. J.C.Boyat, G.Bassi, Compt.Rend., 256 /1963/ 1482.

2. A Vértes, B.Zsoldos, Acta Chim.Acad.Sci.Hung. 65 /1970/ 262.
Ibid, Proc.Conf.Appl.of Mössbauer Effect /Tihany/ 1969.
A.Vértes, T.Székely, T.Tarnóczy.
Acta Chim.Acad.Sci.Hung.Tomus 65 /1970/ 1.

3. A.J.Nozik, M.Kapla, Phys.Rev.,159 /1967/ 273.

4. C.E.Johnson, W.Marshall, G.J.Perlow, Phys.Rev.,126 /1962/ 1503.

5. K.Chandra, S.P.Puri, Phys.Rev.,196 /1968/ 272.

6. V.K.Garg, S.P.Puri, J.Chem.Phys.,54 /1971/ 209.

7. H.N.OK, Phys.Rev., /B/ 4 /1971/ 3870.

8. R.W.Grant, H.Wiedersich, A.H.Muir, Jr.,U.Gonser, W.Delgass, J.Chem.Phys.,45 /1966/ 1015.

9. B.C.Frazer, P.J.Brown, Phys.Rev.,125 /1962/ 1283.

10. A.Vértes, B.Zsoldos, Magy.Kém.Foly.,76 /1970/ 282.
A.Vértes, T.Székely, T.Tarnóczy, Magy.Kém.Foly. 75 /1969/ 172.
P.K.Gallagher, D.W.Johnson, F.Schrey, J.Am.Ceramic Soc., 53 /1970/ 666.

11. W.Klumpp, K.W.Hoffmann, Z.Phys., 227 /1969/ 254.

12. S.L.Ruby, B.J.Zabranský, J.Chem.Phys.,54 /1971/ 4559.

A N E X O A – 2

J. inorg. nucl. Chem., 1975, Vol. 37, pp. 2287–2290. Pergamon Press. Printed in Great Britain

MÖSSBAUER THERMAL DECOMPOSITION STUDIES OF Fe(II) SULPHATE

K. SKEFF NETO and V. K. GARG
Departamento de Física, Fundação Universidade de Brasília, Brasília, Brazil

(*First received* 8 *October* 1974; *in revised form* 9 *December* 1974)

Abstract—Investigations of thermal decomposition of $FeSO_4.H_2O$ by Mössbauer resonance, thermal differential analysis (DTA), thermal gravimetric analysis (TGA), infrared (i.r.), magnetic susceptibility, X-rays and chemical analyses are being reported. An unidentified thermal product A (Q.S. = 1·45 mm/sec) is magnetically ordered at 77K and transition to paramagnetic state takes place at 123·5 K. In aqueous vapours compound A changes reversibly to a non-magnetically ordered compound B (probably Buterlite). Their empirical formulae have been given.

INTRODUCTION

STUDIES of some thermal decomposition products of iron sulphate hydrates have been reported by Vértes *et al.*[1, 2]. Gallaghar *et al.*[3] also studied the thermal decomposition of iron(II) sulphates by conventional thermogravimetry, differential thermal analysis and evolved gas analysis in oxidising and inert atmospheres. The present report is such an investigation of ferrous sulphate monohydrate and its two unidentified thermal products. Compound A with a well resolved doublet (Q.S. = 1·454 ± 0·012 mm/sec) at room temperature, is magnetically ordered at 77 K and the transition to the paramagnetic state takes place at 123·5 ± 0·25 K. In aqueous vapour atmosphere the compound A is reversibly transformed to a new compound B (Q.S. = 0·97 ± 0·01 mm/sec) which does not show magnetic interaction. On reheating of compound B we obtain compound A but now it does not show magnetic interaction at 77 K.

EXPERIMENTAL

The Mössbauer spectra were recorded with a constant acceleration velocity transducer coupled to ^{57}Co in Cu matrix source with an initial activity of 25 mCi in the standard transmission-geometry. The velocity calibration per channel was done with a (1·9 mg $^{57}Fe/cm^2$.)iron foil. The temperature was measured by a copper-constantan thermocouple and the variation of temperature was done with Elcint temperature controller MTC-3. The stability of the temperature was better than 0·03°. Analytically pure $FeSO_4.7H_2O$ was used as the starting material to obtain the $FeSO_4.H_2O$ by the literature[4] method. The i.r. spectra were recorded with KBr disc technique. A thermobalence in conjunction with the digital equipment was used for the thermogravimetric analysis is described elsewhere[5] with standard experimental details of magnetic susceptibility, thermal differential analysis. All spectras were least square fitted with PDP II Computer.

Figure 1 depicts the Mössbauer spectra of $FeSO_4.H_2O$ heated at various temperatures for 12 hr. The Mössbauer spectra at room temperature of $FeSO_4.H_2O$ heated at 593 K shows a pure well resolved doublet with $\delta/Fe = 0{\cdot}44 \pm 0{\cdot}02$ mm/sec and Q.S. = 1·454 mm/sec (Fig. 2). Let this compound be called as A. In Fig. 1 we have compound A with impurity of $FeSO_4.H_2O$ upto 453 K. Figure 2 depicts the Mössbauer spectra of compound A kept in aqueous vapour atmosphere as a function of days. Figure 3 shows the infrared spectra of $FeSO_4.7H_2O$, impure A, pure A and pure B compounds.

DISCUSSION

When $FeSO_4.7H_2O$ is heated in air at a rate of 6°/min up to 473 K, 37·07% of the material is lost and the Mössbauer

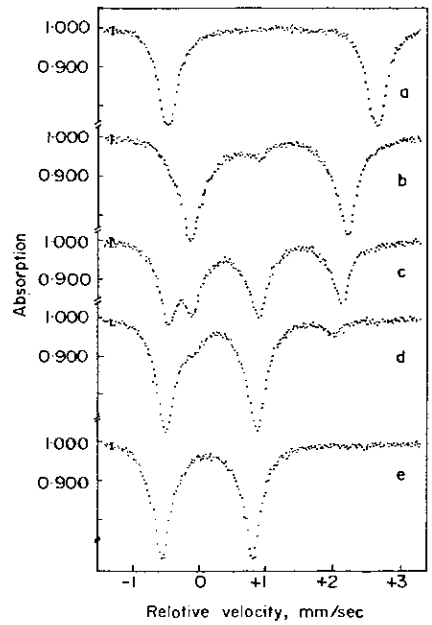

Fig. 1. Mössbauer spectra of: (a) $FeSO_4.H_2O$ at 300 K; (b) Sample (a) heated in air at 378 K for 12 hr Spectra at 378 K; (c) Sample (b) heated in air at 413 K for 12 hr spectra at 413 K in air; (d) Sample (c) heated in air at 453 K for 12 hr spectra at 453 K; (e) Sample (d) heated in air at 593 K for 12 hr spectra at 593 K.

spectra corresponds to nearly as in Fig. 1(b) and the infrared spectra to as in Fig. 3(b). On maintaining the temperature for 12 hr 38·80% of the material is lost, and the Mössbauer spectra corresponds to Fig. 2(a) and i.r. spectra to Fig. 3(c). On heating the $FeSO_4.H_2O$ at 593 K we get a pure compound (called A) with Q.S. = 1·45 mm/sec and $\delta/Fe = 0{\cdot}44 \pm 0{\cdot}02$ mm/sec (Fig. 2a). In the laboratory atmosphere the Mössbauer spectra of this compound A slowly changes over a period of several months but keeping it in aqueous vapour atmosphere the process is speeded up and a new compound with essentially the same isomer shift but with a different quadrupole splitting of 0·97 mm/sec is obtained. Let this compound be called as compound B, (Fig. 2d), the i.r. of this compound is depicted in Fig. 3d. Heating of compound B at 383 K for a few days reconverts it to compound A. If the same procedure is adopted in vacuum or nitrogen atmosphere the $FeSO_4.7H_2O$ results in $FeSO_4$

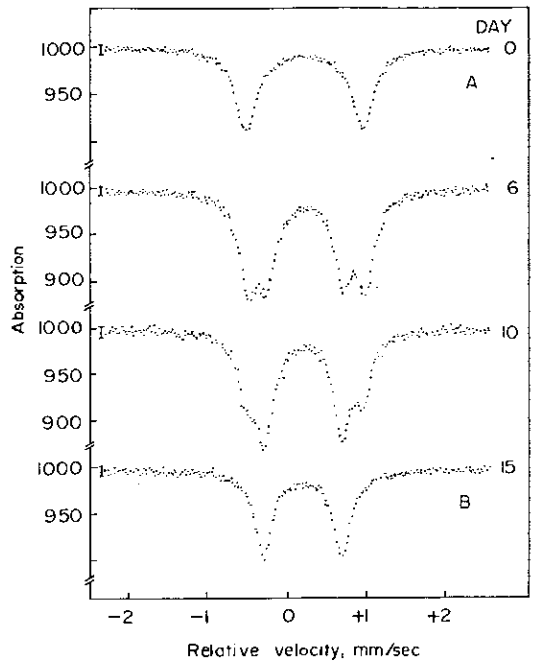

Fig. 2. Mössbauer spectras of sample A exposed to saturated aqueous vapourous atmosphere as a function of days.

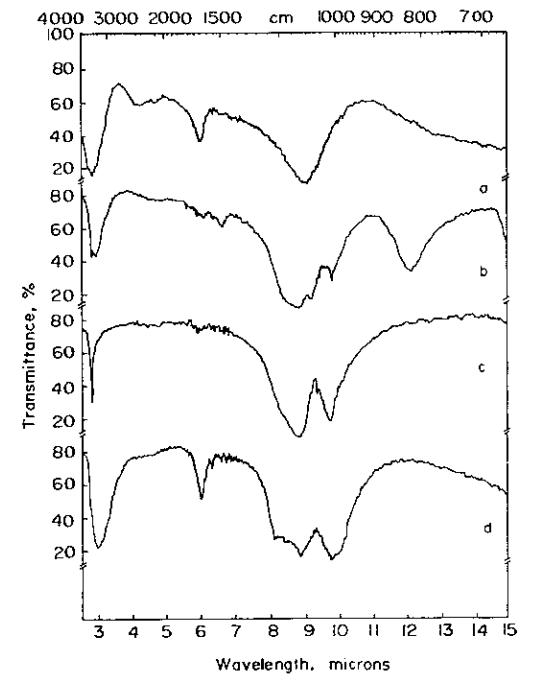

Fig. 3. I.R. spectras of (a) $FeSO_4.7H_2O$, (b) impure A, (c) pure A and (d) pure B.

instead of compound A. Heating of $FeSO_4$ in the same procedure however also does not result in compound A. On heating $FeSO_4$ or compound A at 723 K in air, one line Mössbauer spectra of $Fe_2O(SO_4)_3$ is obtained which is in agreement with Gallaghar[3].

The I.S./Fe of compound A and compound B is 0·445 mm/sec corresponds to Fe(III) high spin compounds but Q.S. is large for the high spin Ferric compounds and it is closer to observed[6, 7, 8] Q.S. for Fe-O-Fe bridge compounds. The characteristic absorption of Fe-O-Fe in i.r. spectra is not indicated in our samples. $FeSO_4.7H_2O$ and compound B show absorption due to HOH bending mode at 1650 cm^{-1} and the broad absorption at about 3450 cm^{-1} corresponding to OH^- stretching mode. These features indicate the presence of water. Compound A has very little absorption at 1650 cm^{-1} and the OH^- absorption near 3500 cm^{-1} is sharp and is at a slightly higher frequency than for compound B. These suggest that compound A does not contain water but contains OH^-. A similar i.r. peak was observed by Vértes *et al.*[1]. The observed and calculated (for the proposed empirical formulae) percentage of Fe, S, O and H for compounds A and B are

	Observed		Calculated for Proposed formulae	
	Compound A	Compound B	$Fe(OH)SO_4$	$Fe(OH)SO_4.2H_2O$
Fe	33·16	27·20	33·06	27·25
S	18·82	15·58	18·98	15·56
O	47·16	53·50	47·36	54·65
H	0·57	2·52	0·59	2·46

The empirical formula of B corresponds to Buterlite whose structure has been determined by Fanfani[9].

Figure 4 shows the Mössbauer spectra of compound A between 77 K and 147 K. The transition to paramagnetic state takes place at 123·5 K. Figure 5 shows the linear curve of H_i^2 as function of temperature for compound A. The data approximately follows the 1/3 power law. The best fit of the data to an expression of the form $H_i(T) = C(1-\frac{T}{T_o})^\beta$, where β and C are constants, T_o is the transition temperature, gives $\beta = 0{\cdot}335 \pm 0{\cdot}005$, $T_o = 123{\cdot}5 \pm 0{\cdot}25$ K and $C = 594{\cdot}94$ usually $C = H_i$ (O) D. Experimentally[10, 11] $\beta = 1/3$ lies with-in the range of

$$0{\cdot}88 < \frac{T}{T_c} \leqslant 0{\cdot}98.$$

On heating compound B we again get compound A but no magnetic interaction is observed. It is known[12] that particle size can have strong influence on the magnetic transition temperature. We have no direct information of the particle size of our samples. If the sample is heated to 873 K to transform to Fe_2O_3 the measured hyperfine field indicates the macroscopic particle size of our sample. The

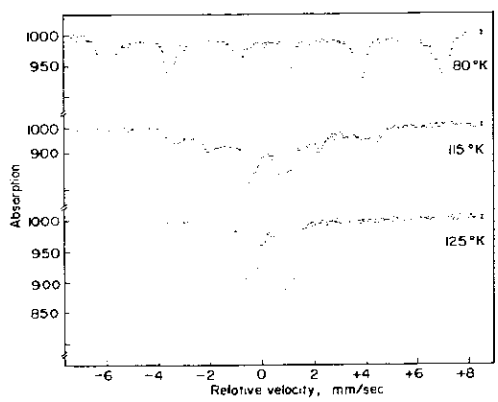

Fig. 4. Mössbauer spectras of compound A as a function of temperature.

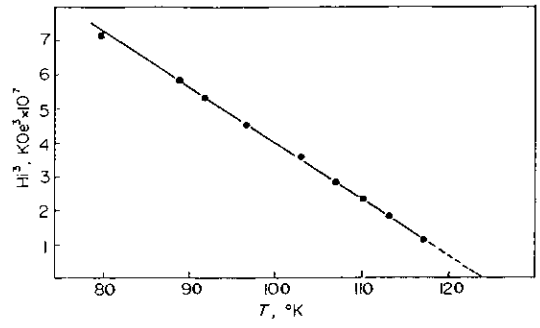

Fig. 5. H_i^3 vs T curve for compound A.

magnetic moment μ of compound A (supposing it to be paramagnetic, is

$$\mu = 2{\cdot}38\mu_B \quad \text{at 100K.}$$
$$\mu = 3{\cdot}78\mu_B \quad \text{at 300 K.}$$

These values are lower than the normal paramagnetic values ($\mu \sim 5{\cdot}9\mu_B$) of iron(III) with the types of ligands under discussion. The low observed moments and their decrease with decreasing temperature for compound A imply that the compound A is a dimer or higher polymer that exhibits low temperature antiferromagnetic exchange. In fact, the observation of well resolved hyperfine splitting at 123·5 K suggests that the system is an extended polymeric antiferromagnet probably involving sulfato bridging. The SO_4^{2-} ion in inorganic compounds shows an absorption in the regions of 1100 cm^{-1}, which has been attributed to the O_3 mode vibration. This mode is degenerate in completely ionic sulphates, where the symmetry of the sulphate ion is T_d. This seems to be the case of $FeSO_4.7H_2O$ (Fig. 3a). When the symmetry of the sulphate ion is C_{3v} (when one of the oxygens is bonded to the metal) the degeneracy is lifted, this seems the case in compound A (Fig. 3c). When the symmetry of the sulphate ion is C_{2v} (when two of the oxygens are bonded to the metal) the degeneracy is lifted still further. The i.r. spectra of compound B (Fig. 3d) shows additional splitting of the sulphate ion composed to compound A (Fig. 3b). Thus this indicates that at least some of the SO_4^{2-} ions are bonded via two oxygens to the iron in this compound.

FWHM of X-ray of compound A is nearly 1° which is nearly five times the experimental resolution indicating that particle size is of the order of 150 Å. This difficulty in interpretation[3] may be to superparamagnetism.

CONCLUSIONS

Figure 6(a) depicts the temperature dependence of various thermal decomposition products of $FeSO_4.7H_2O$. Figure 6(b) depicts the temperature dependence of area of Mössbauer peak lying at positive velocity (Av_+) here each Mössbauer spectra was recorded for a fixed time Δt.

The proposed decomposition scheme in non oxidising (vacuum or nitrogen) atmosphere is

$$FeSO_4.H_2O \xrightarrow{453-643\,K} FeSO_4 + H_2O$$

but in air atmosphere the decompositions is

$$2FeSO_4H_2O + 1/2\,O_2 \xrightarrow{453-643\,K} 2\,FeOHSO_4 + H_2O$$

$$2FeOHSO_4 \xrightarrow{643-723\,K} Fe_2O(SO_4)_2 + H_2O$$

and

$$2\,FeSO_4 + 1/2\,O_2 \xrightarrow{573-723\,K} Fe_2O(SO_4)_2$$

$$Fe_2O(SO_4)_2 \xrightarrow{823-973\,K} Fe_2O_3 + 2SO_3.$$

The rate of heating in air has great influence on the various transitions obtained.

$$2\,FeSO_4.H_2O + 1/2\,O_2 \xrightarrow[\Delta t = 12h]{493\,K} 2\,FeOHSO_4 + H_2O.$$

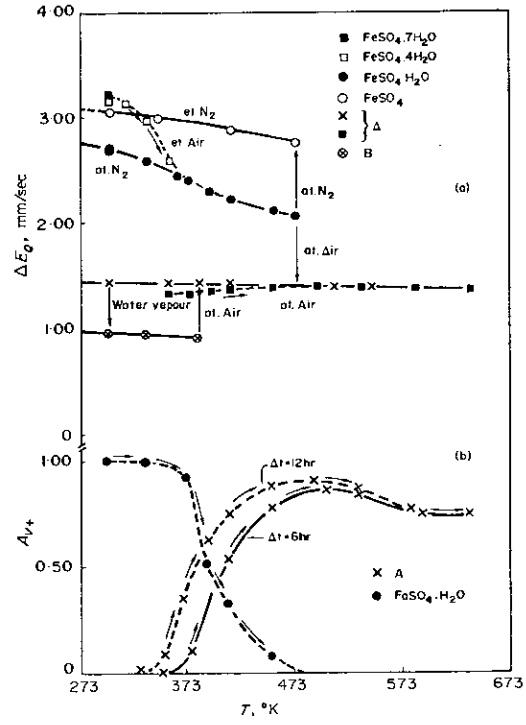

Fig. 6. Temperature dependence of Q.S. of various thermal decomposition products of $FeSO_4.7H_2O$. Temperature dependence of positive peak area (A_{v+}).

Acknowledgements—The authors express their appreciation to Drs. Ann Dufresne for i.r. spectra and some discussions, C. A. Dauwve for magnetic susceptibility, J. M. Knudsen for his interest in the early stages of the work and A. Vértes for helpful suggestions. The chemical analysis was done at Alfred Bernhardt, Mikroanalylisches Laboratorium; West Germany. Partial financial support from Project BNDE, FUNTEC 104 and CNPq is thankfully acknowledged.

REFERENCES

1. A. Vértes and B. Zsoldos, *Acta Chim. Adac. Scient. Hung.* **65**, 3 (1970).
2. A. Vértes, T. Székely and T. Tarnóczy, *Acta. Chim. Acad. Sci. Hung.* **63**, 1 (1970).
3. P. K. Gallaghar, D. W. Johnson and F. Scherey, *J. Am. Ceram. Soc.* 53, 566 (1970).
4. K. S. Neto and V. K. Garg, *Radiochem. Radional. Lett.* **15**, 357 (1973).
5. K. S. Neto, M. S. Thesis, University of Brasília, Brasil (1974).
6. N. N. Greenwood and T. C. Gihh, In *Mössbauer Spectroscopy* pp. 161–163, (Chapman & Hall, London) (1971).
7. V. K. Garg, Ph.D. Thesis, University of Roorkee, *India* (1971), V. K. Garg, N. Malathi and S. P. Puri, *Chem. Phys. Lett.* **11**, 393 (1971); V. K. Garg. P. G. David. T. Matsuzuwa and T. Shinjo, *Bull. chem. Soc. Japan* (In press).

8. H. Schugar, C. Walling, R. B. Jones and H. B. Gray, *J. Am. Chem. Soc.* **89**, 3712 (1967).
9. L. Fanfani, A. Nunzi and P. F. Zanazzi, *Amer. Mineral.* **56**, 751 (1971).
10. E. Callen and H. Callen, *J. Appl. Phys.* **36**, 1140 (1965).
11. U. Bertelsen, J. M. Kaudsen, H. Drog, *Phys. Status Solidi.* **25**, 59 (1967).
12. T. Shinjo, *J. Phys. Soc. Japan* **21**, 917 (1966).

A N E X O A – 3

Solid State Communications, Vol. 28, pp. 43-48.
0038-1098/78/1001-0043 $02.00/0

MAGNETIC PROPERTIES OF $FeOHSO_4$ - I. MÖSSBAUER SPECTROSCOPY

K. Skeff Neto
Departamento de Física, Universidade de Brasília, 70.910 Brasília, DF. Brasil

and

L.C.M. Miranda
Instituto de Física "Gleb Wataghin", Unicamp, 13.100 Campinas, SP, Brasil

(Received 7 July 1978 by R.C.C.Leite)

Mössbauer measurements on $FeOHSO_4$ are presented. A new model based upon the molecular-field approximation for randomly dilute magnets is proposed to explain the observed behavior of the internal field as a function of the temperature.

In this paper we report our Mössbauer measurements on $FeOHSO_4$, and a new model describing the behavior of the magnetization is also proposed. The $FeOHSO_4$ sample was obtained from the thermal decomposition of $Fe\,SO_4 \cdot H_2O$, and consists of an assembly of fine particles. The details of preparation were published elsewhere[1]. The Mössbauer spectrum at various temperatures is shown in Fig. 1. This was done in the usual transmission geometry with a standard constant-acceleration Mössbauer spectrometer. The souree was ^{57}Co in Cu and the velocity calibration per channel was done with an iron foil (1.2 mg $^{57}Fe/cm^2$). The samples were pressed between two alluminum foils at 12 ton/in^2 with a diameter of 17 mm and were used directly as absorbers. The Mössbauer spectrum in Fig. 1 at T = 81 K is typical of superparamagnetic particles[2]. At T = 112 K it already shows a well-resolved six-peak pattern with considerable broadening of the outer peaks and an enhancement of the quadrupole splitting lines. Since these are the only lines which survive above the transition temperature, we shall call them from now on the "paramagnetic lines".

The usual Mössbauer analysis of superparamagnetic systems have quite often been reported in the literature using Neel's theory for the relaxation of single domain particles applied to the variation of the Mössbauer linewidth with temperature[2]. Here we look at another side of this problem, namely the behavior of the internal magnetic field with temperature, and propose a new model based on the molecular-field approximation for randomly dilute alloys for its description. The internal field variation as a function of temperature was obtained by fitting the Mössbauer spectrum in terms of a hyperfine-field distribution P(H). This distribution of hyperfine fields reflects all possible varieties of local environments. The best fit to the experimental data was done similarly to Refs. 3 and 4 using the following model for P(H):

$$P(H) = \begin{cases} A\left[(H-H_o)^2 + (\Gamma_1/2)^2\right]^{-1} & \text{, for } 0<H<H_o \\ B\left[(H-H_o)^2 + (\Gamma_2/2)^2\right]^{-1} & \text{, for } H>H_o \end{cases} \quad (1)$$

The two forms are matched in value at $H=H_o$ and the normalization constant is determined by the condition

$$\int_o^\infty dH\, P(H) = 1 \quad (2)$$

The fitting of the experimental data based on this model is shown in Fig. 1 by the solid curves. The P(H) curves obtained from the fitting of Fig. 1 are plotted in Fig. 2. In Fig. 3 the circles in curve (a) show the variation of the normalized internal field H_o^3, as a function of temperature. Here H_o was obtained from the P(H) curve (Fig. 2).

In the following we suggest a new model based upon the molecular-field approximation for randomly dilute magnets[5] to describe the behavior of H_o^3 versus the temperature. The model proposed assumes that we have around each Fe atom a cell of Z nearest-neighbours in which the magnetization is determined by the local concentration in of Fe atoms and the temperature. We further assume that only the magnetic atoms interact amongst themselves through a molecular field which is proportional to the temperature magnetization of the neighboring atoms. Now, since the paramagnetic line intensity is proportional to the number of paramagnetic Fe atoms, the observed enhancement of the paramagnetic intensity below τ_c=120.2 K(see Fig.1) means that the number of Fe ions that are becoming paramagnetic below τ_c is increasing with temperature. Here τ_c=120.2 K is defined as the actual transition temperature. Physically, this suggests that as one increases the temperature some of the neighboring magnetic atoms are having a large number of spin deviation so that, on the average, they behave as if they were paramagnetic. This

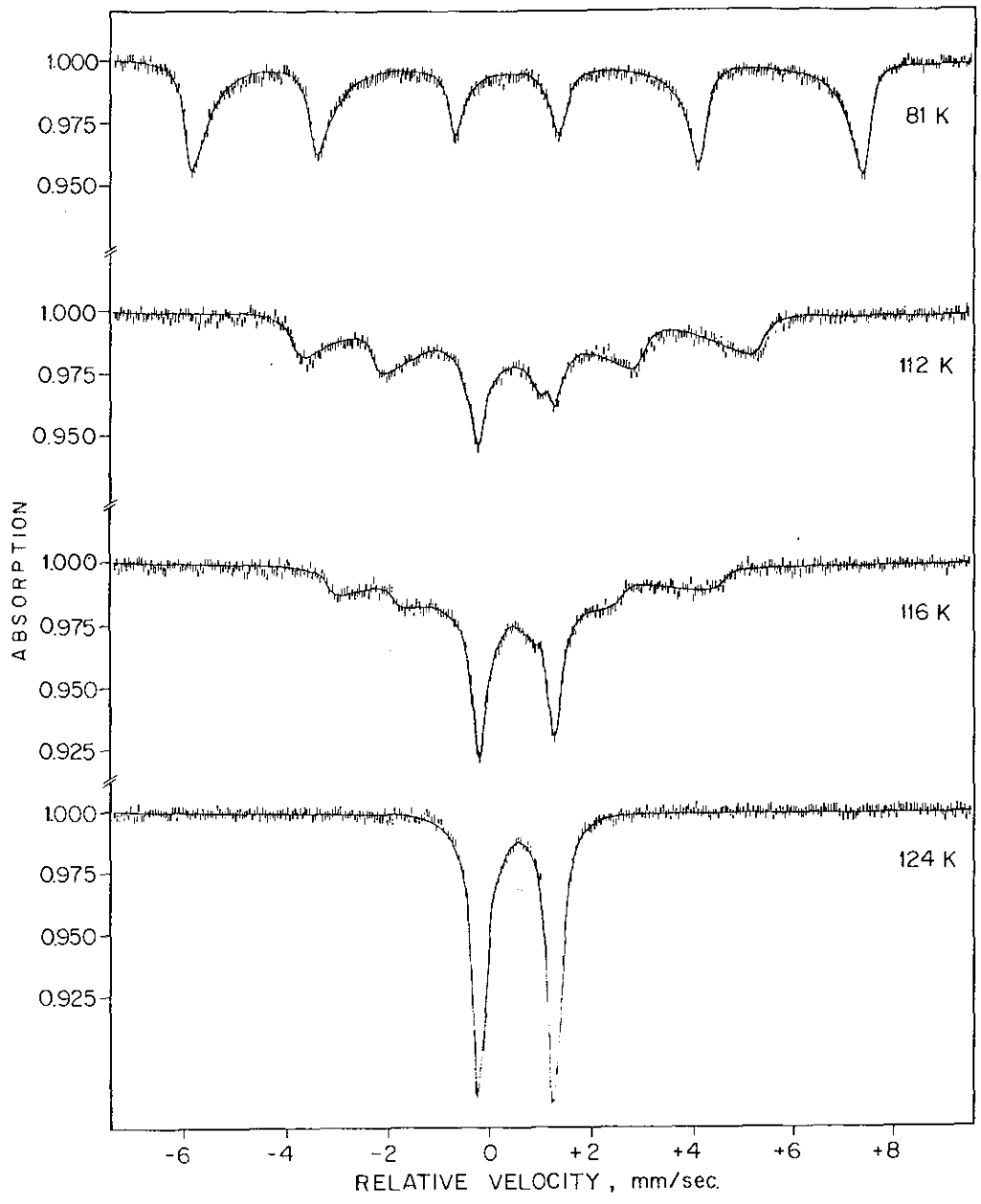

Fig. 1 – Temperature dependence of the Mössbauer spectrum for $FeOHSO_4$. The solid curves are the fittings based on Eq. (1). At T=124 °K the spectrum shows a pure well resolved doublet with δ=0.44 ± 0.02 mm/s relative to Fe metal and Q.S.=1.45 mm/s.

then led us to further consider the concentration m as a function of temperature, namely,

$$m(T)=\lambda\left[1 - I_p(T)/I_p(124^oK)\right],$$

where λ is a constant smaller than unit and $I_p(T)/I_p(124^oK)$ is given by the normalized experimental paramagnetic line intensity. Hence assuming a random magnetic within the molecular-field approximation[5], performing the same calculations as in Ref. 5 and allowing for the variation of m with the temperature, the expression for the magnetization per atom M (= $\langle S_i^Z \rangle$) is then given by[5]

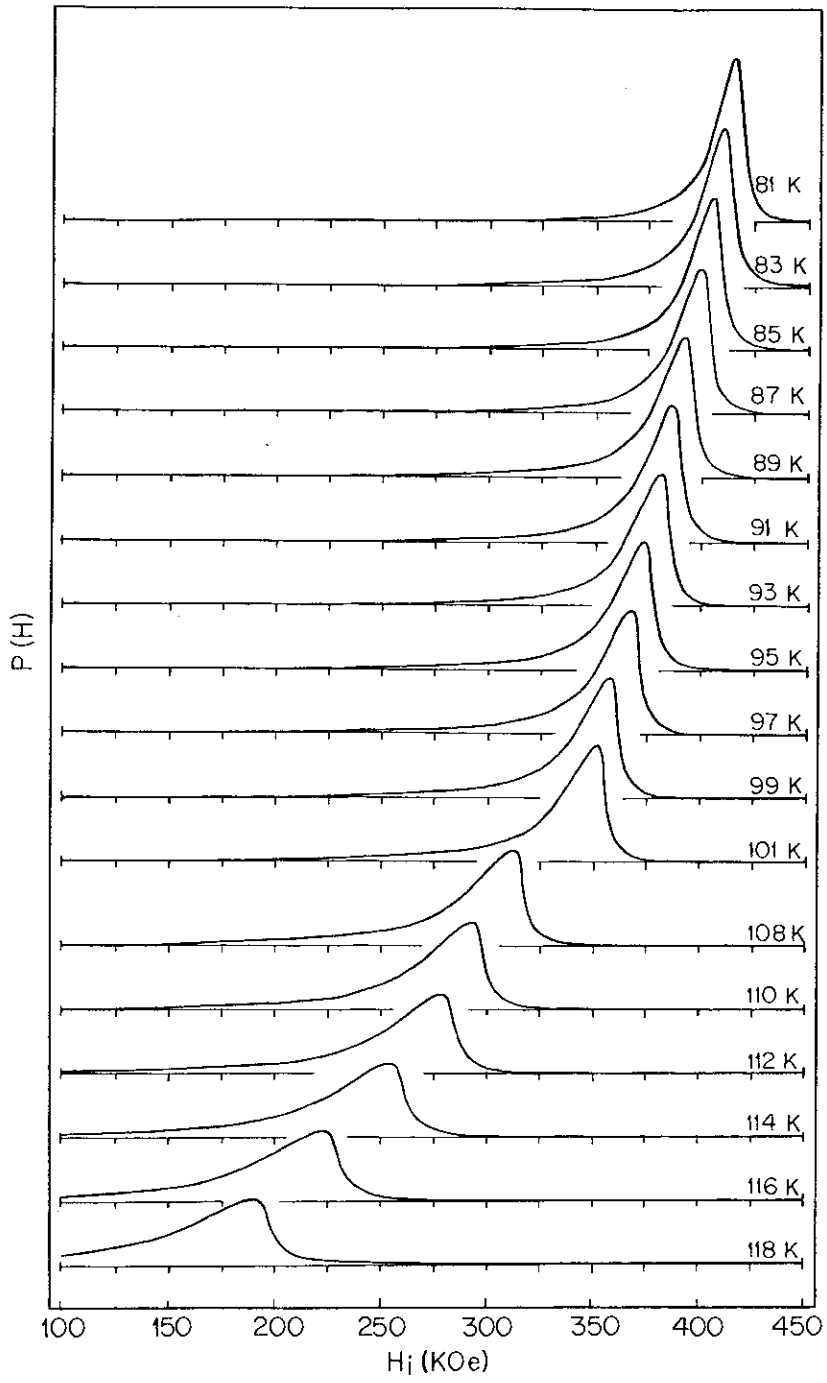

Fig. 2 - Temperature dependence of the hyperfine field distribution for $FeOHSO_4$.

$$\frac{1}{2} - M = \sum_{\nu=0}^{z} \frac{z!\left[m(T)\right]^{\nu}\left[1-m(T)\right]^{z-\nu}}{(z-\nu)!\nu!\left[\exp\frac{2MJ\nu}{K_B T} + 1\right]} \qquad (3)$$

where J is the strength of the nearest-neighbor exchange interaction. In arriving at Eq. (3) we have for simplicity restricted ourselves to the case of spin 1/2. For the dense or pure system, i.e., $m(T<T_c) = 1$, Eq. (3) reduces to the well known molecular-field theory result. This is shown in Fig. 3 bu curve (b). The actual function m(T) was

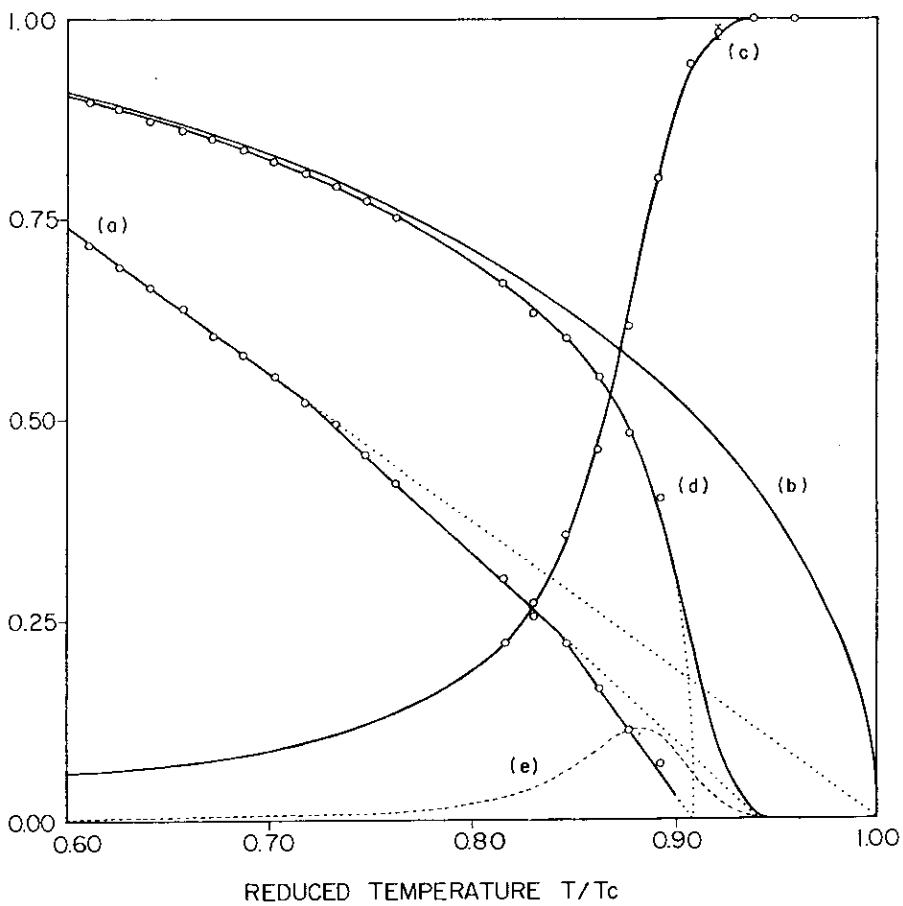

Fig. 3 – Variation of the normalized internal field H_o^3 (a), the reduced magnetization (b) and (d), the paramagnetic concentration $m_p(T)$ (c), and the distribution $P(T)/100$ (e) with temperature for $FeOHSO_4$. The experimental points are represented by circles.

determined by imposing that $(2M)^3$ given by Eq. (3) fits the H_o^3 data. The plot of $(2M)^3$ so obtained is shown by the full line in curve (a) of Fig. 3. In the proposed expression for m(T), λ means that one has as intrinsic disorder in our system even at low temperatures (probably due to paramagnetic $FeOHSO_4$ $2H_2O$ particles), whereas $\lambda I_p(T)/I_p(124^oK)$ accounts for the increasing disorder as the temperature is raised. The points corresponding to $1 - m(T) = m_p(T)$ are shown by the circles in curve (c) of Fig. 3. This function $m_p(T)$ is well represented by the expression $1 - \lambda + \lambda(I_p(T)/I_p(124^oK)$ where $\lambda = 0.98$ and

$$\lambda I_p(T)/I_p(124\ K) = \begin{cases} \dfrac{\left[\tan^{-1}\left(\dfrac{2(T-T_o)}{\Gamma_1}\right) + \tan^{-1}\left(\dfrac{2T_o}{\Gamma_1}\right)\right] \times \lambda}{\tan^{-1}\left(\dfrac{2T_o}{\Gamma_1}\right) + \dfrac{\Gamma_o\sqrt{2\pi}}{\Gamma_1}}, & 0 \le T \le T_o \\ \lambda - \dfrac{2\sqrt{2\pi}\Gamma_o\left[1-\mathrm{erf}\ \dfrac{T-T_o}{\Gamma_o\sqrt{2}}\right] \times \lambda}{\Gamma_1\left[\tan^{-1}\left(\dfrac{2T_o}{\Gamma_1}\right) + \dfrac{\Gamma_o\sqrt{2\pi}}{\Gamma_1}\right]}, & T \ge T_o \end{cases} \quad (4)$$

with T_o=0.88, Γ_o= 0.051 and Γ_1=0.074. The plot of mp(T) as defined above is shown in curve (c) by the full line. It should be emphasized, however, that by plotting Ip(T)/Ip (124°K) directly from the experimental intensities, one gets the same temperature behavior as the one given by Eq. (4) with the same values of T_o, Γ_o and Γ_1. Finally, in curve (d) of Fig. 3 it is shown by the full line the plot of 2M using Eq. (3) together with the present model for m(T) = 1 - mp(T). The circles in this curve are the experimental points H_o.

Now, as is well known[5], in the case of dilute magnets with fixed concentration m of magnetic atoms, the transition temperature is obtained by expanding the equation for M in powers of MJ/K_BT and retaining only the linear term in M. The result one gets for fixed m is that the critical temperature T_c is equal to that of the pure system, $T_c = ZJ/2\ K_B$, times m (i.e., $T_c = mT_c$). In our case, expanding Eq. (3) in powers of M, retaining only the linear term and bearing in mind that as T increases m approaches zero, one gets the following transcendental equation for the transition temperature.

$$T = T_c\, m(T) \qquad (5)$$

from which one obtains,

$$\frac{dT}{T_c} = P(T)\ dT = \frac{dm}{dT} \qquad (6)$$

or:

$$P(T) = \frac{dm}{dT}\ .$$

In other words, the assumption of a temperature-dependent concentration of magnetic atoms means that one has a distribution of transition temperatures[3,4] given by Eq.(6). In our present case, using Eq.(6), P(T) is given by

$$P(T) = \begin{cases} \dfrac{A}{(T-T_o)^2 + (\Gamma_1/2)^2}, & 0 \le T \le T_o \\ \dfrac{A}{(\Gamma_1/2)^2}\exp\left[-(T-T_o)^2/2\,\sigma^2\right], & T > T_o \end{cases} \qquad (7)$$

where T_o=116.7 K, Γ_1=9.8 K, σ=2.9 K and A is the normalization constant. It should be noted that in the case of a dilute system of fixed m, i.e., $m(T) = m\left|1 - \theta(T-T_c)\right|$, where $\theta(T-T_c)$ is the step function, the average value of T with the distribution function $P(T)=dm/dT$ gives the usual molecular-field result for the transition temperature, namely, $T_c=mT_c$. The plot of P(T) for our case is shown in curve (e) of Fig. 3.

In conclusion, we have discussed in this paper the magnetism of $FeOHSO_4$ via Mössbauer spectroscopy. The data for the internal field behavior at relatively high-temperatures was understood within the molecular-field model for random dilute magnets where the concentration of magnetic atoms varies with the temperature. The motivation which led us to this temperature dependent concentration was the strong variation of the paramagnetic line intensities (i.e., the quadrupole splitting line intensities) near the critical temperature. We have then entered in the molecular-field model for random magnets with m given by $\lambda\left[1-I_p(T)/I_p(124^oK)\right]$. The good agreement so obtained means that the hypothesis of a temperature-dependent concentration of magnetic ions recovers the disorder dynamics lost in the usual molecular-field theory (i.e., the neglect of the transverse terms of the Heisenberg Hamiltonian). This is translated in the fact that M(T), here obtained, follows quite well the 1/3-power law. This 1/3-power law for our data is also confirmed by an independent fit of our data for H_o to an expression of the form $H_o(T) = C(1-\tau)^\beta$ where $\tau=T/T_c$. The corresponding values for β, C and T_c one gets are: β=0.34 ± 0.01, C=572.5 ± 0.5 KO_e, T_c = 132.3 ± 0.3 °K(0.60<τ<0.72); β=0.33 ± 0.01, C=610.0 ± 0.5KO_e, T_c=124.0 ± 0.3 °K (0.72<τ<0.84); and β=0.34 ± 0.01, C=674.8 ± 0.5 KO_e, T_c=120.2 ± 0.3 °K (0.84<τ<1.00). Physically, the existence of m(T), and therefore, of a distribution of T_c, is due to the fact that our system consists of an assembly of microcrystals, for which case, the distribution of particle volume, as recently been demonstrated[6], implies in a distribution of critical temperatures.

Acknowledgement - The authors would like to thank Mr. A.S.Aragão for his help in the computational part of this work.

REFERENCES

1. SKEFF Neto,K. and GARG,V.K., J.Inorg. Nucl. Chem. 37, 2287 (1975)
2. ROGGWILLER,P. and KÜNDIG,W., Solid State Commun. 12, 901 (1973); MORUP,S. and TOPSOE,H., Appl. Phys. 11, 63 (1976); KÜNDIG,W., BUMMEL,H., CONSTABARIS,C.and LINDQUIST,R.H., Phys. Rev. 142, 327 (1966)
3. SHARON,T.E. and TSUEI,C.C., Phys. Rev. B5, 1047 (1972)
4. TSUEI,C.C., LUGWORTH,G. and LIN,S.C.H., Phys.Rev. 170, 603 (1968
5. TAHIR-KHELI,R.A., MIRANDA,L.C.M. and REZENDE,S.M., Il Nuovo cimento 30B, 335 (1975)
6. SKEFF Neto,K., LIMA,I.C.C., ALMEIDA; N.S. and MIRANDA,L.C.M., J.Phys. C (in press); see also INTERMAG 78 Conference Proceeding.

Resumé

Des mesures d'effet Mössbauer, sur du $FeOHSO_4$ sont présentées. Nous proposons, ici, un nouveau modèle, basé sur l'approximation du champ moléculaire pour des aimants dilués, afin d'expliquer le comportement observé, pour le champ interne, en fonction de la température.

A N E X O A – 4

J. Phys. C: Solid State Phys., Vnl. 11, 1978. Printed in Great Britain. © 1978

LETTER TO THE EDITOR

On the high-temperature behaviour of magnetically ordered microcrystals

K Skeff Neto†, I C Cunha Lima‡, N S Almeida§ and L C M Miranda§

†Departamento de Física, Universidade de Brasília, 70.000 Brasília, DF, Brazil

‡Departamento de Engenharia Espacial, Instituto Nacional de Pesquisas Espaciais, 12200 São José dos Campos, SP, Brazil

§Instituto de Física, Universidade Estadual de Campinas, 13100 Campinas, SP, Brazil

Received 18 May 1978

Abstract. A simple molecular-field model taking into account the characteristic volume distribution of an assembly of magnetically ordered microcrystals is developed to explain the observed high-temperature behaviour of the magnetisation. It is also shown that the volume distribution implies a distribution of critical temperatures.

The magnetic properties of microcrystals (systems consisting of an assembly of fine magnetic particles of 20–200 Å diameter) are currently a subject of considerable interest. A number of investigations on superparamagnetism (Wohlfarth 1977, Morup and Topsoe 1976) and the discovery of new phenomena like the surface sensitive magnetic anisotropy energy barriers (Dumeste *et al* 1975) and pinning of surface spins (Berkowitz *et al* 1975) have recently been reported. The original description of the magnetisation properties of such systems was suggested by Néel (1949): in these single domain particles the magnetisation vector is held in an easy direction by the crystalline field. At any finite temperature, thermal fluctuations cause the magnetisation to undergo a sort of Brownian rotation around the easy axis, and there is a finite probability that it will instantaneously change its direction into another easy direction. The relaxation time, which indicates how rapidly this transition occurs, was deduced by Néel and is given by Wohlfarth (1975), Morup and Topsoe (1976) and Néel (1949)

$$\tau = \tau_0 \exp(KV/k_B T) \tag{1}$$

where τ_0 is a time of the order of 1 ns, K is the anisotropy constant, V the volume of the microcrystal, and $k_B T$ is the thermal energy.

In this Letter we report on a model calculation for the high-temperature behaviour of the magnetisation of magnetically ordered microcrystals, having a characteristic grain size distribution, and show that the observed one-third power law is adequately accounted for. We begin our discussion by noticing that in a measurement of the magnetic properties of a single-domain particle, what is observed depends on the ratio of the time required for the measurement, τ_{obs}, to the relaxation time, τ, given by equation (1). For $\tau_{obs} \ll \tau$, the particles will show ferromagnetic behaviour whereas for $\tau_{obs} \gg \tau$, the

particles will be superparamagnetic. With the Mössbauer spectroscopy, for instance, the nuclear Zeeman splitting caused by the internal magnetic field at the site of the nucleus can be observed only if the Larmor frequency ν_L of the nuclear spin is larger than τ^{-1} (i.e., τ_{obs} corresponds to ν_L^{-1}). For $\tau \gg \nu_L^{-1}$ the particles will be superparamagnetic and the Zeeman splitting will disappear; for $\tau \approx \nu_L^{-1}$ one observes a partially relaxed magnetic hyperfine spectrum. In this sense the Mössbauer spectroscopy is a particularly suitable tool for investigating superparamagnetism. As an example, in figure 1 we show

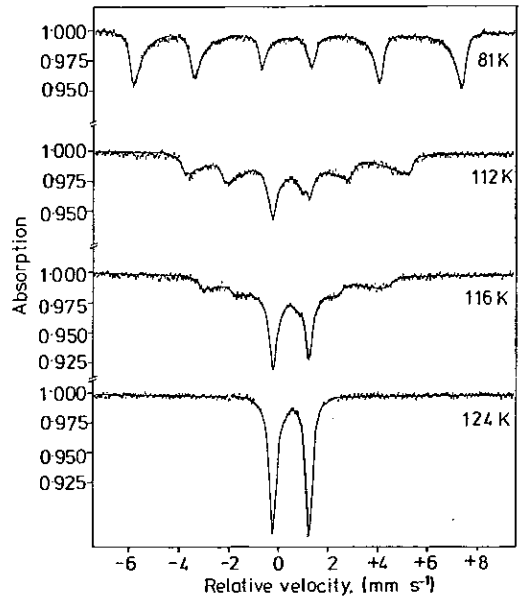

Figure 1. Mössbauer spectra of $FeOHSO_4$ at different temperatures, taken from Skeff Neto and Garg (1975) and Skeff Neto and Miranda (1978).

the Mössbauer spectrum of $FeOHSO_4$ at various temperatures. The experimental details as well as the sample preparation were reported elsewhere (Skeff Neto and Garg 1975, Skeff Neto and Miranda 1978). The Mössbauer spectrum at $T = 112$ K already shows a well-resolved six-peak pattern with a considerable broadening of the outer assymetric peaks and an enhancement of the electric quadrupole splitting lines. These features clearly suggest that there is a distribution of hyperfine fields reflecting all possible varieties of local environments (Tsuei and Lilienthal 1976, Sharon and Tsuei 1972) (i.e. the contribution of all microcrystals in the sample). In the following we show that this distribution of hyperfine fields is essentially due to a particle size distribution. Furthermore, this size distribution determines the observed temperature dependence of the magnetisation when one includes, in the description of our system, the particle anisotropy contribution, as in the usual superparamagnetic relaxation theories (Morup and Topsoe 1976, Néel 1949). To this end we assume an assembly of magnetically ordered particles having a size distribution $P(V)$. The magnetic Hamiltonian for a particle of volume V with uniaxial symmetry may then be written as (Wohlfarth 1977, Morup and Topsoe 1976, Néel 1949)

$$\mathcal{H} = -J\sum_{i,j} \boldsymbol{S}_i . \boldsymbol{S}_j - KV\sum_i (S_i^z)^2 \tag{2}$$

where J is the Heisenberg exchange integral between the z nearest-neighbour spins (S), and KV is the anisotropy energy barrier. Within the molecular-field approximation and for $S = \frac{1}{2}$, it follows from equation (2) that the magnetisation per atom $M = \langle S_i^z \rangle$ (i.e., the thermodynamic average of the z-component of the spin) can be easily calculated and the result is

$$M(V) = \tfrac{1}{2} \tanh[\beta(Jz + KV)M(V)/2] \tag{3}$$

where $\beta = 1/k_B T$. Expanding equation (3) in the limit when $M(V) \to 0$ the transition temperature $T_c(V)$ is readily obtained. One gets

$$k_B T_c(V) = (Jz + KV)/4. \tag{4}$$

The above equation establishes the transition temperatures for a grain of volume V. Since one has a distribution of volume, equation (3) implies that we also have a distribution of critical temperatures.

Now, if one realises that what, for instance, the Mössbauer spectrum gives us is the sum of contributions of the magnetisation of all microcrystals, the experimentally observed value M of the sample magnetisation is then given by the averaged value of $M(V)$ over the volume distribution, namely,

$$M = \int_0^\infty \mathrm{d}V\, P(V)\, M(V). \tag{5}$$

Here $M(V)$ is given by equation (3) and $P(V)$ is the volume distribution which may be known from, say, electron microscopy data. Equation (5) established the connection between our model and the experiment. To proceed we shall further assume a Lorentzian distribution of volume with average volume V_0 and width Γ, i.e.,

$$P(V) = \frac{\Gamma/2}{(\pi/2) + \tan^{-1}(2V_0/\Gamma)} \frac{1}{(V - V_0)^2 + (\Gamma/2)^2}. \tag{6}$$

This representation for $P(V)$ is generally accepted. In particular, in the case of $FeOHSO_4$,

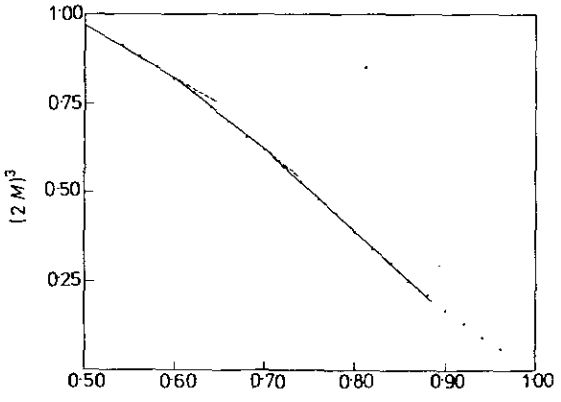

Figure 2. Varition of the magnetisation cubic (compare equations (3), (5) and (6)) versus the reduced temperature for $\alpha = 1{\cdot}01$ and $\eta = 0{\cdot}30$.

Table 1.

$(2M)^3$	$\alpha = 0{\cdot}51$	0·51	1·01	1·01
τ	$\eta = 0{\cdot}20$	0·30	0·20	0·30
0·50	0·92	0·98	0·91	0·97
0·52	0·90	0·96	0·89	0·94
0·54	0·87	0·93	0·86	0·91
0·56	0·84	0·90	0·83	0·88
0·58	0·81	0·87	0·80	0·85
0·60	0·78	0·83	0·76	0·82
0·62	0·74	0·79	0·73	0·78
0·64	0·70	0·76	0·69	0·74
0·66	0·66	0·72	0·65	0·70
0·68	0·62	0·67	0·61	0·66
0·70	0·58	0·63	0·57	0·62
0·72	0·54	0·58	0·53	0·57
0·74	0·49	0·54	0·48	0·53
0·76	0·45	0·49	0·44	0·48
0·78	0·40	0·44	0·40	0·44
0·80	0·36	0·40	0·35	0·39
0·82	0·31	0·35	0·31	0·34
0·84	0·26	0·30	0·26	0·30
0·86	0·22	0·25	0·22	0·25
0·88	0·17	0·21	0·17	0·21
0·90	0·13	0·17	0·13	0·17
0·92	0·09	0·12	0·10	0·13
0·94	0·06	0·09	0·06	0·09
0·96	0·03	0·05	0·03	0·06
0·98	0·01	0·02	0·01	0·03
1·00	0·00	0·01	0·00	0·01

V_0 and Γ are typically of the order of $0{\cdot}52 \times 10^{-18}$ cm^3 ($d = 100$ Å) and $4{\cdot}19 \times 10^{-21}$ cm^3 ($\Delta = 20$ Å), respectively (C A Ribeiro, unpublished).

In figure 2 we show the behaviour of $(2M)^3$ as a function of the reduced temperature $\tau = T/\langle T_c \rangle$ (where $k_B\langle T_c \rangle = (Jz + kV_0)/4$) for $\alpha = kV_0/Jz = 1{\cdot}01$ and $\eta = \Gamma/V_0 = 0{\cdot}30$. The computer data is summarised in table I. It follows from figure 2 and the analysis of table 1 that, in the high-temperature region, the $(2M)^3$-curve is well represented by three successive straight lines indicating that M obeys a one-third power law. The successive bendings are attributed to the fact that we have a volume distribution and that the larger particles take longer (according to equation (1)) to get disordered Finally, one notices that in the temperature region around 0·90, $(2M)^3$ is no longer a straight line. This is due to the fact that actually $P(V)$ is not truly symmetric. The region of high V vanishes more rapidly than the low V region. This is a consequence of the upper critical size, first predicted by Frenkel and Dorfman (1930), below which a particle of ferromagnetic material would consist of a single domain and be in a state of uniform magnetisation. This critical particle size was later estimated by Kittel (1946) and an approximate figure for the radius of a spherical sample of common ferromagnetic materials was found to be 150 Å. The kind of behaviour depicted in figure 2 is actually what is observed via Mössbauer spectroscopy in several systems of magnetically ordered microcrystals (Skeff Neto and Garg 1975, Skeff Neto and Miranda 1978, Kundig *et al* 1966). As an example

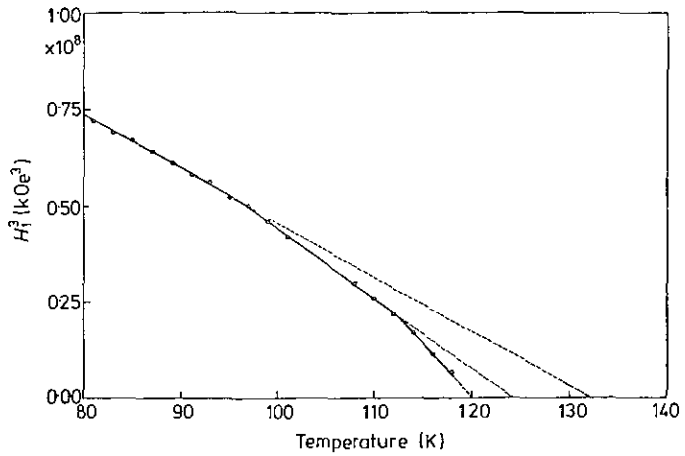

Figure 3. Variation of the internal field cubic with temperature for $FeOHSO_4$ taken from Skeff Neto and Miranda (1978). The experimental points are represented by circles.

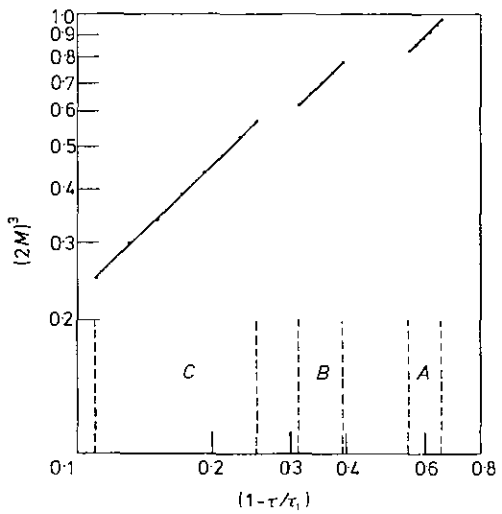

Figure 4. Variation of $(2M)^3$ as a function of $(1 - \tau/\tau_i)$ in a double-log scale for $\alpha = 1{\cdot}01$ and $\eta = 0{\cdot}30$. The symbols are the same as those defined in the text.

we show in figure 3 the plot of the internal field cubic, H_i^3, versus the temperature for $FeOHSO_4$ (Skeff Neto and Garg 1975, Skeff Neto and Miranda 1978). Finally, to best depict the one-third power law we show in figure 4 the log–log plot of $(2M)^3$ as a function of $(1 - \tau/\tau_i)$. Here τ_i ($i = A$, B, or C) refers to the critical temperature in regions A ($0{\cdot}50 \leqslant \tau \leqslant 0{\cdot}60$), B ($0{\cdot}62 \leqslant \tau \leqslant 0{\cdot}70$) and C ($0{\cdot}72 \leqslant \tau \leqslant 0{\cdot}86$), and are obtained by the extrapolation of the three successive straight lines of figure 2; we have $\tau_A = 1{\cdot}15$, $\tau_B = 1{\cdot}01$ and $\tau_C = 0{\cdot}97$. The angular coefficient one gets in these regions are $\tau_A = 1{\cdot}00$, $\tau_B = 1{\cdot}00$ and $\tau_C = 0{\cdot}99$ respectively.

In conclusion, we have demonstrated in this Letter that within the molecular-field

approximation, the volume distribution of a system of magnetically ordered particles is largely responsible for the magnetic properties of these systems. In particular it is responsible for the distribution of critical temperature characteristic of the systems as well as for the observed one-third power law for the magnetisation as a function of the temperature.

References

Berkowitz A E, Lahut J A, Jacobs I S, Levison L M and Forester D W 1975 *Phys. Rev. Lett.* **34** 594
Dumeste J A, Topsoe H and Boudart M 1975 *J. Catal.* **37** 113
Frenkel J and Dorfman J 1930 *Nature* **126** 274
Jacobz I S and Bean C P 1963 in *Magnetism* ed G T Rado and M Sohl, vol III (New York: Academic) p 271
Kittel C 1946 *Phys. Rev.* **70** 965
Kundig W, Bummel H, Constabaris G and Lindquist R H 1966 *Phys. Rev.* **142** 327
Morup S and Topsoe H 1976 *Appl. Phys.* **11** 63
Néel L 1949 *Ann. Geophys.* **5** 99
Roggwiller P and Kundig W 1973 *Salid St. Commun.* **12** 901
Sharon T E and Tsuei C C 1972 *Phys. Rev.* B **5** 1047
Skeff Neto K and Garg V K 1975 *J. Inorg. Nucl. Chem.* **37** 2287
Skeff Neto K and Miranda L C M 1978 *Phys. Rev.* B (submitted for publication).
Tsuei C C and Lilienthal H 1976 *Phys. Rev.* B **13** 4899
Wohlfarth E P 1977 *Physica* **86–88** B 852

A N E X O A - 5

Study of magnetism in fine particles of ferric hydroxysulfate by Mössbauer spectroscopy

P. C. Morais and K. Skeff Neto
Grupo de Física Molecular e Magnetismo, Departamento de Física, Universidade de Brasília, 70 910-Brasília-DF, Brazil

(Received 16 March 1982; accepted for publication 31 August 1982)

Experimental results of magnetization and Mössbauer measurements on ferric hydroxysulfate are presented. The method developed in the preparation and characterization of samples is discussed. In the present paper the magnetic properties are explained taking into account the pattern of particle size distribution of the samples in the region of superparamagnetism. The model is described in the molecular-field approximation for randomly dilute magnets.

PACS numbers: 76.80. + y, 75.60.Jp, 75.40. — s, 75.10.Jm

I. INTRODUCTION

The investigation of magnetic and structural properties of materials in superparamagnetic states has a theoretical and practical interest. The original description of the magnetization properties of such systems is due to Néel,[1] who proposed that in these single domain particles the magnetization vector is held in an easy direction by the crystalline field. At any finite temperature, thermal fluctuations cause the magnetization to undergo alike random rotation around the easy axis, and there is a finite probability that it will instantaneously change its direction in another easy direction. The relaxation time, which indicates how rapidly this transition occurs, was deduced by Néel,[1] Morup and Topsoe,[2] and Tsuei and Lilienthal[3] as

$$\tau = \tau_0 \exp(KV/K_B T), \tag{1}$$

where τ_0 is a time of the order of 1 ns, K is the anisotropy constant, V is the volume of particle, and $K_B T$ is the thermal energy. The superparamagnetic phenomenon occurs more frequently in particles having a diameter of the order of some hundred angstroms.

In the present paper we report and discuss Mössbauer measurements in the usual transmission geometry on ferric hydroxysulfate ($FeOHSO_4$), and the method used in the preparation of samples with different particle size distributions. The magnetic properties of $FeOHSO_4$ are described in the molecular-field approximation for randomly dilute alloys.

II. EXPERIMENTAL PROCEDURES

The $FeOHSO_4$ samples are obtained from the thermal decomposition of $FeSO_4 \cdot 7H_2O$ according to Skeff and Garg.[4,5] A schematic diagram of the experimental procedure for the production of these samples, at two different thermal treatments (250 and 300 °C), is shown in Fig. 1; these samples are identified as A(250) and A(300), respectively, in this paper. In the laboratory atmosphere the Mössbauer spectra of $FeOHSO_4$ change slowly over a period of several months. In an aqueous-vapor atmosphere (75%) the process is speeded up and after 22 days (room temperature) a new compound with essentially the same isomer shift (IS) but with a different quadrupole splitting (QS) is obtained; we denote these compounds B(250) and B(300).

The IS (Fe) of compounds A(250,300) is 0.473 mm/s and for B(250,300) is 0.423 mm/s corresponding to Fe(III) in the high spin configuration, but QS is large for the high spin ferric compounds[6] and it is closer to observed QS for Fe-O-Fe bridge compounds.[7] The QS of compounds A(250,300)

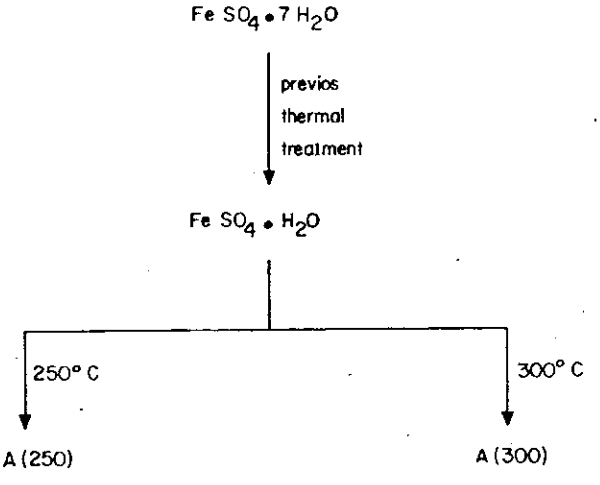

FIG. 1. Schematic experimental steps in the production of the $FeOHSO_4$ samples.

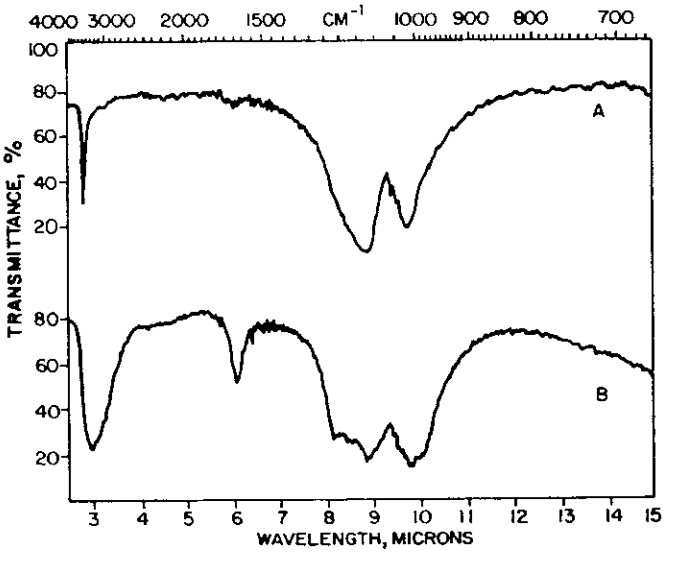

FIG. 2. IR spectra of (a) A and (b) B compounds at room temperature.

 0021-8979/83/010307-08$02.40

and B(250,300), at room temperature is 1.451 and 0.967 mm/s, respectively. The ir spectra of compound B shows absorption due to HOH bending mode at 1650 cm^{-1} and a broad absorption about 3450 cm^{-1} corresponding to OH^- stretching of water. Compound A has a very little absorption at 1650 cm^{-1} and the OH^- absorption near 3500 cm^{-1} is sharp and at a slightly higher frequency than those for compound B(see Fig. 2). These suggest that compound A does not contain water but contains OH^-. The observed and calculated percentage of Fe, S, O, and H for compounds A and B are closely to $FeOHSO_4$ and $FeOHSO_4 \cdot 2H_2O$, respectively. Heating compound B at 200 °C for few days reconverts it to compound A but the magnetic interaction, as seen via the Mössbauer spectrum, is very different.

The $FeOHSO_4$, sample A(250), obtained by the previous thermal treatment was hydrated at room temperature in the presence of aqueous-vapor atmosphere (75%) and the time required for the total hydration was 22 days. The final product was B(250) identified as $FeOHSO_4 \cdot 2H_2O$. The process of hydration will be represented by

$$A(250) \rightarrow A\ B(250)_d,$$

where d represents the days of exposure to the aqueous-vapor atmosphere. The sample A $B(250)_0$ is the A(250) and the sample A $B(250)_{22}$ is the B(250). The process of hydration of A(250) was monitored by Mössbauer spectroscopy, at room temperature, and a Mössbauer spectrum was obtained every two days. In Fig. 3 we show the Mössbauer spectra of A $B(250)_d$ for $d = 0, 6, 12, 22$. The process of dehydration of A $B(250)_d$ by heating at 200 °C for various days may be represented by

$$A\ B(250)_d \rightarrow B\ A(250)_d,$$

where B $A(250)_d$ show the same IR spectrum, IS (Fe) and QS

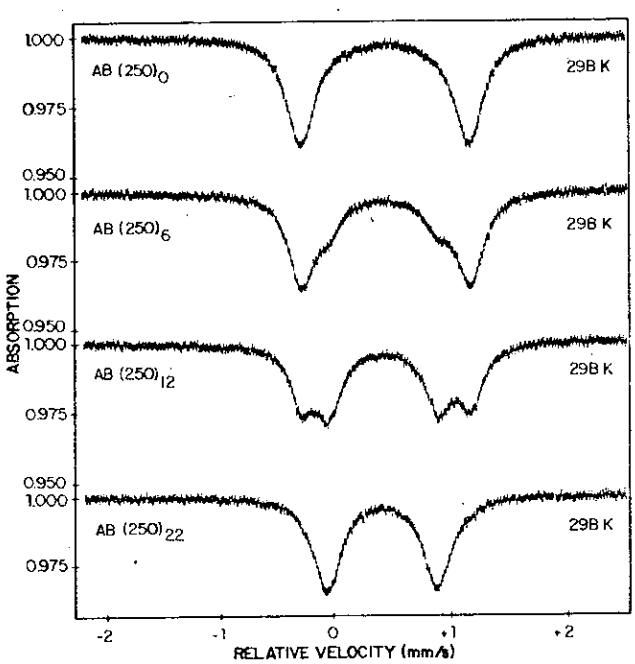

FIG. 3. Mössbauer spectra of A $B(250)_d$, at room temperature, after $d = 0$, 6, 12, and 22 days of hydration.

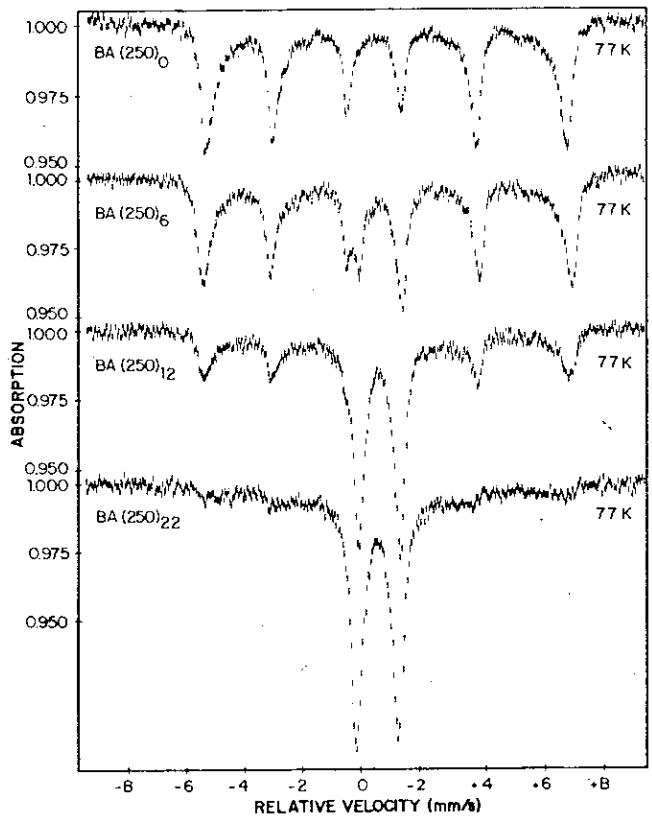

FIG. 4. Mössbauer spectra of B $A(250)_d$, at 77 K, for $d = 0$, 6, 12 and 22.

of A(250), at room temperature, but their Mössbauer spectra differ at low temperature (77 K). In Fig. 4, we show the Mössbauer spectra of B $A(250)_d$ at 77 K. The spectra for three different samples, A(300), B $A(250)_2$, and B $A(250)_4$ obtained at various temperatures are shown in Figs. 5(a), 5(b), and 5(c), respectively. The particle size distribution for one sample, A(300), was obtained by electron microscopy and is shown in Fig. 6. The electron microscopy and the particle size distribution, for B $A(250)_2$ sample, are presented in Figs. 11(a) and 11(b), respectively.

III. ANALYSIS

The empirical formula of the B compound corresponds to Butlerite whose structure has been determined by Fanfani.[8] The magnetic moment of compound A (assumed as paramagnetic), is $\mu = 2.38\ \mu_B$ at 100 K and $\mu = 3.78\ \mu_B$ at 300 K. These values are lower than the usual paramagnetic value ($\mu \sim 5.9\ \mu_B$) for iron (III) having the types of ligants under discussion. For compound A the observed moments and their temperature behavior suggest that it is a dimer. The SO_4^{-2} ion in inorganic compounds shows an absorption in the region of 1100 cm^{-1}, which has been attributed to the O_3 mode vibration.[9] This mode is degenerate in completely ionic sulfates, where the symmetry of the sulfate ion is T_d. When the symmetry of the sulfate ion is C_{2v} (when two of the oxygens are bonded to the metal) the degeneracy is lifted; this seems to be the case for compound A (Fig. 2). Thus this indicates that at least some of the SO_4^{-2} ions are bonded via two oxygens to the iron in this compound. A structural for-

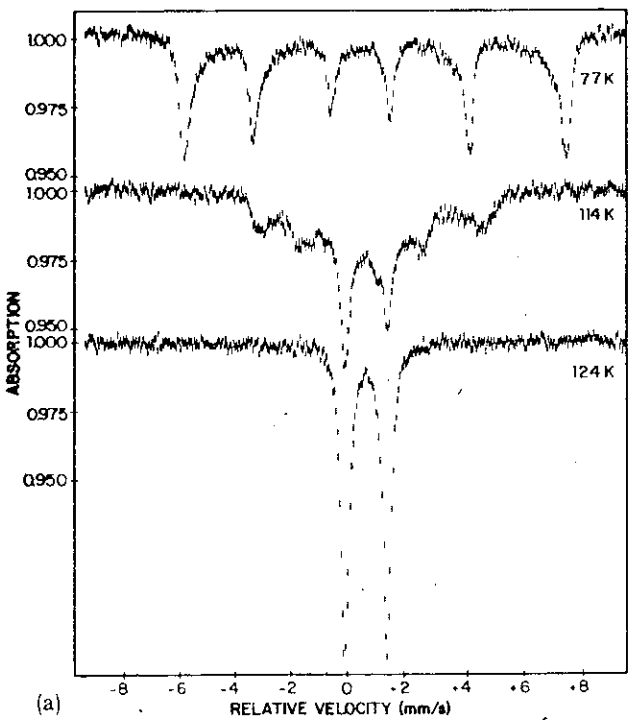

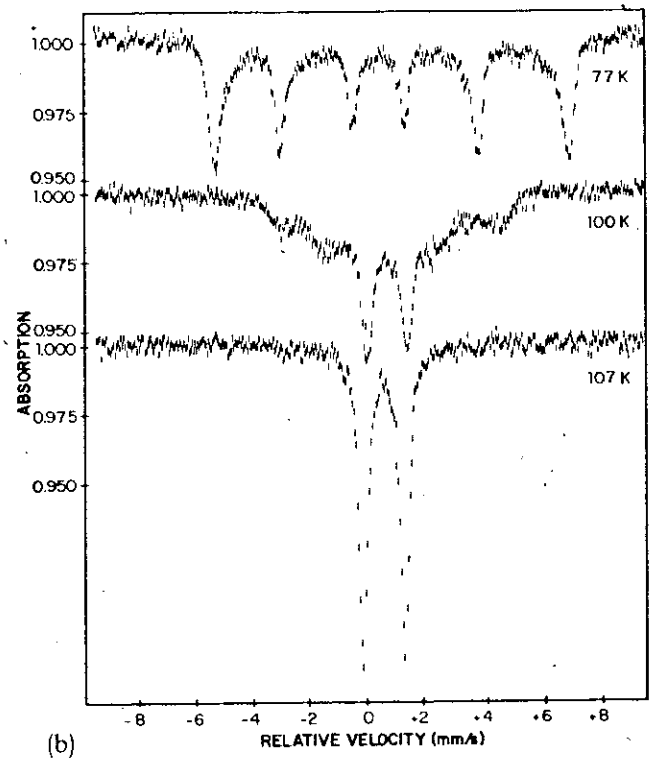

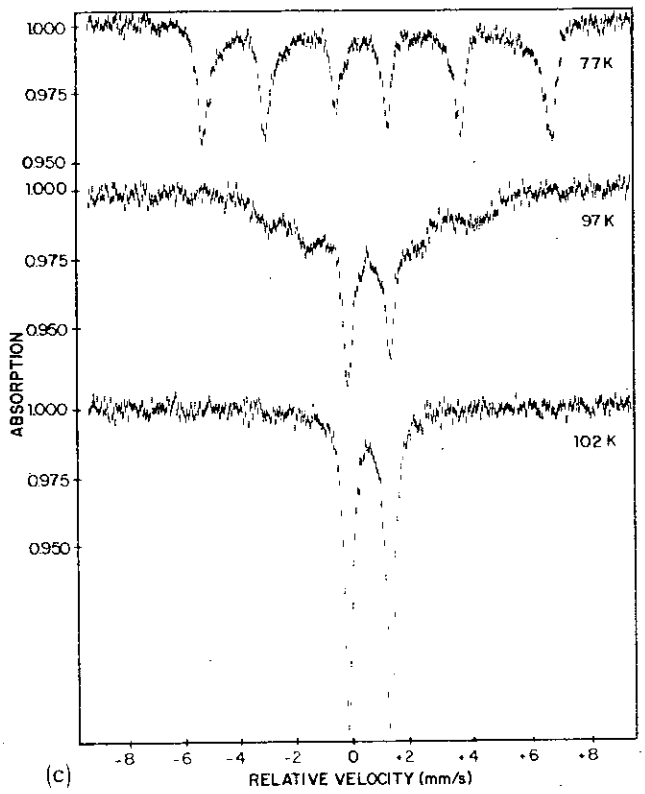

FIG. 5. (a) Mössbauer spectra of A(300) sample at 77, 114 and 124 K. (b) Mössbauer spectra of B $A(250)_2$ sample at 77, 100, and 107 K. (c) Mössbauer spectra of B $A(250)_4$ sample at 77, 97, and 102 K.

mula for the $FeOHSO_4$ compound is suggested below:

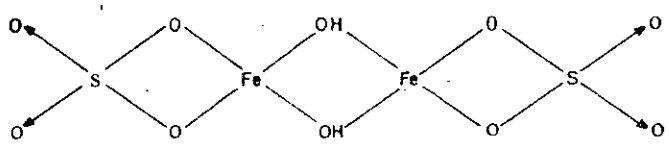

Finally, the distortion generated in the Fe site by the four-member ring in the above structure could be correlated with the anomalous large QS for the high spin ferric compounds.

The Mössbauer spectrum shown in Fig. 4 suggests two different behaviors: firstly, as the days of hydration (d) increase, the quadrupole splitting—which is indicative of the magnetic disordering—appears, and the intensity of the hyperfine splitting (six lines) decreases, and secondly, as the days of hydration (d) increase, the internal field (H_0) grows to

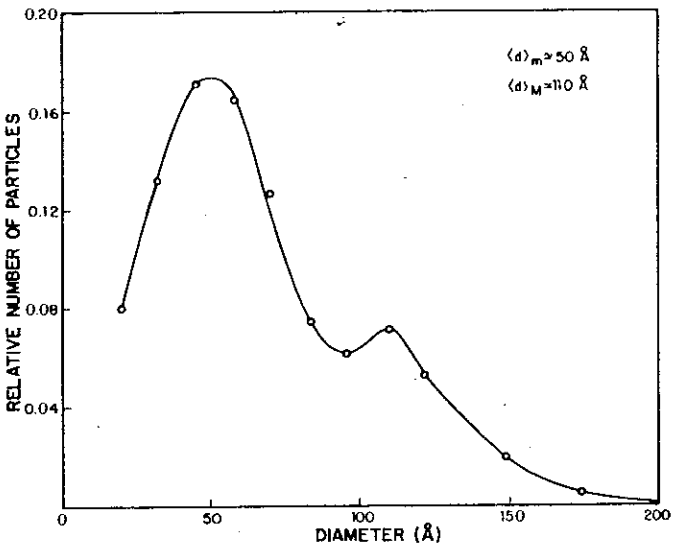

FIG. 6. Particle size distribution for A(300) sample obtained by electron microscropy.

a maximum and then decreases. This behavior is shown in Fig. 7. The internal field (H_0) was obtained by fitting the Mössbauer spectrum in terms of a hyperfine field distribution $P(H)$, similar to that suggested by Sharon and Tsuei[10] and Tsuei *et al.*[11] The expression for $P(H)$ is

$$P(H)=\begin{cases} A\left[(H-H_0)^2+\left(\frac{\Gamma_1}{2}\right)^2\right]^{-1}, & \text{for } 0<H\leqslant H_0, \quad (2a)\\ B\left[(H-H_0)^2+\left(\frac{\Gamma_2}{2}\right)^2\right]^{-1}, & \text{for } H>H_0. \quad (2b)\end{cases}$$

Upon matching these values at $H=H_0$ the normalization constant is determined by the condition

$$\int_0^\infty P(H)dH=1. \tag{3}$$

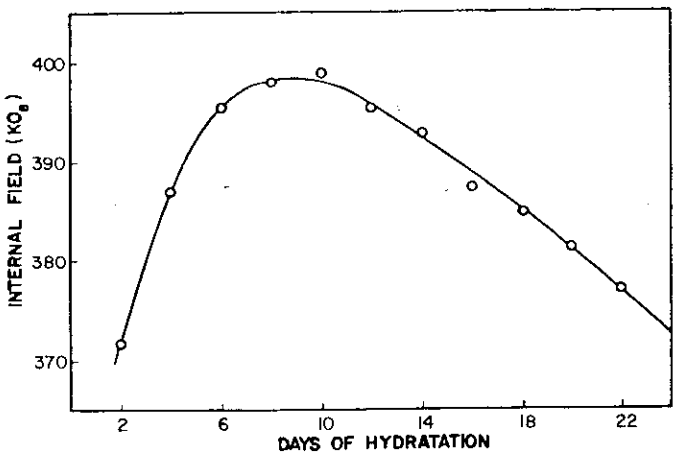

FIG. 7. Magnetic internal field behavior as the days of hydration for B A(250)$_d$ sample (d = 2, 4, 6, 8, 10, 12, 14, 16, 18, 20, 22).

The behavior of the normalized H_0^3 versus temperature for the samples A(300), B A(250)$_2$, and B A(250)$_4$ is shown in Fig. 8. The experimental points are represented by circles and the solid lines represent the best fit of the data to an expression of the form

$$\frac{H_0(T)}{H_0(0)}=D\,(1-T/T_c)^{\beta}, \tag{4}$$

where D and β are constants, $H_0(0)$ and T_c are internal field at 0 K and the transition temperature, respectively. For the sample A(300) the adjusted values are $H_0(0)=(469.6\pm0.5)$ kOe, $D=(1.225\pm0.005)$, $T_C=(131.66\pm0.05)$ K and $\beta=(0.335\pm0.005)$. It follows from Fig. 8 and the analysis of the experimental values of $H_0(T)$ that the values of $[H_0(T)/H_0(0)]^3$ are well represented by a succession of straight lines all indicating that $[H_0(T)/H_0(0)]$ obeys a one-third power

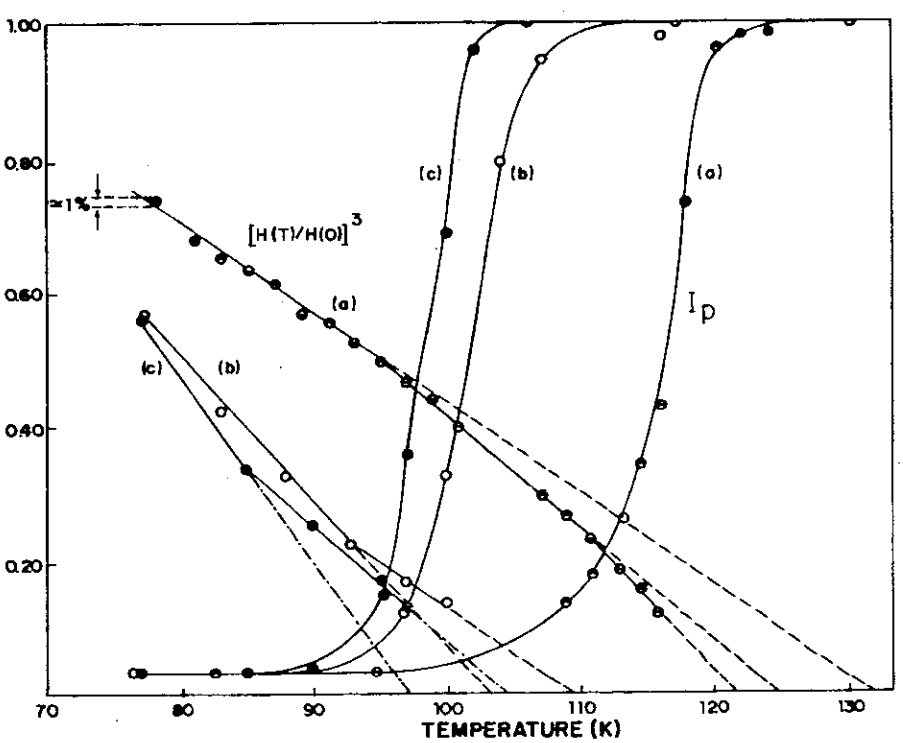

FIG. 8. Experimental values of $[H_0(T)/H_0(0)]^3$ and paramagnetic intensity lines (I_p) as a function of temperature for (a) A(300), (b) B A(250)$_2$, and B A(250)$_4$ samples.

law.

The electron microscopy results for the A(300) sample shows the presence of a particle size distribution centered around two different diameter values, as presented in Fig. 6. The behavior of the internal field (H_0) versus d (days of hydration), for the samples B A(250)$_d$ shown in Fig. 7, was interpreted according to Luborsky[12] and suggests that there is time evolution of the particles diameter in the process of hydration and dehydration of the $FeOHSO_4$.

The Mössbauer spectra at various temperatures, shown in Fig. 5, are typical of superparamagnetic particles. The Mössbauer spectrum for the sample A(300) at 77 K shows the characteristics assymetric broadening and at 114 K shows a well-resolved six-peak pattern with considerable broadening of the outer peaks and an enhancement of the quadrupole splitting lines. Since these are the only lines which survive above the transition temperature, from now on we shall call them the "paramagnetic lines." In the literature the analysis of such systems has been done quite often with the help of Néel theory for the relaxation of single domain particles together with the variation of the Mössbauer line width with temperature in accordance with Roggwiller and Kündig[13] and Kündig *et al.*[14] The theoretical approach of this problem, based upon the Green functions, has been used by Tahir-Kheli and ter Haar,[15] Callen[16] and Tahir-Kheli.[17,18] In our paper we consider another aspect of this problem, namely, that of the behavior of the internal magnetic field with temperature and using the model based upon the molecular-field approximation for randomly dilute alloys as described by Tahir-Kheli *et al.*[19] We consider the presence of a particle size distribution centered around different diameter values (D_i). The presence of such a particle size distribution must be determined by other techniques (for example, electron microscopy). A similar analysis was carried out by Skeff and Miranda[20] to take into account the presence of a particle size distribution centered around only one diameter value (D) but the fit with experimental values of magnetization near the transition temperature is very poor. The model assumes that around each Fe atom there is a cell of Z nearest neighbors for which the magnetization is determined by the local concentration of Fe atoms and by the temperature. In this model the magnetic atoms interact amongst themselves through a molecular field which is proportional to the magnetization temperature of their neighbors. If we consider that "paramagnetic line" intensity is proportional to the number of paramagnetic Fe atoms, we can associate the density of magnetically ordered atoms m as a function of temperature, namely,

$$m(T)=\lambda\left[1-\sum\alpha_i I_p^i(T)/I_p(\theta)\right], \tag{5}$$

where λ, a constant smaller than unit, represents the density of the magnetically ordered atoms at low temperature, α_i is the fraction of particles with diameter centered around D_i, θ is the temperature beyond which no magnetic contribution is felt by the Mössbauer spectrum and the values of $I_p^i(T)/I_p(\theta)$ is given by the normalized "paramagnetic line" intensities. In terms of the molecular-field approximation for the ferromagnetic ordering and allowing for the variation of m with the temperature given by Eq. (5), the expression for the magnetization per atom M is given by

$$\frac{1}{2}-M=\sum_{\nu=0}^{z}\frac{z![m(T)]^{\nu}[1-m(T)]^{z-\nu}}{(z-\nu)!\nu![\exp(2MJ/K_BT)+1]} \tag{6}$$

in the case of spin $S=1/2$. In Eq. (6) z is the number of the nearest-neighbor exchange interaction. The actual function for $m(T)$ was determined by imposing that $(2M)^3$ given by Eq. (6) fits the H_0^3 data.

IV. RESULTS

In the case of dilute magnets where $m(T)$ is a function of temperature it is well known[19,20] that the transition temperature is obtained by expanding the Eq. (6) in powers of MJ/K_BT and retaining only the linear term in M and bearing in mind that as T increases $m(T)$ approaches zero, the following transcendental equation for the transition temperature is obtained

$$T=T_c m(T), \tag{7}$$

from which one obtains an expression for the distribution of transition temperature[10,11] $P(T)$,

$$\frac{dT}{T_c}=\frac{dm(T)}{dT}\,dT$$

or

$$P(T)=\frac{dm}{dT}. \tag{8}$$

The expression for $I_p^i(T)/I_p(\theta)$ for the A(300) sample was adjusted by

$$I_p^i(T)/I_p(\theta)=\begin{cases}\dfrac{\tan^{-1}\left[\dfrac{2(T-T_{0i})}{\Gamma_{1i}}\right]+\tan^{-1}\left(\dfrac{2T_{0i}}{\Gamma_{1i}}\right)}{\tan^{-1}\left(\dfrac{2T_{0i}}{\Gamma_{1i}}\right)+\dfrac{\Gamma_{0i}\sqrt{2\pi}}{\Gamma_{1i}}}, & 0<T\leqslant T_{0i}, \quad (9a)\\[2ex] 1-\dfrac{2\sqrt{2\pi}\Gamma_{0i}\left[1-\operatorname{erf}\left(\dfrac{T-T_{0i}}{\Gamma_{0i}\sqrt{2\pi}}\right)\right]}{\Gamma_{1i}\left[\tan^{-1}\left(\dfrac{2T_{0i}}{\Gamma_{1i}}\right)+\dfrac{\Gamma_{0i}\sqrt{2\pi}}{\Gamma_{1i}}\right]}, & T>T_{0i}, \quad (9b)\end{cases}$$

TABLE I. Experimental adjusted values for the A(300) sample, where T_c is the critical temperature of the sample (K), $H_0(0)$ is the internal field at 0 K (kOe), λ is the density of magnetically ordered atoms at low temperature, α_i is the fraction of particles whose diameter is centered around D_i, τ_1 is the extrapolation of the critical temperature related at region of high magnetic order, τ_2 is the extrapolation of the critical temperature related at region of lower magnetic order, θ is the temperature where does not exist any one magnetic contribution in the Mössbauer spectrum, T_{0i} is the temperature associated with the maximum of $P^i(T)$ and Γ_{0i}, Γ_{1i} are the width of $P^i(T)$ distribution.

T_c	131.62 ± 0.01	θ	0.940 ± 0.002
$H_0(0)$	467.5 ± 0.5	T_{10}	0.900 ± 0.001
λ	0.921 ± 0.001	T_{02}	0.919 ± 0.001
α_1	0.854 ± 0.001	Γ_{01}	0.013 ± 0.002
α_2	0.146 ± 0.001	Γ_{02}	0.049 ± 0.002
τ_1	0.918 ± 0.001	Γ_{11}	0.011 ± 0.002
τ_2	0.948 ± 0.001	Γ_{12}	0.012 ± 0.002

where T_{0i} is the temperature associated with the maximum of $P^i(T)$ distribution centered around diameter D_i and Γ_{0i}, Γ_{1i} are the width of $P^i(T)$ distributions. The corresponding values for these parameters are given in Table I, and $P^i(T)$ is given by

$$P^i(T) = \begin{cases} \dfrac{A}{(T - T_{0i})^2 + (\Gamma_{1i}/2)^2}, & 0 < T \leqslant T_{0i}, \quad (10a) \\ \dfrac{A}{(\Gamma_{1i}/2)^2} \exp\left[-(T - T_{0i})^2 / 2\sigma_i^2 \right], & T > T_{0i}. \quad (10b) \end{cases}$$

In Fig. 9 we show the critical temperature distribution $P(T)$ associated at the A(300) sample.

In Fig. 10 we show the behavior of $[H_0(T)/H_0(0)]^3$, $[H_0(T)/H_0(0)]$, and $m_p(T) = [1 - m(T)]$, where the full line is that obtained by our model and the points are the experimental values obtained for A(300) sample.

V. DISCUSSION

The behavior shown in Fig. 4 is associated with the size of $(1-x)\mathrm{FeOHSO_4} \cdot 2\mathrm{H_2O}$ particles during the process of hydration. The diameter of the particles increases with the days of hydration, and the process of dehydration does not alter them. In Fig. 7 the presence of a critical diameter D_c, associated with the maximum of the internal field H_0, is noticeable. Thus the effective value of the internal field obtained by the Mössbauer spectrum must be determined by the values of D_i relative to D_c, and the relative intensity of each particle size distribution centered around D_i; consequently the initial raising of H_0 (in Fig. 4) as a function of days of hydration is associated with the growing of particles having diameter below the critical value D_c and the subsequent lowering of H_0 is associated with the growing of particles diameter, beyond that diameter. The second observation related to the same Fig. 4, is that of the increase of the "paramagnetic line" intensity and the decrease of magnetic line intensity as

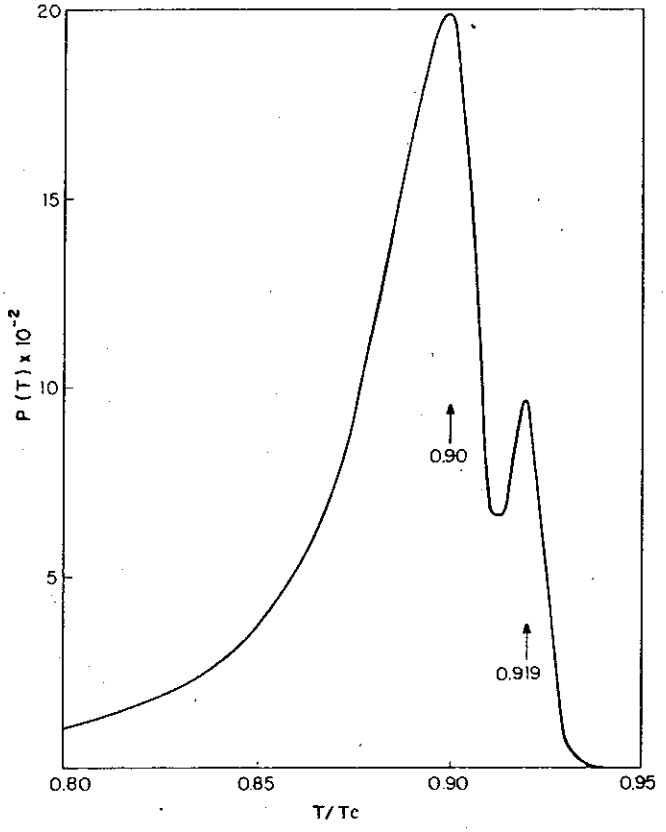

FIG. 9. Critical temperature distribution $P(T)$ relative to the A(300) sample.

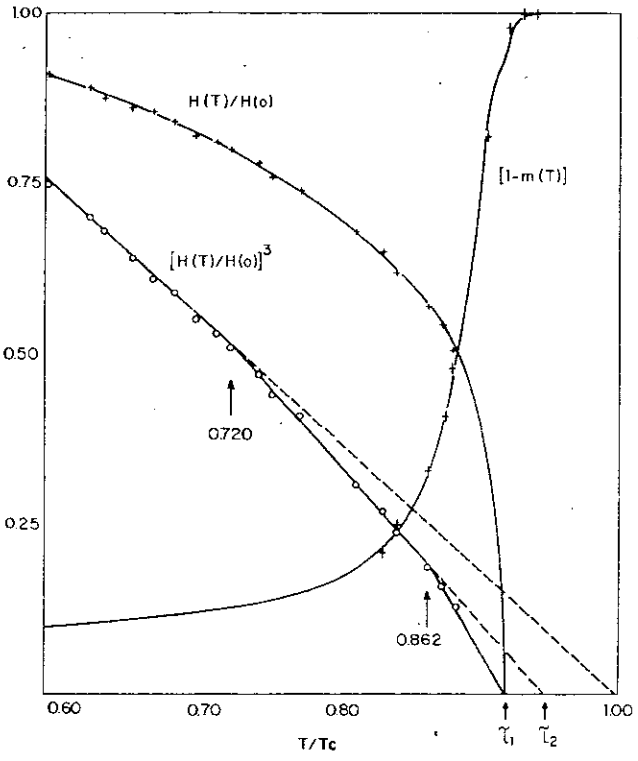

FIG. 10. Behavior of the (a) $H_0(T)/H_0(0)$, (b) $[H_0(T)/H_0(0)]^3$, and (c) $m_p(T) = 1 - m(T)$ vs T/T_c for A(300) sample. The theoretical plot is shown by the full lines and the experimental values are represented by the points.

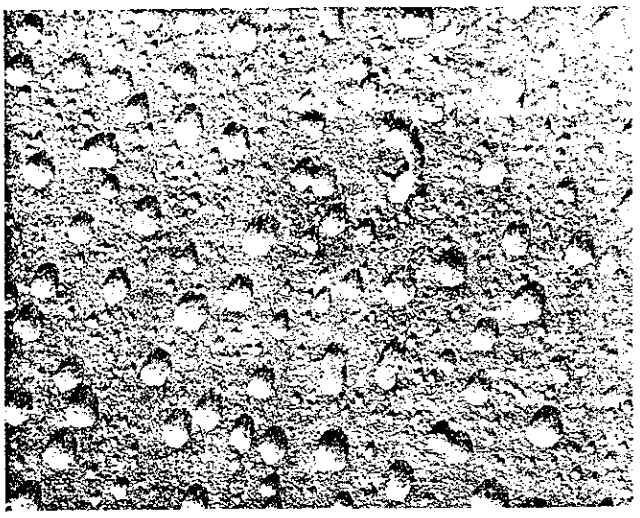

(a)

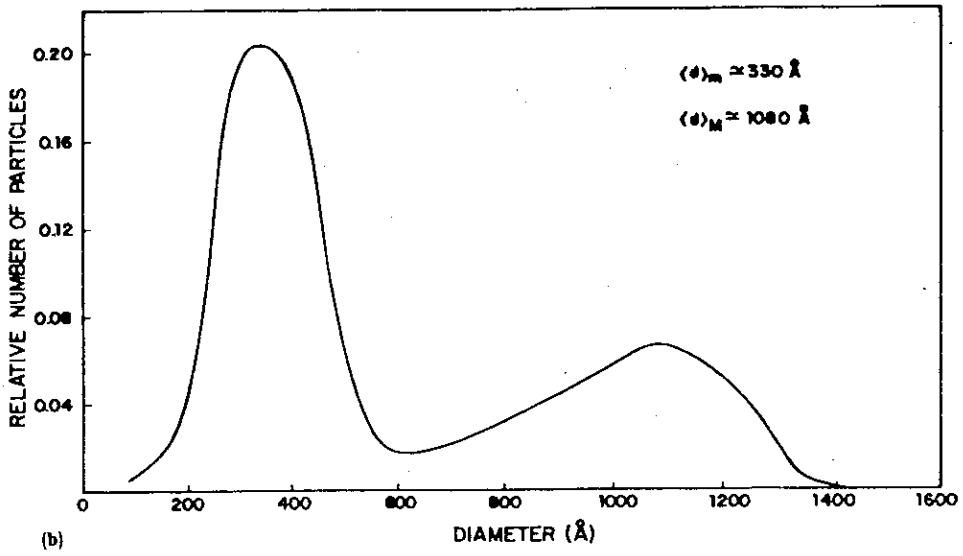

(b)

FIG. 11. (a) Electron microscopy for B A(250)$_2$ sample (44000×). (b) Particle size distribution for B A(250)$_2$ sample obtained by electron microscopy.

a function of days of hydration. These behaviors are understood bearing in mind the lowering of magnetic-ordered atoms fraction or the raising of magnetic-disordered fraction.

The behavior of H_0^3 vs T, for different samples, as depicted in Fig. 8 indicates different transition temperatures of sample. Within experimental error the experimental values of $H_0^3 \times T$ show three regions (straight line) with different angular coefficients for A(300) samples, and two different regions with different angular coefficients for the B A(250)$_2$ sample. In the $H_0^3 \times T$ curve for A(300) samples, the first region (77 K $< T <$ 95 K) corresponds to Mössbauer spectra with a well-resolved six-peak pattern where the broadening of the outer peaks indicates the presence of a distribution of hyperfine fields. However, in this first region the contribution of magnetic disordered atoms is not significant. On the other hand, in the second and third regions of the $H_0^3 \times T$ curve for the A(300) sample, for 95b K $< T <$ 107 K and 107 K $< T <$ 122 K, respectively, the contribution of magnetic disordered atoms is a important one. We associated the magnetic disordering of two final regions with a particle size distribution centered around two different diameters, 50 and 110 Å. Those particles with diameters centered around 50 Å show a magnetization value lower than those with diameters centered around 110 Å, for in this case the A(300) samples are below the critical diameter (D_c). Consequently the second region of the $H_0^3 \times T$ curve is dominated by the magnetic behavior of the high particle diameter (110 Å) and the third region is dominated by the lower particle diameter (50 Å). In the $H_0^3 \times T$ curve for the B A(250)$_2$ sample [Fig. 5(b)] it is noticeable that a magnetic disordering occurs even at 77 K. Here we have two regions, 77 K $< T <$ 93 K and 93 K $< T <$ 110 K, corresponding to two straight lines with different angular coefficients. Once more we associate the magnetic disordering of these two regions with a particle size distribution centered around two different diameters, 330 Å and 1080 Å [see Figs. 11(a) and 11(b)]. The particles with diameters centered at around 330 Å show a magnetization

value higher than those centered around 1080 Å because in the case of the B $A(250)_2$ sample we are above the critical diameter (D_c).

VI. CONCLUSIONS

The experimental transition temperature of the $FeOHSO_4$ sample is sensitive to the pattern of particle size distribution in the regions of superparamagnetism, and the interpretation of their magnetic properties must take into account these distributions. The magnetic order and disorder phenomena may be understood within the molecular-field model for random dilute magnets if one takes into account that the concentration of magnetic atoms varies with temperature. The presence of various regions in the $H_0^{\frac{3}{2}} \times T$ plot which characterize the magnetic order and disorder does not invalidate the one-third power law. The experimental values can be fitted by the expression $M(T)/M(0) = H_0(T)/H_0(0) = D(1 - T/T_c)^{\beta}$.

[1]L. Néel, Ann. Geophys. **5**, 99 (1949).
[2]S. Morup and H. Topsoe, Appl. Phys. **11**, 63 (1976).
[3]C. C. Tsuei and H. Lilienthal, Phys. Rev. B **13**, 4899 (1976).
[4]K. Skeff Neto and V. K. Garg, Riochem. Radional. Lett. **15**, 357 (1973).
[5]K. Skeff Neto and V. K. Garg, J. Inorg. Nucl. Chem. **37**, 2287 (1975).
[6]N. N. Greenwood and T. C. Gibb, *Mössbauer Spectroscopy* (Chapman and Hall, London, 1971), p. 162.
[7]H. Schugar, C. Walling, R. B. Jones, and H. B. Gray, J. Am. Chem. Soc. **89**, 3712 (1967).
[8]L. Fanfani, A. Nunozi, and P. F. Zanazzi, Am. Mineral. **56**, 751 (1971).
[9]A. Vértes and B. Zsoldos, Acta Chim. Acad. Sci. Hung. **56**, 3 (1970).
[10]T. E. Sharon and C. C. Tsuei, Phys. Rev. B **5**, 1947 (1972).
[11]C. C. Tsuei, G. Lugworth, and S. C. H. Lin, Phys. Rev. **170**, 603 (1968).
[12]F. E. Luborsky, J. Appl. Phys. **32**, 171 (1961).
[13]P. Roggwiller and W. Kündnig, Solid State Commun. **12**, 901 (1973).
[14]W. Kündig, H. Bömmel, G. Constabaris, and R. H. Lindquist, Phys. Rev. **142**, 327 (1966).
[15]R. A. Tahir-Kheli and D. ter Haar, Phys. Rev. **127**, 88 (1962).
[16]H. B. Callen, Phys. Rev. **130**, 890 (1963).
[17]R. A. Tahir-Kheli, Phys. Rev. B **6**, 2826 (1972).
[18]R. A. Tahir-Kheli, in *Amorphous Magnetism*, edited by H. O. Hooper and A. M. de Graaf (Plenum, New York, 1973), p. 393.
[19]R. A. Tahir-Kheli, L. C. M. Miranda, and S. M. Rezende, Il Nuovo Cimento B **30**, 335 (1975).
[20]K. Skeff Neto and L. C. M. Miranda, Solid State Commun. **28**, 43 (1978).

A N E X O A - 6

Polyhedron Vol. 2, No. 9, pp. 875 880, 1983
Printed in Great Britain.

0277 5387/83 $3.00 + .00
Pergamon Press Ltd.

SPECTROSCOPIC CHARACTERIZATION OF SUPERPARAMAGNETIC PARTICLES OF THERMOLYTIC PRODUCTS OF FERRIC SULPHATE HYDRATES

P. C. MORAIS and K. SKEFF NETO*

Grupo de Física Molecular e Magnetismo, Departamento de Física, Universidade de Brasília 70 910-Brasília-DF, Brasil

(*Received* 21 *September*, 1982; *accepted* 11 *February* 1983)

Abstract—Superparamagnetic particles of chemically pure samples, in the system $Fe(OH)SO_4/Fe(OH)SO_4 \cdot (H_2O)$, are produced by thermal decomposition of ferric sulphate hydrates. The control of particle size distribution is achieved by successive hydration and dehydration processes monitored by X-ray diffraction, electron microscopy, Mössbauer and IR spectroscopy. The particle size modification is related for the particle growth and two mechanisms are suggested thereon.

Thermal treatments induces oxidation of Fe^{2+} ion to Fe^{3+} in sulphate hydrates. This well-known phenomenon has been reported by many workers.[1-9] The thermal decomposition of Fe^{2+} compounds can be probed by several techniques including Mössbauer spectroscopy, because of its high sensitivity to the valence state of the iron in solids. The oxidation mechanism is that Fe^{2+} is oxidized into Fe^{3+} by hydroxyl radicals which originate from the water of crystallization.[10] However, this mechanism does not specify the chemical formulae of the thermal decomposition products. The present report deals with an investigation of thermal decomposition products of ferrous sulphate monohydrate using Mössbauer, IR and X-ray diffraction. The main thermolytic product is a ferric specimen identified as $Fe(OH)SO_4$.

In an aqueous-vapour atmosphere this compound gives a hydrate $Fe(OH)SO_4(H_2O)_2$ which was confirmed by chemical and spectroscopic analysis. The process of hydration is monitored by X-ray diffraction, Mössbauer and IR spectroscopy. Heating of $Fe(OH)SO_4(H_2O)_2$ reconverts it to $Fe(OH)SO_4$ but the drying process induces a change in volume and alters significantly their magnetic properties. In the present paper we analyze the change on the particle size distribution based on electron microscopy patterns and magnetic measurements. The Mössbauer effect has proved to be a unique tool for the measurement of such magnetic preperties.

*Author to whom correspondence should be addressed.

Another important reason for applying the Mössbauer technique is that no external field must be applied to the sample and the zero-field magnetization may be determined with great accuracy.

EXPERIMENTAL

Analytically pure $FeSO_4(H_2O)$ was used as the original material to obtain the $FeSO_4(H_2O)_4$. This compound is grown from aqueous solution of $FeSO_4(H_2O)_7$ at constant temperature within the range 54–64°C according to the literature.[11] $FeSO_4(H_2O)$ was obtained from the aqueous solution of $FeSO_4(H_2O)_7$ at constant temperature within the range 80–100°C in vacuum for a few days. On heating $FeSO_4(H_2O)$ in air up to 180°C a mixture of compounds was obtained.[12] However, the Mössbauer spectra at room temperature of $FeSO_4(H_2O)$ heated at 250°C for several days shows a pure well resolved doublet with I.S. (Fe) = 0.44 mm/s and Q.S. = 1.45 mm/s as depicted in Fig. 1, spectrum $AB(250)_0$.

This compound was called A (250) or $AB(250)_0$ and in the laboratory atmosphere the Mössbauer spectra changes slowly over a period of several months, but in an aqueous-vapour atmosphere (75%) the process of hydration is speeded up and at the end of 22 days we obtain another pure compound. This compound was called B(250) or $AB(250)_{22}$ and shows a pure well resolved doublet at room temperature as shown in Fig. 1. Compounds A (250) and B(250) show, at room temperature, essentially the same I.S. but a different quadrupole splitting. The Q.S. of B(250) is 0.97 mm/s.

The compounds A(250) and B(250) were

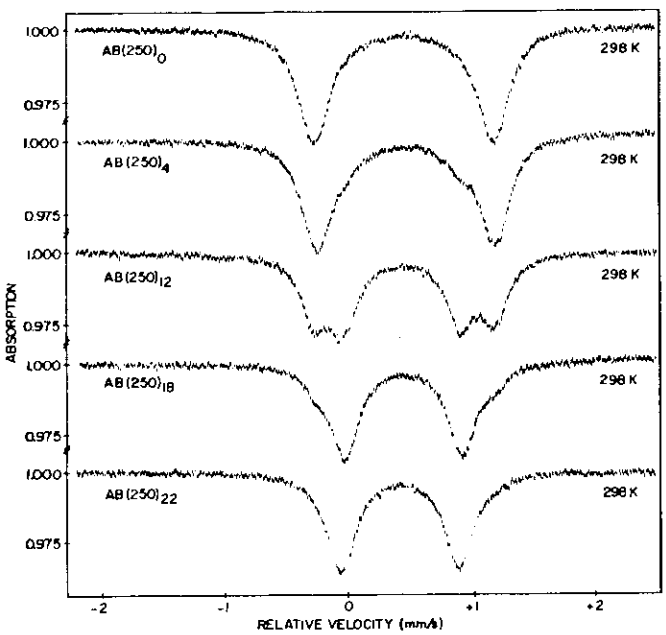

Fig. 1. Mössbauer spectra of $AB(250)_d$, at room temperature, after $d = 0$, 4, 12, 18 and 22 days of hydration.

identified by chemical and spectroscopic measurements as $Fe(OH)SO_4$ and $Fe(OH)SO_4(H_2O)_2$ respectively.[13] The Mössbauer parameters were determined using computer fitting and are listed in Table 1. The process of hydration was monitored, at room temperature, by X-ray diffraction, Mössbauer and IR spectroscopy as shown in Figs. 1–3. During the process of hydration several samples of A(250) were collected after 0, 4, 12, 18 and 22 days of hydration. These samples were heated at 200°C, for several days until the total dehydration so that the final products were $Fe(OH)SO_4$. The Mössbauer spectra of such products at 77 K are depicted in Fig. 4. This process of hydration and subsequent dehydration was followed by electron microscopy and is shown in Figs. 5(a)–(c).

DISCUSSION

The presence of $FeSO_4(H_2O)$, in the vacuum treatment at room temperature of $FeSO_4(H_2O)_4$, can be confirmed by reported Mössbauer parameters.[6,7] A schematic sequence on the thermal and aqueous-vapour treatments is shown below. Here A(250) is the same

$$FeSO_4(H_2O)_7 \rightarrow FeSO_4(H_2O)_4 \rightarrow FeSO_4(H_2O) \downarrow$$
$$BA(250)_d \leftarrow AB(250)_d \leftarrow A(250)$$

as $AB(250)_0$, $AB(250)_{22}$ is the same as B(250) and $BA(250)_d$ are chemically $Fe(OH)SO_4$. The subscript "d" that appears on $AB(250)_d$ may be referred as the days of hydration in an aqueous-vapour atmosphere (75%) at room temperature.

Table 1. The Mössbauer parameters of the A(250), B(250) and those of butlerite

Sample	T(K)	Hint (Koe)	Q.S. (mm/s)	I.S.* (mm/s)	Ref.
A(250)	298	0	1.45	0.44†	[12]
B(250)	298	0	0.97	0.42†	[13]
$Fe(OH)SO_4 \cdot 2H_2O$ ((butlerite)	300	0	0.94	0.42	[22]

*Relative to Fe at 298 K.
†The accuracy is 0.02 mm/s.

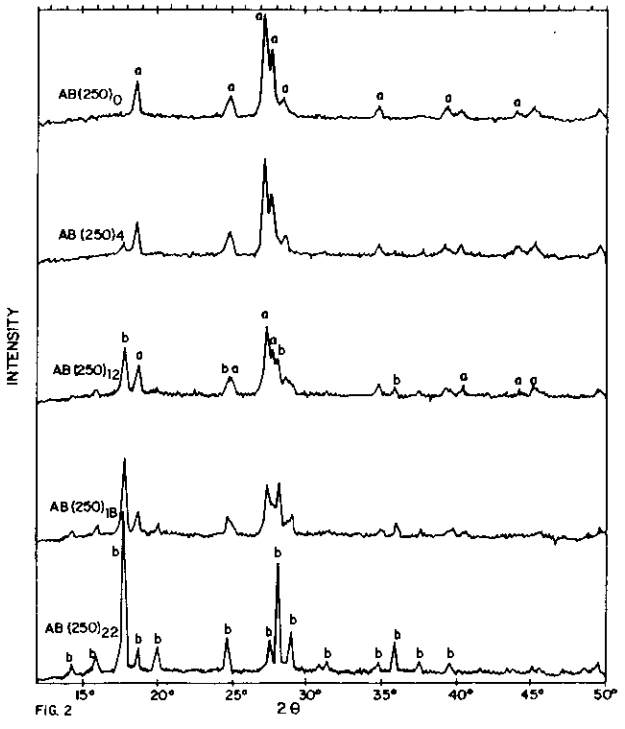

FIG. 2

Fig. 2. X-Ray diffraction patterns of $AB(250)_d$, at room temperature, *a* denotes the diffraction peak related to $Fe(OH)SO_4$ and *b* denotes the diffraction peak related to $Fe(OH)SO_4(H_2O)_2$.

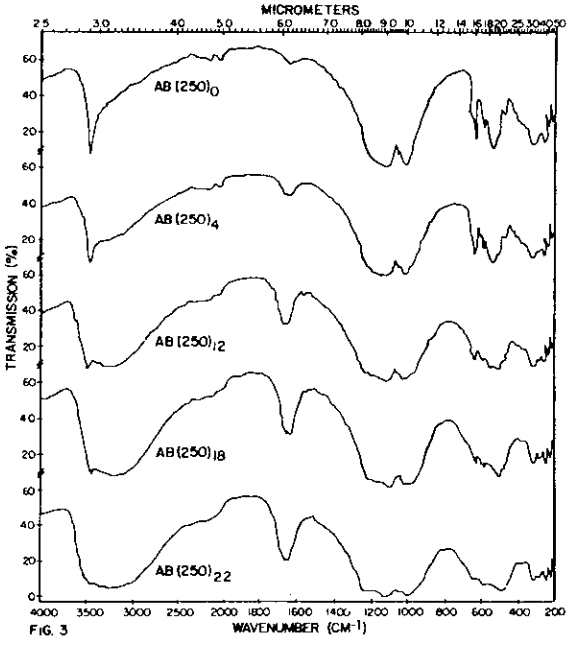

FIG. 3

Fig. 3. IR spectra of $AB(250)_d$, at room temperature, after $d = 0$, 4, 12, 18 and 22 days of hydration.

Comparing the Mössbauer parameters of B(250) compound and those of Butlerite (Table 1) we can conclude that B(250) compound is the Butlerite whose structure has been determined by Fanfani.[14]

In Fig. 1 we show the Mössbauer spectra sequence in the process of hydration at room temperature which convert $Fe(OH)SO_4$ into $Fe(OH)SO_4(H_2O)_2$. Here we represent the process of hydration by

$$Fe(OH)SO_4 \rightarrow x\ Fe(OH)SO_4,$$
$$(1-x)Fe(OH)SO_4(H_2O)_2$$

where "x" is related to "d" parameter with $0 \leq x \leq 1$. The intermediate Mössbauer spectra, for which $0 < x < 1$, shows a superposition of $Fe(OH)SO_4$ and $Fe(OH)SO_4(H_2O)_2$. As shown in Table 1 the values of Q.S. for $AB(250)_0$ and $AB(250)_{22}$ samples is large for the high spin ferric compounds and it is characteristic for Fe–O–Fe bridge compounds.[15]

The X-ray diffraction pattern sequence in the process of hydration, taken at room temperature, is shown in Fig. 2. Here the observed diffraction pattern of $AB(250)_{22}$ sample agree exactly with those of Butlerite listed in the ASTM file. It is worth mentioning that the diffraction pattern of $AB(250)_0$ sample shown in Fig. 2, which we identified as pure $Fe(OH)SO_4$, have not been re-

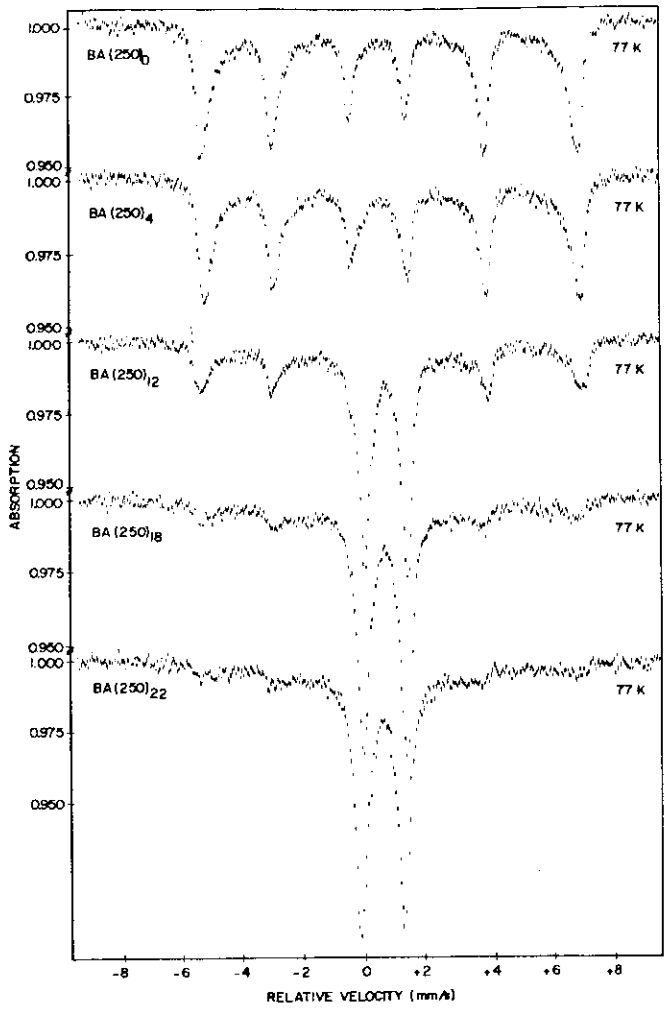

Fig. 4. Mössbauer spectra of $BA(250)_d$, at 77 K, for $d = 0$, 4, 12, 18 and 22.

ported hitherto. The intermediate diffraction patterns shows a superposition of that $Fe(OH)SO_4$ and $Fe(OH)SO_4(H_2O)_2$. Besides the diffraction peaks of $Fe(OH)SO_4(H_2O)_2$ denoted by "*b*" in Fig. 2, there are other peaks which are denoted by "*a*" and related to $Fe(OH)SO_4$.

In order to gain more information about the process of hydration of $Fe(OH)SO_4$, the IR spectra sequence was obtained at room temperature and is shown in Fig. 3. Here the absorption in the region of 1100 cm^{-1} is indicative of the presence of SO_4^{2-} ion in inorganic compounds.[16] The absorption about 1650 and 3450 cm^{-1} corresponds to HOH bending mode and OH stretching of water respectively. This characterizes the $Fe(OH)SO_4(H_2O)_2$ compound as the $AB(250)_{22}$ sample. The very little absorption near 1650 cm^{-1} and a sharp absorption at 4380 cm^{-1} characterize the $Fe(OH)SO_4$ compound as the $AB(250)_0$ sample. The intermediate IR spectra shows a superposition of $AB(250)_0$ and $AB(250)_{22}$ samples.

It is worth noting what would happen in the process of hydration and subsequent dehydration of $Fe(OH)SO_4$. Here the process of dehydration, by heating at 200°C for various days, may be represented by

$$AB(250)_d \rightarrow BA(250)_d.$$

The samples, namely $BA(250)_d$, collected during the process of hydration for $d = 0$, 4, 12, 18, 22 and heated as described above, show the same IR, Mössbauer and X-ray diffraction pattern at room temperature. These spectra show the same patterns as $AB(250)_0$ sample at room temperature. However, as we may expect, the Mössbauer spectra of $BA(250)_d$ samples depict different magnetic interactions at 77 K (see Fig. 4). The interesting fact about the foregoing result is that the process of hydration and dehydration induces a modification on the particle size distribution and change significantly their magnetic properties. In Fig. 4 the

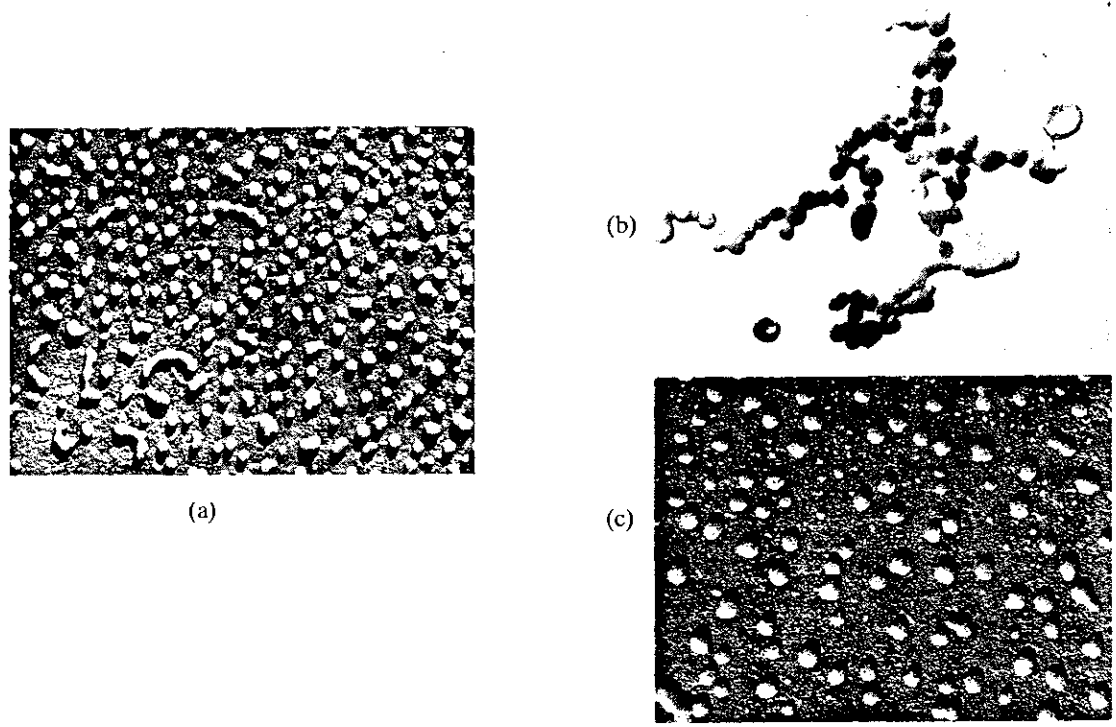

Fig. 5. Electron microscopy patterns. (a) $AB(250)_0$ sample (44.000x). (b) $AB(250)_4$ sample (113.000x). (c) $BA(250)_4$ sample (44.000x).

hfs lines broaden when the days of hydration (d) increase and the low resolution results in merging of the six hyperfine structure components into two lines. This variation of the Mössbauer spectra offers an evidence of superparamagnetic behavior of the $Fe(OH)SO_4$ particles.[17,18] Another behaviour clearly displayed in Fig. 4 is the increase of the internal field (H_0), as the days of hydration, to a maximum and subsequent decrease. This behaviour was associated with the growth of the $Fe(OH)SO_4$ particles as a function of "d" and the presence of a maximum in the value of the internal field (H_0) was associated with the existence of a critical diameter.[13]

The process of evolution in the particle size distribution may be suggested by the analysis of electron microscopy patterns shown in Fig. 5 and by the evolution of the X-ray diffraction sequence shown in Fig. 2. In Fig. 2 the narrowing of the X-ray lines during the process of hydration is an indication of a recrystalization process. In Fig. 5 we show the electron microscopy patterns of $AB(250)_0$, $AB(250)_4$ and $BA(250)_4$ which represents the process of hydration of $Fe(OH)SO_4$ for 4 days and subsequent heating at 200°C for various days until the total dehydration. In this process the diameter of particles has grown approx. 75%. Here the dimensional changes during drying process occur because the particles are brought into close contact and porosity is reduced. The driving force is due to the decrease of total surface energies which comes about because of the particle contact and particle growth. The atoms in the small particles are transferred to the larger particles, and the pores are replaced by solid material.[19] The electron microscopy patterns, X-ray diffraction sequence and the magnetic nature of the samples suggest two distinct but concurrent mechanisms to this mass transfer in the process of the particle growth in accordance with Burke[20] and Mackenzie and Shuttleworth.[21] They are illustrated schematically in Fig. 6. Burke[20] analyzed the diffusion mechanism (Fig. 6a) which involves the movement of atoms and the countermovement of lattice vacancies. There is an accompanying shrinkage of bulk volume which maintains contact of the

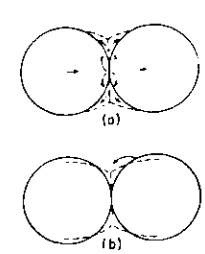

Fig. 6. Schematic of mass transfer mechanisms. (a) Diffusion.[19] (b) Liquid phase.[20]

particle and brings the particle centers closer together. Mackenzie and Shuttleworth[21] studied the liquid phase sintering (Fig. 6b) which involves the removal of ions or atoms from surfaces of higher energy and depositing them on surfaces of lower energy. The highest-energy surfaces are those with small radii of convex curvature: the lowest-energy surfaces are those with small radii of concave curvature.

CONCLUSION

We have analyzed the process of production of chemically pure samples in form of small particles. By means of successive hydration and dehydration we can control adequately the particle size distribution. This is an important point because the magnetization in an amorphous material is very sensitive to the particle size distribution. In the present work we used the chemical system $Fe(OH)SO_4$/$Fe(OH)SO_4(H_2O)_2$ for two reasons; firstly the process of successive hydration and dehydration is chemically reversible and secondly the $Fe(OH)SO_4$ exhibit superparamagnetic properties.

The use of several techniques for monitoring the process of dimensional changes is very important because they ensure the reversible character in the chemical transformation. The Mössbauer spectroscopy shows the superparamagnetic behavior and the electron microscopy depict the particle size distribution. The particle size control in the process of growth was oriented by the mechanism suggested herein.

REFERENCES

1. B. C. Frazer and P. J. Brown, *Phys. Rev.* 1972, **125**, 1283.
2. C. E. Johnson, W. Marshall and G. J. Perlow, *Phys. Rev.* 1962, **126**, 1503.
3. J. C. Boyat and G. Bassi, *Compt. Rend* 1963, **256**, 1482.
4. A. J. Nozik and M. Kapla, *Phys. Rev.* 1967, **159**, 273.
5. K. Chandra and S. P. Puri, *Phys. Rev.* 1968, **196**, 272.
6. A. Vértes and B. Zsoldos, *Acta Chim. Acad. Scient. Hung.* 1970, **65**, 3.
7. A. Vértes, T. Székely and T. Tarnoczy, *Acta Chim. Acad. Scient. Hung.* 1970, **63**, 1.
8. P. K. Gallaghar, D. W. Johnson and F. Scherey, *J. Am. Ceram. Soc.* 1970, **53**, 566.
9. V. K. Garg, S. P. Puri, *J. Chem. Phys.* 1971, **54**, 209.
10. P. Gütlich, S. Odar, B. W. Fitzsimmons and N. E. Erickson, *Radiochimica Acta* 1968, **10**, 147.
11. K. Skeff Neto and V. K. Garg, *Radiochem. Radional. Lett.* 1973, **15**, 357.
12. K. Skeff Neto and V. K. Garg, *J. Inorg. Nucl. Chem.* 1975, **37**, 2287.
13. P. C. Morais and K. Skeff Neto, *J. Appl. Phys.* 1983, **54**(1), 307.
14. L. Fanfani, A. Nunzi and P. F. Zanazzi, *Am. Min.* 1971, **56**, 751.
15. H. Schugar, C. Walling, R. B. Jones and H. B. Gray, *J. Am. Chem. Soc.* 1967, **89**, 3712.
16. R. A. Nyquist and R. O. Kagel, *Infrared Spectra of Inorganic Compounds*, pp. 264–299. Academic Press, New York (1971).
17. K. Skeff Neto, I. C. Cunha Lima, N. S. Almeida and L. C. M. Miranda, *J. Phys. C* 1978, **11**, 695.
18. K. Skeff Neto, L. C. M. Miranda, *Solid State Commun.* 1978, **28**, 43.
19. D. MacLean, *Grain Boundaries in Metals*. Oxford University Press, London (1957).
20. J. E. Burke, *Recrystallization and Sintering in Ceramics, Ceramic Fabrication Processes*. Wiley, New York (1958).
21. J. K. MacKenzie and R. Shuttleworth, *Proc. Phys. Soc. London* 1949, **B62**, 833.
22. N. Sakai, H. Sekizawa and K. Ôno, *J. Inorg. Nucl. Chem.* 1981, **43**, 1731.

A N E X O A – 7

Electron paramagnetic resonance linewidth of superparamagnetic particles[a)]

P. C. Morais, A. L. Tronconi, and K. Skeff Neto
Grupo de Física Molecular e Magnetismo, Departamento de Física, Universidade de Brasília, 70.910—Brasília, DF, Brazil

(Received 20 June 1983; accepted for publication 11 August 1983)

Superparamagnetic particles have been investigated by electron magnetic resonance. We have shown that the temperature dependence of the linewidth (above the freezing temperature) is sensitive to the pattern of particle size distribution. The behavior of the linewidth as a function of temperature is explained if we assume an anisotropic Dzyaloshinskii–Moriya type of interaction where the relaxation process occurs by a longitudinal component.

PACS numbers: 75.60.Jp, 75.50.Kj, 76.30. — v

I. INTRODUCTION

In the last years several studies of the magnetic resonance linewidth have been done on a reasonable number of magnetic amorphous materials and a theoretical and practical interest has evolved. The experimental results have given information about the spin freezing phenomenon which is though to be related to finite clusters of spins weakly coupled to the infinite ferromagnetic cluster near the percolation limit.[1,2] However, the experimental magnetic resonance linewidth data presented in the literature differ from the theoretical approaches proposed since then, in the region of high temperature,[3,4] i.e., well above the freezing temperature (T_f). This is the temperature below which the relaxation process of the system via the finite clusters becomes bottlenecked.

Superparamagnetic particles of ferric hydroxysulfate ($FeOHSO_4$) were produced by thermal decomposition of ferric sulfate hydrates according to Skeff Neto and Garg.[5,6] Some theoretical approaches have been proposed to explain the magnetic properties of such systems.[7,8] Recently, we reported Mössbauer spectroscopy measurements and proposed a more general model, based upon the molecular-field approximation for randomly dilute ferromagnets, to explain the superparamagnetic behavior of the ferric hydroxysulfate particles. This model takes into account the pattern of the particle-size-distribution dependence of the magnetic properties.[9]

In the present paper we look at another side of the problem of the magnetic properties of fine particles; namely, we report the behavior of the magnetic resonance linewidth measurements as a function of temperature and propose a new approach to explain the experimental data above the freezing temperature.

II. EXPERIMENTAL RESULTS

An amorphous ferromagnetic sample of ferric hydroxysulfate is obtained by thermal decomposition of monohydrate ferrous sulfate, at 250 °C in an air atmosphere, according to the following chemical reaction:

$$FeSO_4 \cdot H_2O \rightarrow FeOHSO_4.$$

The spectroscopic characterization of $FeOHSO_4$ is made by x-ray, infrared, and Mössbauer measurements.[10] This $FeOHSO_4$ sample must be identified as A (250) in order to relate it to other papers.

The magnetic resonance data were taken using a noncommercial X-band spectrometer tuned around 9.038 GHz in the microwave attenuation range 26.0 dB. The temperature was lowered from 286.8 to 101.5 K using a liquid N_2 flux technique; below 112.4 K no magnetic resonance signal was detected. Some typical resonance curves, representing the conventional derivative of the absorptive components of the microwave susceptibility as a function of the applied field H, are shown in Fig. 1. The curves have fairly large linewidths and are asymmetric. The linewidth, defined between the peaks of the absorption derivative, increase from about 0.7 to 2.0 kG as the temperature is lowered towards the freezing temperature. The experimental values of microwave resonance linewidth and corresponding temperatures are shown in Table I. In Fig. 2 we show the temperature dependence of the resonance linewidth ($\Gamma - \Gamma_0$) in

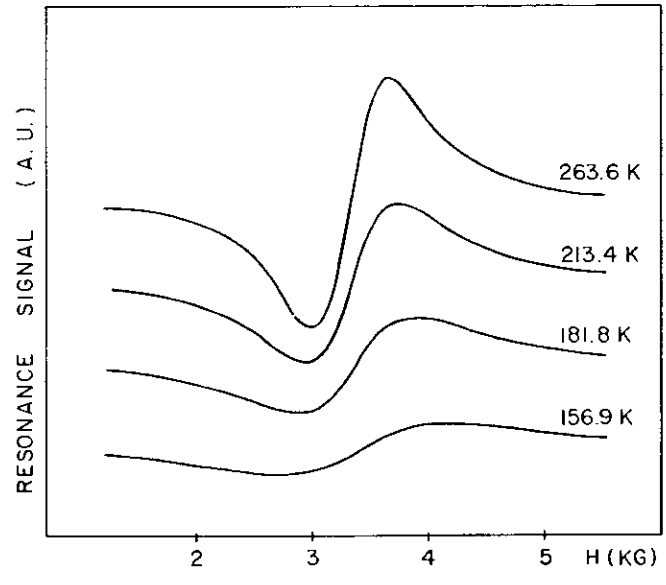

FIG. 1. Resonance signals, i.e., field derivatives of the absorptive component of the microwave susceptibility at some different temperatures. Sample A (250).

a) Partially supported by CNPq.

 0021-8979/84/103744-03$02.40

TABLE I. Experimental values of EPR linewidth (Γ) and linewidth broadening ($\Delta\Gamma$) related to $\Gamma_0 = 0.630 \pm 0.004$ kG, for A(250) sample.

T (K)	Γ (kG)	$\Delta\Gamma$ (kG)
141.2 ± 0.1	1.940 ± 0.004	1.310 ± 0.004
149.0	1.645	1.015
156.9	1.470	0.840
164.1	1.297	0.667
170.4	1.194	0.564
176.1	1.097	0.467
181.8	1.036	0.406
186.7	1.002	0.372
192.0	0.952	0.322
197.5	0.921	0.291
202.5	0.879	0.249
207.9	0.855	0.225
213.4	0.831	0.201
219.2	0.806	0.176
224.3	0.785	0.155
229.9	0.771	0.141

a semilog plot, where Γ_0 is very close to the temperature independent value of Γ observed at higher temperatures. The experimental points are represent by circles.

III. THEORY

Two kinds of systems have been related to the spin freezing phenomenon. In the type I systems one observes a paramagnetic to ferromagnetic transition at T_c and a ferromagnetic to cluster glass transition at T_f.[11] In the type II systems the transition is from paramagnetic to cluster glass transition at T_f.[12] In our case the experimental data show that we have a type I system which is dependent on the particle size distribution.[7,9] To describe the dynamics of our system we use a geometric picture of a dilute ferromagnet consisting of an infinite cluster of spins with a long range magnetic order coexisting with a distribution of finite clusters of spins whose diameters are centered around two different mean value diameters $<d_j>$. The presence of such a bimodal distribution of finite clusters, well defined agglomerates of spins, is verified by electron microscopy.[9,10]

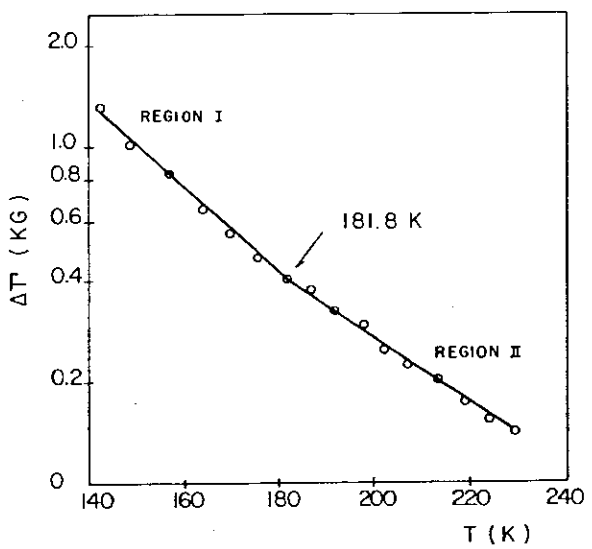

FIG. 2. Temperature dependence of the EPR linewidth of superparamagnetic A (250) particles. Note the logarithmic vertical scale.

Within the geometric picture described above, we consider the low-energy excitations of the infinite ferromagnetic cluster as spin waves and treat the coupling of these modes to the finite clusters as a double relaxation channel for the infinite cluster driven by the microwave field, similarly to Continentino approach.[13] We assume that the relaxation process, above the freezing temperature, occurs via an anisotropic Dzyaloshinskii–Moriya (DM) type of interaction between spins in the infinite and finite clusters, according to Fert and Levy,[14] and that the longitudinal relaxation mode is the most important one. We thus have the Hamiltonian which describes spin waves in an infinite ferromagnetic island interacting with finite clusters, with a diameter distribution centered around a mean value $<d_j>$:

$$H = \Sigma_\kappa \epsilon_\kappa a_\kappa^+ a_\kappa + \mathbf{D}\cdot\boldsymbol{\sigma}\times\mathbf{S}, \tag{1}$$

where κ is the wavevector of the magnons, $\epsilon_\kappa = \Delta + D_0\kappa^2$ the energy of the spin waves with stiffness constant D_0, and Δ a spin wave gap arising from anisotropic interactions between spins. The a_κ^+, a_κ are Holstein–Primakoff (HP) boson operators and the coupling D describes an effective anisotropic DM interaction between the spin S in the infinite cluster and the spins of the finite clusters, which is described by the Pauli matrices σ_i according to Van Vleck.[15]

The effect of the spin wave-cluster interaction on the spin wave propagation can be described by a damping $\Omega^j(\omega)$ of these modes given by

$$\Omega^j(\omega) = \frac{8\ SN^j}{N_0} D^2 I_M \chi^j(\omega), \tag{2}$$

where $\chi^j(\omega)$ is the dynamical longitudinal susceptibility component and $D_x^2 = D_y^2 = D_z^2 = D^2$ for all clusters. In Eq. (2), N^j is the number of finite clusters whose diameters are centered around the mean value $<d_j>$ and N_0 is the number of spins in the infinite cluster. The dynamical longitudinal susceptibility component is given by[15]

$$\chi^j(\omega) = \frac{1}{4\,KT}\,\mathrm{sech}^2(E/2\,KT)\frac{1}{1 - i\omega\tau}, \tag{3}$$

for a cluster population whose diameter is centered around $<d_j>$. Here, we assume that the application of an external magnetic field H causes the magnetization vector of the particles to undergo a sort of Brownian motion around the easy axis, due to thermal fluctuations, within an asymmetric double well with barrier height v and asymmetry parameter E, as shown in Fig. 3. The relaxation time τ^j of the particles assumed in such case is given by

$$\tau^j = \tau_0^j \exp(v/KT)\mathrm{sech}(E/2KT). \tag{4}$$

Furthermore, we assume that the asymmetry parameter follows a constant distribution function such as

$$f^j(E) = \begin{cases} N_0^j, & 0 < E < E^j_{\mathrm{MAX}} \\ 0, & \text{otherwise,} \end{cases} \tag{5}$$

and that the reduction in the number of clusters with high barriers, due to the random nature of the sample, is taken into account by using an exponential distribution function of the form[16]

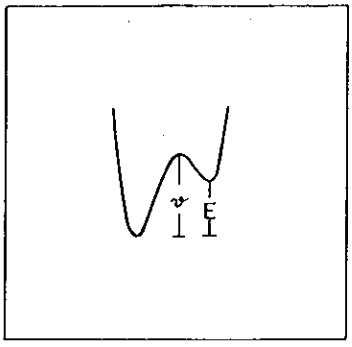

FIG. 3. Asymmetric double-well potential of barrier heigth v and asymmetry parameter E.

$$g^j(v) = \frac{1}{v_0^j} e^{-v/v_0^j}, \tag{6}$$

where v_0^j is an activation energy related to T_f^j by $KT_f^j = v_0^j / |\ln \omega\tau_0^j|$.

The broadening of the magnetic resonance linewidth ($\delta\Gamma_j$) due to the random nature of the clusters with energy splittings between E and $E+\delta E$ and activation energy between v and $v+\delta v$ is given by $\delta\Gamma_j = \delta\Omega^j/\hbar\gamma$, where γ is the gyromagnetic ratio. Therefore, the magnetic resonance linewidth broadening of all clusters whose diameters are centered around $<d_j>$ is given by

$$\Delta\Gamma_j(\omega) = \frac{8\,S}{\hbar\gamma N_0} D^2 \int_0^\infty \int_0^\infty \times [I_M \chi^j(\omega)]\, f^j(E)\, g^j(v)\, dE\, dv. \tag{7}$$

This integral is evaluated taking $0 < \alpha = KT/v_0^j < 0.1$ and $\omega\Gamma^j < 1$, according to our experiment, to give

$$\Delta\Gamma_j(\omega) = \frac{\pi S N^j}{\hbar\gamma N_0} \frac{D^2}{v_0^j} \exp(-T/T_f). \tag{8}$$

The solid lines in Fig. 2 represent the best fit of the experimental data by a succession of straight lines using Eq. (8) and $\Gamma_0 = 0.630 \pm 0.004$ kG. Two values of T_f can be estimated (T_f^1 and T_f^2) and related to each particle size distribution with two differents mean values of activation energy (v_0^1 and v_0^2). The relative proportion of the particles in the two populations can be estimated taking the ratio N^1/N^2 in Eq. (8). The physical parameters obtained by this fit, related to each distribution of particles and consequently to each straight line region in Fig. 2, is summarized in Table II, where we assume $\tau_0^1 = \tau_0^2 \simeq 1$ ns and $D = 1.23\times10^{-4}$ eV.

TABLE II. Physical parameters related to A(250) sample.

Region	T (K)	T_f (K)	v_0 (eV)	D (eV)	Composition (%)
I	$T<181.8$	33.9	0.012	1.23×10^{-4}	74.5
II	$T>181.8$	45.4	0.016	1.23×10^{-4}	25.5

IV. CONCLUSIONS

The spin-freezing phenomenon in superparamagnetic particles is sensitive to the pattern of particle size distribution. A geometric picture of a dilute ferromagnet consisting of an infinite island of spins coexisting with a distribution of finite superparamagnetic clusters may be used to explain the linewidth behavior of the EPR lines as a function of temperature above T_f if we assume an anisotropic DM type of interaction between the two types of spins and that at high temperatures the relaxation process occurs via a longitudinal relaxation component. Furthermore, this type of temperature dependence is observed for many other spin glass systems.[4]

EPR measurements of the linewidth as a function of temperature, besides electron microscopy measurements, can be used as a topographic technique to study the pattern of particle size distribution above the freezing temperature. This possibility is important to understand the relation between the spin-freezing and superparamagnetic phenomena.

ACKNOWLEDGMENTS

The authors wish to express their appreciation to the members of the Resonance group of the UFMG-Brasil, specialy to Professor A. S. Chaves and Professor G. M. Ribeiro for their hospitality and interest throughout this work. This work was partially supported by CNPq.

[1]B. R. Coles, B. V. B. Sarkissian, and R. H. Taylor, Philos. Mag. B 37, 489 (1978).
[2]B. V. B. Sarkissian, Philos. Mag. B 39, 413 (1979).
[3]S. M. Bhagat, M. L. Spano, H. S. Chen, and K. V. Rao, Solid State Commun. 33, 303 (1980).
[4]S. M. Bhagat, M. L. Spano, and J. N. Lloyd, Solid State Commun. 38, 261 (1981).
[5]K. Skeff Neto and V. K. Garg, Radiochem. Radional. Lett. 15, 357 (1973).
[6]K. Skeff Neto and V. K. Garg, J. Inorg. Nucl. Chem. 37, 2287 (1975).
[7]K. Skeff Neto, I. C. Cunha Lima, N. S. Almeida, and L. C. M. Miranda, J. Phys. C. 11, L 695 (1978).
[8]K. Skeff Neto and L. C. M. Miranda, Solid State Commun. 28, 43 (1978).
[9]P. C. Morais and K. Skeff Neto, J. Appl. Phys. 54, 307 (1983).
[10]P. C. Morais and K. Skeff Neto, Polyhedron 2, 875 (1983).
[11]S. M. Bhagat, J. A. Geohegan, and H. S. Chen, Solid State Commun. 36, 1 (1980)
[12]M. B. Salamon and R. M. Herman, Phys. Rev. Lett. 41, 1506 (1978).
[13]M. A. Continentino, J. Phys. C 16, L 71 (1983).
[14]A. Fert and P. M. Levy, Phys. Rev. Lett. 44, 1538 (1980).
[15]J. H. Van Vleck, J. Appl. Phys. 35, 882 (1964).
[16]K. S. Gilroy and W. A. Phillips, Philos. Mag. B 43, 753 (1981).

A N E X O B - 1

Detection of ferromagnetic resonance by photoacoustic effect

O. A. Cleves Nunes, A.M.M. Monteiro, and K. Skeff Neto
Departamento de Física-Universidade de Brasília, 70 910 Brasília-DF-Brasil

(Received 12 June 1979; accepted for publication 23 August 1979)

By exploring the simple periodic heat-flux principle of the photoacoustic cell we propose and demonstrate experimentally the usefulness of the photoacoustic cell for studying the ferromagnetic resonance. An interesting feature of this technique is that it offers special advantages over conventional spectroscopic methods used in ferromagnetic resonance because of the simplicity of measurements. An application is made for the case of an iron thin foil.

PACS numbers: 78.20.Hp, 76.50. + g, 75.50.Bb

Several authors[1-7] have shown that photoacoustic spectroscopy (PAS) is a useful tool for the study of solid and semisolid matter. The theory of PAS for solid materials was developed by Rosencwaig and Gersho.[4] According to these authors, when modulated light impinges on a solid in an enclosed cell, an acoustic signal is produced within the cell.

 0003-6951/79/210656-03$00.50

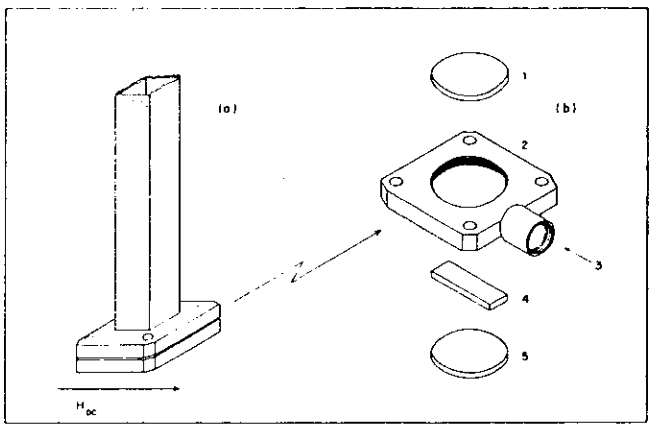

FIG. 1. (a) Geometry of the photoacoustic-cell—waveguide system used for observing ferromagnetic resonance in iron. (b) The photoacoustic cell. 1,5, teflon windows; 2, brass cell; 3, microphone connection; 4, iron foil absorber.

The primary source of this acoustic signal arises from the periodic heat flow from the solid to the surrounding gas (such as air) as a consequence of the periodic heating of the sample by the absorption of modulated light. The periodic flow of this heat into the gas cell produces pressure fluctuations in the cell, which are detected by a microphone, and the resulting signal is amplified and measured by a lock-in amplifier.

In the present work we propose to extend the above described method to the absorption of modulated microwaves by a ferromagnetic substance placed in an external dc magnetic field. We present the experimental results for a thin iron foil 0.001 in. thick.

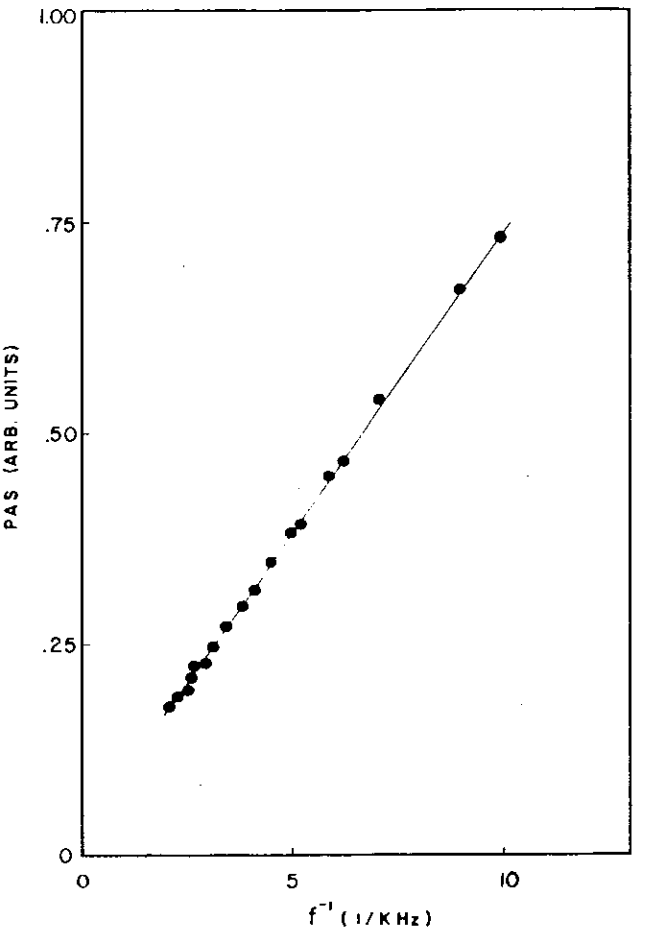

FIG. 3. Variation in the amplitude of the photoacoustic signal with the reciprocal of the modulation frequency.

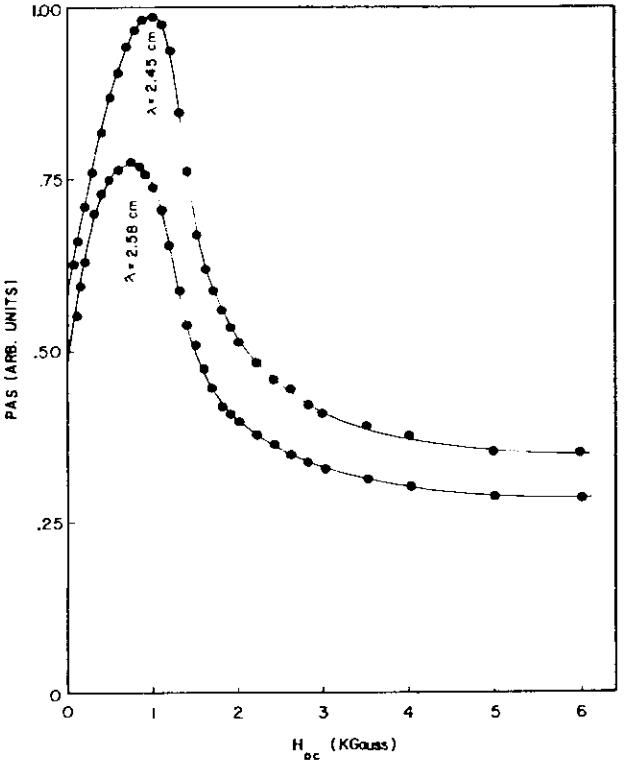

FIG. 2. Photoacoustic signal (PAS) versus external dc magnetic field H_{DC}. The curves displayed correspond to two different microwave frequencies.

In 1946 Griffiths[8] reported that iron, nickel, and cobalt exhibited an anomalous dependence of their high-frequency losses on the strength of an imposed dc magnetic field. This anomaly was in essence the discovery of "ferromagnetic resonance."

Kittel[9] has derived equations governing the resonance condition for ferromagnetic materials by solving classically the equations of motion of the bulk magnetization. The classic theory of this effect gives, for the resonance condition,

$$\hbar\omega_{res} = g\mu_B H_{eff}, \tag{1}$$

where H_{eff} is the effective field "seen" by the spins in the ferromagnetic specimen and it is given, for a flat specimen with the dc magnetic field parallel to the plane of the specimen, by

$$H_{eff} = [(H_{DC} + 4\Pi M_S)H_{DC}]^{1/2}. \tag{2}$$

Our experimental apparatus consisted of a small volume brass cell. The sample to be investigated was placed inside the cell containing air at room temperature and a small capacitive microphone as is illustrated schematically in Fig. 1(b). The geometry was such that both the applied dc magnetic field and the applied microwave magnetic field were mutually perpendicular. Both magnetic fields were

placed in the plane of the foil as schematized in Fig. 1(a). The photoacoustic cell was positioned at the microwave resonant cavity. The photoacoustic signal from one miniature capacitive microphone mounted on the sample cell wall was detected by a lock-in amplifier [Princeton Applied Research (PAR) Model 122] tuned to a modulation frequency of about 100 Hz.

In Fig. 2 we present the photoacoustic signal (PAS) as a function of the applied dc field for two different values of microwave frequencies (wavelengths) and illustrate the resonance phenomena. The value of the dc magnetic field required for resonance was found to be about 750 G at 11.6 GHz (2.58 cm) and about 1000 G at 12.2 GHz (2.45 cm). These field values satisfy Eq. (1) when Eq. (2) is used to describe the effective field. In Fig. 3 we present the amplitude of the PAS signal as a function of the reciprocal of the modulation frequency. It shows the essential agreement of the experiment with the theory of the photoacoustic effect.[4]

The great advantage of the present method over the conventional one[10] is that the magnitude of the PAS signal is directly proportional to the amount of microwave power absorbed by the specimen.

[1]A. Rosencwaig, Opt. Commun. 7, 305 (1973).
[2]A. Rosencwaig, Anal. Chem. 47, 592 A (1975).
[3]J.G. Parker, Appl. Opt. 12, 2947 (1973).
[4]A. Rosencwaig and A. Gersho, J. Appl. Phys. 47, 64 (1976).
[5]F.A. McDonald and G.C. Wetsel,Jr., J. Appl. Phys. 49, 2313 (1978).
[6]C.C. Ghizoni, M.A.A. Siquerira, H. Vargas, and L.C.M. Miranda, Appl. Phys. Lett. 32, 554 (1978).
[7]J.J. Barret and M.J. Belly, Appl. Phys. Lett. 34, 144 (1979).
[8]J.H.E. Griffiths, Nature 158, 670 (1946).
[9]C. Kittel, Phys. Rev. 73, 155 (1948); 71, 270 (1947).
[10]*Technique of Metal Research*, edited by E. Passaglia (Wiley, New York) Vol. 6, part 2, p. 79.

 0003-6951/79/210658-03$00.50

A N E X O B – 2

phys. stat. sol. (a) 68, K25 (1981)
Subject classification: 19; 22.8.2

Departamento de Física, Universidade de Brasília[1])

Microwave Resonance Absorption in Ferrites by the Photoacoustic Effect

By
O. A. C. NUNES, M. A. AMATO, and K. SKEFF NETO

The photoacoustic effect /1 to 4/ is simply the generation of an acoustic signal by a sample exposed to modulated light. The sample is heated to the extent that it absorbs the incident light and the energy gained is lost through non-radiative processes. Because the light is chopped, the temperature rise is periodic at the chopping frequency, and it is this periodic temperature rise at the surface of the sample that in turn causes a modulation of the gas pressure in the enclosed chamber. This is how the sound originates.

Even though the photoacoustic technique in the visible has been an extremely active field, to our knowledge, only recently an extension of the above described method to the microwave region has been reported by Nunes et al. /5/, for investigating the photoacoustic effect of a well known phenomenon in solids at this region i.e., the ferromagnetic resonance (FMR). In this note, we show experimental evidence that ferrimagnetic resonance can also be investigated using the photoacoustic effect as a probe.

Ferrimagnetic resonance can be pictured as the coupling of a microwave field with the Larmor precession of the net magnetization inside a ferrimagnetic sample. The equation of motion for a two-sublattice ferrimagnetic /6, 7/ of which the magnetizations are assumed to be antiparallel provides for the resonance condition

$$\hbar\omega_{res} = \gamma_{eff}\hbar H_{eff} \,, \tag{1}$$

where γ_{eff} is the effective magneto-mechanical ratio and H_{eff} is the effective field "seen" by the spins in the specimen. We can expect to induce spin energy absorption as the precession frequency of the net magnetization about the applied dc magnetic field equals the frequency of the incident microwave field. This energy is subsequently transferred to the lattice as heat by the spin-lattice relaxation mechanism and this will be the source for the generation of the photo-

1) 70.910 Brasília, D.F., Brazil.

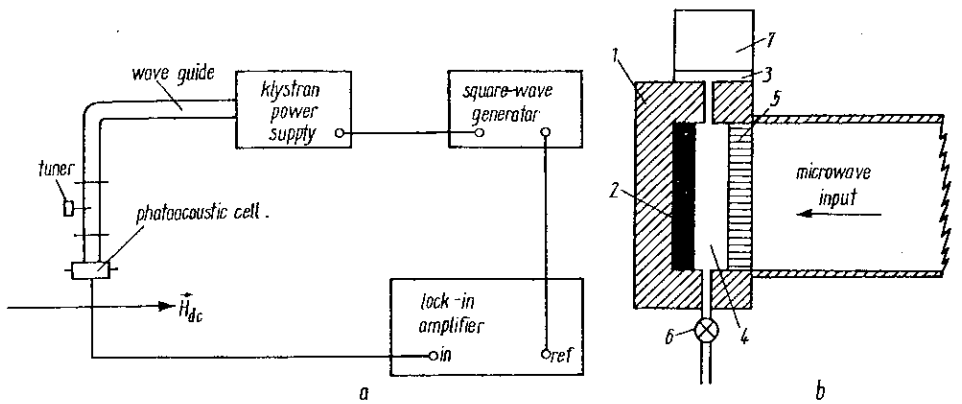

Fig. 1. a) Microwave-photoacoustic system for exciting the sample. b) The photoacoustic cell: 1 brass walls of the sample chamber, 2 ferrite sample, 3 microphone cavity, 4 sample chamber, 5 teflon window, 6 needle valve, 7 microphone

acoustic signal.

On a thin plane (200 μ inch thick) specimen of a magnetic oxide in form of magnetic recording tape (γ-Fe_2O_3), measurements were made at 11.4 GHz with the specimen inside the photoacoustic cell fitted across the wave guide. The field of an electromagnet was located parallel to the plane of the specimen and perpendicular to the microwave magnetic field. The photoacoustic signal generated inside the sample was measured as a function of the applied dc magnetic field by a lock-in amplifier tuned to a modulation frequency of 100 Hz.

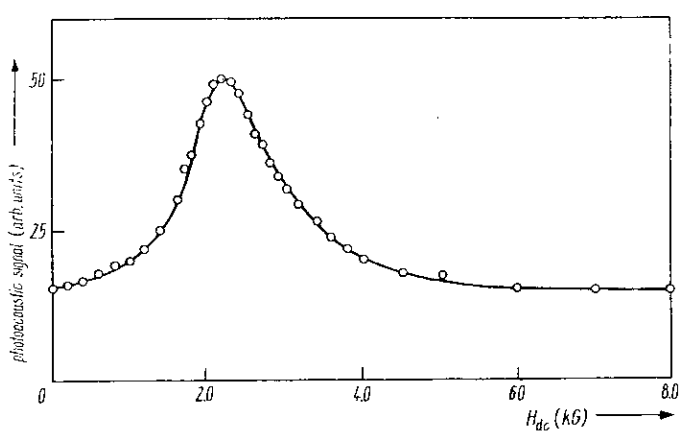

Fig. 2. Photoacoustic signal versus dc magnetic field H_{dc}

In Fig. 1a we show the microwave rig for exciting the sample. Fig. 1b shows the photoacoustic chamber. In Fig. 2 we present the photoacoustic signal as a function of the dc magnetic field and illustrate the resonance phenomenon.

The feasibility of the photoacoustic technique and the fact that the photoacoustic signal is a direct measurement of the amount of microwave power absorbed of the sample reveals this technique as a powerful tool for further investigations. Furthermore, because of the greater skin depth of ferrites caused by the high resistivity a relatively large volume of the specimen participates in the absorption process allowing a most detailed investigation of the inner layers of the specimen.

References

/1/ A.G. BELL, Amer. J. Sci. 20, 205 (1980).

/2/ J.G. PARKER, Appl. Optics 12, 2947 (1973).

/3/ A. ROSENCWAIG, Analyt. Chem. 47, 592 A (1975).

/4/ A. ROSENCWAIG and A. GERSHO, J. appl. Phys. 47, 64 (1976).

/5/ O.A.C. NUNES, A.M.M. MONTEIRO, and K. SKEFF NETO, Appl. Phys. Letters 35, 656 (1979).

/6/ R.K. WANGSNESS, Phys. Rev. 86, 146 (1952).

/7/ S. FONER, in: Magnetism, Ed. RADO and SUHL, Academic Press, New York 1963 (p. 415).

(Received April 30, 1981)

A N E X O B – 3

Simple photoacoustic cell operating at N_2 liquid temperature

O. A. Cleves Nunes, A. M. M. Monteiro, and K. Skeff Neto

Universidade de Brasília, Departmento de Físico, 70.910-Brasília-D.F., Brazil

(Received 6 April 1981; accepted for publication 26 May 1981)

A simple low-temperature photoacoustic cell operating at the liquid N_2 temperature is described. An application is made for monitoring the thermal agitation of a spin system close to its order–disorder critical temperature.

PACS numbers: 43.35.Sx, 78.20.Hp, 07.20.Mc

It is well recognized that the statistical mechanical connection between entropy and degree of order permits magnetic order to be investigated by specific heat measurements. In particular anomalous variations of specific heat with temperature are found close to a critical temperature at which magnetic order is destroyed by thermal agitation.

Since in the conversion process of light into sound which is the physical foundation of the photoacoustic effect (PAS),[1–4] the thermal properties of the sample, such as specific heat play an important role, the possibility of specific heat measurements is strongly enhanced.[5–12]

In this note we describe a simple, low temperature photoacoustic cell operating at the N_2 liquid temperature and demonstrate its applicability to monitoring the thermal agitation of a spin system. We consider the specific case of an FeO sample, by observing the behavior of the photoacoustic signal of this system in the neighborhood of its order–disorder transition temperature.

A simple low-temperature photoacoustic cell operating at liquid N_2 temperature is represented in Fig. 1. The cell is made of a quartz tube of 5.0 mm of internal diameter. The sample to be investigated is deposited inside the cell. The cell is filled with helium and is introduced inside a Dewar flask containing liquid N_2. In order to reduce the cell volume and to ensure a perfect illumination of the sample, an optical fiber of 3.0 mm of diameter is inserted inside the cell tube. The cell is then connected against the aluminum body of the microphone cavity by a ring to ensure helium tightness. In order to prevent a large difference of pressure between the two membranes of the microphone when the temperature is lowered to liquid N_2 temperature, a pressure manometer is used to stabilize the same pressure in the cavity of the microphone. The sample temperature is raised from liquid N_2 temperature by means of an internal heater winding in close contact with the sample and is monitored by means of a thermocouple placed in contact with the sample compartment. The photoacoustic signal is generated within the cell by illuminating the sample with a 150-W of modulated mercury lamp light and detected by a lock-in amplifier tuned to a modulation frequency of 100 Hz. The experimental setup is displayed in Fig. 2.

 0034-6748/81/091413-03$00.60

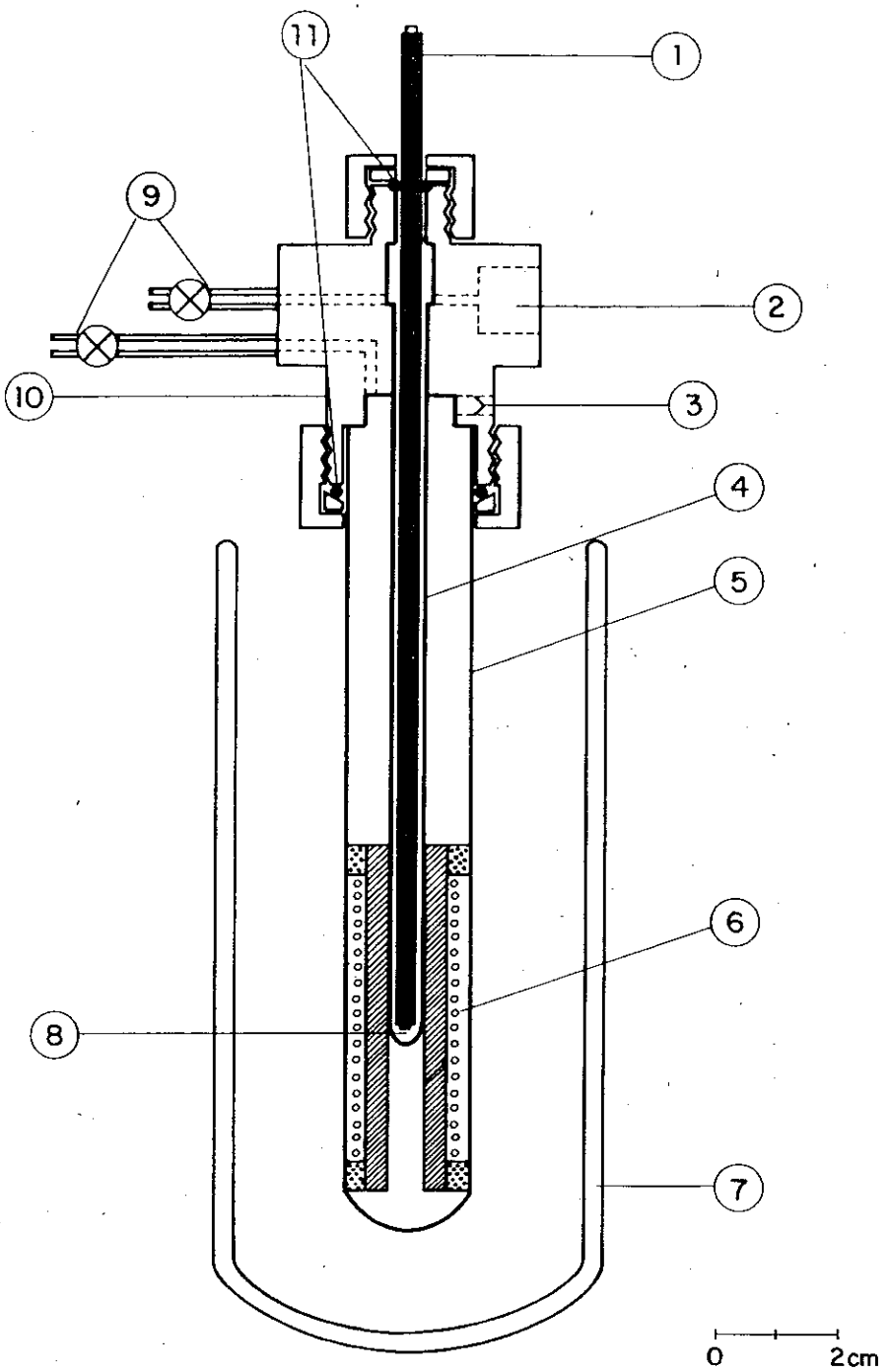

FIG. 1. The photoacoustic cell operating at liquid N_2 temperature: (1) optical fiber, (2) microphone compartment, (3) thermocouple and electrical connections, (4) quartz tube, (5) cell body, (6) heater winding, (7) Dewar flask with liquid N_2, (8) sample, (9) needle valve, (10) cell-body support, (11) O rings.

In Fig. 3 we present the behavior of the photoacoustic signal of our particular spin system which consisted of a polycrystalline sample of FeO weighing 10.0 mg as a function of the temperature. This sample was chosen because the magnetic properties are known in the range of temperature used in this experiment. We can see that the jump in Fig. 3 in the interval of temperature (180–200) K is then attributed to the jump of the specific heat, therefore defining the order–disorder critical temperature for the FeO.

In conclusion, we have presented in this note a simple low-temperature cell operating at N_2 liquid temperature and its applicability for monitoring the thermal agitation of any spin system close to their order–disorder phase transition, considering, as an example, the case of an FeO-powdered sample. We believe that once the photoacoustic signal is strongly dependent on the specific heat of the sample, which in turn is a function of the temperature, the photoacoustic technique can be of great help in elaborating and characterizing new materials.

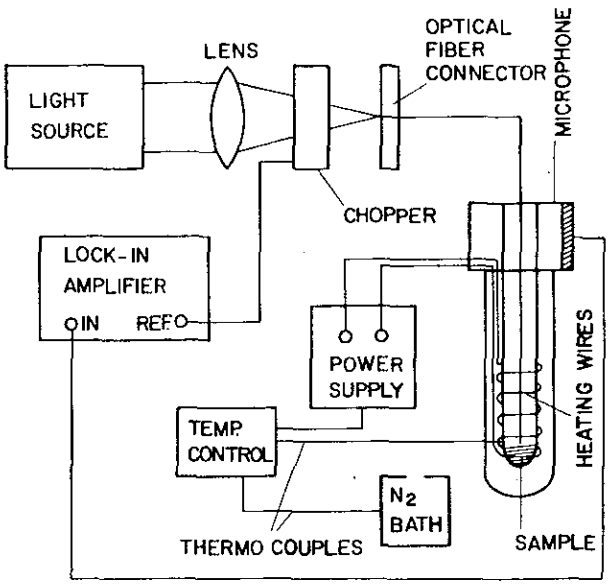

FIG. 2. Experimental setup used for measuring the photoacoustic signal at liquid N_2 temperature.

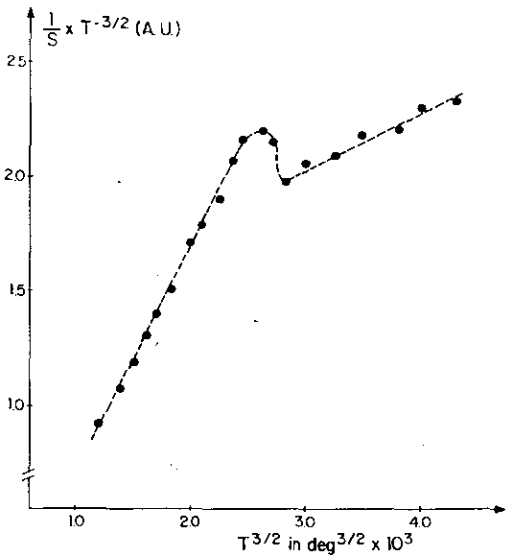

FIG. 3. Photoacoustic signal ($S^{-1} \times T^{-3/2}$) of the polycrystalline sample of FeO as function of the temperature ($T^{3/2}$).

[1] A. G. Bell, Am. J. Sci. **20**, 205 (1880).
[2] A. Rosencwaig, Phys. Today **28**, 23 (1975).
[3] A. Rosencwaig and A. Gersho, J. Appl. Phys. **47**, 64 (1976).
[4] F. A. McDonald and G. C. Wetsel, Jr., J. Appl. Phys. **49**, 2313 (1978).
[5] M. J. Adams and G. F. Kirkbright, Analyst (London) **102**, 281 (1977).
[6] M. A. A. Siqueira, C. C. Ghizoni, J. I. Vargas, E. A. Menezes, H. Vargas, and L. C. M. Miranda, J. Appl. Phys. **51**, 1403 (1980).
[7] C. Pichon, M. Le Liboux, D. Fournier, and A. C. Boccara, Appl. Phys. Lett. **35**, 435 (1979).
[8] R. Florian, J. Pelzl, M. Rosenberg, H. Vargas, and R. Wernhardt, Phys. Status Solidi A **48**, 35 (1978).
[9] J. C. Murphy and L. C. Aamodt, J. Appl. Phys. **48**, 3502 (1977).
[10] M. B. Robin and N. A. Kuebler, J. Chem. Phys. **66**, 169 (1977).
[11] J. B. Smith and G. A. Laguna, Phys. Lett. **56** A, 223 (1977).
[12] J. F. McClelland and R. N. Knisely, Bull. Am. Phys. Soc. **24**, 315 (1979).

A N E X O B – 4

phys. stat. sol. (a) 76, K209 (1983)
Subject classification: 7; 22.8.1

Departamento de Física, Universidade de Brasília[1])

Piezoelectric Detection of the Photoacoustic Signal

By
A. L. TRONCONI, K. SKEFF NETO, and M. A. AMATO[2])

Photoacoustic has become, since 1973, a valuable analytical and research technique for optical investigation on solid matter /1 to 3/ particularly on matter that are opaque or transparent to light.

The photoacoustic effect arises when intensity-modulated light impinges on a sample. If the sample absorbs any amount of incident radiation, optical energy levels within the sample are excited, and when these levels deexcite, they generally do so through non-radiative or heat producing processes. This absorption results in a periodic localized heating of the sample.

The most common experimental technique for the detection of the photoacoustic signal is the one involving the gas-microphone cell, the signal detected due to the modulation of the gas pressure in the enclosed chamber. It has been found to be suitable for many applications, particularly at low modulation frequency. However, when one is dealing with large samples it proves to be inadequate. Since the photoacoustic detection is primarily the detection of the internal heat produced within the sample by the de-excitation of the optical energy levels, it is possible to measure this internal heating by the stresses produced in a piezoelectric detector in contact with the sample. The piezoelectric detection has been used with success by many authors for the determination of the optical absorption coefficient in solids /2, 4/.

In this letter an experimental study of the photoacoustic effect using a piezoelectric detector is provided. Fig. 1 shows the experimental apparatus for the study of the photoacoustic signal as a function of the modulation frequency in the microwave region for a wavelength of $\lambda = 2.8$ cm. Fig. 2 shows the relevant data for a sample of aluminium (a disc of 1 mm thickness, 20 mm diameter) coupled elastically to a ceramic detector of barium titanate ($BaTiO_3$). Curves c and b represent the measurement of the intensity of the radiation generated by

1) 70.910 Brasília, D.F., Brazil.

2) Partially supported by CNPq.

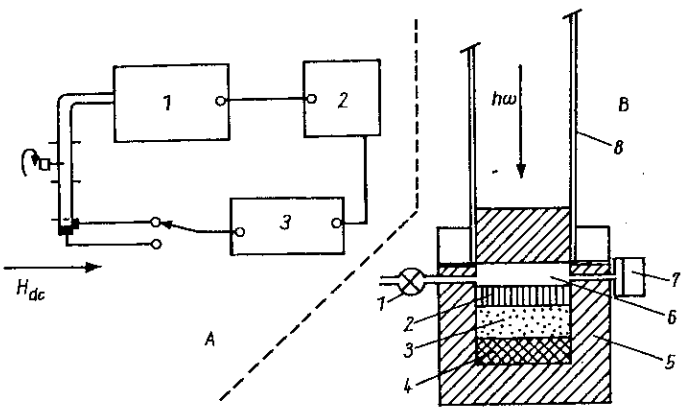

Fig. 1. A photoacoustic spectrometer incorporating a piezoelectric transducer. A) 1 microwave generator, 2 square wave generator, 3 lock-in amplifier; B) 1 valve, 2 ferrite, 3 aluminium, 4 piezoelectric detector ($BaTiO_3$), 5 teflon wall, 6 air, 7 microphone, 8 wave guide

the microwave as a function of the modulation frequency using a diode 1N 23 B-type and the system Al-$BaTiO_3$ (as shown in Fig. 1), respectively. Curve a shows the normalized result, i.e., curve b divided by curve c. One can see easily from the graph that for the low-frequency region the photoacoustic signal varies as $\omega^{1/2}$ ($\omega = 2\pi f$; f modulation frequency) and in the limit of high frequency as ω^{-1}. The theory developed by White /5/ does not explain satisfacto-

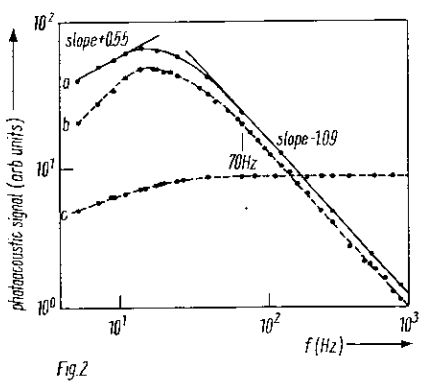

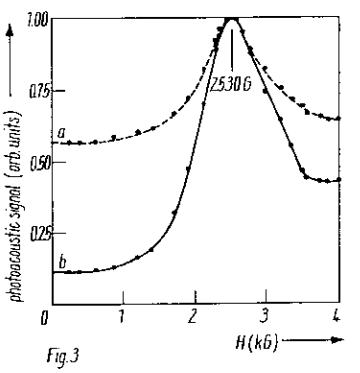

Fig. 2. Photoacoustic signal versus the modulation frequency for Al (log-log scale). Curves as indicated in the text

Fig. 3. Photoacoustic signal versus the magnetic field, H_{dc} (a) gas-microphone cell, (b) $BaTiO_3$ as a detector; T = 25 °C, λ = 3.6 cm

rily these results. A simple theory is proposed in /6/.

To demonstrate the effectiveness of the piezoelectric detector, Fig. 3 provides a comparison between the conventional method (gas microphone), curve a to the piezoelectric detection of the photoacoustic signal, curve b. It illustrates the ferromagnetic resonance. The signal is enhanced approximately by a factor of two near resonance for the piezoelectric detection. As a final comment, this technique has been studied when the incident radiation has its wavelength in the visible range of the electromagnetic spectrum.

References

/1/ A. ROSENCWAIG, in: Advances in Electronics and Electron Physics, Vol. 46, Ed. I. MARTON, Academic Press, New York 1978 (p. 207).

/2/ A. HORDVIK and H. SCHLOSSBERG, Appl. Optics 16, 101 (1977).

/3/ O.A.C. NUNES, M.A. AMATO, and K. SKEFF NETO, phys. stat. sol. (a) 68, K25 (1981).

/4/ A. HORDVIK and L. SKOLNIK, Appl. Optics 11, 2919 (1977).

/5/ R.M. WHITE, J. appl. Phys. 34, 2123 (1963).

/6/ A.L. TRONCONI, K. SKEFF NETO, and M.A. AMATO, to be published.

(Received February 10, 1983)

A N E X O B – 5

Simple model for measurements of the photoacoustic signal by a piezoelectric detector in the microwave region

A. L. Tronconi, M. A. Amato, P. C. Morais, and K. Skeff Neto
Grupo de Física Molecular e Magnetismo, Departamento de Física, Universidate de Brasília, 70.910, Brasília-DF, Brasil

(Received 22 February 1983; accepted for publication 21 November 1983)

In this paper a piezoelectric detection of the photoacoustic signal in the microwave region using barium titanate as a detector is carried out. The results in the low modulation frequency (below 30 Hz) are fitted very well by White's theory. For frequencies above 70 Hz a new and simple theory is presented. The effectiveness of this technique is demonstrated in the detection of the ferromagnetic resonance.

INTRODUCTION

In the last few years a new spectroscopic technique has evolved into an extremely powerful research tool. This technique, discovered by Bell[1] about 110 years ago, is called photoacoustic spectroscopy (PAS). The theoretical interpretation of this phenomenon was given by Parker[2] and its application to solid materials was expanded by Rosencwaig and Gersho.[3,4]

The sample to be investigated, in the conventional photoacoustic spectroscopy, is placed inside a closed chamber containing a suitable gas, and the photoacoustic signal, generated when a modulated radiation shines on the sample surface, is detected by a sensitive microphone. Recently, aside from several applications, this "conventional" photoacoustic effect (PAS) has been used for detection of ferromagnetic resonance.[5,6]

In this paper we report an unconventional experimental arrangement for the detection of the photoacoustic signal, replacing the conventional closed cell containing a gas by a piezoelectric ceramic detector. Here, the piezoelectric barium titanate detector is elastically coupled to the sample to be investigated (in our case a 1-mm-thick Al disk), and the photoacoustic signal is related to the elastic wave stress amplitude. This "unconventional" photoacoustic spectroscopy has been found to be suitable for many applications,[7,8] particularly in the microwave region.[9] Also, for solids, the use of the piezoelectric detector for measuring optically generated acoustic signals offers greater versatility than the microphone technique because they can operated from 4 to 700 K (Ref. 10) and with frequency response range giving from one to several megahertz.[11] Furthermore, the feasibility of detecting only the acoustic waves rather ac or impulse mode offers an additional freedom to the experimentalist.

EXPERIMENTAL RESULTS

A scheme of the experimental arrangement used in our photoacoustic absorption measurements is shown in Fig. 1. The block diagram [Fig. 1(a)] is composed of a microwave generator (Model 626 A/HP), a square wave generator to allow amplitude modulation of microwave (Model 211 A/HP), a lock-in amplifier for phase sensitive detection and [Fig. 1(b)] a detail of the photoacoustic cell coupled to the wavegide where a sample of aluminum (a disk of 1-mm thickness, 20-mm diameter) is attached elastically to the barium titanate detector.

Figure 2 shows the behavior of the photoacoustic signal, at room temperature, as function of the modulation frequency according to Fig. 1. The microwave radiation frequency is tuned at 12.65 GHz ($\lambda = 2.8$ cm). The thickness of the aluminum sample (1 mm) ensures that the incident microwave radiation is absorbed only by the sample. Curves C and B represent the measurements of the intensity of radiation generated by the microwave as a function of the modulation frequency using a diode 1N23 B type and the system aluminum detector, respectively. Curve A shows the normalized result. One can easily see from this curve that the photoacoustic signal varies with $f^{1/2}$ for low frequency (below 30 Hz) and with f^{-1} for high frequency (above 70 Hz), where f represents the modulation frequency. Here, the behavior of the slope in the graph changes abruptly in the region 30–70 Hz.

Now, as an example of the high sensitivity of the barium titanate detector, in the photoacoustic spectroscopy, Fig. 3 shows a comparison between the ferromagnetic resonance curves as function of the magnetic dc field, obtained by the

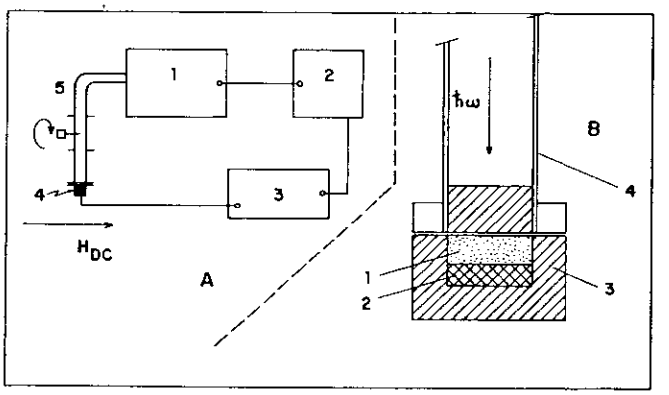

FIG. 1. Photoacoustic spectrometer incorporating a piezoelectric detector. (a) 1—Microwave generator, 2—square wave generator, 3—lock-in amplifier, 4—photoacoustic cell, 5—waveguide. (b) 1—Aluminum disk, 2—piezoelectric detector ($BaTiO_3$), 3—Teflon wall, 4—waveguide.

 0021-8979/84/171462-03$02.40

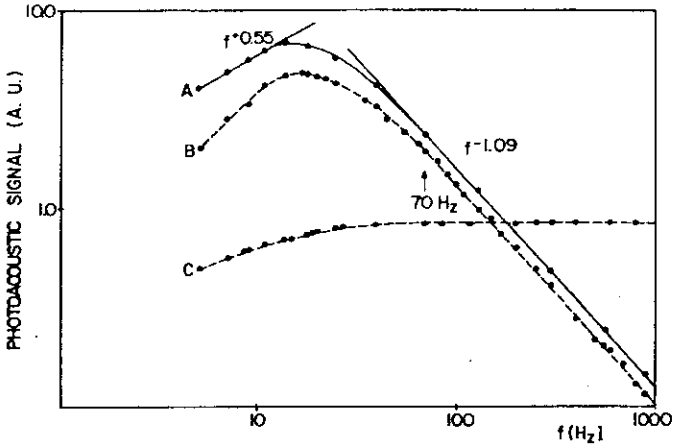

FIG. 2. Photoacoustic signal modulation frequency for the aluminum (log-log scale). A—Normalized result. B—Measurements of the intensity radiation using a diode 1N23B. C—Measurements of the intensity radiation using the system aluminum detector.

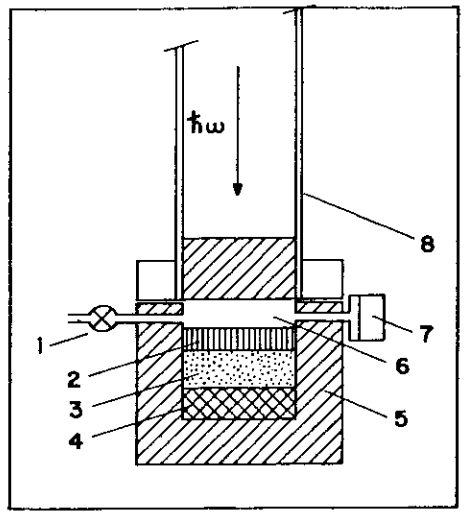

FIG. 4. Photoacoustic cell used in the ferromagnetic resonance experiment. 1—Valve, 2—ferrite, 3—aluminum, 4—piezoelectric detector ($BaTiO_3$), 5—Teflon wall, 6—air, 7—microphone, 8—waveguide.

conventional cell in accordance with Nunes *et al.*[5] (curve A) and by the unconventional one (curve B), in the microwave region. Here, the experimental results clearly show that the normalized photoacoustic absorption signal, obtained by the unconventional arrangement, is enhanced approximately by a factor of 2 compared to that obtained by the conventional one, in the region of ferromagnetic resonance. However, the experimental data show that off resonance the detected signal from the conventional cell is more intense than that from the unconventional one. This is probably due to electronic contributions, e.g., paramagnetic electronic resonance, which apparently are more easily detected by the conventional cell. This problem requires more detailed attention. The experimental arrangement that enables us to measure simultaneously the photoacoustic absorption signal as a function of the external dc field, by conventional and unconventional techniques, is shown in Fig. 4. The experimental measurements have been made using a microwave radiation at 10.6 GHz ($\lambda = 3.6$ cm) and the sample was a commercial ferrite.

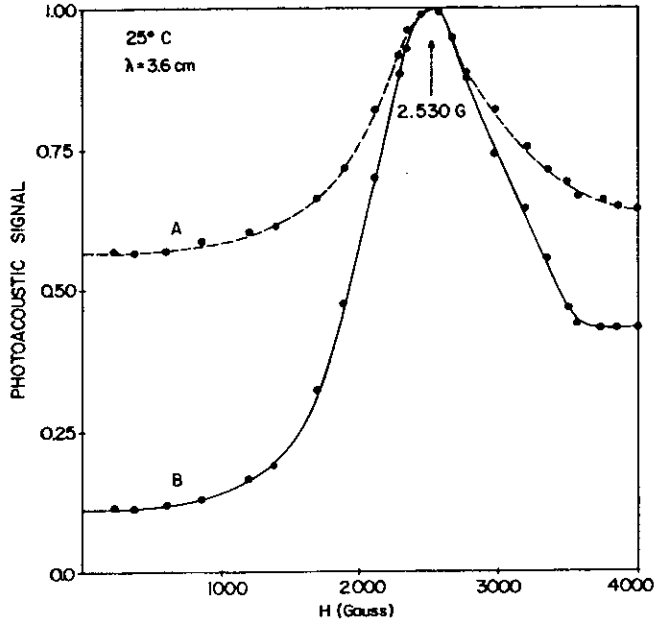

FIG. 3. Photoacoustic signal vs the magnetic field H_{dc}. A—gas-microphone cell and B—piezoelectric detector ($BaTiO_3$).

THEORY

The problem of elastic wave generation in isotropic elastic bodies, under several transient heating conditions, was considered by White.[12] However, his theory does not explain satisfactorily our experimental results concerning the PAS signal as a function of the modulation frequency in the microwave region, as shown in Fig. 2. A simple theory is proposed here to explain our experimental results.

We assume a one-dimensional model.[13] The sample is a disk with thickness l and is elastically coupled to a piezoelectric detector, as shown in Fig. 5. The physical parameters used here are the following: K, the thermal conductivity (cal/cm s °C); ρ, the density (g/cm^3); C, the specific heat (cal/g °C); $\alpha = K/\rho c$, the thermal diffusivity (cm^2/s); $a = (\omega/2\alpha)^{1/2}$, the thermal diffusion coefficient (cm^{-1}); $\mu = 1/a$, the thermal diffusion length (cm); β, the optical absorption coefficient (cm^{-1}); $\mu_\beta = 1/\beta$, the absorption length (cm); $\omega = 2\pi f$, the modulation frequency of the incident radiation in radians per second; λ_l, the first Lamè constant (g/cm s^2); R, the modulus of rigidity (g/cm s^2); B, the bulk modulus; C_t, the thermal expansion coefficient (°C^{-1}); V_L the velocity

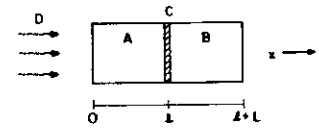

FIG. 5. Cross-sectional view by a simple model sample-piezoelectric detector. A sample, B detector, C elastic boundary, and D incident modulated radiation.

of compressional wave propagation in an unbounded medium (cm/s).

The well known relationship between the stress (ϵ) and the strain (χ) for a solid absorber subjected to a modulated radiation is given by

$$\epsilon(x) = (\lambda_l + 2R)\chi - BC_t\,\phi\,(x), \tag{1}$$

where $\phi(x)$ represents the temperature distribution in the sample at the steady state. When the sample absorbs any amount of incident radiation, optical energy levels within the sample are excited, and when these levels deexcite, they do so through nonradiative or heat producing processes. This absorption results in a periodic localized heating of the sample and the equation of motion for the x component of particle displacement in the material media, can be written in the form

$$\frac{d^2u(x)}{dx^2} + \xi^2 u(x) = \psi C_t \frac{d\phi(x)}{dx}, \tag{2}$$

where $\xi = \omega/v_L$, $v_L^2 = (\lambda_l + 2R)/\rho$, $\psi = B/\rho v_L^2$ and $u(x)$ = displacement of a point of the medium. In our case, the sample is thermally thick ($l \gg \mu$) and so the spacial distribution temperature function is given by

$$\phi(x) = Ue^{-\sigma x} - Ee^{-\beta x}, \quad 0 < x < l, \tag{3}$$

with $\sigma = (1+i)a$.

This last equation takes into account the fact that the sample and the piezoelectric detector have similar thermal properties. The values of constants are

$$E = \frac{\beta I_0}{2K(\beta^2 - \sigma^2)}, \tag{4}$$

and

$$U = \frac{\beta^2 I_0}{2K\sigma(\beta^2 - \sigma^2)}, \tag{5}$$

where I_0 represents the intensity of incident radiation flux (W/cm^2) on the sample. Consequently, the solution for $u(x)$ is

$$u(x) = Ae^{-i\xi x} + De^{i\xi x} - \frac{\psi C_t U\sigma}{\xi^2 + \sigma^2}e^{-\sigma x} + \frac{\psi C_t E\beta}{\xi^2 + \beta^2}e^{-\beta x}, \tag{6}$$

and the relationship between $u(x)$ and the strain is $\chi = du(x)/dx$. The boundary conditions imposed by the experimental arrangement are $\epsilon(0) = \epsilon(l) = 0$, determining the values of A and D. Then,

$$\frac{\epsilon(x)}{\rho v_L^2} = \frac{du(x)}{dx} - \psi C_t \phi(x). \tag{7}$$

As noted above, our sample is thermally thick ($l \gg \mu$) and optically opaque ($l \gg \mu_\beta$) because our sample is an aluminum disk. Therefore, $e^{-\sigma l} \simeq 0$ and $e^{-\beta l} \simeq 0$, and the physical characteristics of the sample enables one to assume that $\mu \gg \beta$. Such approximation, when considered in Eqs. (6) and (7), produces the following relation

$$\epsilon(x) = \frac{BC_t U\xi^2}{\xi^2 + \sigma^2}(e^{-i\xi x} - e^{-\sigma x}). \tag{8}$$

Now, the thermally thick sample approximation, in the region of low modulation frequency, can be understood by boundary conditions related to a semi-infinite cylinder. With such conditions, Eq. (8) gives

$$\epsilon(x) = \frac{BC_t U\xi^2}{\xi^2 + \sigma^2}e^{-i\xi x}. \tag{9}$$

Then, since the transducer output voltage is proportional to the mean value of $\epsilon(x)$ over the detector, the PAS signal is proportional to

$$\mathrm{Re}[\langle\epsilon(x)\rangle] = Pf^{1/2}, \tag{10}$$

where $P = \sqrt{\pi}BC_t I\alpha^{3/2}/2Kv_L^2$, according to the experimental data displayed in Fig. 2, for modulation frequency below 30 Hz.

In the region of high modulation frequency, i.e., above 70 Hz in our experiment, we assume that the major contribution to the stress is due to the mean temperature distribution in the sample along to the x axis. Consequently, in accordance to this approach, the expression to the stress is

$$\epsilon(x) = BC_t(Ue^{-\sigma x} - Ee^{-\beta x}), \tag{11}$$

and its mean value is given by

$$\langle\epsilon(x)\rangle = \frac{1}{l}\int_0^l \epsilon(x)dx = Gf^{-1}, \tag{12}$$

where $G = iBC_t I_0\alpha/4\pi Kl$. Again, the transducer output voltage is proportional to $\langle\epsilon(x)\rangle$ and the PAS signal goes as f^{-1} in accordance to the experimental results displayed in Fig. 2, for a modulation frequency above 70 Hz.

CONCLUSIONS

It has been shown that an unconventional photoacoustic technique, using a piezoelectric barium titanate detector, can be successfully used for solid samples in the microwave region either to study the behavior of the PAS signal as a function of the modulation frequency or to study ferromagnetic resonance.

The theoretical approach presented here accounts for the experimental behavior of the PAS signal as a function of the modulation frequency in the microwave region.

ACKNOWLEDGMENT

The authors thank CNPq for partial financial support.

[1] A. G. Bell, Am. J. Sci. **20**, 305 (1880).
[2] J. G. Parker, Appl. Opt. **12**, 2974 (1973).
[3] A. Rosencwaig and Gersho, J. Appl. Phys. **47**, 64 (1976).
[4] A. Rosencwaig, in *Optoacoustic Spectroscopy and Detection*, edited by Y. H. Pao (Academic, London, 1977), p. 193.
[5] O. A. Cleves Nunes, A. M. M. Monteiro, and K. Skeff Neto, Appl. Phys. Lett. **35**, 656 (1979).
[6] W. Wettling, W. Jantz, and L. Engelhardt, Appl. Phys. A **26**, 19 (1981).
[7] A. Hordvik and H. Scholossberg, Appl. Opt. **16**, 101 (1977).
[8] Michael M. Farrow, Roger K. Burnham, Max Auzanneau, Steven L. Olsen, Neil Purdie, and Edward M. Eyring, Appl. Opt. **17**, 1093 (1978).
[9] A. L. Tronconi, K. Skeff Neto, and M. A. Amato, presented at the Third International Conference, of Photoacoustic and Photothermal Spectroscopy, held at Paris 5–8, April 1983.
[10] J. B. Callis, J. Res. Nat. Bur. Stand. Sec. A **80**, 413 (1976).
[11] D. L. White, in *Physical Acoustic*, edited by W. P. Mason (Academic, New York, 1964), Vol. 1, Pt. B, p. 351.
[12] R. M. White, J. Appl. Phys. **34**, 3559 (1963).
[13] A. L. Tronconi, MS. thesis, Universidade de Brasília, Brasil, 1982.

A N E X O C – 1

Solid State Commun., 52, 181 (1984)

SPIN - FREEZING PHENOMENON IN PSEUDOBROOKITE*

N. M. L. Köche, P. C. Morais and K. Skeff Neto
Grupo de Física Molecular e Magnetismo
Departamento de Física, Universidade de Brasília
70910 - Brasília- D.F. - Brasil

* Work partially supported by CNPq.

ABSTRACT

The temperature dependence of EPR linewidth broadening in polycrystalline Fe_2TiO_5 is discussed. From the comparison between our EPR data and those reported in the literature we can conclude that our sample exhibits a true thermodynamic spin-glass transition at $T_f = 53.4 \pm 0.5k$. We present an expression to explain the behavior of the EPR linewidth broadening as a function of temperature.

In recent years many experimental and theoretical studies have been performed on systems which show a transition into the spin-glass phase. The ac susceptibility measurements exhibit quite clearly a cusp which has been used as one of the simplest methods to determine the freezing temperature (T_f). The freezing temperature is related to the formation of strongly coupled spin clusters embedded in a "sea" of weakly coupled spins. This behavior has been noted over the years in a variety of alloys[1-10] and more recently in insulating materials[11-13]. As has been pointed out by Bhagat et al[14], the influence of the spin freezing seems to be the same whether the system is dilute or concentrated, crystalline or amorphous, paramagnetic or ferromagnetic, transition metal or rare-earth.

Here we report EPR (~9GHz) measurements on the insulating oxide Fe_2TiO_5 (pseudobrookite). Atzmony et al.[15] reported extensive experimental results which show that single crystals of pseudobrookite behave as anisotropic spin-glasses below T_f = 55 K. Furthermore, the authors pointed out that ac susceptibility measurements, carried out in fields of 20-100 Oe at 300-2000 Hz, yielded similar results (T_f = 55 K). At this point it is important to observe that the frequency dependence of the ac susceptibility cusp has become a testing ground for the various descriptions of the spin-glass transitions[13,1] There are basically two competing theoretical approaches to explain the spin-glass transition. One of them predicts a true thermodynamic transition[17-22] while the other uses a "pseudo-transition" picture[23,24] which is merely a manifestation of the

slowing down of cluster thermal fluctuations to a time interval comparable with the experimental measurement time. Therefore, the frequency dependence of the spin-glass transition has been used as an experimental support for the pseudo-transition" picture.

The purpose of the present work is to report the temperature dependence of the EPR linewidth in Fe_2TiO_5. From this we can estimate the freezing temperature, which is in good accordance with the ac susceptibility data reported by Atzmony et al[15], in spite of the time scale of the measurements: $\sim 10^{-9}$sec for EPR (our data) and $\sim 10^{-2}$-10^{-3}sec for χ_{ac} (Atzonomy et al data). Therefore, it seems reasonable to conclude that the spin-glass transition in pseudobrookite behaves as a true magnetic transition rather than a magnetic "blocking" transition. Another important point that we would like to stress is concerned to the usefulness of the EPR technique in investigating the critical dynamics of the spin-glass transition. The advantages of the EPR technique is that it is not necessary to work at low temperatures, i.e., at temperatures near T_f. This is because the spin-glass transition dominates the magnetic behavior over a very wide temperature range beyoud T_f, as has been observed by Bhagat et al[14]. These authors have concluded, from the analysis of the EPR measurements obtained by several investigators and using differents materials, that if a system exhibits spin-freezing, its EPR linewidth, has a nearly universal dependence on temperature, even for temperatures much above T_f.

Recently a geometric picture of a dilute ferromagnet has been used to explain the freezing behavior of superparamagnetic particles[25]. In this picture an infinite cluster of spins with long-range magnetic order coexists with finite clusters of spins. The model is a generalization of Sarkissian's approach[21] and takes into account anisotropic interactions between spins. To explain the temperature behavior of the EPR linewidth above T_f we consider the low-energy excitations of the infinite cluster as spin waves and treat the coupling of these modes to the finite clusters as a relaxation channel for the infinite cluster driven by a microwave field. We propose that the relaxation process, above T_f, is dominated by a longitudinal mode and occurs via an anisotropic Dzyaloshinskii - Moriya (DM) type of interaction betwenn spins in the infinite and finite clusters. The Hamiltonian which describes the dynamics of a such system is

$$H = \sum_k \epsilon_k a_k^+ a_k + \vec{D} \cdot \vec{\sigma} \times \vec{S} \quad , \qquad (1)$$

Where k is the wavevector of the low-energy excitations, $\epsilon_k = \Delta + D_o k^2$ is the energy associated with the excitations, D_o is the stiffness constant and Δ is a spin wave gap arising from anisotropic interactions between spins. The a_k^+, a_k are Holstein-Primakoff boson operators, the σ_i are the Pauli matrices and the coupling $\vec{D}$ describes an effective DM interaction between the spin $\vec{S}$ in the infinite cluster and the spins of the finite clusters. After taking into account the damping due to the spin wave - cluster interaction on the spin wave propagation we can show that the temperature dependence of the EPR linewidth

broadening is described by a simple relation:

$$\Delta\Gamma\ (T) = A \exp\ (-T/T_f) \qquad (2)$$

In the equation above, A is a constant characteristic of the system and T_f is the freezing temperature. A more detailed description of the calculation related to the Eq. 2 is described elsewhere[25].

Our measurements were performed using an X-band spectrometer tuned around 9.0305 GHz. The temperature was lowered from 321.1 to 174.8K using a liquid N_2 flux technique. The temperature variation during each measurement was always less than 0.3 K. Below 174.8 K no EPR signal was detected. The loss of EPR signal when the temperature is lowered toward T_f has been associated to the growth of finite clusters[2]. In Fig. 1 we show some typical resonance curves with fairly large linewidths. These lines were computer fitted to lorentzian lines and the temperature dependence of the resonance linewidth broadening ($\Delta\Gamma = \Gamma - \Gamma_o$) is shown in a semilog plot (Fig. 2). Here Γ_o means the temperature independent value of Γ observed at higher temperatures. The sample (Fe_2TiO_5) used here has been sinterized from a stoichiometric mixture of polycrystalline Fe_2O_3 and TiO_2 after heating at 1100°C during 48 hours in an air atmosphere. We have used X-ray diffraction at room temperature and Mössbauer at room temperature and 4.2 K to characterize our sample (results not shown here). The data are in a good agreement with those reported by Atzmony et al[15]. The solid line in Fig. 2 represents the best fit to the experimental data using Eq. 2

and Γ_o = 2.5 ± 0.1 Kg. The adjusting parameters are A = 74.2 ±0.1Kg and T_f = 53.4 ± 0.5 K.

In conclusion, from the comparison between our EPR measurements (T_f = 53.4 ± 0.5 K) and the ac susceptibility data reported elsewhere[15] (T_f = 55K) we can conclude that Fe_2TiO_5 exhibits a true thermodynamic spin-glass transition at T_f. The shift ΔT_f = 1.6 ± 0.5 arising between our EPR and those χ_{ac} data may be due to the polycrysttaline nature and the thermal method of preparation of our sample. For similar magnetic systems the EPR measurements are specially useful in investigating the critical dynamics of the spin-glass transition. Finally, the model used here, based on an anisotropic DM type of interaction betwqen spins, seems to be a reasonable description of the true thermodynamic spin-glass transition. However, whether the spin-glass transition is a true phase transition or a "pseudo-transition" is still controversial for several other spin-glass systems.

ACKNOWLEGMENT

The authors wish to express their sincere thanks to the members of the resonance group of the UFMG-Brasil, specially to Professors R. Gazzinelli, A. S. Chaves and G. M. Ribeiro for their hospitality and interest in our work.

FIGURE CAPTIONS

FIG. 1 EPR spectra of polycrystalline Fe_2TiO_5 at several different temperatures.

FIG. 2 Temperature dependence of the EPR linewidth broadening of polycrystalline Fe_2TiO_5 (pseudobrookite). Note the logarithmic vertical scale.

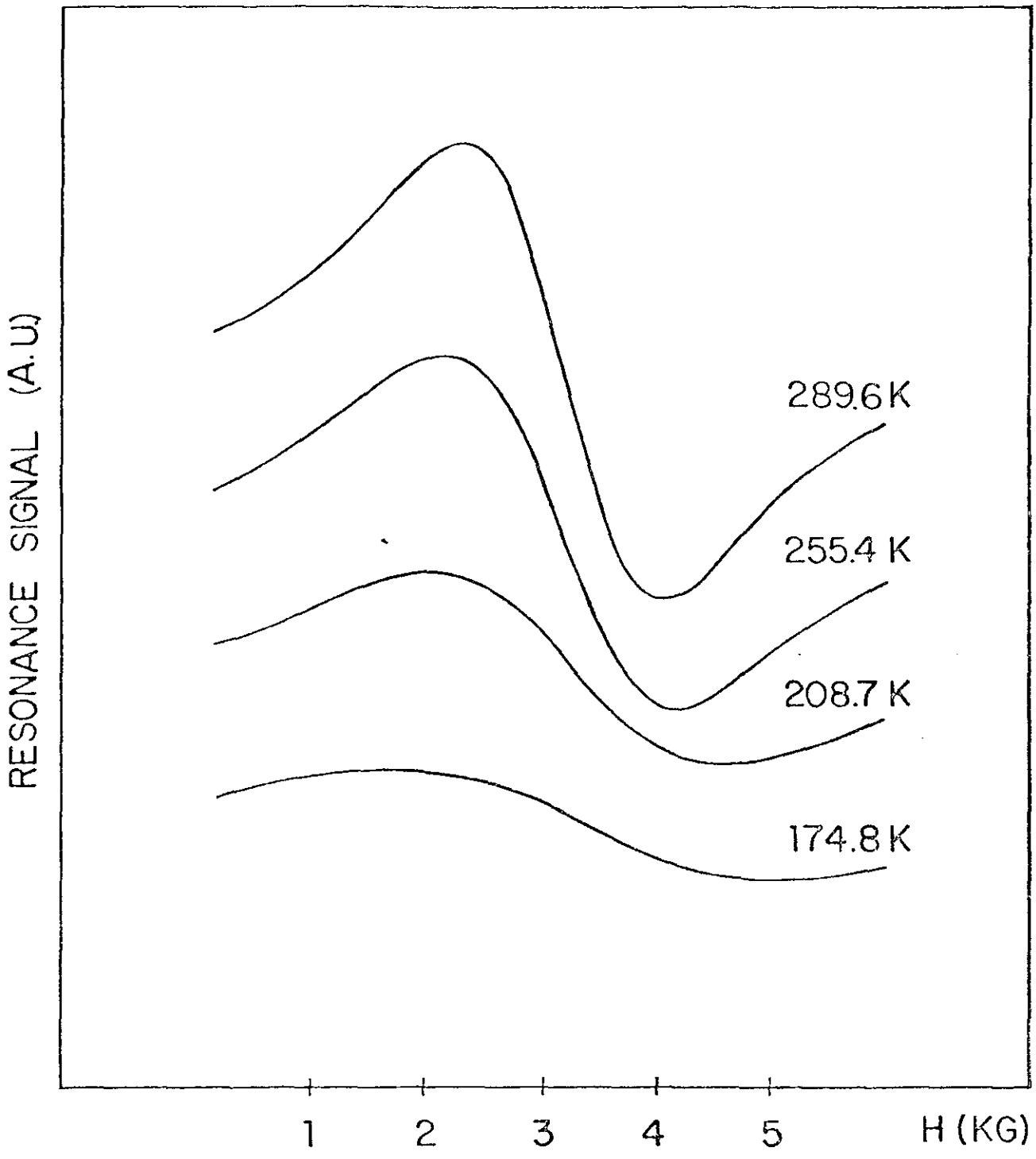

Fig. 1

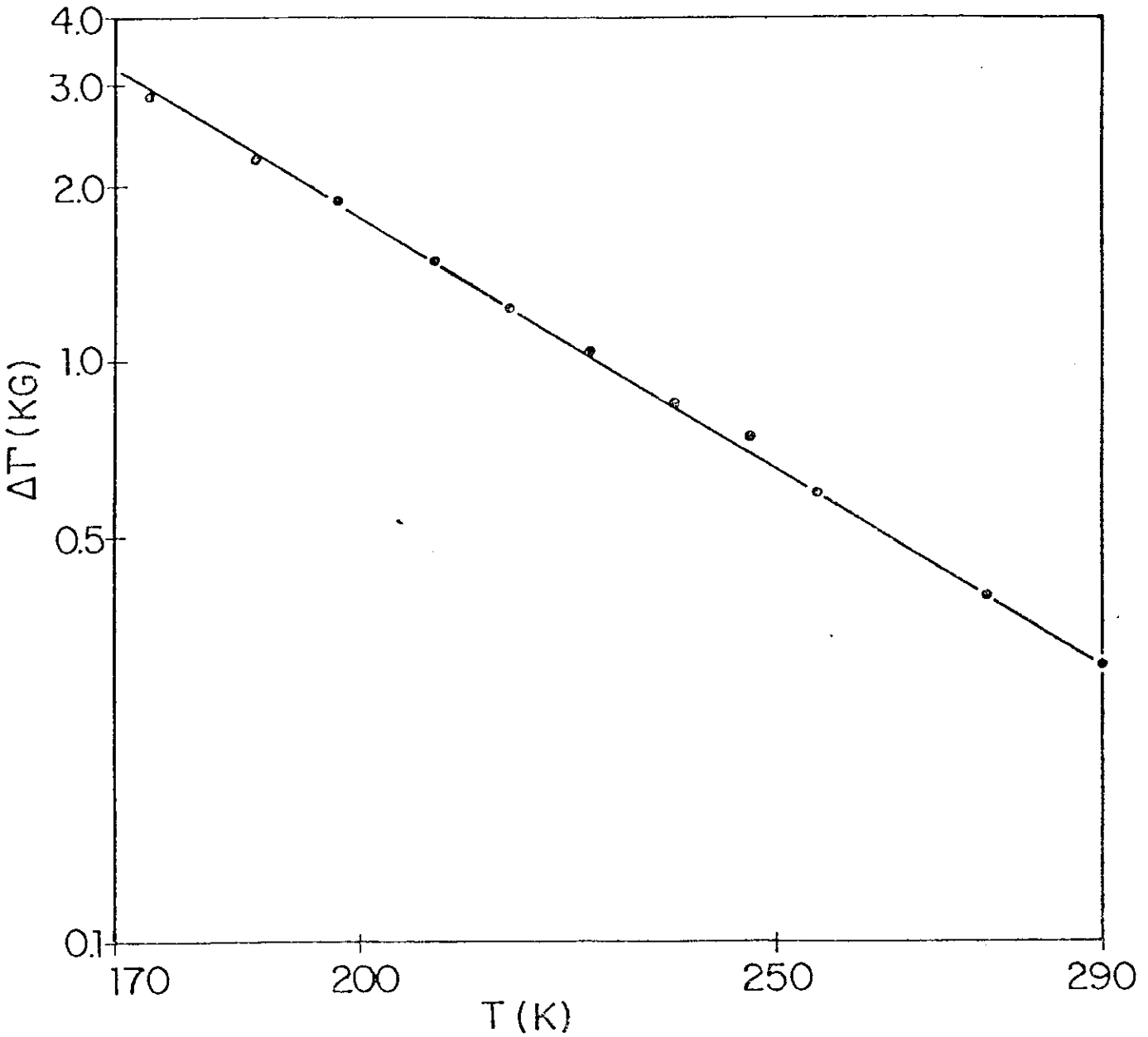

Fig. 2

REFERENCES

1. J. P. Jamet and A. P. Malozemoff, Phys. Rev. B 18, 75 (1978).

2. M. B. Salamon and R. M. Herman, Phys. Rev. Lett. 41, 1506 (1978).

3. E. D. Dahlberg, M. Hardiman, R. Orbach and J. Souletic, Phys Rev. Lett. 42, 401 (1979).

4. D. W. Forester, N. C. Koon, J. H. Schelleng and J. J. Rhyne, J. Appl.Phys. 50, 7336 (1979).

5. B. V. B. Sarkissian, J. Phys. F. 11, 2191 (1981).

6. Y. Yeshurun, M. B. Salamon and K. V. Rao, Phys. Rev. B 24, 1536 (1981).

7. J. W. Lynn, R. W. Erwin, J. J. Rhyne and H. S. Chen, J. Appl. Phys. 52, 1738 (1981).

8. D. G. Onn, J. Appl. Phys. 52, 1788 (1981).

9. V. Manns, R. A. Brand, W. Keune and R. Marx, Solid State Commun. 48, 811 (1983).

10. M. Rots, L. Hermans and J. Van Cauteren, Solid State Commun. 49, 131 (1984).

11. H. Maletta and W. Felsch, Phys. Rev. B 20, 1245 (1979).

12. K. Katsumata, T. Nire and M. Tanimoto, Phys. Rev. B 25, 428 (1982).

13. G. P. Singh, M. von Schickfus and H. Maletta, Phys. Rev. Lett. 51, 1791 (1983).

14. S. M. Bhagat, M. L. Spano and J. N. Lloyd, Solid State Commun. 38, 261 (1981)

15. H. Atzmony, E. Gurewitz, M. Melamud, H. Pinto, H. Shaked, G. Gorodetsky, E. Hermon, R. M. Hornreich, S. Shtrikman and B. Wanklyn, Phys. Rev. Lett. 43, 782 (1979).

16. C. A. M. Mulder, A. J. van Duynevelt and J. A. Mydosh, Phys. Rev. B 25, 515 (1982).

17. P. W. Anderson, J. Appl. Phys. 49, 1599 (1978).

18. S. Kirkpatrick and D. Sherington, Phys. Rev. B 17, 4384 (1979).

19. M. V. Medvedev, Phys. Stat. Sol. (b) 91, 713 (1979).

20. K. Levin, C. M. Soukoulis and G. S. Grest, J. Appl. Phys. 50, 1695 (1979).

21. B. V. B. Sarkissian, Phil. Mag. B 39, 413 (1979).

22. M. A. Coutinentino, J. Phys. C: Solid State Phys. 16, L 71 (1983).

23. A. P. Murani, J. Appl. Phys. 49, 1604 (1978).

24. J. L. Tholeuce and R. Tournier, Physica 86B, 873 (1977).

25. P. C. Morais, A. L. Tronconi and K. Skeff Neto, J. Appl. Phys. (in press).

A N E X O C - 2

J. Appl. Phys. (in press)

TEMPERATURE DEPENDENCE OF THE MÖSSBAUER LINEWIDTH OF SUPERPARAMAGNETIC PARTICLES OF FERRIC HYDROXYSULFATE*

P. C. Morais, A. L. Tronconi

and

K. Skeff Neto

Grupo de Física Molecular e Magnetismo

Departamento de Física, Universidade de Brasília

70910 - Brasília, DF - Brasil

* Work Partially Supported by CNPq.

ABSTRACT

The Mössbauer linewidth broadening of superparamagnetic particles of ferric hydroxysulfate, near the point where the paramagnetic lines begin to appear, has been investigated as a function of temperature. This behavior is explained by a geometric picture of an assembly of magnetically ordered single-domain particles whose magnetic moments moves within an asymmetric double-well potential. A relaxation model is presented which combines the conventional theory of superparamagnetism with an exponential distribution of energy barriers.

PACS numbers : 76.80. + y, 75.60. Jp, 75.50. Kj, 76.90. + d

INTRODUCTION

Superparamagnetic behavior is related to the magnetic ordering of extremely small particles. Although this phenomenon was discovered about half a century ago, on a colloidal suspension of Fe_3O_4 particles[1], it continues to be a matter of intensive studies[2-10]. In the conventional theory of superparamagnetism, an assembly of magnetically ordered single-domain particles hold their magnetic moment in an easy direction due to the crystal field[11]. Thermal fluctuations cause the magnetic moment of the particle to undergo a sort of Brownian motion around the easy axis, and there is a finite probability that the magnetic moment spontaneously change its direction, moving within a double-well potential. In this picture the relaxation time of the magnetic moment of the particles is described by[12]

$$\tau = \tau_o \exp (v/K_BT), \qquad (1)$$

where $v = KV$ is the activation energy, K is the magnetocrystalline anisotropy, V is the particle volume and τ_o is of the order of 1ns.

In the last two decades Mössbauer spectroscopy has become an important technique to understand superparamagnetism, in part due to the qualitative relation between Mössbauer spectra shapes and Eq. (1). That equation compares the activation energy (v) with the thermal excitation energy (K_BT). At low temperature, in the magnetically ordered phase, the Mössbauer spectra of Fe^{57}

nuclei show a pattern of six hyperfine lines[13,14]. When the temperature is increased the hyperfine lines become asymmetrically broader and a quadrupole doublet[15,16] or a single line[17,18] begins to appear. The intensity of the doublet or the singlet increases with increasing temperature and at higher temperatures only these lines survive. These are the fundamental features of superparamagnetism as seen through Mössbauer spectroscopy.

In the present paper we analyse the broadening of the hyperfine Mössbauer lines, as a function of temperature, in a system which exhibits superparamagnetism. This linewidth broadening is more sensitive to the temperature in the range near (above and below) the point where the paramagnetic lines begin to appear. Here, we focus our attention, on that range of temperature and the broadening is explained using a relaxation model. The model describes the superparamagnetic relaxation process in terms of transitions, within a double-well potential, of the magnetic moments of the particles. Our experimental data were obtained using a ferric hydroxysulfate sample which shows a bimodal particle size distribution.

EXPERIMENTAL DETAILS

The experimental data are related to the $|1/2> \rightarrow |3/2>$ Mössbauer transition in an amorphous sample of ferric hydroxysulfate. The spectroscopic characterization of the $FeOHSO_4$ sample, labeled here as A(300), is described elsewhere[19]. The particle size distribution was determined by electron microscopy. The sample shows a bimodal distribution of diameters as depicted in Fig. 1.

The Mössbauer spectra were obtained using a conventional constant-acceleration spectrometer in the standard transmission geometry. The spectra were recorded using a source of Co^{57} in Cu matrix with an initial activity of 25 m Ci. In Fig. 2 we show the spectra of the A(300) sample at various temperatures.

The linewidths of the hyperfine Mössbauer lines were obtained by fitting the experimental data using a hyperfine-field distribution P(H). The best fit of the Mössbauer spectra was done by the following model

$$P(H) = \begin{cases} A\left[(H - H_o)^2 + (\Gamma_1/2)^2\right]^{-1} ; \text{ for } 0 < H \leq H_o & (2a) \\ B\left\{(H - H_o)^2 + (\Gamma_2/2)^2\right]^{-1} ; \text{ for } H > H_o \ . & (2b) \end{cases}$$

This phenomenological approach is very similar to that proposed by Sharon and Tsuei[20] and Tsuei et al.[21]. The fitting of the experimental data based upon this model is shown in Fig. 2 by the solid lines.

The adjusted values of the linewidths of the hyperfine lines (Γ) were taken as $\Gamma = 1/2\ (\Gamma_1 + \Gamma_2)$, with Γ_1 and Γ_2 given by the P(H) model described above. The experimental linewidth broadening ($\Delta\Gamma = \Gamma - \Gamma_o$) as a function of temperature is represented in Fig. 3 by points. Here the value of Γ_o was taken as 5.59 KOe because this is the natural linewidth of Fe^{57} at low temperature.

THEORY

Our model describes the dynamics of an assembly of magnetically ordered single-domain particles under zero external field. Each of those particles may be considered as a single entity, a well defined agglomerate of spins, with total spin S (typically, S is of the order of 10^3). We assume a geometric picture where the magnetic moments of the particles moves within a doble-well potential with an anisotropic barrier energy given by $v = KV$. This two-level system may be related to two distinct values of ψ ($\psi_1 = 0$ and $\psi_2 = \pi$), where ψ is the angle between the magnetic moment of the particle and the easy axis. In a crystalline solid the symmetric double-well model has been used as a fairly good approach to explain the magnetic relaxation process. However, in our case we have an amorphous solid which shows a bimodal distribution of diameter (see Fig. 1). Therefore, it is reasonable that our experimental data must be analysed in terms of a distribution of barrier height ($v = KV$). Furthermore, we argue that the same variations in local environment that produce variations in $v = KV$ will certainly produce inequivalent potential wells, giving an asymmetric double-well potential. It is important to mention that the asymmetric model has already been used in connection with the unusual low-temperature properties of amorphous solids.[22-26]

The model assumes that we have a system of N such particles distributed between the two energy levels. This distribution is fixed at low temperature, but at high temperatures

thermal fluctuations of the magnetic moments about equilibrium are induced. Experimentally, we mean by high temperatures those near the point where Mössbauer paramagnetic lines begin to appear. Hence, there will be a finite probability per unit time (W_{12}) for the magnetic moment of any one of the particles to hop from ψ_1 to ψ_2. The inverse transition probability (W_{21}) is related to the first one by the Boltzmann factor. If we introduce the variable n, defined as the difference in population between the two levels, the dynamics of the system is described by

$$\frac{dn}{dt} = \frac{n_o - n}{\tau} \quad , \tag{3}$$

where n_o represents the thermal-equilibrium population difference at a given temperature and τ is the relaxation characteristic time, assumed here to be given by Eq. (1). From a physical reasoning, we would expect that relaxation process to be described by a susceptibility expression of the form

$$\chi(T) = \frac{1}{1 - iw_o \tau} \quad , \tag{4}$$

similarly to the Debye model. Here, w_o is the thermal-equilibrium transition probability per unit time at a given temperature. Now, it's reasonable to describe the Mössbauer linewidth broadening, within this model, by the imaginary part of the susceptibility

$$\Delta\Gamma = \Gamma' \frac{w_o \tau}{1 + w_o^2 \tau^2} \quad , \tag{5}$$

where Γ' must be determined experimentally. Since we have an assembly of particles which shows a certain particle-size distribution, the experimental linewidth broadening must be averaged by a weight function. This weight function must describe the reduction of the number of particles at high activation energy. To account for these arguments we use the weight function proposed by Gilroy and Phillips[24].

$$g(v) = \frac{1}{v_0} \exp\ (-\ v/v_0) \quad , \tag{6}$$

where v_0 is a characteristic activation energy related to each component of the bimodal distribution of particle size. Consequently, the experimental linewidth broadening of the Mössbauer hyperfine lines, related to each component of the bimodal distribution, must be given by

$$< \Delta\Gamma(T) > = \int_0^\infty \Gamma'\ \mathrm{Im}\ |x(T)|\ g(v)\ dv. \tag{7}$$

The above integral can be solved by taking $y = w_0\tau_0 \exp(v/K_BT)$ and $\alpha = K_BT/v_0$, and writing Eq. (7) as

$$< \Delta\Gamma(T) > = \frac{\Gamma'}{v_0} (w_0\tau_0)^{\alpha} \ell n\ (w_0\tau_0) \ . \tag{8}$$

At this point we introduce a characteristic temperature related to each component of the bimodal distribution (θ) by $K_B\theta = v_0/\ell n\ |w_0\tau_0|$. Using this definition in Eq. (8) we have

$$< \Delta\Gamma(T) > = \Gamma'(T/\theta) \exp(T/\theta) \ . \qquad (9)$$

The physical meaning of the characteristic temperature (θ) is that below θ the magnetic moment of a superparamagnetic particle, withim an asymmetric double-well potential, is bottlenecked to move as in a thermal-relaxation channel.

DISCUSSION

The experimental behavior of the linewidth as a function of temperature (Fig. 3) shows two distinct regions: I ($T \leq 106$ K) and II ($T \geq 106$ K). Fitting the experimental data according to Eq. (9) we have two distinct values of θ; $\theta^{I} = 62.7$ K and $\theta^{II} = 14.7$ K. These temperatures are related to the two components of the bimodal particle-size distribution, depicted in Fig. 1. Those particles whose diameters are centered around 110 Å have their magnetic moments moving at temperatures above 14.7 K. This means that the average magnetic moment of small particles (50 Å) is lower than the average magnetic moment of the other component of the assembly (110 Å). Therefore, the critical diameter, for which the average magnetic moment of a particle is a maximum, is located above 110 Å for $FeOHSO_4$ particles. At temperatures between 101 and 108 K the system behaves as if it undergoes a phase transition. In this range the system shows a change in the slope of the plot of Fig. 3 and the Mössbauer paramagnetic lines begin to appear. The relation between the temperature ($T \simeq 106$ K) at which this change occurs

and the others characteristic features of the system needs more detailed attention.

CONCLUSIONS

Mössbauer measurements of the hyperfine linewidth broadening as a function of temperature, together with electron microscopy measurements, may contribute to the understanding of superparamagnetism. A dynamical model based upon an asymmetric double-well potential weighted by an exponential function may be used to explain the experimental data. The broadening is mainly related, withim the range of temperature considered, to a relaxation process of the magnetic moment of the superparamagnetic particles. A characteristic temperature (θ), below which the thermal relaxation process is bottlenecked can be estimated.

ACKNOWLEDGEMENT

The authors are grateful to Prof. R. Osório for a critical reading of the manuscript.

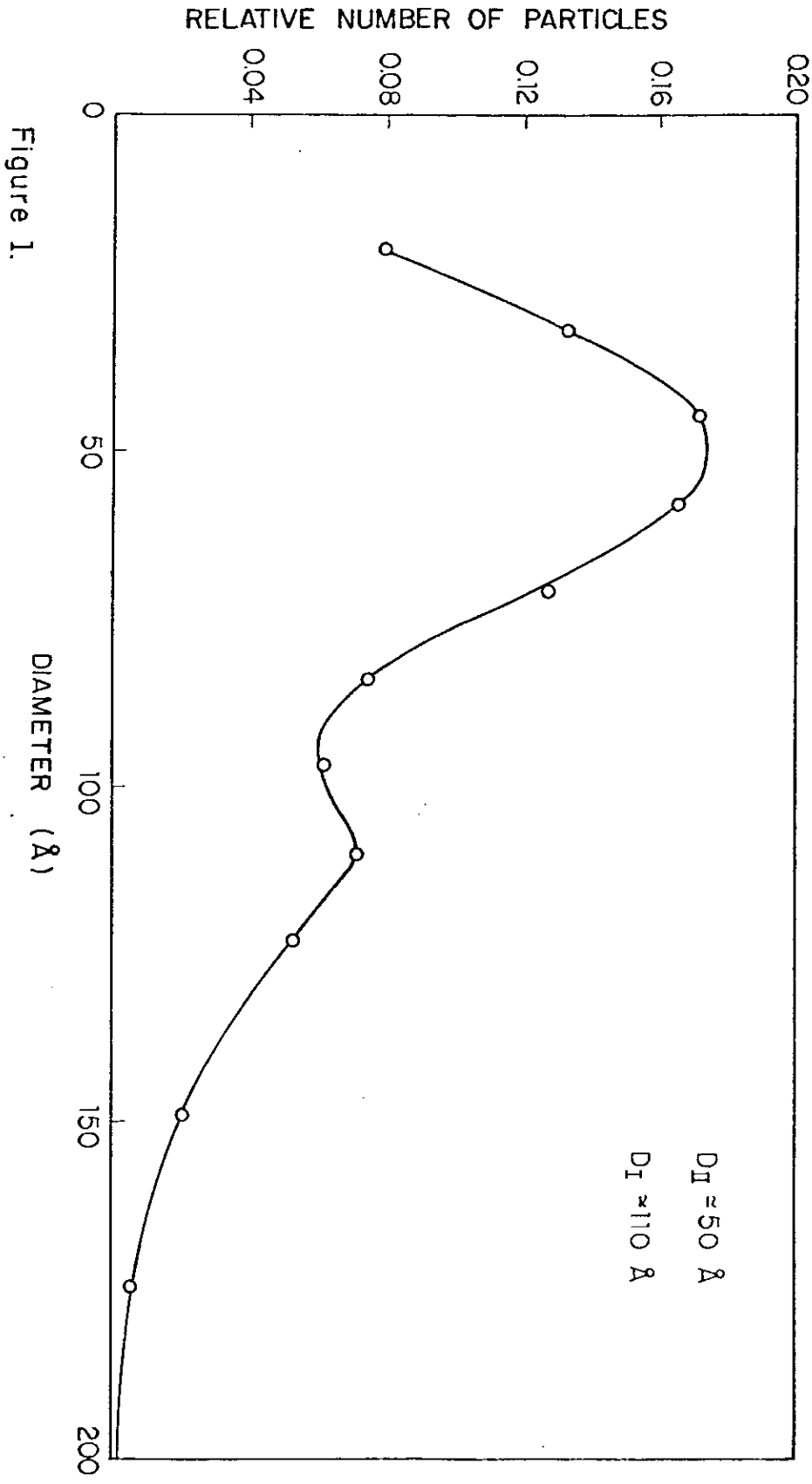
RELATIVE NUMBER OF PARTICLES
0.04
0.08
0.12
0.16
0.20
0
50
100
150
200
DIAMETER (Å)
$D_{II} \approx 50$ Å
$D_I \approx 110$ Å

Figure 1.

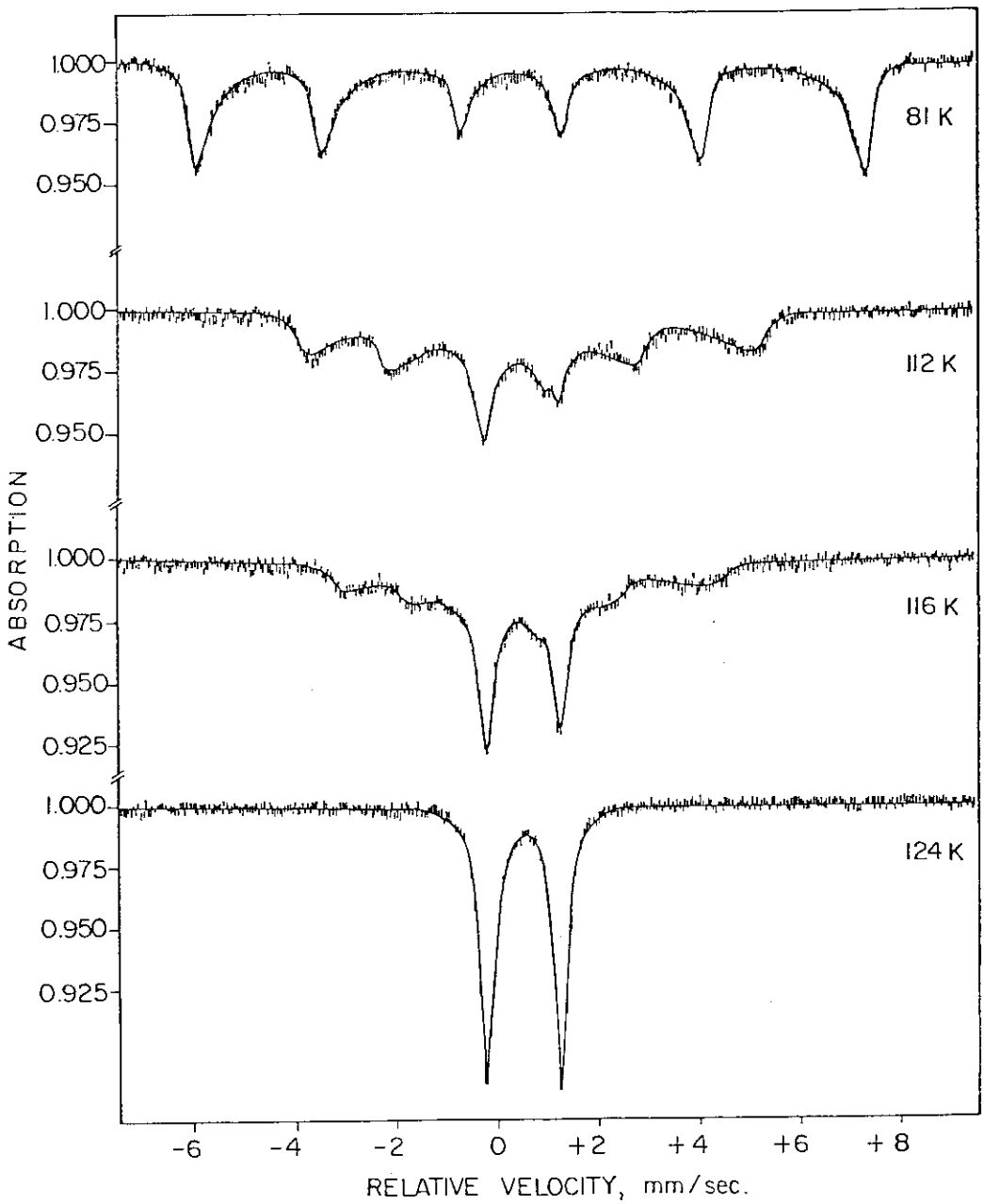
1.000
0.975
0.950
81 K
1.000
0.975
0.950
112 K
1.000
0.975
0.950
0.925
116 K
1.000
0.975
0.950
0.925
124 K
ABSORPTION
-6
-4
-2
0
+2
+4
+6
+8
RELATIVE VELOCITY, mm/sec.

Figure 2.

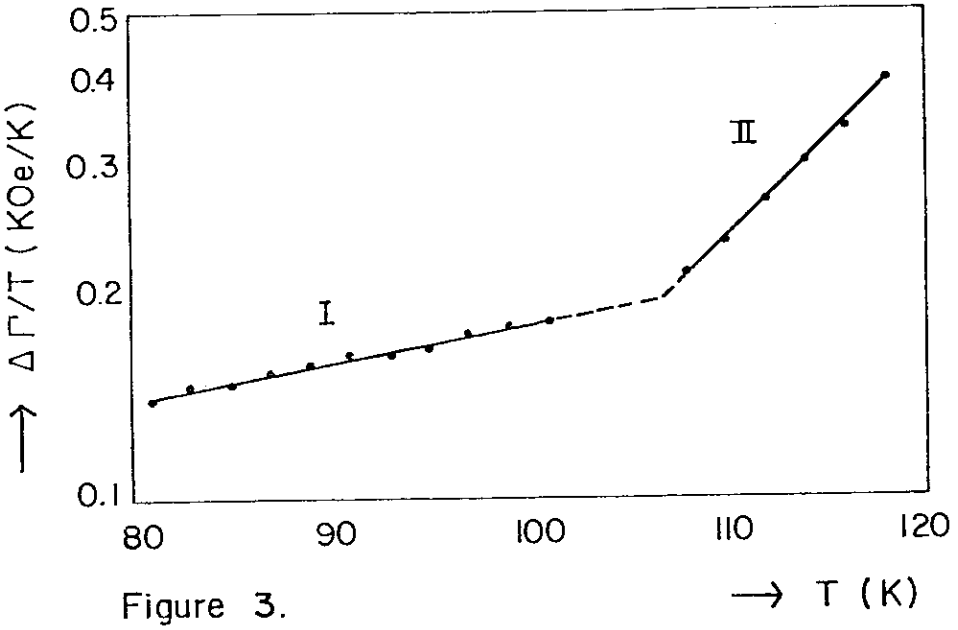

Figure 3.

FIGURE CAPTIONS

Fig. 1 - Particle size distribution of the A(300) sample obtained by electron microscopy.

Fig. 2 - Temperature dependence of the Mössbauer spectrum of the A(300) sample. The solid curves are fittings based on Eq. (2).

Fig. 3 - Temperature dependence of the Mössbauer hyperfine linewidth broadening of the A(300) sample. Note the logarithmic vertical scale.

REFERENCES

1. W. C. Elmore, Phys. Rev. 54, 1092 (1938).

2. S. Morup, J. A. Dumesic and H. Topsoe, in "Applications of Mössbauer Methodology" vol. 2, edited by R. L. Cohen (Academic Press, New York) p. 1, 1980.

3. J. L. Dormann, Revue Phys. Appl. 16, 275 (1981).

4. I. D. Morokhov, V. I. Petinov, L. I. Trusov and V. F. Petrunin, Sov. Phys. - Usp. 24, 295 (1981).

5. R. B. Goldfarb and C. E. Patton, Phys. Rev. B 24, 1360 (1981).

6. S. Morup, H. Topsoe and B. S. Clausen, Phys. Scr. 25, 713 (1982).

7. S. Morup, M. B. Madsen, J. Franck, J. Villadsen and C. J. W. Koch, J. Mag. & Magn. Mater. 40, 163 (1983).

8. G. N. Belozerskii and B. S. Pavlov, Sov. Phys. - Solid State 25, 974 (1983).

9. E. P. Wohlfarth, J. Mag. & Magn. Mater. 39, 39 (1983).

10. R. W. Chantrell, J. Mag. & Magn. Mater 40, 1 (1983).

11. L. Neel, Compt. Rend. 228, 664 (1949).

12. C. P. Bean, J. Appl. Phys. 26, 1381 (1965).

13. P. Roggwiller and W. Kündig, Solid State Commun. 12, 901 (1973)

14. K. Skeff Neto, I. C. Cunha Lima, N. S. Almeida and L. C. M. Miranda, J. Phys. C: Solid State Phys. 11 L, 695 (1978).

15. S. M. Aharoni and M. H. Litt, J. Appl. Phys. 42, 352 (1971).

16. P. C. Morais and K. Skeff Neto, J. Appl. Phys. 54, 307 (1983).

17. T. K. McNab, R. A. Fox and A. J. F. Boyle, J. Appl. Phys. 39, 5 703 (1968).

18. H. Rummel, R. L. Cohen, P. Gutlich and K. W. West, Appl. Phys. Lett. 40, 477 (1982).

19. P. C. Morais and K. Skeff Neto, Polyhedron 2, 875 (1983).

20. T. E. Sharon and C. C. Tsuei, Phys. Rev. B 5, 1947 (1972).

21. C. C. Tsuei, G. Lugworth and S. C. H. Lin, Phys. Rev. 170, 603 (1968).

22. W. A. Phillips, J. low Temp. Phys. 7, 351 (1972).

23. P. W. Anderson, B. I. Halperin and C. Varma, Phil. Mag. 25, 1 (1972).

24. K. S. Gilroy and W. A. Phillips, Phil. Mag. B 43, 735 (1981).

25. M. A. Continentino, J. Phys. C: Solid State Phys. 16, L 71 (1983).

26. P. C. Morais, A. L. Tronconi and K. Skeff Neto, J. Appl. Phys. (in press).

A N E X O C - 3

Phys. Stat. Solidi (a), 85 (1), (1984)

THE USEFULNESS OF THE PHOTOACOUSTIC CELL FOR MAGNETIC MEASUREMENTS*

N. M. L. Köche, P. C. Morais and K. Skeff Neto
Grupo de Física Molecular e Magnetismo
Departamento de Física, Universidade de Brasília
70910 - Brasília, D.F. - BRASIL

* Work partially supported by CNPq

In the conventional photoacoustic spectroscopy (PAS) a gas-microphone cell has been used to detect the photoacoustic signal. Basically, the PAS signal is detected as a periodic gas pressure fluctuation in an enclosed chamber, as described elsewhere |1|.

In the present letter we report magnetic measurements, namely, ferromagnetic resonance and magnetization curve, taken with a gas-microphone cell, similar to that used in the PAS detection. In Fig. 1 we show the block diagram used in our experiments. The spacial configuration of the modulation coils(A) is similar to that used by Foner |2|. The waveguide (Fig. 1) is attached to an X-band FMR spectrometer. In Fig. 2(A) we show a detail of the end of the waveguide and in Fig. 2(B) a detailed description of the gas-cell is made. To illustrate the versatility of the system described above we have used a commercial ferrite. The magnetization measurements are made by the microphone attached to the PAS cell (Fig. 2(B)) and the FMR measurements are made using the microphone attached to the end of the waveguide (Fig. 2(A)). The screw in Fig. 2(B) is used to prevent vibrations of the elastic membrane when FMR measurements are made.

For magnetization measurements we observe that the presence of a D.C. magnetic field modulated by an A.C. magnetic field (modulation coils) moves the sample around an equilibrium position. The pressure fluctuation inside the gas cell is detected by the capacitive microphone. The amplitude of this pressure fluctuation is taken as proportional to the magnetization of the sample. From this we obtain the magnetization curve as shown in

Fig. 3(A). The linearity of the system is displayed in the inset of Fig. 3, where we have in (C) the output of the lock-in amplifier versus miligrams of iron (Mössbauer iron foil) at 7KG. In Fig. 3(D) we show the residual signal due to the metallic foil of the capacitive microphone. At this point we note that the FET of the capacitive microphone has been pulled out and connected directly with the pre-amplifier. Furthermore, we note that the motion of the elastic membrane must be harmonic, for linearity requirements. In Fig. 3(B) we have the FMR curve detected by photoacoustic spectroscopy at 9.1 GHz. A more detailed description of this measurement is described by Nunes et al and A.C. Tromboni et al [3,4].

In conclusion, we have pointed out that similar experimental arrangements can be used successfully in a variety of experimental measurements. The inset in Fig. 3 shows clearly the sensibility and the linearity of the method.

ACKNOWLEDGEMENT

The authors wish to express their sincere thanks to the members of the resonance group of the UFMG - Brasil, specially to Professors R. Gazzinelli, A. S. Chaves and G. M. Ribeiro for their hospitality and interest.

FIGURE CAPTIONS

Fig. 1 Block diagram (A)- modulation coils, (B) - Waveguide, (C)- PAS cell, (D)- signal generator and audio amplifier, (E)- preamplifier, (F)- lock-in amplifier, (G)- magnetic poles.

Fig. 2 (A) 1 - teflon, 2- microphone, 3- duct for pressure adjust (B) 1- screw, 2- duct for pressure adjust, 3- elastic membrane, 4- sample, 5- teflon O-ring, 6-microphone.

Fig. 3 Experimental data of the ferrite at room temperature. (A) magnetization curve, (B) ferromagnetic resonance curve, (C) output of the lock-in amplifier versus miligrams of iron at 7Kg, (D) residual signal of the metalic foil of the microphone.

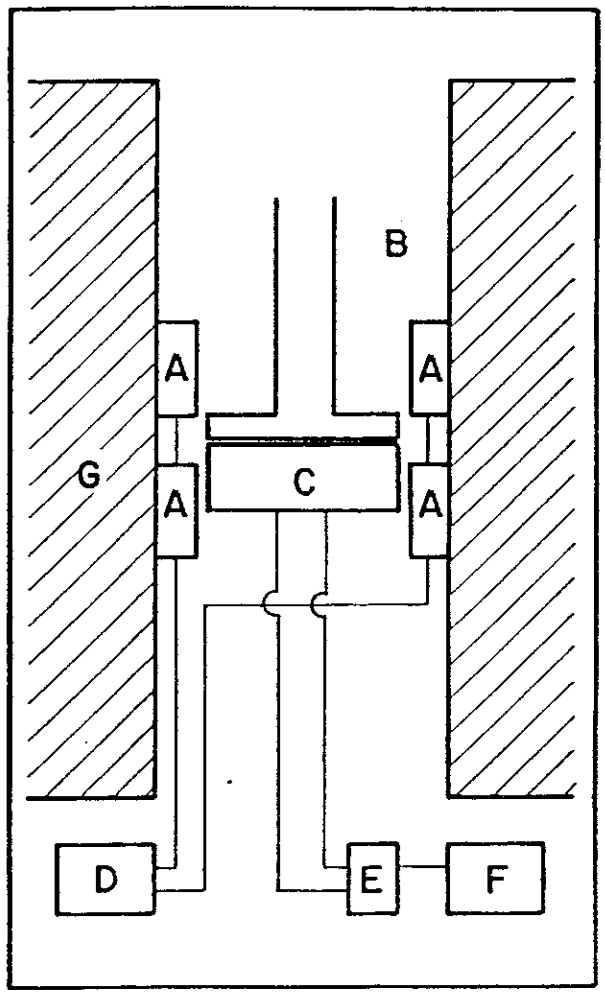

Fig. 1

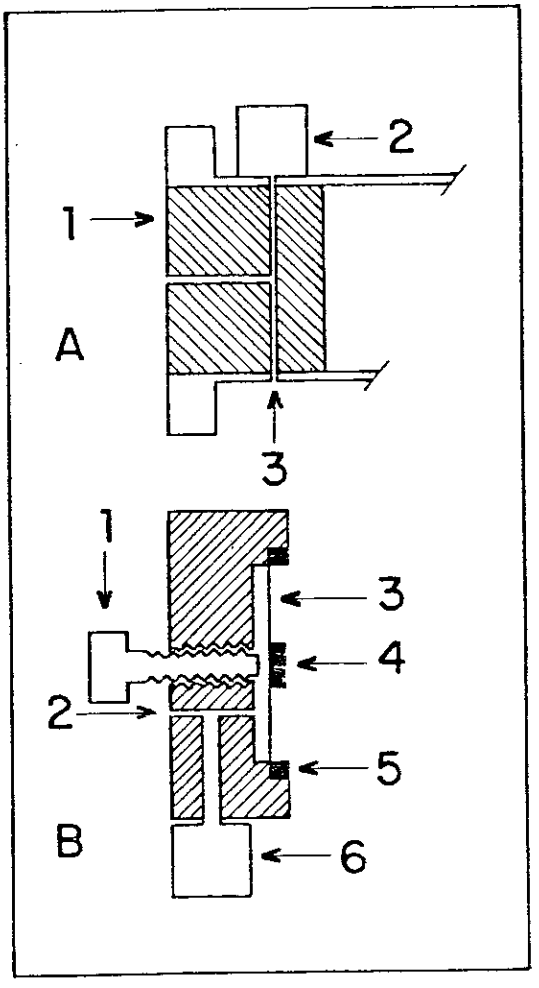

Fig.2

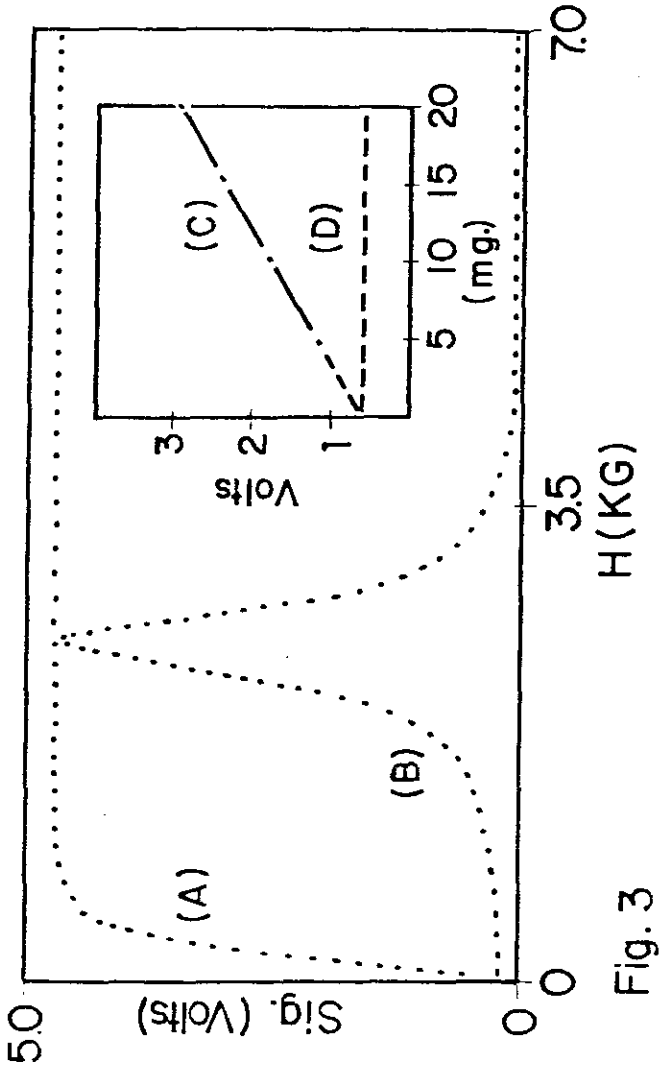

Fig. 3

REFERENCES

1 A. Rosencwaig, in "Optoacoustic Spectroscopy and Detection", Ed. by Y. H. Pao, Academic Press, London 1977, p. 193; In "Advances in Electronics and Electron Physics", Vol. 46, Ed. by L. Marton, Academic Press, New York 1978, p. 208; in "Photoacoustics and Photoacoustic Spectroscopy", Chem. Analysis, Vol. 57, Ed. by P. F. Elving, F. D. Winefordner, I. M. Kolthoff and A. Witley, Interscience Publishers 1980.

2 S. Foner, Rev. Sci. Instrum. 27, 548 (1956); Rev. Sci. Instrum. 30, 548 (1959); Rev. Sci. Instrum. 45, 1181 (1974); Rev. Sci. Instrum. 46, 1425 (1975).

3 O. A. C. Nunes, M. A. Amato and K. Skeff Neto, Phys. Stat. Sol. (a) 68, K25 (1981)

4 A. L. Tronconi, K. Skeff Neto and M. A. Amato, Phys. Stat. Sol. (a) 76, K209 (1983)

A N E X O C - 4

Phys. Stat. Solidi (a), 86, 924 (1984)

PHOTOACOUSTIC SIGNAL BEHAVIOR NEAR THE FERROMAGNETIC RESONANCE FIELD*

P. C. Morais, A. L. Tronconi, and K. Skeff Neto

Grupo de Física Molecular e Magnetismo
Departamento de Física, Universidade de Brasília
70910 - Brasília, D.F. - BRASIL

* Work partially supported by CNPq

ABSTRACT

Experimental data of the photoacoustic signal behavior near the ferromagnetic resonance field are presented. The photoacoustic signal goes as $f^{-\delta}$ ($f > 100$ Hz), where f is the modulation frequency. The δ values are positive and tend to one when the external magnetic field tends to the resonance field. A theoretical approach, based upon in an thermally thick and optically opaque sample approximation, is proposed.

INTRODUCTION

After the basic papers[1-3] on the photoacoustic effect (PAE) appeared, the main objects of research in this field have been the photoacoustic detection of physical phenomena and the improvement of the photoacoustic spectroscopy (PAS) as a powerful and versatile technique[4-14]. Basically, the physical principle of PAS is the conversion of electromagnetic radiation into a periodic heat flux when intensity-modulated radiation shines on a sample surface. This occurs because part of the modulated radiation is absorbed by the sample (excitation of energy levels) and a nonradiative de-excitation process reconverts it into a periodic heat-flux. Then, elastic waves are generated as a result of the motion of the medium due to a periodic thermal expansion process. Conventionally, the sample to be investigated is placed inside a closed gas cell and the periodic heat flux is detected by a sensitive microphone as described elsewhere[6].

Recently, we have reported an "unconventional" experiment arrangement for the detection of the photoacoustic effect. There, we have replaced the conventional closed gas cell by a piezoelectric ceramic detector[15]. In this arrangement the sample to be investigated is elastically coupled to the piezoelectric detector (barium titanate in our case) and the photoacoustic signal is related to the mean value of the elastic wave stress amplitude $\langle \varepsilon \rangle$. We have used this unconventional photoacoustic technique more succesfully either to study the behavior of the photoacoustic signal as a function of the

modulation frequency in the microwave region or to detect the ferromagnetic resonance signal[16].

In the present paper we report a more systematic study of the frequency dependence of the photoacoustic signal near the ferromagnetic resonance field (piezoelectric detection). We have used a commercial ferrite sample whose ferromagnetic resonance field is 0.2865 T when the microwave radiation is tunned at 9.38 GHz, at room temperature.

EXPERIMENTAL

The experimental set up used in our experiment is that of a non commercial X-band FMR spectrometer (Fig. 1). A detail of the end of the waveguide, where the sample is placed, is shown in Fig. 2. A typical ferromagnetic resonance curve is shown in Fig. 3, using a modulation frequency of 105 Hz. As we had pointed out above, the purpose here is to study the behavior of the photoacoustic signal as a function of the modulation frequency, around the ferromagnetic resonance field. This behavior is summarized in Fig. 4 for several values of the DC magnetic field. Note that our experimental data were for a modulation frequency above 100 Hz. The photoacoustic signal behavior for low modulation frequency (in our case below 100 Hz) may be explained by a model proposed by White[17]. In his model, the photoacoustic signal go as $f^{1/2}$ (for piezoelectric detection), where f is the modulation frequency. However, for high modulation frequency (in our case above 100 Hz) the experimental data shows that the

photoacoustic signal go as $f^{-\delta}$ (for piezoelectric detection), where δ assume a wide range of positive values (see the legend in Fig. 4). In a recent work we have proposed a model where δ tends to one in the limit of a thermally thick and optically opaque sample[18]. In the following we will discuss the experimental data presented here within the same basic assumptions of our model.

DISCUSSION

The sample used in our measurements has a disk shape with thickness ℓ. The sample is elastically coupled to the piezoelectric detector via a quartz rod (see Fig. 2). Here we assume a one-dimensional model, i.e., the PAS signal is related to the elastic waves traveling along the axis of the quartz rod (x-axis). The relationship between the stress (ε) and the strain (χ) for a solid absorber subjected to a modulated radiation is given by

$$\varepsilon(x) = (\lambda_1 + 2R)\ \chi(x) - B\ C_t\ \phi(x), \qquad (1)$$

where λ_1 is the first Lamé constant (K g/m x s^2), R is the modulus of rigidity (Kg/mxs^2), B is the bulk modulus (N/m^2) and C_t is the thermal expansion coefficient ($^oC^{-1}$). In Eq. 1 the function $\phi(x)$ represents the spacial part of a temperature distribution function $\phi(x,t)$. This $\phi(x,t)$ function describes the shift on temperature from the equilibrium, due to the PAE. It is reasonable suppose that $\phi(x,t)$ may be described by

$$\phi(x,t) = \phi(x)\ \exp(i\omega t) \qquad (2)$$

where ω is the frequency of the chopper. From a physical viewpoint the spacial part of $\phi(x,t)$ take into account that PAE occurs in subsurface regions (in our case). The temperature distribution function work out as a drive force for the elastic waves and comes from the PAE. The differential equation which describes an elastic plane wave in an homogeneous medium is[19]

$$\frac{d^2\mu(x,t)}{dx^2} - \frac{1}{v_L^2}\frac{d^2\mu(x,t)}{dt^2} = 0 \quad , \tag{3}$$

where $v_L^2 = (\lambda_1 + 2R)/\rho$ is the velocity of the elastic waves along the x-axis, ρ is the density of the medium (Kg/m^3) and $\mu(x,t)$ describes the displacement of a point of the medium. In the presence of a heat source proportional to $d\phi(x,t)/dx$ we have from Eq. 3

$$\frac{d^2\mu(x,t)}{dx^2} - \frac{1}{v_L^2}\frac{d^2\mu(x,t)}{dt^2} = D\,\frac{d\phi(x,t)}{dx} \quad , \tag{4}$$

where $D = B\ C_t/v_L^2$. From the above we would expect that the motion of the media must be described by $\mu(x,t) = \mu(x)\exp(i\omega t)$. The spacial part of $\phi(x,t)$ and $\mu(x,t)$, which must describe the behavior of the system at the steady state, follows the differential equation

$$\frac{d^2\mu(x)}{dx^2} + \xi^2\,\mu(x) = D\,\frac{d\phi(x)}{dx} \quad , \tag{5}$$

where $\xi = \omega/v_L$. We would expect three contributions to the $\phi(x)$ function, namely, the thermal diffusion coefficient (σ), the optical absorption coefficient (β) and the thermal diffusion

length (θ). However, as a first approximation we observe that the sample (a ferrite disk of 2.0mm thickness) used here is seen as thermally thick. This means that $\ell >> \theta$ and consequently the spacial distribution temperature function may be given by

$$\phi(x) = A_1 \exp(-\sigma x) + A_2 \exp(-\beta x) , \qquad (6)$$

where x runs over the sample lenght. The values of the constantes which appear in Eq. 6 are

$$A_1 = \frac{\beta^2 I_o}{2K\sigma(\beta^2-\sigma^2)} \qquad (7.a)$$

and

$$A_2 = \frac{-\beta I_o}{2K(\beta^2-\sigma^2)} , \qquad (7.b)$$

where $\sigma = (1+i)a$, $a=(\omega/2\alpha)^{1/2}$ is the thermal diffusion coefficient (m^{-1}), $\alpha = K/\rho c$ is the thermal diffusivity (m^2/s), K is the thermal conductivity ($j/mxsx\ ^oC$), C is the specific heat ($j/Kgx\ ^oC$), β is the optical absorption coefficient (m^{-1}) and I_o represents the intensity of incident radiation flux on the sample (W/m^2). At this point we assume that, for high modulation frequency, the major contribution to the stress is due to the temperature distribution in the sample. Therefore, from Eq. 1 we have

$$\varepsilon(x) \simeq -B C_t \phi(x). \qquad (8)$$

Since the photoacoustic signal is related to the mean value of $\varepsilon(x)$ along the sample length, we must take from Eq. 8

$$\langle \varepsilon(x) \rangle = \frac{1}{\ell} \int_0^{\ell} \varepsilon(x)\, dx \quad , \qquad (9)$$

where ℓ is the thickness of the sample. From Eqs. 6 and 8 we have

$$\langle \varepsilon(x) \rangle = \frac{1}{\ell} \int_0^{\ell} -B\, C_t \left[A_1 \exp(-\sigma x) + A_2 \exp(-\beta x)\right] dx \quad . \qquad (10)$$

In our case the frequency dependence of the PAS signal is very sensitive to the DC magnetic field near resonance (see Fig. 3). When the external DC field goes to the resonance field of the sample, it becomes optically opaque, i.e., $\ell >> \mu_\beta = 1/\beta$ and $\exp(-\beta\ell)$ vanishes. In this limit and bearing in mind that our sample is thermally thick ($\exp(-\sigma\ell) \simeq 0$) we have

$$\langle \varepsilon(x) \rangle \simeq \frac{i\, B\, C_t\, I_o\, \alpha}{4\, \pi\, K\, \ell} \left(\frac{1}{f}\right) \quad , \qquad (11)$$

after integration of Eq. 10.

CONCLUSION

In conclusion, our model describes fairly well the behavior of the PAS signal near the ferromagnetic resonance field. Theoretically the PAS signal goes as f^{-1} in the resonance field and our experimental data shows that the signal goes as $f^{-0.96}$. Near the resonance field (out of resonance) the assumption of a optically opaque sample is not fully correct and the signal goes as $f^{-\delta}$, with δ assuming positive values (see Fig. 4).

ACKNOWLEGMENT

We wish to express our sincere thanks to the members of the resonance group of the UFMG - Brasil, specially to Professor R. Gazzinelli, A. S. Chaves and G. M. Ribeiro for their hospitality and interest in our work.

FIGURE CAPTIONS

FIG 1 (A) - diode detector, (B) and (F) - isolator, (C) and (E)- attenuator, (D) - frequency meter, (G) - klystron, (H)- power supply, (I) - amplifier and signal selector, (J)- sinoidal generator signal, (K) - rectangular generator signal, (L) - frequency meter, (M) - lock-in amplifier, (N) - voltmeter, (O)- xy-plotter, (P) - oscilloscope, (Q)- audio amplifier, (R)- side-wall coupler, (S)- waveguide end (see. Fig. 2).

FIG 2 (A)- Waveguide, (B)- sample, (C)- quartz rod, (D)- piezoelectric detector.

FIG 3 (A)- reflection resonance curve (diode detection), (B) absorption resonance curve (piezoelectric detection).

FIG 4 Photoacoustic signal versus modulation frequency for the ferrite (log-log scale) at (A)- 2865 G (δ= 0.96), (B) 2500 G (δ= 0.84), (C)- 2000 G (δ= 0.82), (D)- 1500 G(δ= 0.81), (E)- 1000 G (δ= 0.80), (F)- 500 G(δ= 0.78).

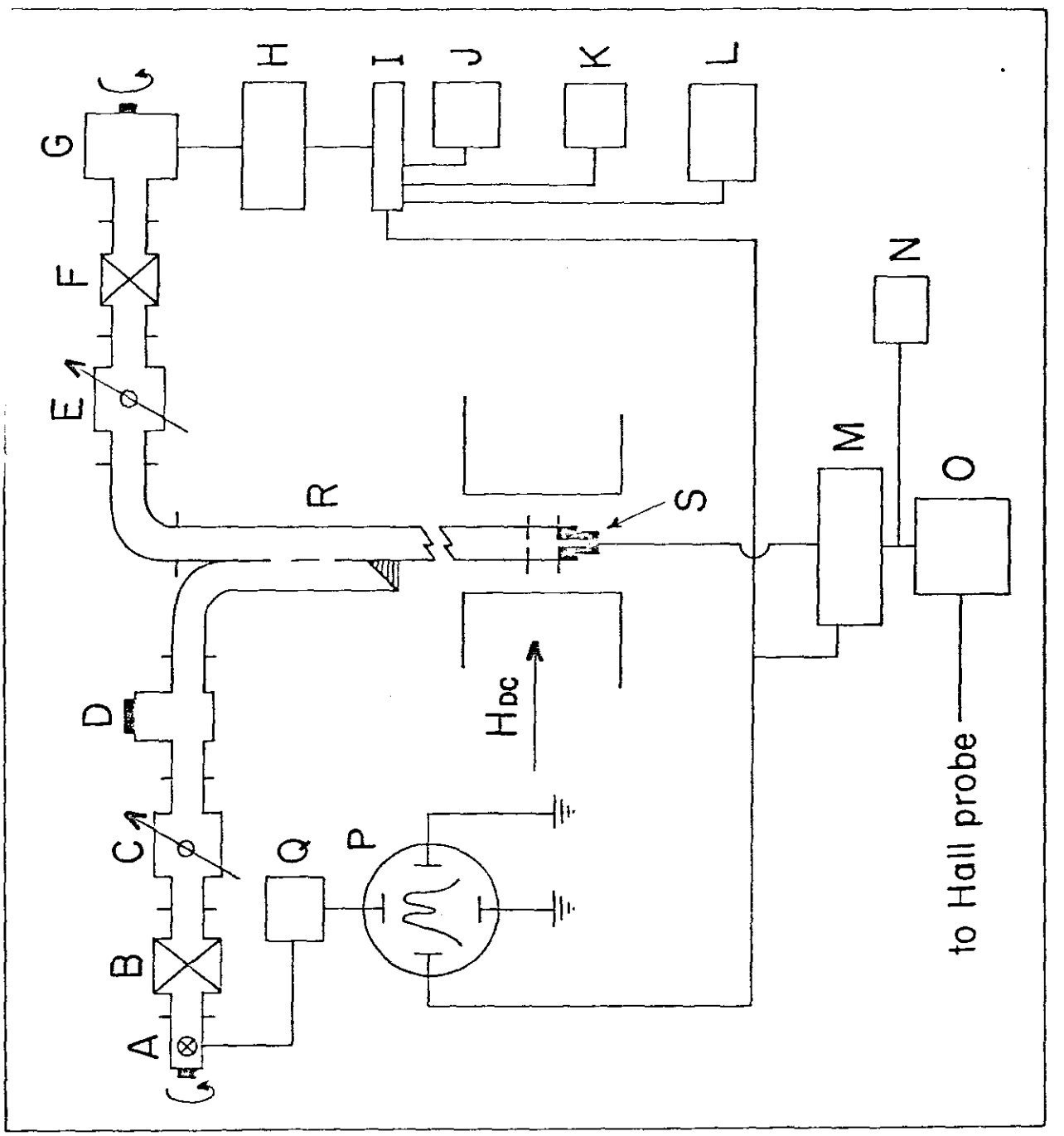

Fig. 1

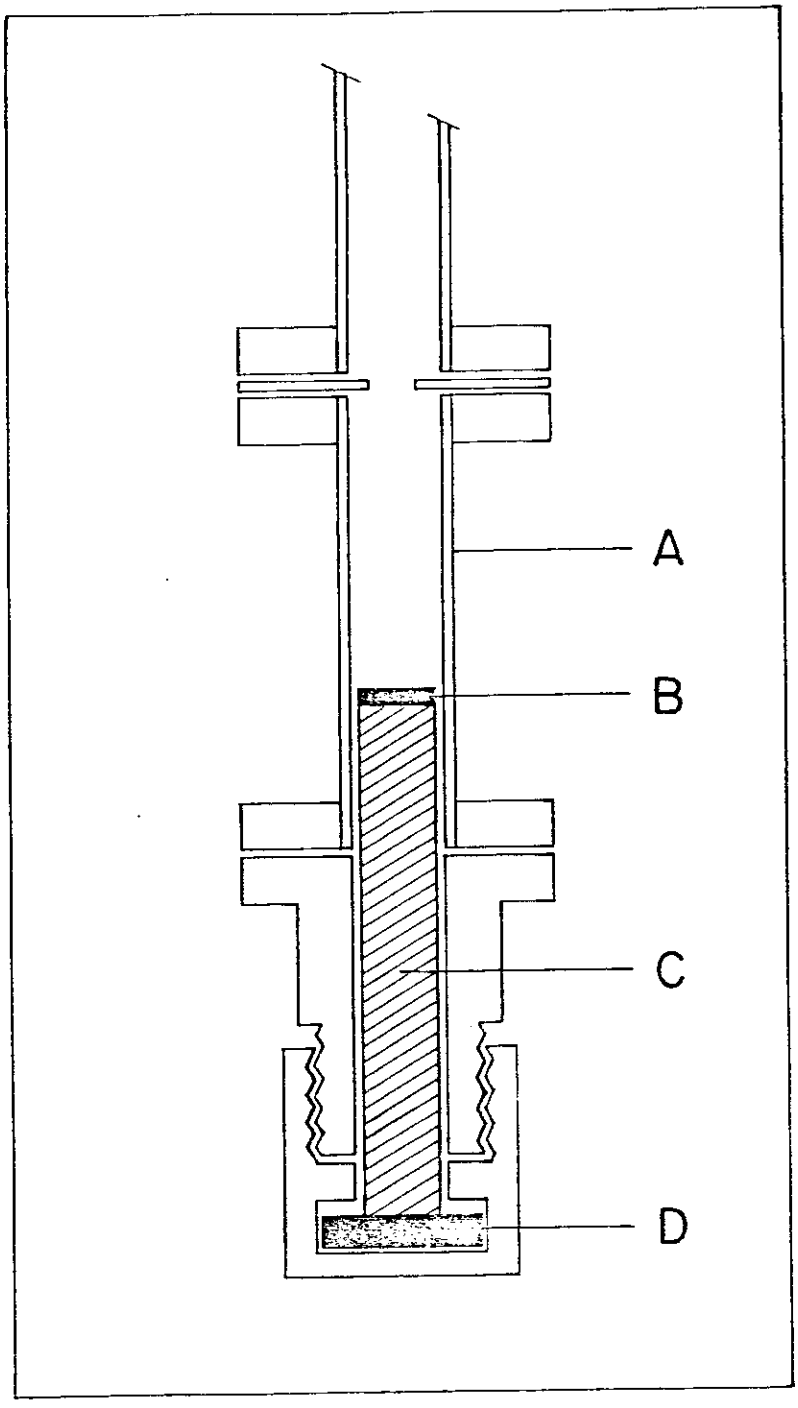

Fig. 2

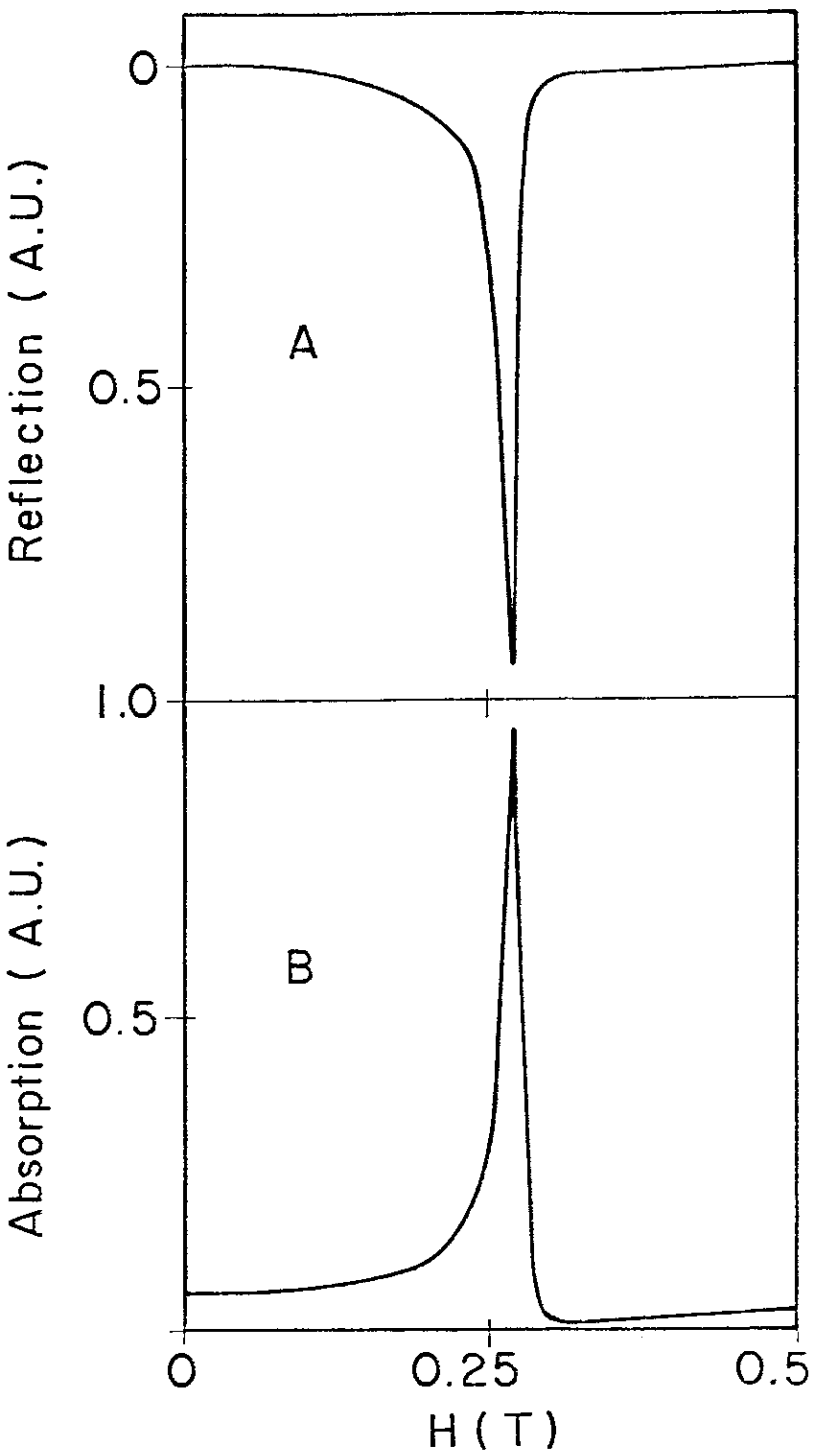

Fig. 3

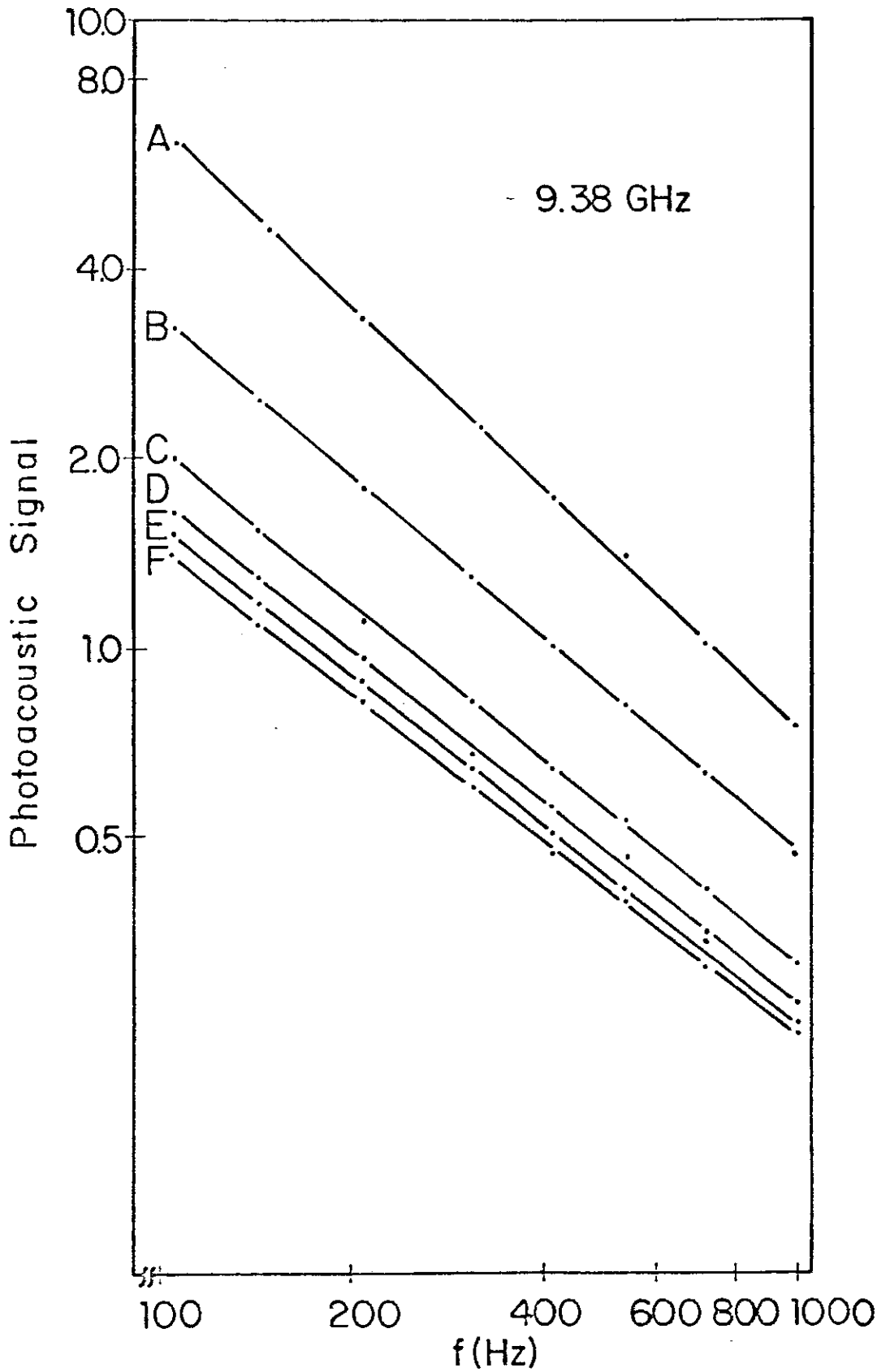
10.0
8.0
4.0
2.0
1.0
0.5
Photoacoustic Signal
A
B
C
D
E
F
9.38 GHz
100
200
400
600
800
1000
f (Hz)

Fig. 4

REFERENCES

1. J. G. Parker, Appl. Opt. 12, 2974 (1973).

2. T. H. Maugh, Science 188, 38 (1975)

3. A. Rosencwaig and A. Gersho, Science 190, 556 (1975); J. Appl. Phys. 47, 64 (1976).

4. A. Rosencwaig, Opt. Commun. 7, 305 (1973); Science 181, 657 (1973); Anal. Chem, 47, 592 (1975); Phys. Today 28,23 (1975)

5. A. Rosencwaig and S. S. Hall, Anal. Chem. 47, 548 (1975).

6. A. Rosencwaig, in "Optoacoustic Spectroscopy and Detection", Ed. by Y. H. Pao, Academic Press, London 1977, p. 193; in "Photoacoustics and Photoacoustic Spectroscopy", Chem. Analysis, Vol. 57, Ed. by P. F. Elving, F. D. Winefordner, I. M. Kolthoff and A. Witley, Interscience Publishers 1980.

7. D. Chahen, G. Bults, H. Garty and S. Malkin, J. Biochem & Biophys.Methods 3, 293 (1980).

8. R. Tilgner, Appl. Opt. 20, 3780 (1981).

9. A. Mandelis, Chem. Phys. 81, 185 (1983).

10. F. Anzel, J. Phys. Colloq. 44, 489 (1983).

11. O. A. Cleves Nunes, A. M. M. Monteiro and K. Skeff Neto, Appl. phys. Lett. 35, 656 (1979).

12. C. Evora, R. Landers and H. Vargas, Appl. Phys. Lett 36, 864 (1980).

13. W. Wettling, W. Jantz and L. Engelhardt, Appl. Phys. A 26, 19 (1981).

14. T. Inagaki, M. Motosuga and E. T. Arakawa, Phys. Rev. B28, 4211 (1983).

15. A. L. Tronconi, K. Skeff Neto and M. A. Amato, Phys. Stat. Sol. (a) 76, K209 (1983).

16. A. L. Tronconi, Master of Science thesis, Universidade de Brasília, Brasil 1982.

17. R. M. White, J. Appl. Phys. 34, 3559 (1963).

18. A. L. Tronconi, M. A. Amato, P. C. Morais and K. Skeff Neto, J. Appl. Phys. (in press).

19. L. Landau et E. Lifchitz, in "Théorie de l'élasticité", E'ditions Mir, Moscou 1967, p. 129.

A N E X O C - 5

The Rev. Sci. Instrum. (in press)

MICROVIBRATING SAMPLE MAGNETOMETER: A FORCE TYPE MEASUREMENT

P. C. Morais, N. M. L. Köche, A. L. Tronconi and K. Skeff Neto
Grupo de Física Molecular e Magnètismo
Departamento de Física, Universidade de Brasília
70910 - Brasília, D. F. - Brasil

* Work partially supported by CNPq

ABSTRACT

A simple microvibrating sample magnetometer (MVSM), particularly inexpensive, sensitive and versatile has been developed. An alternating magnetic field superposed to a steady uniform magnetic field is applied to the sample. The sample undergoes a periodic motion around an equilibrium position, causing a pressure fluctuation within a closed gas cell which is detected as an acoustic signal by a microphone.

PACS number: 07.55. + x, 07.20. Mc

INTRODUCTION

Measurements of magnetic moments have been done by the following three types of methods: (1) indirect methods, (2) force methods and (3) induction methods. In indirect methods the magnetization of a sample is related to a particular physical phenomenon. Despite their high sensitivity indirect methods are suitable to a limited class of materials. Examples of indirect methods are Hall effect[1], Faraday effect[2], EPR[3], NMR[4] and Mössbauer[5] measurements. The other two types of methods have found widespread applications in both academic research and industry. The force methods involve the measurements of a force exerted on a sample placed in an inhomogeneous magnetic field. The induction methods are based on the measurements of a signal induced by moving the sample with respect to detecting coils. An example of a force method is the Faraday magnetic balance[6]; an example of an induction method is the vibrating sample magnetometer[7].

In the present work we have combined some advantages of both force and induction methods in an inexpensive, sensitive and versatile microvibrating sample magnetometer (MVSM). Our experimental arrangement, which we shall describe in detail in the following section, is based on the force method. The underlying principle is the application of an alternating (low frequency) magnetic field superposed to a steady uniform magnetic field. A sinusoidal force is exerted on the sample by the alternating magnetic field. This force is communicated to a damped resonant elastic membrane to which the sample is

attached. The driving force of such motion is given by

$$\vec{F} = (\vec{M} \cdot \vec{\nabla})\, \vec{H}eff \ , \qquad (1)$$

where $\vec{H}eff$ is the effective field acting on the sample and $\vec{M}$ is the magnetization of the sample. The resulting mechanical vibrations cause pressure fluctuations within a closed gas cell, which are detected by a sensitive microphone, as an acoustic signal. Therefore the magnetization of the sample is taken as proportional to the acoustic signal. Supposing an adiabatic behavior of the gas inside the gas cell, the acoustic signal (A.S.) must be proportional to the amplitude of the pressure fluctuation (dP/dt). This is given by

$$A.S. \sim dP/dt = \gamma\, (P_o/V_o)\, dV/dt \ , \qquad (2)$$

Where $\gamma = C_p/C_v$ is the ratio of specific heats of the gas, P_o is the equilibrium pressure inside the cell, V_o is the volume of the cell at the equilibrium pressure and dV/dt describes the dynamic of the system along the vibration axis.

I EXPERIMENTAL DETAILS

The essential parts of the MVSM are shown by the schematic diagram of Fig. 1. We discuss two differents configurations where the direction of vibration axis is either parallel or perpendicular to the external uniform magnetic field. From now on the parallel and perpendicular configurations will be labeled as axial and transverse geometry, respectively. In Fig. 2 we show a more detailed view of the gas cell. In the

axial geometry, suitable for room temperature measurements, the alternating magnetic field is given by a pair of coils with axes coinciding with the axis of the gas cell (see Fig. 1). Here, the sample is positioned in the middle point between the coils and the cell is mechanically isolated from the coils. The alternating frequency of the coils is tuned near the mechanical resonance frequency of the system. Near the resonance frequency the pressure fluctuation must increase according to the quality factor of the resonance system. However, the frequency range very close to the mechanical resonance frequency must be avoided to prevent larger errors due to fluctuation in the acoustic signal. In Fig. 3 we report the behavior of the acoustic signal for a natural iron sample (Mössbauer iron foil) as a function of the sample weight, at room temperature. In that figure the acoustic signal does not cross the origin because we have a residual signal due to the metallic foil of the capacitive microphone. Another point to be stressed here is that the FET of the microphone has been pulled out and connected directly with the pre-amplifier.

The transverse geometry, suitable for temperature variation measurements, shows a similar performance. In this geometry, the acoustic cell, discussed in Fig. 2, is attached to a rod and the sample is placed at the other end of the rod. Here, a system of two elastic membranes makes the rod vibrate only in one direction. In Fig. 4 we show a detailed view of the transverse geometry where the sample is positioned at the center of the coil arrangement. The coil configuration used here is similar to the Mallinson[8] configuration, namely, a planar

arrangement of four coils. This coil system has been used sucessfully as detection coils in the vibrating sample magnetometer.

The coupling of the MVSM with other experimental techniques may be used to illustrate the versatility of our system. In Fig. 5 we have the microvibrating sample magnetometer (transverse geometry) coupled to a ferromagnetic resonance spectrometer. This arrangement has been used in our laboratory to take magnetization and ferromagnetic resonance measurements at the same time. In Fig. 6 we show the MVSM coupled to an electron paramagnetic resonance cavity. This arrangement is very usefull to take measurements in polycrystalline samples. An example of this is showed in Fig. 7 where the magnetization curve (dotted line) and electron paramagnetic resonance curve (full line) were obtained for a commercial polycrystalline ferrite.

II DISCUSSIONS AND CONCLUSIONS

In reality the MVSM described above represents a force method. The force methods are characterized by their high sensitivity and we believe that after some improvement our magnetometer may be as sensitivy as the Faraday Balance. In contrast to the Faraday method, where the field gradient, and therefore the sensitivity, is a function of the steady field (wich must be determined empirically), an analytical sensitivity function may be defined to the MVSM for a given coil arrangement.[9] This makes the MVSM suitable to study the field dependence of

magnetization. On the other hand, the MVSM shows an important characterization of the induction methods; the acoustic signal is directly proportional to the sample magnetization at all fields.

The sensitivity as well as the signal-to-noise ratio may be taken from Fig. 8, for the MVSM as it currently exists. The curve in Fig. 8 was obtained from a polycrystalline iron foil (5 mg) in the range of zero to 6 KG. The sweep-time (H_{DC}) and time constant (loock-in) were 5 min. and 1 seg., respectively.

In conclusion, we have combined some advantages of force and induction methods in an inexpensive, sensitive and versatile magnetometer. Based on the so - called principle of reciprocity[8] we can calculate a sensitivity function and to study the effects of the coil geometry and sample geometry. The sensitivity of the MVSM may be improved too by using more convenient coil designs, elastic membranes, gas cells and microphone detectors.

ACNOWLEDGEMENT

We wish to tanks the members of the resonance group of the UFMG - Brasil, for their interest in our work. In special to Prof. A. S. Chaves for their valuable comments.

REFERENCES

1. D. J. Craik, J. Phys. E 1, 1193 (1968)

2. M. C. Day, L. D. Hulett and D. E. Willis, Rev. Sci. Instrum. 31, 1142 (1960).

3. S. Schultz and E. M. Gullikson, Rev. Sci. Instrum. 54, 1383 (1983)

4. I. Koveski, J. Magn. Res. 43, 1 (1981).

5. R. B. Frankel, N. A. Blum, S. Foner, A. J. Freeman and M. Schieber, Phys. Rev. Letters 15, 958 (1965)

6. G. Felton and Ch. Schwink, J. Phys. E 13, 487 (1980)

7. S. Foner, Rev. Sci. Instrum. 30, 548 (1959).

8. J. Mallinson, J. Appl. Phys. 37, 2514 (1966)

9. A. Zieba and S. Foner, Rev. Sci. Instrum. 53, 1344 (1982).

FIGURE CAPTIONS

FIG. 1 - Block diagram of the MVSM. (1) electromagnet, (2) and (4) modulating coils (axial geometry), (3) gas cell, (5) FET and pre-amplifier, (6) signal generator and audio amplifier, (7) lock-in amplifier.

FIG. 2 - Gas cell detail. (1) aluminum gas cell body, (2) microphone chamber, (3) duct for pressure adjust, (4) support bracket attachement, (5) elastic membrane, (6) sample holder.

FIG. 3 - (A) acoustic signal versus sample weight (Mössbauer iron foil) and (B) residual signal due to the metalic foil of the microphone.

FIG. 4 - Block diagram of the transverse MVSM. (1) gas cell (see Fig. 2), (2) and (3) elastic membranes, (4) acrylic road, (5) modulating coils, (6) sample holder.

FIG. 5 - Block diagram of the MVSM coupled to the FMR spectrometer. (1) FMR spectrometer, (2) sample, (3) MVSM(see Fig.4), (4) modulating coils for resonance detection, (5) modulating coils of the MVSM, (6) signal and audio amplifier (FMR), (7) signal and audio amplifier (MVSM), (8) and (9) lock-in amplifiers, (10) capacitive microphone.

FIG. 6 - View of the MVSM coupled to the EPR cavity.

FIG. 7 - Magnetization (---) and EPR (—) measurement obtained by the system showed in Fig. 6. The sample was a polycrystalline ferrite.

FIG. 8 - Acoustic signal versus H_{DC} for a polycrystalline iron sample (5 mg). Data taken from MVSM in the transverse geometry.

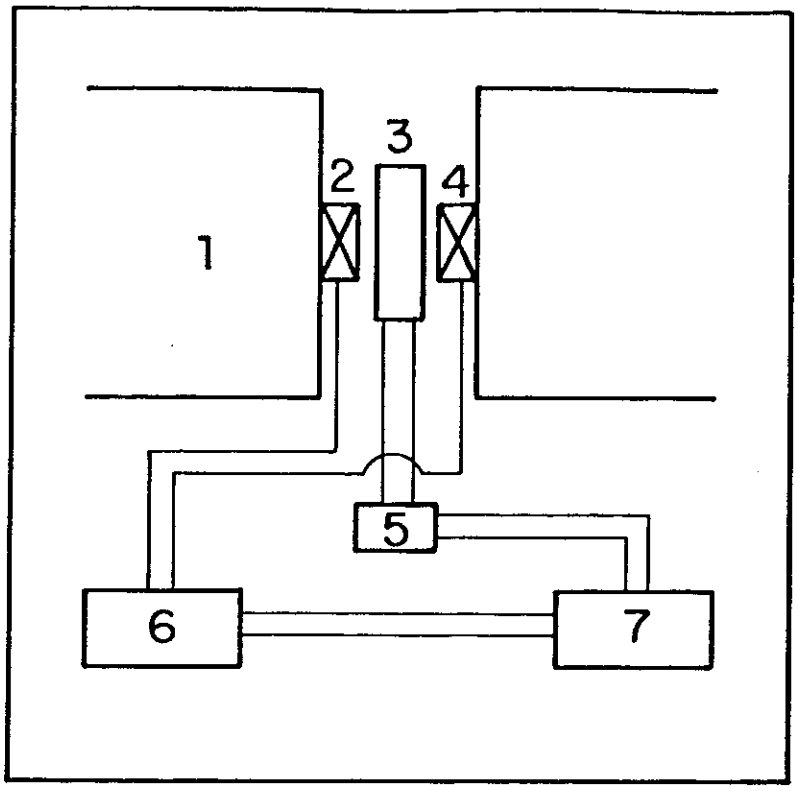

Fig. 1

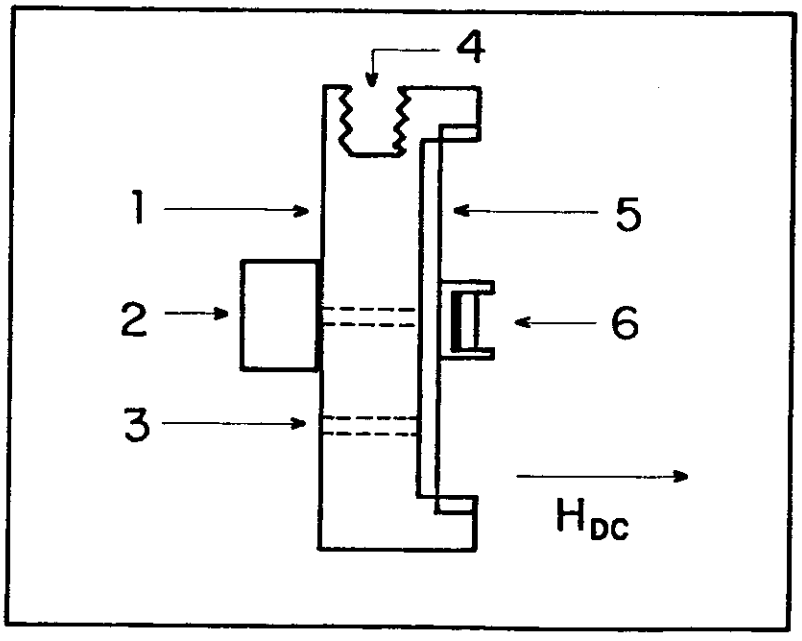

Fig. 2

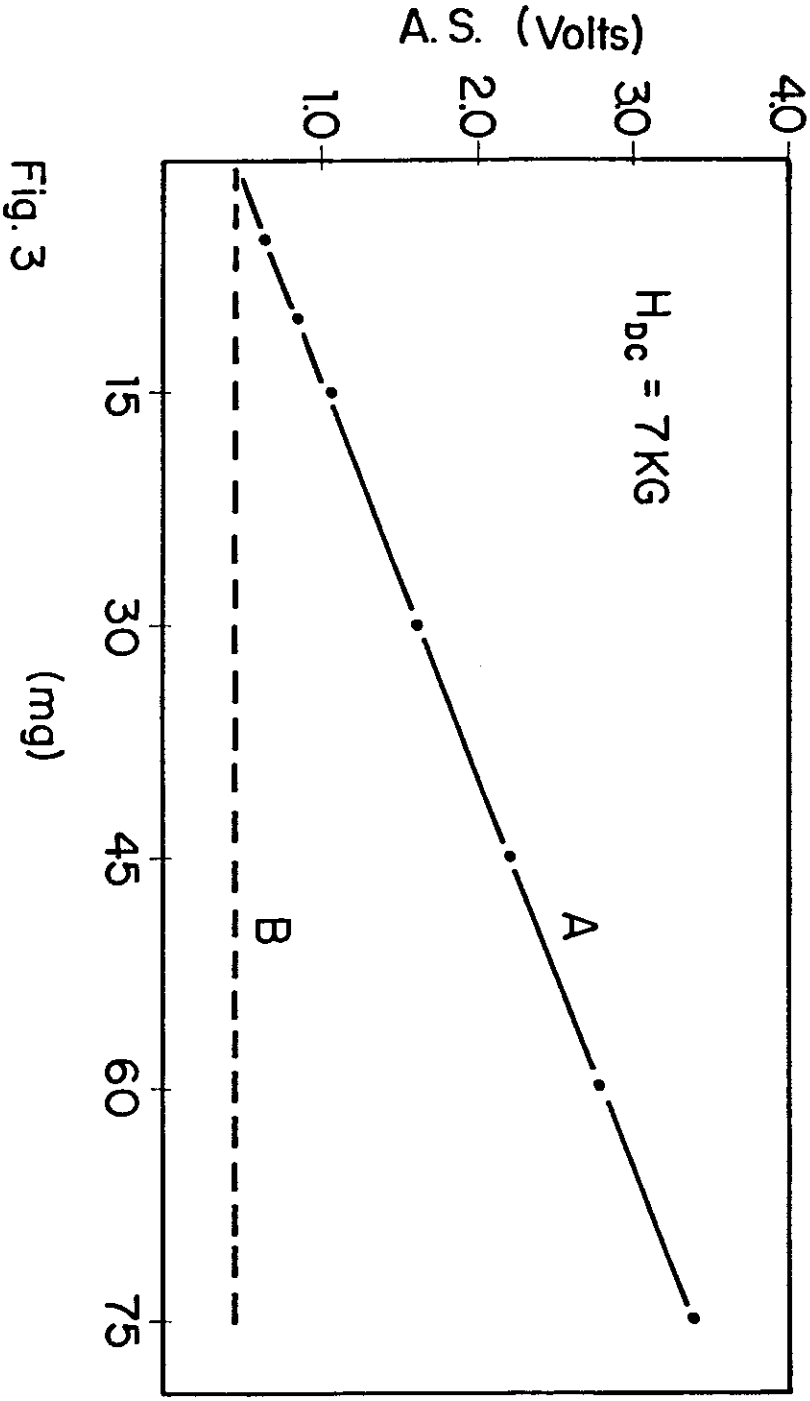

Fig. 3

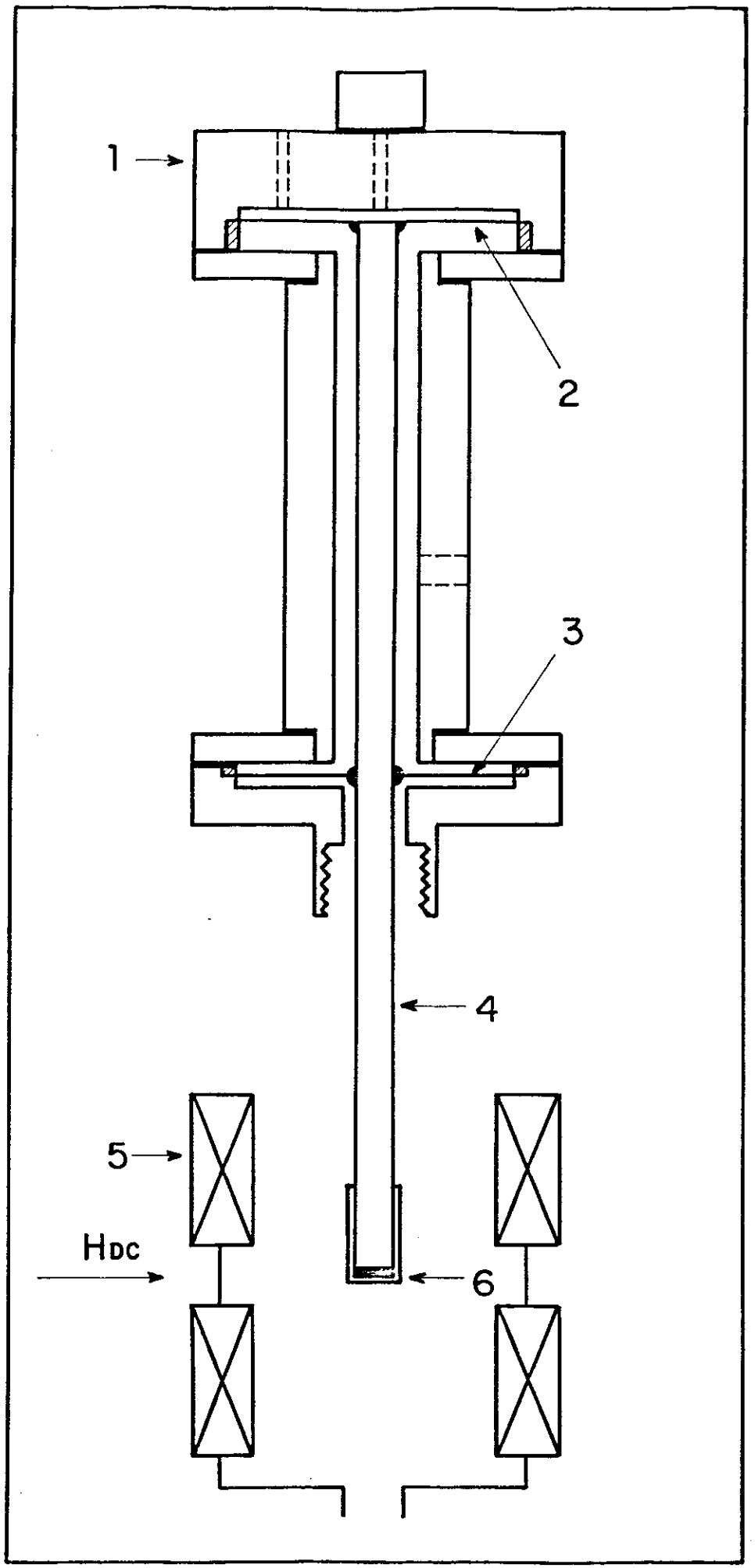

Fig. 4

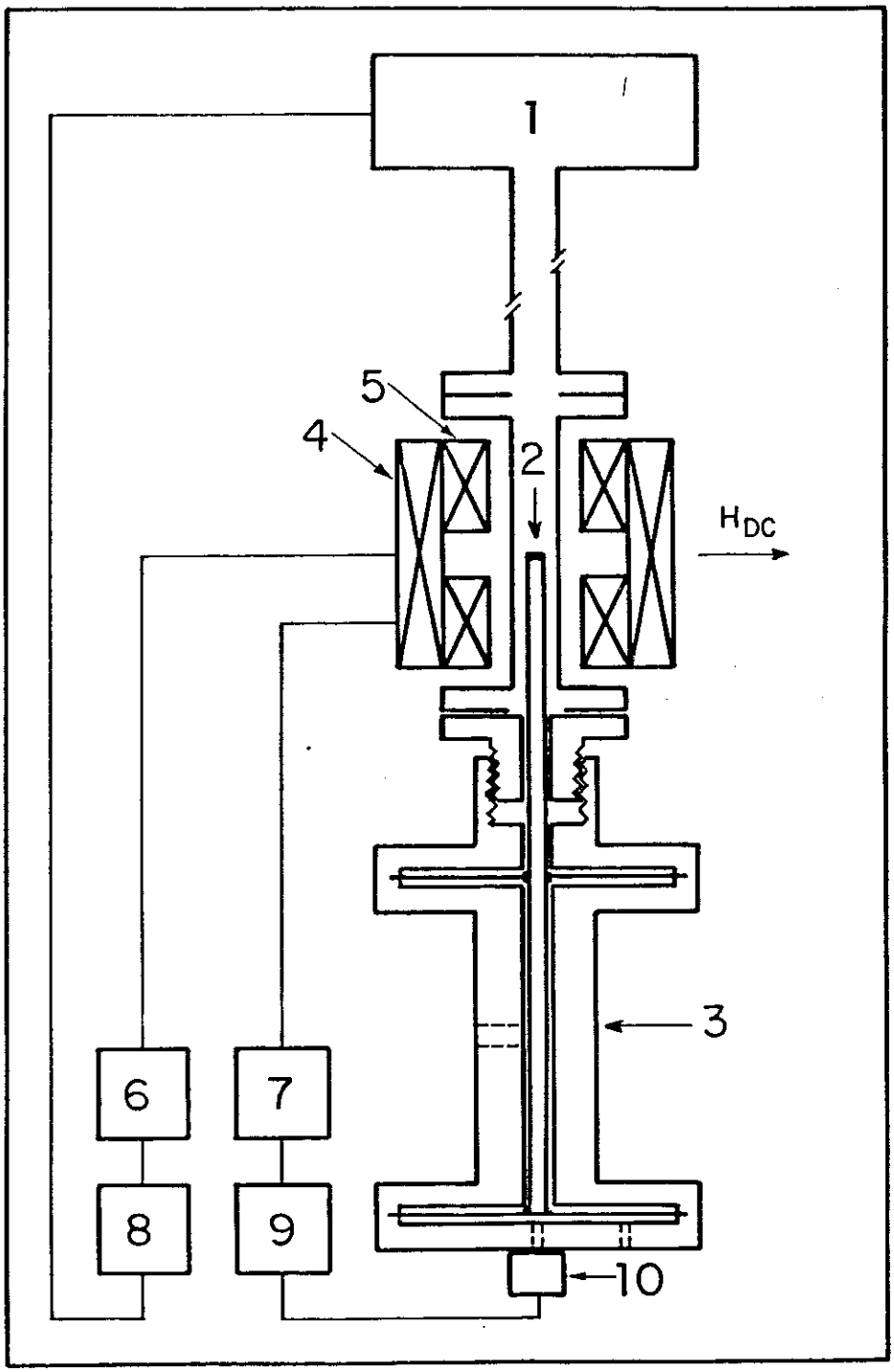

Fig. 5

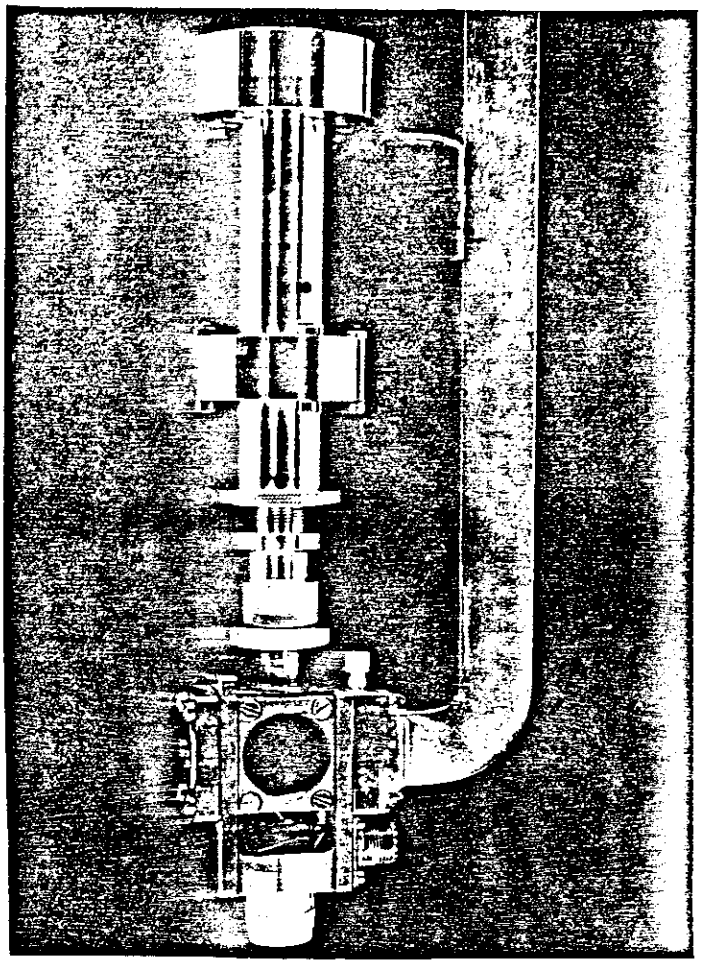

Fig. 6

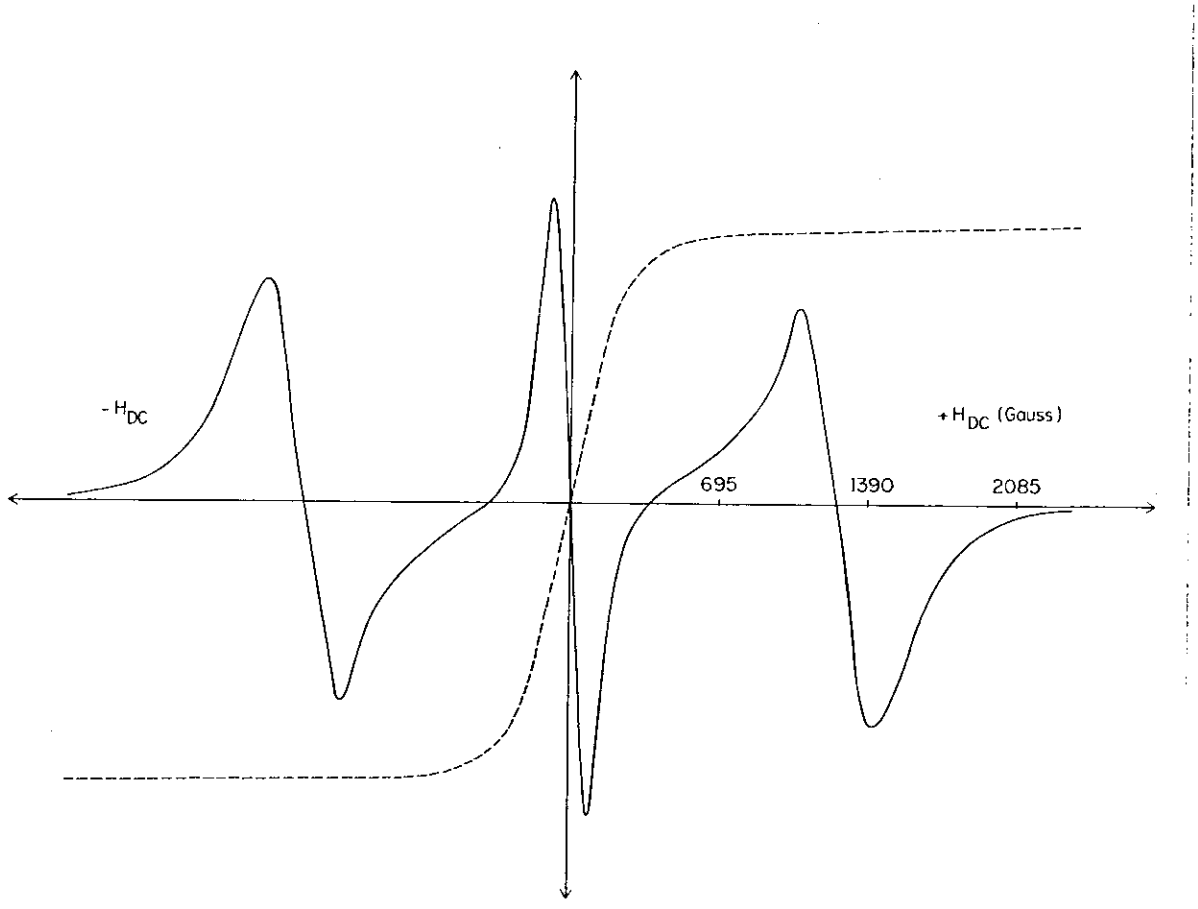

Fig. 7

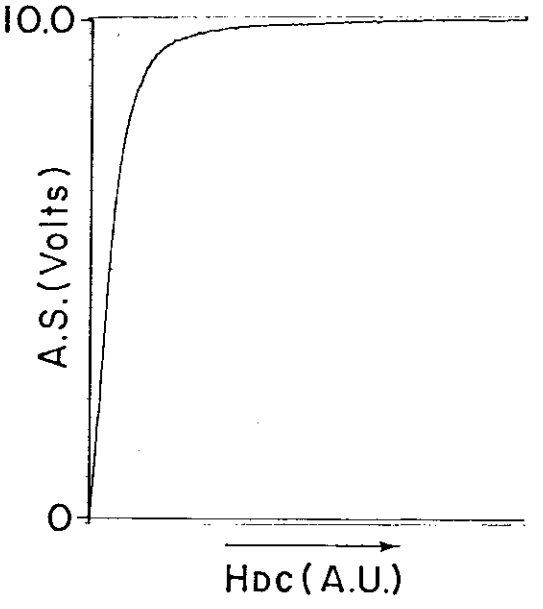

FIG. 8

A N E X O D - 1

ON THE ORDER AND DISORDER BEHAVIOR OF SUPERPARAMAGNETIC PARTICLES OF FERRIC HYDROXYSULFATE SEEN THROUGH MÖSSBAUER SPECTROSCOPY.*

P.C. Morais and K. Skeff Neto
Grupo de Física Molecular e Magnetismo
Departamento de Física, Universidade de Brasília
70910 - Brasília, D.F. - Brasil

* Work partially supported by CNPq

ABSTRACT

A connection between the temperature behavior of the internal magnetic field and the Mössbauer linewidth broadening for a system which exhibits superparamagnetism is proposed.

PACS number: 76.80. + y, 75.60. Jp, 76.90. + d

I INTRODUCTION

In the last years we have studied some aspects of the order and disorder behavior in fine particles of ferric hydroxysulfate[1-5]. The choice of this system is mainly due to the fact that we know how to control its hydration and dehydration process, purification, chemical stability and particle size distribution[2]. As it is a well know fact, the magnetic properties of fine particles is very sensitive to the pattern of particle size distribution in the region where the system exhibits superparamagnetism. This fact is particularly confirmed when one analyzes the Mössbauer spectroscopy data. At low temperatures the Mössbauer spectra of Fe^{57} nuclei shows a pattern of six hyperfine lines characteristic of a magnetically ordered phase. When the temperature is increased the internal magnetic field decreases and goes to zero at the magnetic phase transition temperature, the hyperfine lines become asymmetrically broader and we have the increasing of the intensity of either the quadrupole doublet or the singlet. At higher temperatures either the doublet or the singlet survives. These are the fundamental features of superparamagnetism seen through Mössbauer spectroscopy. In the following we shall summarize the most important aspects of our system, concerning to the order and disorder behavior. We shall take two different viewpoints. First we shall consider the temperature dependence of the internal magnetic field H(T) and second the temperature dependence of the Mössbauer linewidth broadening $\Delta\Gamma(T)$, at

zero external field. Afterwards we will call the attention on the fact that some parameters related to both approaches are connected themselves in a simple manner.

II THE MODELS

The temperature dependence of the internal magnetic field has been previously studied in a ferric hydroxysulfate sample which shows a bimodal particle size distribution[3]. The diameters of such a bimodal distribution are centered around two mean values (D_1 = 50 Å and D_2 = 110 Å). To explain the temperature dependence of the internal magnetic field and the validity of the one-third power law in the overall range of temperature, i.e., near and far from the magnetic phase transition, we propose that the density of magnetically ordered atoms "m" must be a function of temperature[3],

$$m(T) = \lambda \left[1 - \sum_i \alpha_i \, (Ip^i(T)/Ip(T_o))\right], \qquad (1)$$

where λ is a characteristic constant of the magnetic system ($\lambda \leq 1$). Physically λ represents the density of magnetically ordered atoms at low temperature. The fraction of magnetically ordered atoms, at low temperature and distributed between the particles which compose the bimodal assembly, is given by α_i (i = 1,2). From Mössbauer measurements we have the values of $Ip(T)/Ip\ (T_o)$, i.e., the ratio of paramagnetic line intensities as a function of temperature. T_o is the temperature beyond which no magnetic contribution is felt by Mössbauer spectroscopy. In our previous work[3] we have used an expression for $Ip^i(T)/Ip(T_o)$

in order to adjust the experimental data given by $Ip(T)/Ip(T_o)$. Thus, we have a description of m(T) given by Eq. 1. The model used to analyze the temperature dependence of the reduced internal magnetic field (H(T)/H(0) vs. T) was based upon the molecular-field approximation for randomly dilute alloys. Within this approach, by taking m(T) given by Eq. 1 a relation for the magnetization M is found[3] in the case of spin S = 1/2

$$\frac{1}{2} - M = \sum_{\nu=0} \frac{z! \left[m(T)\right]^{\nu} \left[1 - m(T)\right]^{z-\nu}}{(z-\nu)!\ \nu! \left[\exp(2MJ/kT)+1\right]} \qquad (2)$$

In this equation z is the number of the nearest-neighbor exchange interaction. At this point we take the reduced magnetization M(T)/M(0) as the experimental values given by H(T)/H(0). The behavior of the normalized H(T)/H(0) versus temperature is shown in Fig. 1(b). The experimental points are represented by crosses and the solid line represents the best fit of the data to the Eq.2. The circles in Fig. 1(a) represent the experimental values of $[H(T)/H(0)]^3$ versus temperature and the solid line represents the third power of the points described by the full line in Fig.1(b). In Fig. 1(c) we show the experimental points $Ip(T)/Ip(T_o)$ by crosses and the full line by $[1 - m(T)]$. The adjusted parameters based on the model described above are summarized in Table I. On the other hand, we have also used the well know expression

$$H(T)/H(0) = A\,(1 - T/T_c)^{\beta}, \qquad (3)$$

to adjust our experimental data. Note from Fig. 1(a) that we have three distinct regions corresponding to three straight lines. In spite of their different angular coefficients all they show, within the experimental error, the same value for the critical exponent (β). The adjusted parameters from Eq. 3 are summarized

in table II. The presence of such regions has been understood as a manifestation of the order and disorder effect related to the presence of a bimodal particle size distribution. In the first region ($T \leq 95K$) we assume that the magnetic disorder is mainly due to the temperature effect, being nearly independent of the topographic characteristics of the system. However, in the second ($95K \leq T \leq 107K$) and third ($T \geq 107K$) regions the effect of the clusters appear to be very important. In the second region we have the effect on the magnetic behavior of the system due to particles whose diameters are centered around $D_2 = 110$ Å. In the third region we have the contribution of the particles whose diameters are centered around $D_1 = 50$ Å. Therefore, according to our interpretation, the critical diameter for fine particles of ferric hydroxysulfate is located above a diameter of 110 Å.

Recently, we analyze in the same system the broadening of the hyperfine Mössbauer lines as a function of temperature[5]. The Mössbauer data are related to the $|1/2> \rightarrow |3/2>$ transition. The linewidth broadening is more sensitive to the temperature in the range near the point where the paramagnetic lines begin to appear, i.e., in the range of temperatures corresponding to the second and third regions of Fig. 1(a). To explain this broadening we have assumed a relaxation model where the magnetic moments of the particles moves within a double-well potential. We also assume that the local magnetic

anisotropy destroys the original symmetry of the two level system related to the magnetic moment of the particles. This assumption has been used to explain unusual low-temperature properties of amorphous solids[6-11]. Since we have an assembly of particles which shows a bimodal particle size distribution, the description of the linewidth broadening must include a weight function. This function describes the reduction of the number of particles with high activation energy barrier. After taken these points into account, the experimental linewidth broadening of the Mössbauer hyperfine line, related to each component of the bimodal distribution is given by[5]

$$\Delta\Gamma^{i}(T) = \Gamma_i' \, (T/\theta_i) \exp (T/\theta_i), \qquad (4)$$

where Γ_i' is a constant related to the system and $\theta_i (i=1,2)$ is a characteristic temperature related to each component of the bimodal distribution. The physical meaning of θ_i is that at temperatures below θ_i the magnetic moment of the particles with diameters around D_i is bottlenecked to move as in a thermal-relaxation channel. In Fig. 2 we show the experimental data of $\Delta\Gamma/T$ vs. T by points. The full lines represent the best fit of the experimental data by using Eq. 4. We have assumed that the presence of this two distinct regions is related to the bimodal particle size distribution. The behavior of the system in the range of $T \lesssim 106$ K is dominated by the particles with diameters centered around $D_2 = 110$ Å ($\theta_2 = 62.7$K). The other component of the assembly, i.e., the particles with diameters centered around $D_1 = 50$ Å ($\theta_1 = 14.7$K) dominates the behavior of the

system in the range of $T \gtrsim 106K$.

III ANALYSIS

In the present work we propose a simple connection between the parameters used in the description of the order and disorder behavior of our system. Those parameters arose from both the temperature dependence of the internal magnetic field and of the temperature dependence of the linewidth broadening. From the above seems to be reasonable to use the following approximation for the density of paramagnetic atoms

$$m_p(T) \approx \lambda - m(T) \qquad (5)$$

By using Eq. 1 and the data of Fig. 1(c) we see that m(T) tends to λ, at low temperatures, i.e., $\sum_i \alpha_i \, I_p^i(T)/I_p(T_o)$ goes to zero. At high temperatures, i.e., when T goes to T_c, the experimental values of $Ip(T)/Ip(T_o)$ tends to one and m(T) must goes to $\lambda \left[1 - \sum_i \alpha_i\right]$. Therefore near the magnetic phase transition we have

$$m_p(T) \approx \lambda \sum_i \alpha_i \qquad (6)$$

The analysis of Fig. 1(a) clearly shows that the effect of the superparamagnetism is to shift the magnetic phase transition temperature from $T_c = (131.62 \pm 0.01)K$ to $\tau_1 = (120.83 \pm 0.01)K$. This shift may be understood if we consider the influence of $m_p(T)$ over Tc, near the phase transition. At this point we argue that, in the absence of superparamagnetism, the value

of λ must tends to one and τ_i to T_c. In our case τ_1 means the actual phase transition temperature of the sample. Therefore, the shift of the transition temperature from T_c to τ_1 may be related to the decrease of the density of magnetically ordered atoms at low temperature (λ). Probably, this fact arises from the effect of thermal fluctuations of the magnetic moment of the clusters. From these arguments and looking at the data presented above we suggest the following relationship between τ_i and T_c,

$$\tau_i = m_p(T)\ T_c \qquad (7)$$

where τ_i represent the actual phase transition temperature of the system (in our case i = 1) and $m_p(T)$ is given by Eq. (5). If we use the adjusted values of λ, α_1, α_2 and T_c given above we obtain τ_1 = 121.22K, according to Eqs. 5 and 7. This is in a good accordance with the adjusted value for τ_1 = (120.83 ± 0.01)K obtained in our previous work (Ref. 3). Another point which arises from Eq. 7 is a possible connection between the two approaches discussed before. We note from that equation two contributions for τ_i; $\delta_i = \lambda\ \alpha_i\ T_c$ for i = 1,2. From our data we have δ_1 = 103.5K and δ_2 = 17.7K. Furthermore, we note that δ_1 and δ_2 are related to the particle assembly whose diameters are centered around D_1 = 50 Å and D_2 = 110 Å, respectively. From Fig. 2 we see that the δ_1 = 103.5K value may be related to the temperature where the $\Delta\Gamma/T$ vs. T curve change its slope. Then, above δ_1 the temperature behavior of the linewidth broadening seems to be dominated by the particles with

diameters around D_1 = 50 Å. To see what happen with the other component (δ_2), we must use the adjusted values for Γ_2' and θ_2 into Eq. 3 for $T \lesssim 106K$. These values are Γ_2' = 5.19K Oe and θ_2 = 62.7K. From this values we can calculate the temperature (T') below which the Mössbauer hyperfine lines become symmetrical. The broadening of the hyperfine lines, due to the cluster effect, is supposed to occurs above this temperature (T'). Experimentally this occurs when $\Delta\Gamma$ = 1.86K Oe and by using Eq. 4 we obtain T' = 17.1K. At this point we assume that the T' = 17.1K value is related to the δ_2 = 17.7K. Then, in the range of temperature between δ_2 and δ_1 ($\delta_2 \lesssim T \lesssim \delta_1$) the behavior of the linewidth broadening is dominated by the particles whose diameters are centered around D_2 =110 Å .

IV CONCLUSION

In conclusion, the experimental phase transition temperature of our system (a bimodal particle size distribution) may be though as a result of two contributions $\delta_i = \lambda \alpha_i T_c$ (i = 1,2). These contributions may be related with the temperature dependence of the Mössbauer hyperfine line broadening by using a relaxation model based upon an asymmetrical double-well potential. Finally, we want to point out that this is a tentative analysis of the superparamagnetic behavior of our system through Mössbauer data, and we believe that is worth-while to apply to other systems before it can be fully adopted.

TABLE I

T_c	(131.62±0.01)K
H(0)	(467.5±0.5)KO_e
λ	0.921±0.001
α_1	0.854±0.001
α_2	0.146±0.001
τ_1	(120.83±0.01)K
τ_2	(124.78±0.01)K
T_o	(123.72±0.01)K

TABLE II

T_c^*	(131.66±0.01)K
$H^*(0)$	(469.6±0.5)KO_e
A	1.225±0.001
τ_1^*	(121.65±0.01)K
τ_2^*	(124.42±0.01)K
T_o^*	(124.02±0.01)K
β	0.335±0.001

FIGURE CAPTIONS

FIGURE 1 - Behavior of the (a) $\left[H(T)/H(0)\right]^3$, (b) $H(T)/H(0)$ and (c) $m_p(T) = 1 - m(T)$ vs. T/T_c for a bimodal particle size distribution of ferric hydroxysulfate (Ref. 3).

FIGURE 2 - Temperature dependence of the Mössbauer linewidth broadening in a semi-log scale for our sample (Ref. 5)

REFERENCES

1. K. Skeff Neto and L. C. M. Miranda, Solid State Commun. 28, 43 (1978)

2. P. C. Morais and K. Skeff Neto, Polyhedron 2, 875 (1983)

3. P. C. Morais and K. Skeff Neto, J. Appl. Phys. 54, 307 (1983)

4. P. C. Morais, A. L. Tronconi and K. Skeff Neto, J. Appl. Phys. 55, 3744 (1984)

5. P. C. Morais, A. L. Tronconi and K. Skeff Neto, J. Appl. Phys. (in press)

6. P. W. Anderson, B. I. Halperim and C. M. Varma, Philos. Mag. 25, 1 (1972).

7. J. J. Perjean and J. Souletie, J. Phys. 41, 1335 (1980).

8. K. S. Gilroy and W. A. Phillips, Philos. Mag. B 43, 753 (1981)

9. M. A. Continentino, J. Phys. C 16, L71 (1983).

10. D. M. Herlach, E. F. Wassermann and R. Willnecker, Phys. Rev. Lett. 50, 529 (1983).

11. E. F. Wassermann and D. M. Herlach, J. Appl. Phys. 55, 1709 (1984).

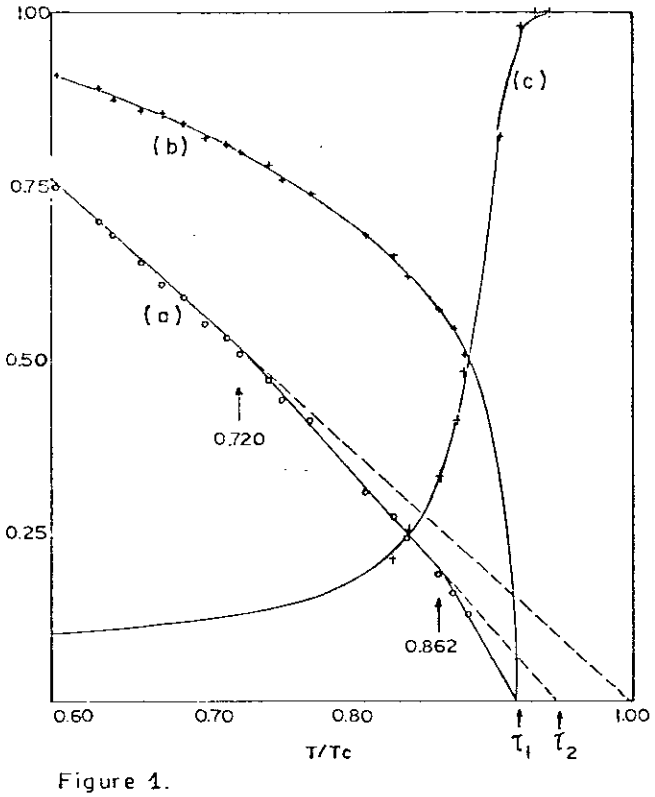

Figure 1.

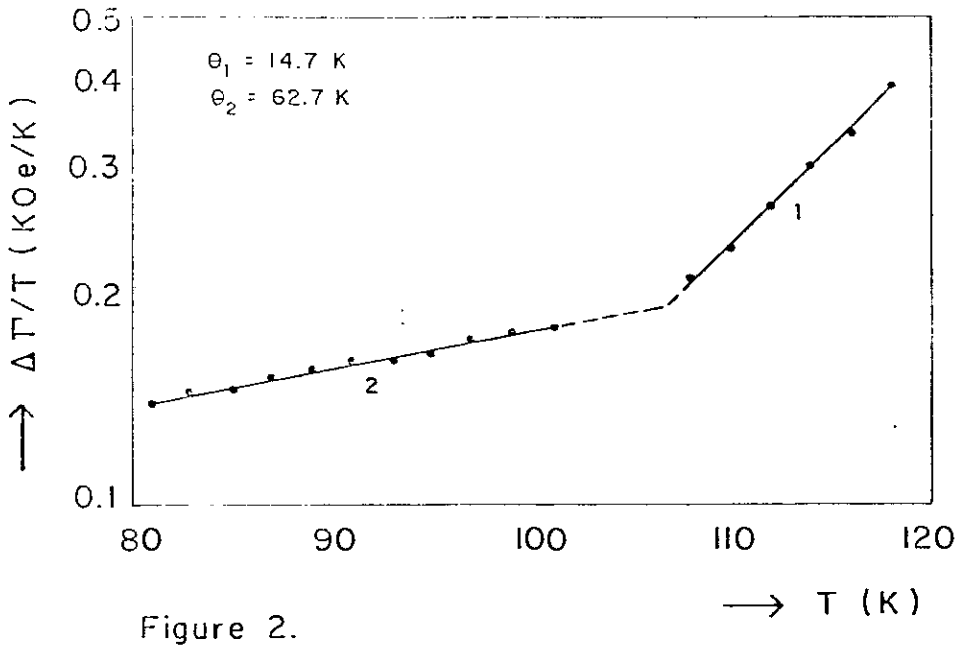
0.5
0.4
0.3
0.2
0.1
θ_1 = 14.7 K
θ_2 = 62.7 K
1
2
80
90
100
110
120
⟶ ΔT/T (KOe/K)
⟶ T (K)

Figure 2.

A N E X O D - 2

Experimental Evidence of a Multiphase Magnetic System in Fine Particles of Ferric Hydroxysulfate*

P. C. Morais and K. Skeff Neto
Grupo de Física Molecular e Magnetismo
Departamento de Física, Universidade de Brasília
70 910 - Brasília, DF - Brasil

* Work partially supported by CNPq

ABSTRACT

Magnetization data, obtained by a microvibrating sample magnetometer are presented. These data are obtained at different values of an external field applied to a sample which shows a bimodal particle-size distribution. The bendings in the M^3 X T plot are taken as an evidence of magnetic reorderings. These magnetic reorderings are discussed extensively.

PACS Number: 75.60 - d, 75.60. Jp, 75.50. Kj

I - INTRODUCTION

The theoretical and practical interest in the physical properties of non-crystalline solids has been increased mainly due to the fact that their properties can change profoundly when such materials are subjected to different treatments (thermal, magnetic, electric, mechanical, etc). By using X-ray[1,2] and neutron diffraction[3-5] techniques many of the observed changes can be correlated with the atomic and the magnetic rearrangements normally associated with order-disorder processes. Among the different types of physical behavior the magnetic properties has been found to be one of the most sensitive to order-disorder. Mainly to the fact that a non-crystalline solid does not exhibit a simple magnetic configuration when there is more than one strong interaction, particularly if the interactions make conflicting demands on the orientation of the different atomic moments. Indeed, this is thought to be the basic reason for the existence of multiphase magnetic systems in many important materials[6].

In the present work we report magnetization measurements in a system composed by a bimodal particle-size distribution of ferric hydroxysulfate. The experimental data were taken at different external fields (H_{ext}) from 80 K to 230 K. We have used a microvibrating sample magnetometer (MVSM) which will be described briefly. Finally, we compare the data obtained using the MVSM with previously obtained data from Mössbauer spectroscopy[7-9] (zero field) and electron paramagnetic resonance[10] (X-band).

II - EXPERIMENTAL DETAILS

Recently we developed a simple microvibrating sample magnetometer particularly inexpensive, sensitive and versatile[11]. Here, the MVSM was used in the transverse geometry, suitable for temperature variation measurements. In Fig. 1 we show a detailed diagram of the MVSM coupled to a variable temperature system. The underlying principle of the MVSM is the application of an alternating (low frequency) magnetic field superposed to a steady uniform magnetic field (H_{ext}). Then a sinusoidal force $\vec{F} = (\vec{M} \cdot \vec{\nabla}) \vec{H}_{eff}$ is applied on the sample by the alternating field. Here $\vec{H}_{eff}$ is the effective field acting on the sample and $\vec{M}$ is its magnetization this force is applied to a damped resonant elastic membrane in which the sample is attached. The resulting mechanical vibration cause a pressure fluctuation inside a closed gas cell, which is detected by a sensitive microphone as an acoustic signal. We take the magnezation of the sample as proportional to the acoustic signal. In Fig. 2 we show the body of the MVSM.

III - RESULTS AND DISCUSSIONS

The used sample has a bimodal particle-size distribution whith diameters centered around $D_1 = 50$ Å and $D_2 = 110$ Å. The magnetic behavior of this sample has also been studied by Mössbauer spectroscopy at zero external field[9]. The Mössbauer data show the presence of a magnetic ordered phase below $T \simeq 121$ K. Furthermore, those data show a quadrupole doublet coexisting with an asymmetrically broader Zeeman pattern in the range $106\ K \lesssim T \lesssim 121\ K$. This fact has been taken as an evidence of the superparamagnetic behavior of

the system. We proposed a phenomenological approach to explain the zero-field magnetization taking into account the magnetic disorder introduced by the presence of a bimodal particle-size distribution with superparamagnetic ordering. The model is based on a molecular-field approximation for randomly dilute magnets. Basically, the model assumes a temperature dependence for the density of magnetically ordered atoms m(T). Experimentally m(T) is related to the intensity of Mössbauer paramagnetic lines. From this approach it was possible to derive a distribution of critical temperatures $P(T) = dm(T)/dT$ (see ref. 9). This temperature distribution shows two distinct peaks at T_{01} = (118.46 ± 0.01) K and T_{02} = (120.96 ± 0.01) K. The T_{01} value was related to the first component of the assembly (D_1 = 50 Å) and T_{02} to the second component (D_2 = 110 Å).

However, a deeper insight of the magnetic phases which appear in our system comes out from magnetization measurements performed at non-zero external field. The circles in Fig. 3 summarize the temperature (T) dependence of the magnetization (M) obtained by the MVSM. In this figure the presence of two distinct keaks at 125 K and 165 K has been taken as an experimental evidence of a multiphase magnetic system. Also, a similar behavior has been taken as an evidence for the existence of short-range and long-range magnetic ordering coexisting in the material through a thermodynamic equilibrium[12,13]. Furthermore, as it is well know, the high temperature region (here T > 165 K) corresponds to a phase with long-range magnetic order, while the low temperature region (T < 165 K) corresponds to magnetic phases with short-range order. By assuming that the critical exponent is 1/3 in the overall range of

temperature, irrespective of the magnetic interaction (long- or short-range) we shall be able to make a more detailed analysis of the experimental data showed in Fig. 3. In Fig. 4 we show the temperature dependence of the third-power of the magnetization. At this point we shall assume that; either the presence of a change in the slope or the presence of an apparent discontinuity in the experimental values of the M^3 x T plot or both, may be taken as an evidence of a magnetic ordering change. These changes appear in Fig. 4 and we shall use them to discuss the nature of the magnetic interactions in our sample.

From previous[7-9] (Mössbauer) and present (magnetization) experimental data it has become evident that our sample shows an essentially ferrimagnetic order below 105 K (BB' line in Fig. 4), in the presence of an external field, 10 KG $\leq H_{ext} \leq$ 18 KG. By looking at the first straight line (T < 105 K) in Fig. 4 we conclude that the magnetization of the system would fall to zero at the same temperature (T_c = 325 K), independent of the value of the external field used here. This fact suggests that the system would present a continuous magnetic phase transition from a ferrimagnetic to an antiferromagnetic state through a spin rearrangement process in such a way that above T_c = 325 K the system would present an essentially pure antiferromagnetic ordering. Experimental evidence of exchange coupled ferri-antiferromagnetic systems has been pointed out by several authors in the last twenty years[14]. In reality the magnetic behavior of our system does not follow from the above described model. When the temperature reachs T = 105 K the system decides to follow another way. To explain the actual magnetic behavior displaied in Fig. 4 we shall

make the following assumptions. First, the topographic characteristic of the system (a bimodal assembly) does not enable the existence of a long-range magnetic order above a given temperature. This temperature must be related to the topographic characteristics of the system. Second, inside each component of the assembly it is possible to coexist two magnetic phases above a given temperature through a thermodynamic equilibrium. Here, these phases are assumed to be ferri and antiferromagnetic. The temperature above which the ferri/antiferro equilibrium is turned on will be refered as the activation temperature (T_A). Experimentally the activation temperature is nearly field independent in the range of our experiment (10 KG $\leq H_{ext} \leq$ 18 KG). This is physically reasonable since the internal field (H_{int}) obtained by Mössbauer spectroscopy is of the order of 400 K Oe, for our sample. Then, we shall expect that in our experiment the external field introduce little variation on T_A ($H_{ext}/H_{int} \simeq 0.05$). On the other hand, we shall expect a most provable temperature activation related to each component of the bimodal assembly. Then, we expect two distinct values of T_A (T_A^i, $i = 1, 2$) for our system, namely, T_A^1 ($D_1 = 50$ Å) and T_A^2 ($D_2 = 110$ Å). Furthermore, the above described thermodynamic equilibrium appear to be sensible to both external field and temperature in such a way that the equilibrium is reachs when the free energy of the system is minimized. Third, we assume that each component of the assembly goes to an essentially superparamagnetic state above a certain temperature T_B^i (where $T_B^i > T_A^i$). According to Candela and Haines[15] T_B is called the blocking temperature and corresponds to the temperature where the relaxation time of a particle is of the order of 10^2 seg. Again, as a consequence of the topographic characteristic

of our system we shall expect a most provable blocking temperature related to each component of the assembly. Naturally, according to the relaxation model for fine particles we shall expect a linear dependence between T_B and H_{ext}[16,17].

Taking into account the above assumptions we shal be able to discuss the actual magnetic behavior displaied in Fig. 4. The magnetic order of the system below 105 K is essentially ferrimagnetic. The ferri/antiferro equilibrium in the first component of the assembly (D_1 = 50 Å) is turned on near 105 K. In reality the activation temperature related to the first component of the assembly occurs at T_A^1 = 111 K. This will be make clear from the data showed in Fig. 6. This explain the bending of the M^3 x T plot above 105 K. Therefore, the fall in the magnetization of the system, above 105 K, is due to the decreases of the effective magnetic moment of the particles that from the first component of the assembly. For the second assembly component (D_2 = 110 Å) the ferri/ antiferro equilibrium is turned on at T_A^2 = 165 K. Again, we shall see this from Fig. 6. This fact explain the fall in the M^3 x T plot above T_A^2. To understand the relationship between the values of T_A^i (i = 1, 2) we look at the Mössbauer data already published[9]. These data show that the magnetic ordering inside the particles that form the second assembly component is higher than the magnetic ordering inside the particles that forms the first. Therefore, according to Luborsky[18,19] our system has a particles-size distribution below its critical diameter. Then, we can use two mean values J^i (i = 1, 2) to describe the exchange energy inside the particles related to each component of the bimodal assembly ($J^2 > J^1$). From this analysis, it seems physically reasonable to suppose that the activation energy ($k T_A^i$) must be porportional to J^i. Within

this approach we shall expect that the ratio T_A^1/T_A^2 will be of the order of J^1/J^2. Also a first approximation for J^1/J^2 comes out from the behavior of the experimental data presented in ref. 18 in which fine particles of $CoFe_2O_4$, Co and Fe shows a simple relationship between the internal field (H_{int}) and the diameter of the particles, below the critical point ($D < D_{cr.}$). The internal field goes approximately as the square root of the diameter (for $D < D_{cr.}$). If we assume that the internal field is proportional to the exchange energy we must have

$$J^1/J^2 \simeq (D_1/D_2)^{1/2} \quad . \tag{1}$$

Using the above presented data we have $T_A^1/T_A^2 = 0.673$ which is in a good accordance with the ratio $J^1/J^2 = (D_1/D_2)^{1/2} = 0.674$.

The bending in the M^3 vs. T plot along the line AA' and above 12 KG may be explained considering the ferri/antiferro equilibrium inside the particles which form the first component of the assembly. At temperatures above the BB' line the antiferromagnetic phase grows at the expense of the ferrimagnetic phase and consequently the magnetization of the sample falls. However, at temperatures above the AA' line (for $H_{ext} > 12$ KG) this equilibrium is reversed, i.e., the ferrimagnetic phase is recovered at the expense of the antiferromagnetic phase and consequently the magnetization is partially recovered. An evidence that this process occurs via a thermodynamic equilibrium may be observed by looking at the relationship between temperature and external field along the AA' line (above 12 KG). If one increases the external field the temperature related to the intersection of the slopes shift to higher values. This may be seen as a consequence of a general behavior of systems in thermodynamic equilibrium where H_{ext} works out as an external agent.

At temperatures above the CC' line (see Fig. 4) we assume that the first component of the assembly goes to an essentially superparamagnetic state. Then, according to our third assumption the points over the CC' line show the expected behavior between H_{ext} and T_B^1. The relationship between those parameters comes from the relaxation time for fine particles, described by[16]

$$\tau = \tau_o \exp\left(\frac{KV}{kT} + \frac{\alpha\mu^2/D^3}{kT} + \beta\frac{\mu H_{ext}}{kT}\right) , \qquad (2)$$

where K, V, μ, D, α and β are the magnetocrystalline anisotropy, the volume, the magnetic moment, the diameter and geometric factors associated to the particle, respectively. If one uses the blocking temperature concept ($T = T_B$ if $\tau \simeq 10^2$ seg) assuming that τ_o is of the order of 10^{-9} seg, we have

$$25\ k\ T_B \simeq K\ V + \frac{\alpha\mu^2}{D^3} + \beta\mu H_{ext}. \qquad (3)$$

Suzdalev et al.[16,17] compare the magnetic dipole interaction ($\alpha\mu^2/D^3$) and the anisotropy energy (KV) for fine particles of iron. They assume in their calculations that $KV \simeq \alpha\mu^2/D^3$ at high temperatures i.e., when the particles goes to a superparamagnetic state. Then Eq. 3 reduces to

$$25\ k\ T_B \simeq 2\ KV + \beta\mu H_{ext}. \qquad (4)$$

Assuming that the most provable values for the blocking temperatures (T_B^1) occurs along the CC' line we can use Eq. 4 to fit the experimental values $T_B^1 \times H_{ext}$. From this fitting we obtain the following mean values, $\mu^1 = 1.01 \times 10^3\ \mu_B$, $T_B^1\ (H_{ext} = 0) = 117.5$ K and $K^1 = 3{,}1 \times 10^5$ J/m^3. We used $\beta = 0.1$, i.e., the same value used by Suzdalev et al. (refs. 16,17) for fine particles of iron.

Note that the T_B^1 ($H_{ext} = 0$) value is approximately equal to the most provable critical temperature (T_{01}) related to the first component, and obtained by Mössbauer data (ref. 9). Then, we shall identify T_{01} and T_{02} as T_B^1 and T_B^2 respectively. We observe that a similar analysis of $T_B \times H_{ext}$ for the second component of the assembly can not be made taking into account only the presented data. The reason for this comes from the fact that B5.4% of the iron atoms appear inside the particles of the first component of the assembly. Therefore, the macroscopic magnetic behavior of the system is dominated by the magnetic behavior of the first component. However from the adjusted values of T_{01} and T_{02} we can estimate K^1 and K^2. This is made by using Eq. 4 at $H_{ext} = 0$. The values are $K^1 = 3.13 \times 10^5$ J/m^3 and $K^2 = 3.00 \times 10^5$ J/m^3. From the adjusted value of $\mu_1 = 1.01 \times 10^3\ \mu_B$ we can estimate the μ_2 since $\mu_1/\mu_2 \cong J^1/J^2$, i.e., $\mu_2 \simeq 1.50 \times 10^3\ \mu_B$.

The experimental evidence for the essentially pure superparamagnet behavior of a given system comes out from the superposition of the M vs. H_{ext}/T plot at different temperatures. From Fig. 5 we see that this behavior occurs at temperatures well above 159 K. To be more precise the system as a whole goes to a pure superparamagnetic state at temperatures above $T_{SPM} = 186$ K, i.e., at temperatures above the EE' line (cf. Fig. 4). Above this temperature (T_{SPM}) the $M/(H_{ext}/T) \times T$ plot becomes constant. In Fig. 6 we show the behavior of $\phi = M/(H_{ext}/T)$ as a function of temperature. We note two distinct regions; one of high magnetic order (above T_{SPM}) and the other with low magnetic order (below T_{SPM}). We expect that the data presented in Fig. 6, i.e., $\phi \times T$ must be nearly field independent. Then, the activaction temperatures T_A^i as well as the superparamagnetic temperature of the system come

from inflection points (T_A^1 and T_{SPM}) and from an apparent discontinuity (T_A^2). We want to call attention at the point T_Θ = 63 K in Fig. 6 that represents the interesection of two straight lines, both in the region of low magnetic order. Recently, the T_Θ = 63 K point has been interpreted as the temperature above which the magnetic moment of the particles works out as a system relaxation channel. This fact has been used to explain the Mössbauer linewidth broadening at zero field[20].

Finally, we note that the acutal phase transition temperature of the system (τ_c) tends to T_c = 325 K as the H_{ext} goes to zero. This behavior is showed in the inset of Fig. 4. The τ_c values were obtained by extrapolation of the last straight line in Fig. 4, i.e., above T_{SPM} for various values of external field.

IV - CONCLUSIONS

The anlysis of the magnetization via a M^3 vs. T plot becomes particularly interesting when one is dealing with assembly of magnetically ordered fine particles subjected to a variable external field. In our case there exist an activation temperature (T_A). At T_A a given particle decides to change its magnetic ordering via a thermodynamics equilibrium. Lossly speaking we can say that an antiferromagnetic phase percolate through a ferrimagnetic phase. The same particle decides at a different temperature to show a superparamagnetic ordering. This temperature is known as the blocking temperature (T_B). Also in a sample which shows a multimodal particle-seze distribution one must expect a multimodal distribuition of caracteristic temperature (T_A, T_B). The magnetic reordering related to both T_A or T_B are correlated to the presence of bendings and discontinuities or both in the M^3 x T plot at a given external field. In Fig. 7 we whow a phase diatram obtained from the

magnetization measurements. Finally, it is possible to gain a deeper understanding about the fine particles magnetic ordering by correlating the characteristic temperature (T_A^i and T_B^i) with more fundamental physical parameters. In fact, our present analysis suggests that the exchange energy appears to be very sensible to the dimensions of the clusters in the limit where they behave as single entities.

FIGURE CAPTIONS

FIG. 1 - Block diagram of the MVSM and temperature variable syste. (1) elastic membranes, (2) teflon ring, (3) acoustic chamber, (4) duct for pressure adjust, (5) microphone, (6) pre-amplifier, (7) lock-in amplifier, (8) milivoltmeter, (9) temperature control, (10) signal generator and audio amplifier, (11) modulation coils, (12) heater, (13) sample, (14) copper wall, (15) electrical connection, (16) dewar, (17) teflon connection, (18) stainless-ste l wall, (19) acrylic rod, (20) temperature sensor (sample), (21) gas flux, (22) magnetometer body.

FIG. 2 - Microvibrating sample magnetometer.

FIG. 3 - Temperature dependence of the magnetization for a bimodal particle-size distribution of $FeOHSO_4$ (D_1 = 50 Å) and D_2 = 110 Å).

FIG. 4 - Temperature dependence of the third power of the magnetization. The data are the same of Fig. 3.

FIG. 5 - $M \times H_{ext}/T$ curve obtained from the data presented in Fig. 3.

FIG. 6 - $\phi = M/(H_{ext}/T)$ vs. T curve obtained from magnetization data (Fig. 3). The regions of low magnetic order (L.O.) and high magnetic order (H.O.) are presented.

FIG: 7 - Phase diagram obtained for the $FeOHSO_4$ sample discussed here. (1) and (2) represent the first (D_1 = 50 Å) and second (D_2 = 110 Å) components of the assembly. F, A, S and P are ferri-, antiferro-, and paramagnetic ordering, respectively.

REFERENCES

1. G. S. Cargill III, J. Appl. Phys. 41, 12 (1970).

2. B. C. Giessen and C. N. J. Wagner, "Structure and Properties of Non-Crystalline Metallic Alloys Produced by Rapid Quenching of Liquid Alloys", in "Physics and Chemistry of Liquid Metals", S. Beer, Ed., Marcel Dekker, New York (1972).

3. R. A. Cowley and W. J. L. Buyers, Rev. Mod. Phys. 44, 406 (1972).

4. J. W. Cable, Phys. Rev. B15, 3477 (1977).

5. W. Y. Ching and D. L. Huber, Phys. Rev. B26, 6164 (1982).

6. D. W. Carnegie, Jr. and H. Claus, Phys. Rev. B30, 407 (1984).

7. K. Skeff Neto and L. C. M. Miranda, Solid State Commun. 28, 43 (1978).

8. K. Skeff Neto, I. C. Cunha Lima, N. S. Almeida and L. C. M. Miranda, J. Phys. C11, L 695 (1978).

9. P. C. Morais and K. Skeff Neto, J. Appl. Phys. 54, 307 (1983).

10. P. C. Morais, A. L. Tronconi and K. Skeff Neto, J. Appl. Phys. 55, 2310 (1984).

11. P. C. Morais, N. M. L. Köche, A. L. Tronconi and K. Skeff Neto, Rev. Sci. Instrum. - (in press).

12. R. Hahn and E. Kneller, Z. Metallk. 49, 426 (1958).

13. M. J. Marcinkowski and N. Brown, J. Appl. Phys. 32, 375 (1961).

14. W. H. Meiklejohn, J. Appl. Phys. 33, 1328 S (1962).

15. G. A. Candela and R. A. Haines, Appl. Phys. Lett. 34, 868 (1979).

16. A. P. Amulyavichus and I. P. Suzdalev, Sov. Phys. JETP 37, 859 (1973).

17. Yu. F. Krupyanski and I. P. Suzdalev, Sov. Phys. JETP 38, 859 (1973).

18. F. E. Luborsky, J. Appl. Phys. 32, 171S (1961); 33, 1909 (1962).

19. E. F. Kneller and F. E. Luborsky, J. Appl. Phys. 34, 656 (1963).

20. P. C. Morais, A. L. Tronconi and K. Skeff Neto, J. Appl. Phys. (in press).

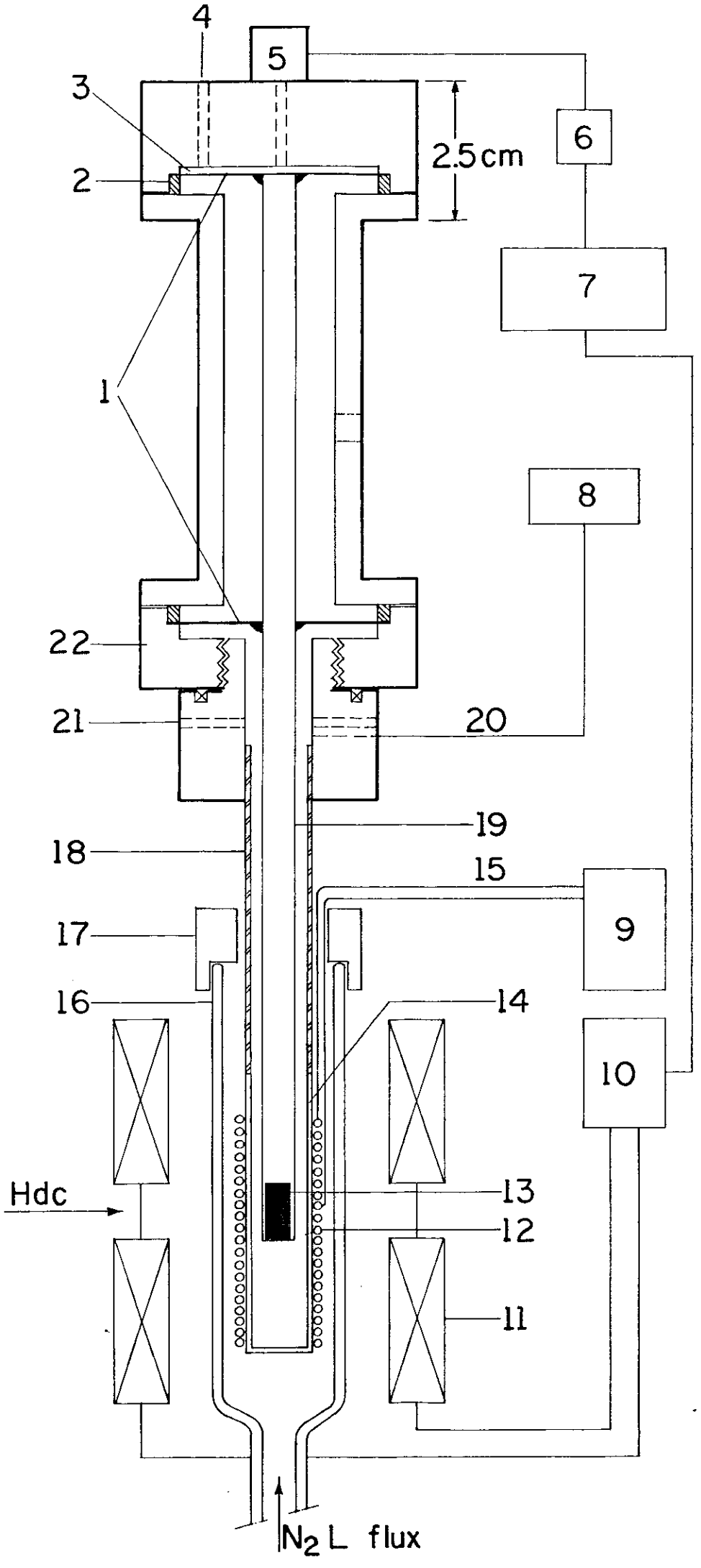

IG. 1

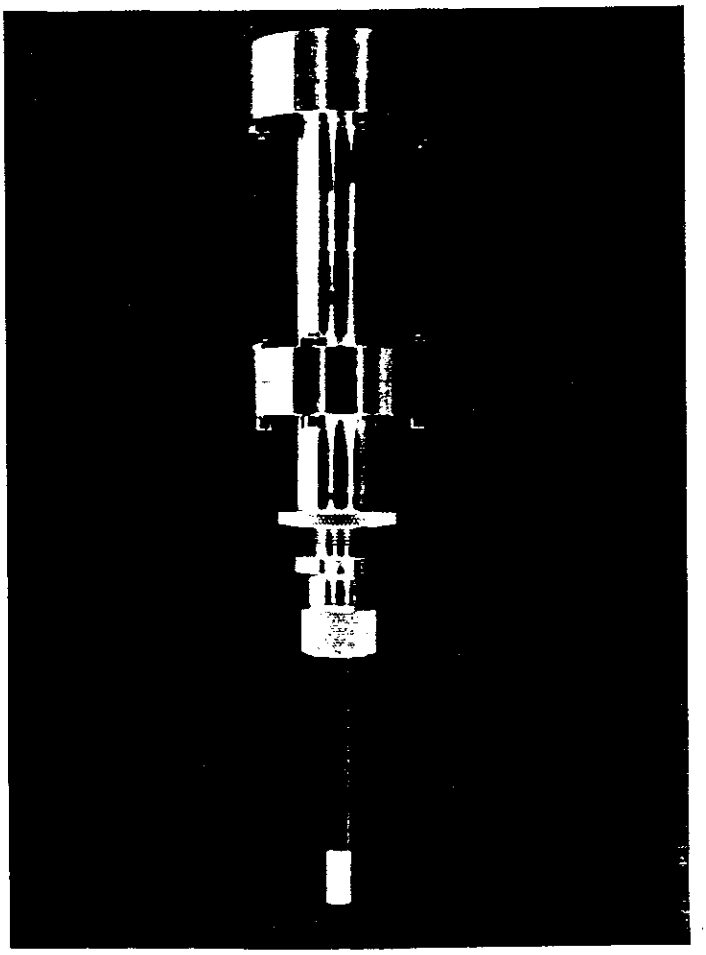

FIG. 2

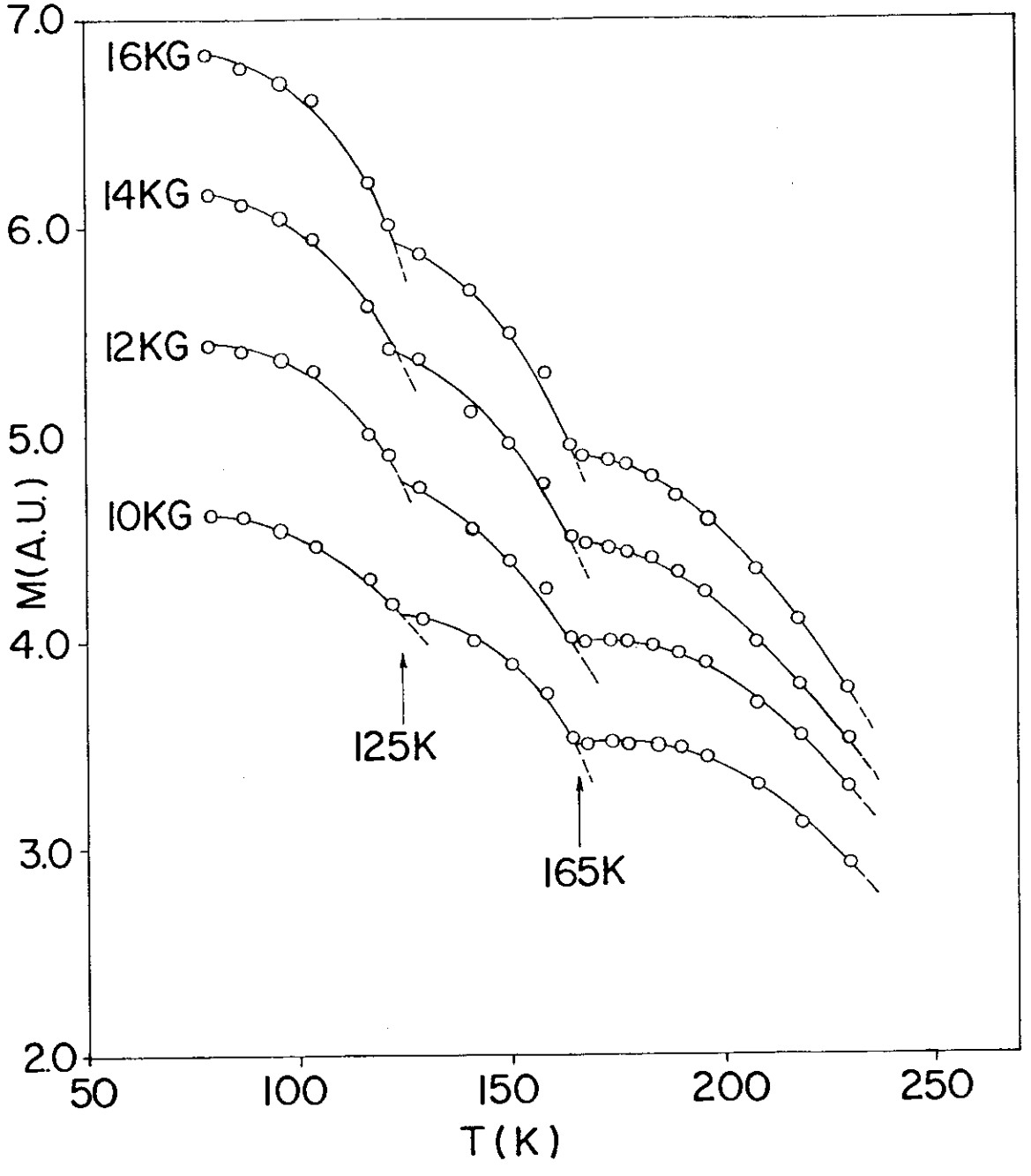
7.0
6.0
5.0
4.0
3.0
2.0
M(A.U.)
16KG
14KG
12KG
10KG
125K
165K
50
100
150
200
250
T(K)

FIG. 3

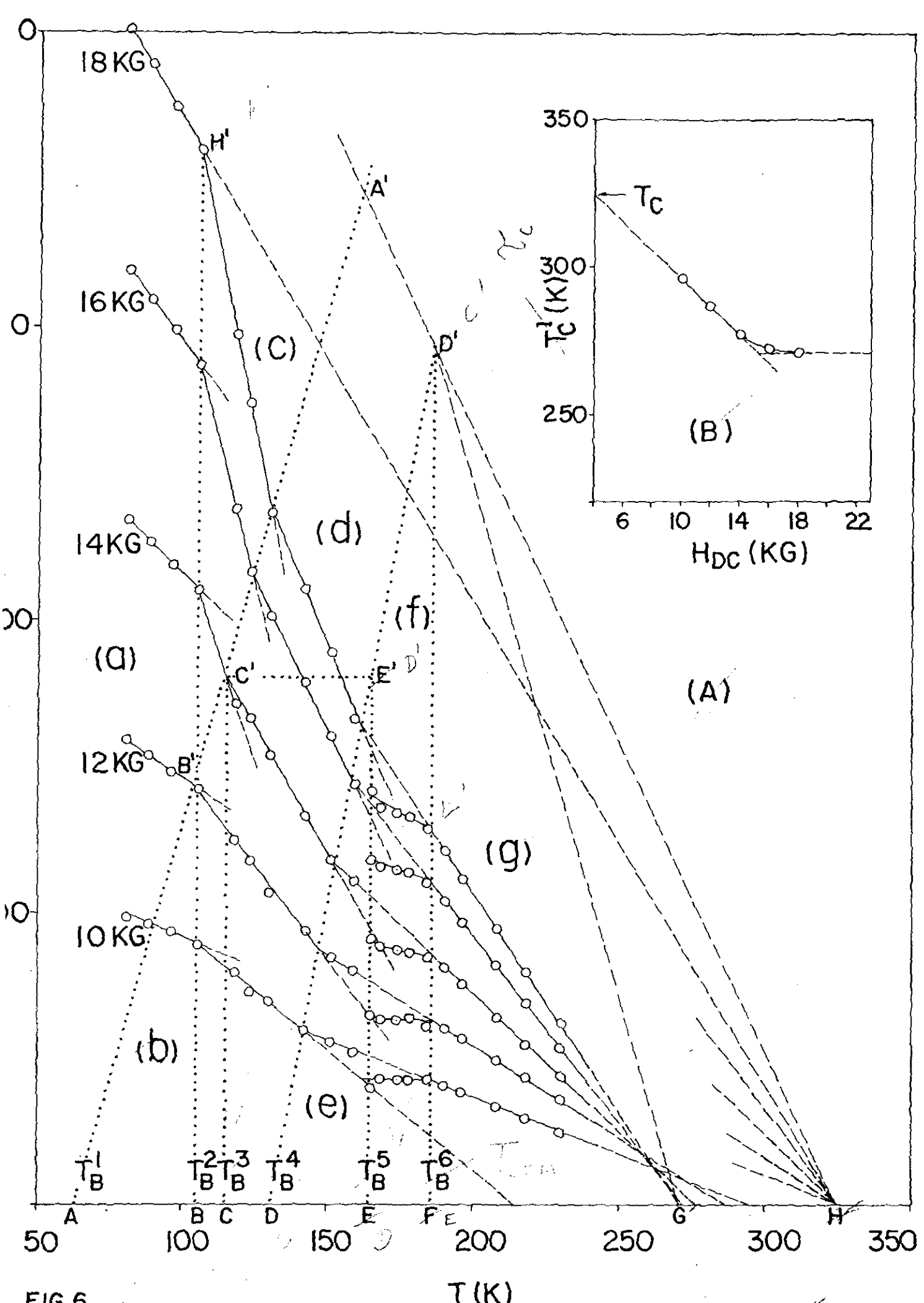
18KG
16KG
14KG
12KG
10KG
H'
A'
D'
C'
E'
B'
(A)
(B)
(C)
(D)
(E)
(F)
(G)
(a)
(b)
T_C
T_C' (K)
H_{DC} (KG)
T_B^1 T_B^2 T_B^3 T_B^4 T_B^5 T_B^6
A B C D E F G H
T (K)

FIG. 6

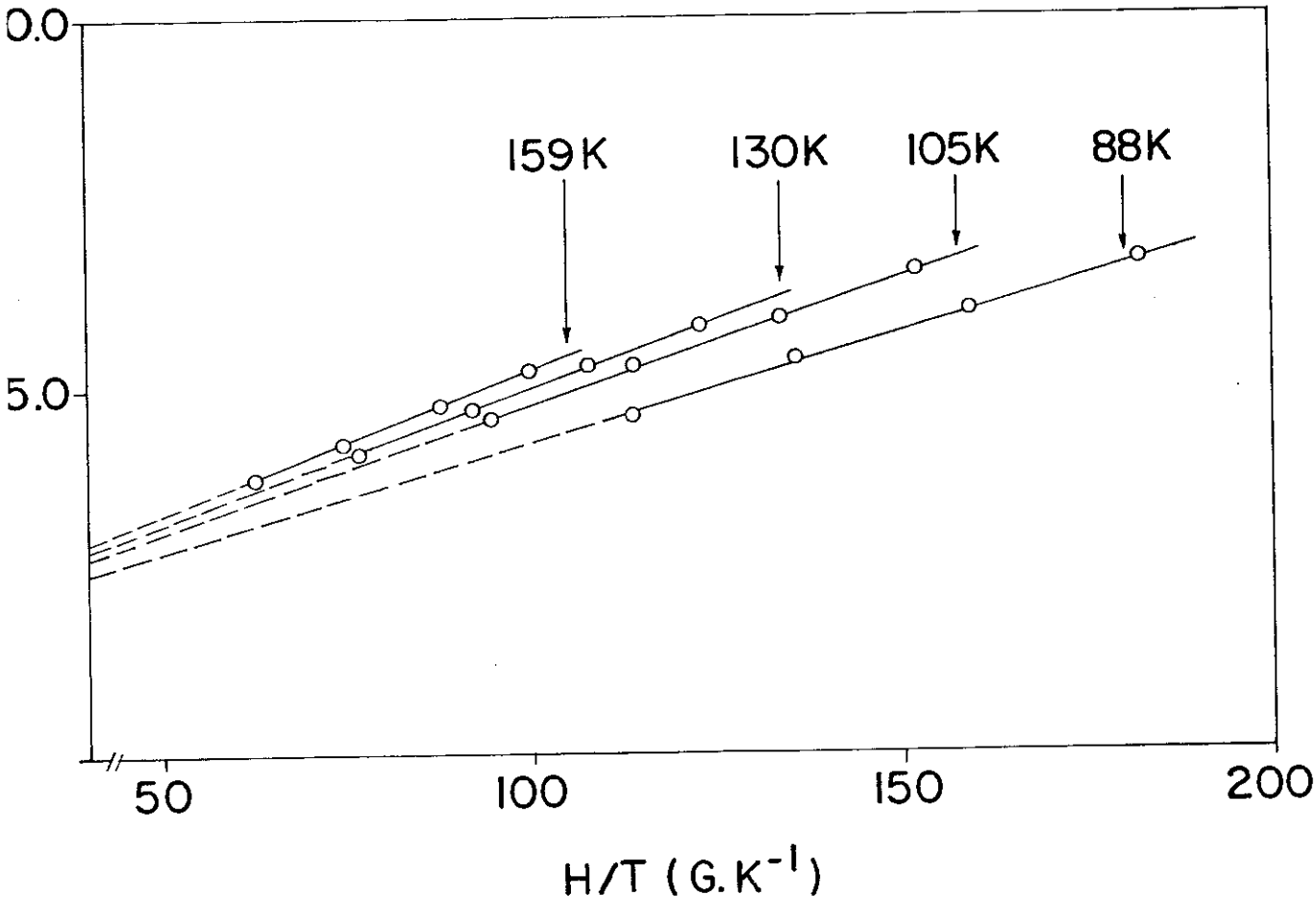

FIG. 5

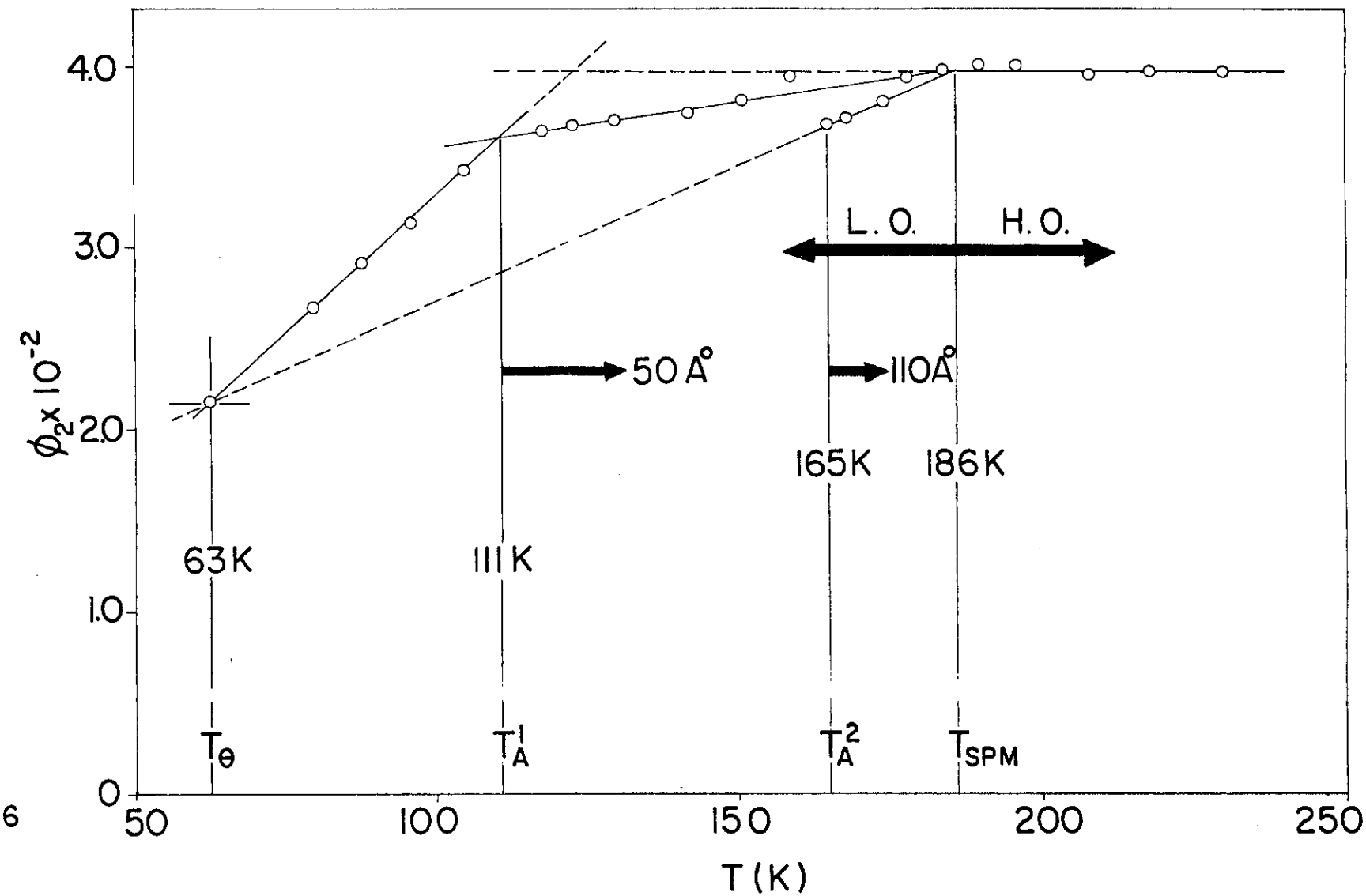
4.0
3.0
2.0
1.0
0
$\phi_2 \times 10^{-2}$
50
100
150
200
250
T(K)
L.O.
H.O.
50 A°
110A°
165K
186K
63K
111K
T_θ
T_A^1
T_A^2
T_{SPM}

FIG. 6

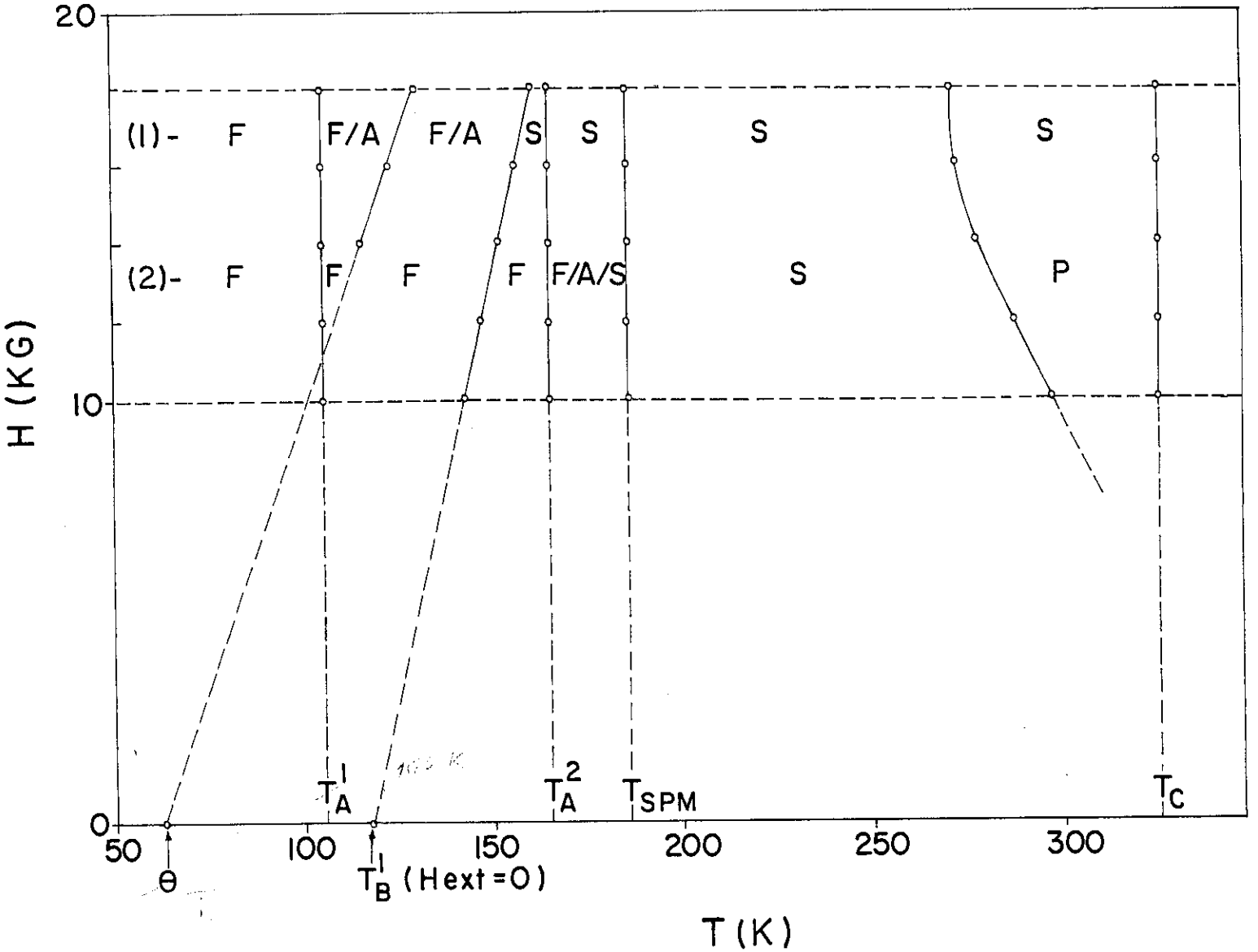
20
10
0
H (KG)
(1)- F F/A F/A S S S S
(2)- F F F F F/A/S S P
T_A^1
T_A^2
T_{SPM}
T_C
50
100
150
200
250
300
θ
T_B^1 (Hext=0)
T (K)

FIG. 7

A N E X O D - 3

HIGH TEMPERATURE BEHAVIOR OF ELECTRON SPIN RESONANCE LINEWIDTH IN FINE PARTICLES OF FERRIC HYDROXYSULFATE*.

M. C. L. Lara, N. M. L. Köche, P. C. Morais and K. Skeff Neto

Grupo de Física Molecular e Magnetismo

Departamento de Física, Universidade de Brasília

70 910 - Brasília, D.F. - Brasil

*Work partially supported by CNPq.

ABSTRACT

The temperature dependence of the electron spin resonance linewidth broadening ($\Delta\Gamma$) is analyzed. Bendings in the $\Delta\Gamma$ vs. T plot may be related to magnetic ordering changes. It is proposed that the freezing temperature, obtained by ESR measurements, must be taken as the one related to the range of temperatures where the sample behaves as a paramagnet.

Experimentally, a cusp in the susceptibility curve has been used as one of the simplest method to characterize the freezing temperature[1,2] (T_f). This is the temperature below that the system goes to a spin-glass state[3-12]. In the last years, electron spin resonance (ESR) experiments have been used to investigate such system[13-15]. This experiments are based on the fact that the ESR line broader and shift as the temperature is lowered towards T_f. Some theoretical work has been carry out to explain the exeperimental results. Particularly successful are the models in which is assumed an anisotropic type of interaction between the spins[16-18]. Based on such interactions it has been possible to explain both the ESR linewidth and lineshift without use of adjustable parameters.

Recently, we proposed a model to explain the ESR linewidth broadening ($\Delta\Gamma$) as a function of temperature[19]. The experimental available data show a strong temperature dependence only for the linewidth broadening. In fact, the experimental data related to the lineshift show a fluctuation around a constant value rather than a systematic behavior[20].

To describe the dynamics of such systems above T_f we used a geometric picture of a dilute ferromagnet consisting of an infinite cluster of spins with long range magnetic order coexisting with finite clusters of spins. We consider the low-energy excitations of the infinite ferromagnetic cluster as spin waves. Also, we treated the coupling of the spin waves to the finite clusters as a relaxation channel for the infinite cluster driven by the microwave field. Furthermore, we assumed that the relaxation process, above T_f, is dominated by a longitudinal mode and occurs

via an anisotropic Dzyaloshinsky-Moriya (DM) type of interaction between spins in the infinite cluster and the spins in the finite clusters. We want to point out that Gabay and Toulouse[21] find that the transverse part of the spin-glass order parameter disappears for $T > T_f$, while the longitudinal part remains. The Hamiltonian used to describes the proposed model is[19]

$$H = \sum_k \varepsilon_k \, a_k^+ \, a_k + \vec{D} \cdot \vec{\sigma} \times \vec{S} \, , \qquad (1)$$

where k, $\varepsilon_k = \Delta + D_o \, k^2$, D_o and Δ are the wavevector related to the low-energy excitations, the energy of the spin waves, the stiffness constant and a spin wave gap arising from anisotropic interactions between spins, respectively. The a_k^+, a_k are Holstein-Primakoff boson operators and the coupling $\vec{D}$ describes an effective anisotropic DM interaction between the spin $\vec{S}$ in the infinite cluster and the spins $\vec{\sigma}$ of the finite clusters. The effect of the spin wave - cluster interaction on the spin wave propagation can be described by a damping factor $\Omega(\omega)$ of these modes, where ω is the microwave frequency. The damping factor can be related to the imaginary part of the longitudinal susceptibility component $\chi(\omega)$ according to

$$\Omega(\omega) = \frac{8SN}{N_o} \, D^2 \, I_m\{\chi(\omega)\} \quad , \qquad (2)$$

where

$$\chi(\omega) = (1/4kT) \, \mathrm{sech}^2(E/2kT) \frac{1}{1 - i\omega\tau} \qquad (3)$$

In the formula above: N_o, N and $E = \omega_r \hbar$ are the number of spins

in the infinite cluster, the number of finite clusters and the Zeeman energy of the finite clusters in the local molecular field produced by the dilute ferromagnetic system, respectively. The longitudinal relaxation time (τ) for the spin-wave emission and absorption was taken as $\tau = \tau_o \exp(v/kT)\,\mathrm{sech}(E/2kT)$ and $D^2 = D_x^2 = D_y^2 = D_z^2$. Within such a model the dynamics of the system is described taking into account the presence of an asymmetric double-well potential with an asymmetry parameter E and a barrier heigth v.

Since we are dealing with materials which show a particle-size distribution it is physically reasonable to expect a distribution of energy splittings (E) and activation energies (v). To take into account the contribution of E into the ESR linewidth broadening we assumed a step function with value E_o for $0 \leq E \leq E_{max}$ and zero otherwise. For the energy barrier we assumed an exponential probability function $g(v) = (1/v_o)\exp(-v/v_o)$. The expressions above give directly the linewidth $\delta\Gamma = \Omega(\omega)/\hbar\gamma$, where γ is the gyromagnetic ratio. After averaging $\delta\Gamma$ over E and v we get for the experimental resonance linewidth broadening

$$\Delta\Gamma(T) = \frac{SN}{\hbar\gamma N_o}\,\frac{D^2}{v_o}\exp(-T/T_f), \qquad (4)$$

where $kT_f = v_o/|\ln \omega\tau_o|$.

In the present work we analyze the ESR linewidth in a sample of $FeOHSO_4$ which shows a bimodal particle-size distribution with diameters centered around two mean values $d_1 = 50$ Å and $d_2 = 110$ Å. The ESR line is asymmetrically broader and this

asymmetry increases with the temperature. Then, the ESR profiles is analyzed in connection with the topographic characteristic of the system. This is made by using the following model

$$P(H) = \begin{cases} A\left[(H - H_o)^2 + (\Gamma_1/2)^2\right]^{-1}; & \text{for } 0 < H \leq H_o \quad (5a) \\ B\left[(H - H_o)^2 + (\Gamma_2/2)^2\right]^{-1}; & \text{for } H > H_o \quad (5b) \end{cases}$$

where the normalization constant is determined by requiring continuity of $P(H)$ at $H = H_o$ and the condition

$$\int_o^\infty dH\, P(H) = 1 \quad . \qquad (6)$$

We assume that Γ_1 and Γ_2 ($\Gamma_1 \geq \Gamma_2$) are related to d_1 and d_2, respectively. There are two reasons for this assumption. First, the width of the distribution of the first component of the bimodal assembly ($d_1 = 50$ Å) is higher than the second one ($d_2 = 110$ Å). Second, the internal magnetic field inside of the particles which compose the first component is lower than the second one. These facts are discussed in a previous work (cf. ref. 22). The experimental linewidth is given by $\Delta\Gamma_i = \Gamma_i - \Gamma_o$ ($i = 1, 2$), where Γ_o is the linewidth near $T_c = 325$ K.

In Fig. 1 we present the temperature dependence of the linewidth broadening $\Delta\Gamma_i$ ($i = 1, 2$). Note that both $\Delta\Gamma_1$ and $\Delta\Gamma_2$ vs. T goes by straigth lines, in a semilog plot, i.e., they are fitted by Eq. 4. Furthermore observe that below $T = 145$ K the $\Delta\Gamma_1 \times T$ curve coincides with the $\Delta\Gamma_2 \times T$ one and above $T = 145$ K this coincidence does not occurs. This behavior may be understood at the

light of some recent results. From Mössbauer and magnetization measurements we can conclude that our sample behaves as a multiphase magnetic system when one goes from N_2L to the room temperature[23]. In the presence of an external field between 12 KG and 18 KG the sample shows an essentially ferrimagnetic order below 111 K. Between 111 K and 186 K the system shows a complex mixed magnetic phase (ferrimagnetic, antiferromagnetic and superparamagnetic). Above 186 K the system goes to an essentially superparamagnetic state and the magnetization goes to zero near 300 K for external field below 10 KG. Taking into account these facts we can conclude that below 145 K (see Fig. 1) the ESR measurements does not distinguish between the two components of the assembly. At this point we argue that in this first region ($T \leq 145$ K) the density of paramagnetic centers is so low that it is not possible to them to feel the topographic characteristic of the system, i.e., there exist a low concentration of paramagnetic centers in the surface of the particles. However, the density of paramagnetic centers increases with the temperature. Then, between 145 K and 213 K (see Fig. 1) the density of paramagnetic centers reachs a level in which it is possible to distinguish between the centers located in the surface of the particles forming each component of the assembly. Consequently, the $\Delta\Gamma_1$ vs. T curve does not coincide with the $\Delta\Gamma_2$ vs. T one. This range of temperature is characterized by a mixed magnetic phase. Finally, above 213 K the system is essentially in a superparamagnetic state and the density of paramagnetic centers is near from its saturation point, i.e., near $T_c = 325$ K. Now, the density of paramagnetic centers in the surface of the particles is sufficently high to distinguish the topographic caracteristic of system.

This density can by taken as porportional to the ESR area travessed. In fig. 2 we show the temperature dependence of the normalized area, i.e., the area normalized to its value at T_c = 325 K. The normalized area (Fig. 2), as well as, the linewidth broadening go approximately by straighth lines. From this behavior one can introduce the variable $\phi = \Delta A^*/\Delta T$, where A^* is the normalized area. Then, the system goes to a paramagnetic state when ϕ goes to zero. If one plots the T_f values obtained from Fig. 1 against the corresponding ϕ values obtained from Fig. 2 we obtain the linear relationship showed in the inset of Fig. 2.

In the present work we propose that the freezing temperature obtained by ESR measurements, by using an expression similar to the Eq. 4, must be taken as the one related to the range of temperatures where the system behaves as a paramagnet. Then, the corresponding T_f^i values are those characterized by $\phi \to 0$ (see the inset of Fig. 2). They are T_f^1 = 94 K and T_f^2 = 63 K for the particles with meam diameters centered around d_1 = 50 Å and d_2 = 110 Å, respectively. A first argument in favor of our proposal comes from recent experiments performed ou Ag Mn (2.6% Mn)[24]. The experimental data has been discussed based on the assumption that for $T > T_f$ the spin-glass shows the same macroscopic symmetry as a paramagnet, i.e., the susceptibility follows a Curie rather than a Curie-Weiss law. Also, the freezing temperature of the pseudobrookite recently determined by ESR measurements (near T_c) agrees with the T_f value determined by the susceptibility cusp, within the experimental error (see ref. 25). A third observation is related to Mössbauer measurements performed at zero external field. If one takes the temperature dependence of the third-power

of the normalized internal field one determines a bending in the $[H_{int}(T)/H_{int}(0)]$ x T curve at T = 94.8 K. Such bending is accompanied by the presence of a relaxed Mössbauer spectrum[22]. Finally, a recent analysis of the Mössbauer linewidth broadening (zero external field) shows the existence of a temperature (θ) above which the magnetic moment of the particles moves within an asymmetrical double-well potential. That motion behaves as a relaxation channel and the fitted temperature is θ = 62.7 K[26].

To conclude we observe that the bendings in the semilog $\Delta\Gamma$ x T plot (Fig. 1) may be related to magnetic ordering changes rather than experimental fluctuations of $\Delta\Gamma$ near T_c. In our case the magnetic ordering changes can be confirmed by magnetization and Mössbauer measurements. Similar behavior has been observed in several non-crystalline materials, where the experimental points systematically shift from the linear behavior at high temperatures in a semilog plot, i.e., at low values of $\Delta\Gamma$[13]. Finally we observe an approximate proportionality between T_f^i and the mean diameter (di)

$$T_f^i \propto (d_i)^{-1/2} \qquad (7)$$

In our case $T_f^2/T_f^1 = 0.670$ and $(d_1/d_2)^{1/2} = 0.674$. Then, the freezing temperature decreases as the magnetic ordering increases. A similar behavior is found in the amorphous $(Fe_x\ Ni_{1-x})_{75}\ P_{16}\ B_6\ Al_3$ where the freezing temperature decreases as the value of x is raised, i.e., when the magnetic ordering is increased[27].

FIGURE CAPTIONS

FIG. 1 - Temperature dependence of the ESR linewidth of a bimodal particle-size distribution of $FeOHSO_4$. $\Delta\Gamma_1$ and $\Delta\Gamma_2$ are related to the particles with diameters centered around d_1 = 50 Å and d_2 = 110 Å, respectively. The points are the experimental values and the full lines represent the best fit to the Eq. 4.

FIG. 2 - Temperature dependence of the normalized are ($A^* = A(T)/A(325\ K)$) of the ESR curves. The inset shows the relationship between T_f and $\phi = \Delta A^*/\Delta T$.

REFERENCES

1. R. R. Galazka, S. Nagata and P. H. Keesom, Phys. Rev. B22, 3344 (1980).

2. H. Atzmony, E. Gurewitz, M. Melamud, H. Pinto, H. Shaked, G. Gerodetsky, E. Hermon, R. M. Hornreich, S. Shtrikman and B. Wanklyn, Phys. Rev. Lett. 43, 782 (1979).

3. J. P. Jamet and A. P. Malozemoff, Phys. Rev. B18, 75 (1978).

4. M. B. Salamon and R. M. Herman, Phys. Rev. Lett. 41, 1506 (1978).

5. E. D. Dahlberg, M. Hardiman, R. Orbach and J. Souletic, Phys. Rev. Lett. 42, 401 (1979).

6. D. W. Forester, N. C. Koon, J. H. Schelleng and J. J. Rhyne, J. Appl. Phys. 50, 7336 (1979).

7. B. V. B. Sarkissian, J. Phys. F 11, 2191 (1981).

8. Y. Yeshurun, M. B. Salamon and K. V. Rao, Phys. Rev. B24, 1536 (1981).

9. J. W. Lynn, R. W. Erwin, J. J. Rhyne and H. S. Chen,, J. Appl. Phys. 52, 1738 (1981).

10. D. G. Onn, J. Appl. Phys. 52, 1788 (1981).

11. V. Manns, R. A. Brand, W. Kenne and R. Marx, Solid State Commun. 48, 811 (1983).

12. M. Rots, L. Hermans and J. Van Cauteren, Solid State Commun. 49, 131 (1984).

13. S. M. Bhagat, M. L. Spano and J. N. Lloyd, Solid State Commun. 38, 261 (1981).

14. S. B. Oseroff, Phys. Rev. B25, 6584 (1982).

15. A. Manoogian, B. W. Chan, R. Brun del Re, T. Donofrio and J. C. Wooley, J. Appl. Phys. 53, 8934 (1982).

16. M. A. Continentino, J. Phys. C 16, L71 (1983)

17. P. M. Levy, C. Morgan-Pond and R. Raghavan, Phys. Rev. Lett. 50, 1160 (1983).

18. W. M. Saslow, Phys. Rev. B30, 461 (1984).

19. P. C. Morias, A. L. Tronconi and K. Skeff Neto, J. Appl. Phys. 55, 3744 (1984).

20.

21. M. Gabay and G. Toulouse, Phys. Rev. Lett. 47, 201 (1981).

22. P. C. Morais and K. Skeff Neto, J. Appl. Phys. 54, 307 (1983).

23. P. C. Morais and K. Skeff Neto, J. Appl. Phys. (submited).

24.

25. N. M. L. Köche, P. C. Morais and K. Skeff Neto, Solid State Commun. (in press).

26. P. C. Morais, A. L. Tronconi and K. Skeff Neto, J. Appl. Phys. (in press).

27. S. M. Bhagat, M. L. Spano, H. S. Chen and K. V. Rav, Solid State Commun. 33, 303 (1980).

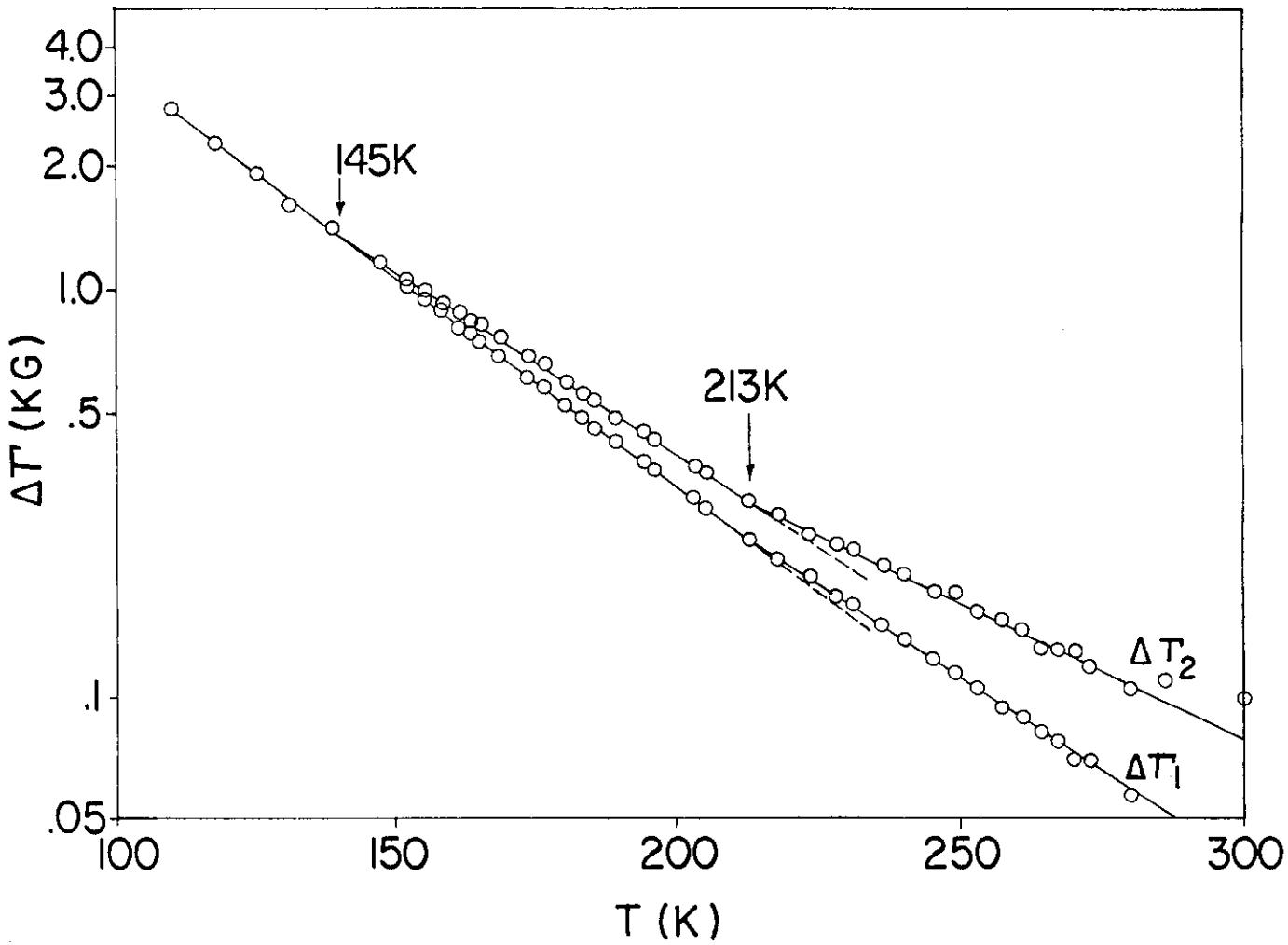

FIG. 1

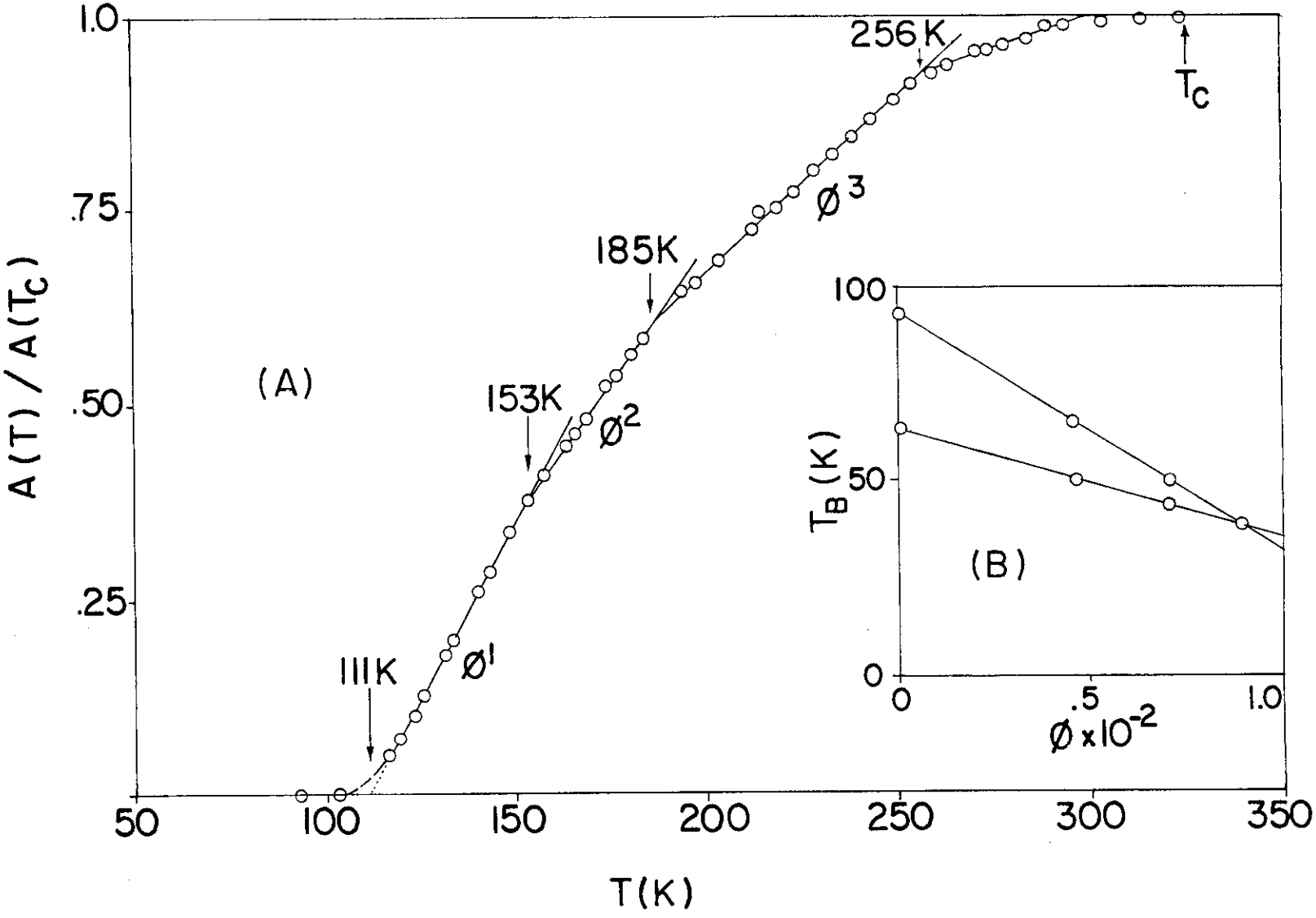
1.0
.75
.50
.25
A(T) / A(Tc)
(A)
256K
Tc
185K
153K
111K
Ø1
Ø2
Ø3
50
100
150
200
250
300
350
T(K)
100
50
0
TB (K)
(B)
0
.5
1.0
Ø x10-2

FIG. 2

A N E X O D - 4

A N E X O - E

INTRODUÇÃO A ESPECTROSCOPIA MÖSSBAUER

K. SKEFF NETO

FIS. UnB (Nota Interna) 6-1975

I N D I C E

PARTE I - Introdução ao Efeito Mössbauer

PARTE II - Instrumentação Mössbauer e Técnicas Esperimentais

PARTE - I

INTRODUÇÃO AO EFEITO MÖSSBAUER

I-1 INTRODUÇÃO

A emissão e absorção ressonante livre de recuo de raios gama em sólidos, foram descobertas por Rudolf L. Mössbauer em 1957. Esta descoberta, resultado da aplicação de princípios de Física Nuclear e Estado Sólido, em um experimento simples tem sua interpretação publicada[1] em 1958, marcando o início do Efeito Mössbauer.

A despeito da grande contribuição ao estudo das propriedades nucleares de baixas energias, o Efeito Mössbauer, possibilitando uma alta resolução energética do método, rapidamente atraiu os cientistas e executar experimentos que incluem Física Molecular, Estado Sólido, Relatividade, Química, Metalurgia, Mineralogia, Biologia e Tecnologia.

I-2 OBSERVAÇÃO DO EFEITO MÖSSBAUER

Em Heidelberg, no Instituto Max Planck para Pesquisas Médicas, Mössbauer observou um aumento no espalhamento ressonante, quando estudava o espalhamento de raios gama de 129 KeV do Ir^{191} por Ir em Pt, contrariando portanto, as previsões clássicas[2,3].

Mössbauer obteve absorção ressonante no Ir, à temperatura ambiente, sem girar a fonte ou empregar outros métodos[4] para compensar a energia perdida devido ao recuo.

Métodos de excitação térmica e recuo prévio na direção apropriada são outros métodos bem sucedidos para compensar a energia de recuo. Molmfors[4] discutiu o espalhamento ressonante antes da descoberta de Mössbauer.

A energia de recuo, $R = \frac{E_\gamma^2}{2Mc^2}$ [valores típicos de R se encontram na faixa de 10^{-2} eV a 10 eV], do Ir^{191}, R = 0.05 eV é muito maior que a largura de linha calculada para o raio gama de 129 KeV, $\Gamma = 5 \times 10^{-6}$ eV [$\Gamma.\tau = \hbar$, valores típicos de Γ se encontram dentro do intervalo 10^{-10} eV a 10^{-4} eV].

Com o intuito de reduzir este espalhamento, Mössbauer congelou fonte e absorvedor e esperava um decréscimo no efeito. No entanto, o espalhamento ressonante aumentou mais ainda, surpreendentemente.

Fornecendo velocidades pequenas da ordem de alguns cm/seg., Mössbauer obteve uma linha de absorção com largura duas ve

zes superior à largura da linha natural. Este resultado estava de acordo com a emissão e absorção livre de recuo, teoria esta desenvolvida por Lamb[5], em 1938 para a absorção de neutrons lentos e adaptada aos raios gama por Mössbauer.

I-3 FATOR DE DEBYE-WALLER (fator - f)

Considerando núcleos (átomos) presos na rede cristalina, três casos devem ser analisados[6] nos processos de emissão e absorção de raios gama por estes núcleos:

a) Se a energia de recuo do átomo for maior que a sua energia de ligação química, o átomo será arrancado de sua posição na rede. Neste caso vale a análise feita para o átomo livre. Energias de ligação química são da ordem de 10 eV.

b) Se a energia de recuo do átomo livre é grande comparada com a energia característica de vibração da rede, mas menor que a energia de deslocamento, o átomo permanecerá em seu lugar na rede e dissipará esta energia aquecendo-a. Energias de vibração da rede são da ordem de 10^{-2} eV.

c) Se a energia de recuo é menor do que a energia de fonon, nenhuma energia é cedida aos osciladores da rede, não havendo, portanto, mudanças de estado em nenhum destes osciladores. Este tipo particular de transição é chamado "transição sem recuo" e estas transições representam o que chamamos de Efeito Mössbauer.

Existe uma probabilidade f de que haja emissão sem que haja mudança no estado da rede e esta probabilidade é chamada de fator Debye-Waller ou simplesmente fator f e está calculada para diferentes modelos em diversos trabalhos[6-12].

Usando-se o modelo de Debye e para uma rede monoatômica de átomos idênticos, na aproximação de $T << \Theta$

$$f = \exp - \frac{E_o^2}{2Mc^2k\Theta}\left(\frac{3}{2} + \frac{\pi^2T^2}{\Theta^2}\right) \qquad (I\text{-}1)$$

A condição para o aparecimento de um grande número de transições sem recuo é que[10]:

$R = \frac{E_\gamma^2}{2Mc^2} \leq k\Theta$, esta condição impõe um limite superior de $E_\gamma \sim 150$ KeV para energias de transição apropriadas para a absorção Mössbauer.

Da eq. (I-1) vemos que f é maior para uma menor energia

de recuo (menor energia de radiação, E_o, e maior massa do núcleo, M), menor energia térmica (mais baixa temperatura, T) e ligação mais forte do núcleo na rede (maior temperatura de Debye, 0).

Uma outra expressão para o fator f que é muito usada nas análises mais qualitativas é obtida usando o modelo dos osciladores harmônicos para representar o sólido:

$$f = \exp \frac{-\langle x^2 \rangle}{\lambda^2} \qquad (I-2)$$

onde x é a amplitude de vibração do núcleo e λ é o comprimento de onda da radiação emitida ou absorvida pelo núcleo ($\lambda = \frac{\lambda}{2\pi}$).

I-4 ISÓTOPOS MÖSSBAUER

Mössbauer descobriu a emissão de raios gama sem recuo no Ir^{191}. No entanto, existem 42 nuclídios nos quais o efeito é observado[25] e há possibilidades deste número aumentar.

Muitas das discussões nesse nos capítulos seguintes referem-se ao Fe^{57}, o mais usado de todos os nuclídios Mössbauer. Por essa razão, o esquema de decaimento é mostrado na Fig. I-1 e seus parâmetros na Tabela I-1.

Esta fonte consiste de Co^{57}, que por processos "K-captura", decai para o Fe^{57}. O nível 14.4 KeV é usado nos experimentos Mössbauer.

I-5 PARÂMETROS DE UM ESPECTRO MÖSSBAUER

Um gráfico de transmissão, intensidade de raios gama versus velocidade Doppler (Fig. I-3) é conhecido como espectro Mössbauer.

No Efeito Mössbauer usamos velocidade Doppler para variar a energia de radiação e varrer a região de ressonância

Os parâmetros importantes de um espectro Mössbauer são:

a) forma de linha
b) largura de linha
c) intensidade de linha

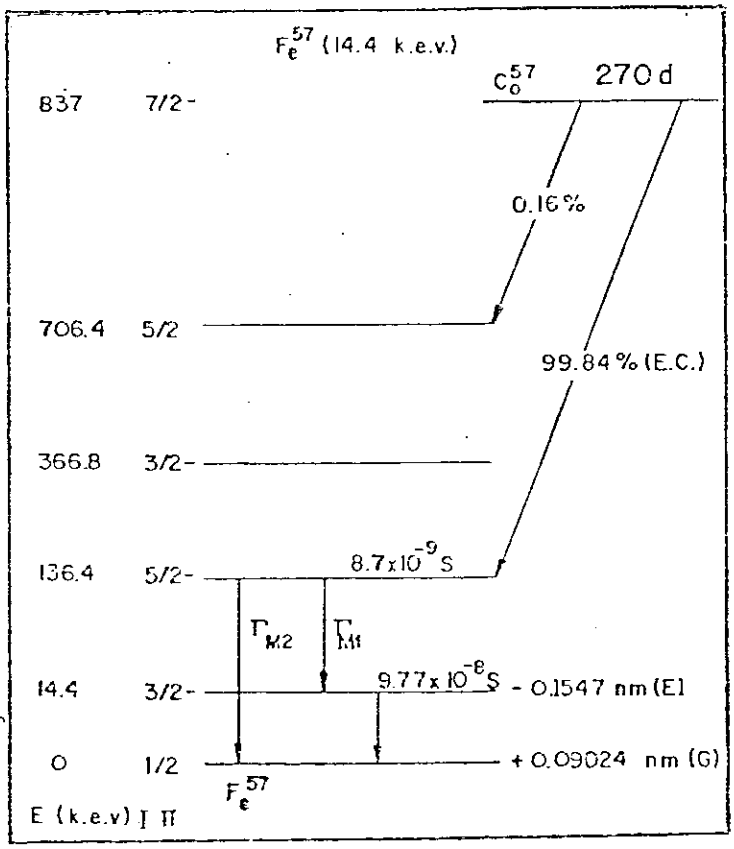

Fig. I-1 - Esquema de decaimento do Co^{57}

TABELA I-1

Parâmetros do Fe^{57} (Raio 14.4 KeV)	
PROPRIEDADES MEDIDAS	
Meia vida do estado excitado	$9,77 \times 10^{-8}$ seg
Coeficiente de conversão interna total	9,00
Abundância isotópica natural, IA	2,19%
Spin e paridade do estado fundamental, I_f	$1/2^-$
Spin e paridade do estado excitado, I_e	$3/2^-$
Momento magnético do estado fundamental, μ_f	+ 0,09024 nm
Momento magnético do estado excitado, μ_e	- 0,15470 nm
Momento do quadrupolo do estado fundamental Q_f	0,0
Momento do quadrupolo do estado excitado Q_e	0,286
Seção de choque de Ressonância Máxima	$2,38 \times 10^{-18}$ cm^2
Seção de choque de espalhamento atômico	$5,5 \times 10^{-21}$ cm^2
PARÂMETROS DERIVADOS	
Largura da linha natural	$4,669 \times 10^{-12}$ KeV
	0,095 mm/s
Largura observável	0,19427 mm/s
Energia de recuo	$1,9567 \times 10^{-3}$ cm
Seção de choque de ressonância	$2,3554 \times 10^{-18}$ cm^2
Temperatura de Dobye, θ	420°K
Fração livre de recuo, f com θ = 420°K	f(90°K) = 0,92
	f(300°K)= 0,79

d) Posição de linhas.

a) A forma de linha, ou distribuição de probabilidade, para a radiação resultante da transição de um núcleo fixo no espaço, do estado excitado para o estado fundamental seria uma (Breit-Wigner) Lorentziana forma de linha.

Adotando para o decaimento o modelo de um oscilador, lentamente amortecido pela radiação[13], e identificando o espectro desta com a densidade de probabilidade de frequência do foton teremos:

$$I(\omega) = \frac{1}{2\pi\tau} \quad \frac{1}{(\omega-\omega_o)^2 + \frac{1}{4\tau^2}} \qquad (I-3)$$

onde τ é a constante de decaimento ou seja, a vida média do núcleo.

A densidade de probabilidade de energia do foton será:

$$P(L) = \frac{\Gamma}{2\pi} \quad \frac{1}{(L-E_o)^2 + \frac{\Gamma^2}{4}} \qquad (I-4)$$

aqui $\hbar\omega = E$ e $\Gamma\tau = \hbar$.

Apenas no caso ideal, as linhas, devido à emissão e absorção, apresentam a forma de linha natural. Em experimentos reais as linhas são alargadas.

b) As fontes de alargamento de linha podem ser as seguintes:

i) Efeitos experimentais

ii) Efeitos fundamentais (Estado Sólido)

i) Efeitos experimentais incluem vibrações externas, ângulo sólido finito, resolução de velocidade e espessura finita da fonte e do absorvedor.

Fig. I-2

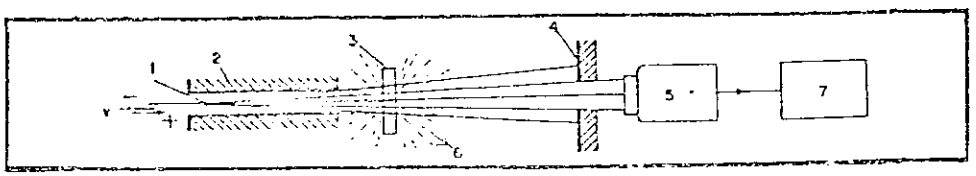

1. Fonte, 2-4. Colimadores (Pb), 3. Absorvedor, 5. Detetor (raio gama), 6. Espalhamento ($\vec{v}$ na região de ressonância), 7. Sistema de contagem.

Considerando o espectro de absorção, como uma Lorentziana de largura Γ, Visscher[8,14] relacionou a largura aparente Γ_{ap} com a espessura efetiva do absorvedor, T:

$$\frac{\Gamma_{ap}}{\Gamma} = 2{,}00 + 0{,}27\ T \qquad , \ 0 \leqslant T \leqslant 5$$

$$\frac{\Gamma_{ap}}{\Gamma} = 2{,}02 + 0{,}29\ T - 0{,}005\ T^2 \ , \ 4 \leqslant T \leqslant 10 \qquad (I-5)$$

A espessura efetiva do absorvedor é dada por:

$$T = f'na\sigma_o t \qquad (I-6)$$

onde f' é o fator f do raio gama absorvido sem perda de energia, n o número de átomos por cm^3, a é a fração de átomos ressonantes do absorvedor, t a espessura do absorvedor e σ_o a seção de choque de absorção máxima na ressonância.

Margulius e Ehrmann[15] calcularam o alargamento relativo Γ_{ap}/Γ, forma de linha e largura de linha para diferentes absorvedores. Heberle[16] calculou largura de linha para várias espessuras de absorvedores.

Wertheim[17] calculou o alargamento da linha devido aos efeitos de ângulo sólido, proporcional a

$$\frac{VD}{16d^2} \qquad (I-7)$$

onde V é a velocidade da fonte, D é o diâmetro da janela do detetor e d a distância entre fonte e absorvedor (Fig. I-2).

ii) Os efeitos de estado sólido são extremamente importantes, dando informações microscópicas sobre o sólido:

a) Estruturas hiperfinas parcialmente relaxadas (processos de flipe de spins), super-paramagnetismo, flutuações próximas à temperatura dos cristais e fenômenos de relaxação paramagnética.

b) Comportamento anarmônico da rede.

c) Movimento atômico devido à difusão e movimento Browniano dos átomos ou moléculas.

d) Associação de fontes Mössbauer ou absorvedores com vários tipos de defeitos, isto é, os átomos Mössbauer podem não ser uniformemente incorporados na rede cristalina.

Fluck[18] reportou alguns valores típicos de largura de linha para diferentes estados de carga do ferro:

0,31 mm/seg	Fe^{3+}
0,24 mm/seg	Fe^{2+}
0,23 mm/seg	Fe (complexos)
0,22 mm/seg	Fe (metálico)

c) Quando a energia da radiação está na região de ressonância temos um decréscimo na taxa de contagem do detetor.

O espectro de energia da linha de emissão das "transições sem recuo", que incidem sobre o absorvedor[10] é dada por:

$$I(E,v) = \text{const.} \frac{1}{(E - E_o - \frac{E_o v}{c})^2 + \frac{\Gamma^2}{4}} \qquad (I-8)$$

onde E_o é a energia de ressonância e $E_o v/c$ é o deslocamento da linha de emissão devido ao efeito Doppler, associado à velocidade relativa $\vec{v}$ entre fonte e absorvedor (Fig. I-2).

A seção de choque de ressonância nuclear sem recuo[10] é dada por:

$$\sigma(E) = \sigma_o' \frac{\Gamma^2/4}{(E - E_o)^2 + \frac{\Gamma^2}{4}}, \qquad \sigma_o' = f\sigma_o \qquad (I-9)$$

onde $\sigma_o = \frac{1}{1+\alpha} \frac{2I_{ex}+1}{2I_f+1} 2\pi \lambda_o^2$ é a seção de choque exatamente na ressonância ($E = E_o$), $\lambda_o = \hbar c/E_o$, α é o coeficiente de conversão interna I_{ex} e I_f são os spins dos estados excitado e fundamental, respectivamente.

Depois da radiação passar pelo absorvedor o que estaremos medindo[10] é a intensidade

$$I(v) = \text{const.} \int_0^\infty I(E,v) e^{-\sigma(E)n}\, dE \qquad (I\text{-}10)$$

onde n é o número de isótopos ressonantes por unidade de área no absorvedor.

Considerando que o absorvedor seja muito fino, $n\sigma_o << 1$, podemos mostrar (Fig. 1-3) que a eq. (I-9) nos levará:

$$\frac{I(v)}{I(\infty)} = 1 - \frac{n f_a f_s \sigma_o}{2} \cdot \frac{v_{1/2}^2}{v^2 + v_{1/2}^2} \qquad (I\text{-}11)$$

onde $I(\infty)$ é a intensidade fora da região de ressonância, f_a e f_s os fatores f do absorvedor e fonte respectivamente e $v_{1/2} = \frac{\Gamma c}{E_o}$.

Quando temos alvos não muito finos, onde a condição $n\sigma_o << 1$ não é satisfeita, pode-se mostrar[8] que a curva é ainda uma Lorentziana, porém com uma largura diferente de 2Γ, sendo isto um efeito da auto-absorção de raios gama no absorvedor.

d) Deslocamentos ou posição da linha é de máximo interesse e corresponde à diferença de energia entre os níveis da fonte e absorvedor.

O espectro Mössbauer pode ser de uma, duas, seis linhas ou de natureza complexa de acordo com o deslocamento ou desdobramento dos níveis nucleares.

Essas divisões causadas por interações hiperfinas, são extremamente importantes para investigações de propriedades do estado sólido.

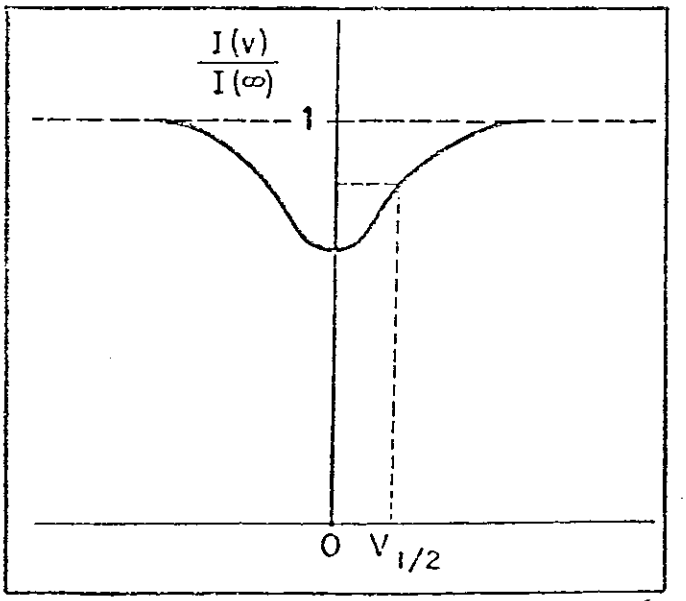

Fig. 1-3 Transmissão através de um absorvedor ressonante.

I-6 INTERAÇÕES HIPERFINAS

O efeito Mössbauer é hoje essencialmente uma técnica usada no estudo das interações do núcleo com a sua vizinhança[19,20,25-27] as chamadas interações hiperfinas.

Devido ao pequeno valor de Γ das transições nucleares, que são envolvidas no efeito Mössbauer, a absorção ressonante é extremamente sensível às variações de energia da radiação gama. Por essa razão pequenas interações entre o núcleo e os elétrons orbitais que não podem ser observadas diretamente por outros métodos manifestam-se marcantemente no efeito Mössbauer.

É então a influência do envolvimento eletrônico na transição gama nuclear, tanto na emissão quanto na absorção que determina a estrutura hiperfina do espectro Mössbauer. As interações hiperfinas surgem de dois tipos de interações tendo origem na distribuição de carga estática e dinâmica dos elétrons e núcleos. Essas são chamadas interações eletrostáticas e magnéticas.

I-6-1 INTERAÇÕES ELETROSTÁTICAS

A interação eletrostática[6-9, 13], do núcleo, no campo eletrônico e cristalino, pode ser expressa por:

$$W = \int \rho V dt \qquad (I-12)$$

onde ρ é a densidade de carga nuclear, V o potencial externo e dt o elemento de volume.

Desenvolvendo V em série de Taylor (o sistema de eixos tem origem no centro de massa nuclear) até a ordem 2 em torno de $\vec{r} = 0$:

$$V = V_o + (\vec{\nabla}V)_{\vec{r}=0}.\vec{r} + \frac{1}{2}\sum_{i=1}^{3}\sum_{j=1}^{3}\left(\frac{\partial^2 V}{\partial x_i \partial x_j}\right)_{\vec{r}=0} x_i x_j$$

Escrevendo $V_{ij} = \left(\frac{\partial^2 V}{\partial x_i \partial x_j}\right)_{\vec{r}=0}$, $-\vec{E} = (\vec{\nabla}V)_{\vec{r}=0}$, teremos:

$$W = V_o Ze - \vec{E}.\vec{P} + \frac{1}{6}\sum_{ij}\sum V_{ij}\int (3x_i x_j - r^2\delta_{ij})\rho dt + \frac{1}{6}\left(\sum_i V_{ii}\right)\int \rho r^2 dt \qquad (I-13)$$

O primeiro termo representa a energia de um núcleo puntual. Como êle independe do estado quântico do núcleo, desloca igualmente todos os níveis nucleares, não alterando as energias de transição.

O segundo têrmo é nulo por dois motivos: o núcleo ocupa sempre posição tal que o campo elétrico seja nulo; além disto os

estados nucleares têm paridade definida, o que resulta em um momento dipolar P nulo para o núcleo.

Restam somente os dois últimos termos. O último provem da dimensão finita do núcleo (representamos por δE) e o terceiro da sua não esfericidade (representamos por ΔE).

I-6-1a. DESLOCAMENTO ISOMÉRICO

A interação de monopolo elétrico ou deslocamento isomérico nuclear, que se manifesta com um deslocamento da velocidade zero no centro do espectro de ressonância Mössbauer (Fig. I-4), é devido à interação eletrostática entre a distribuição de carga do núcleo e aqueles eletrons que têm probabilidade diferente de zero de ocupar a região nuclear.

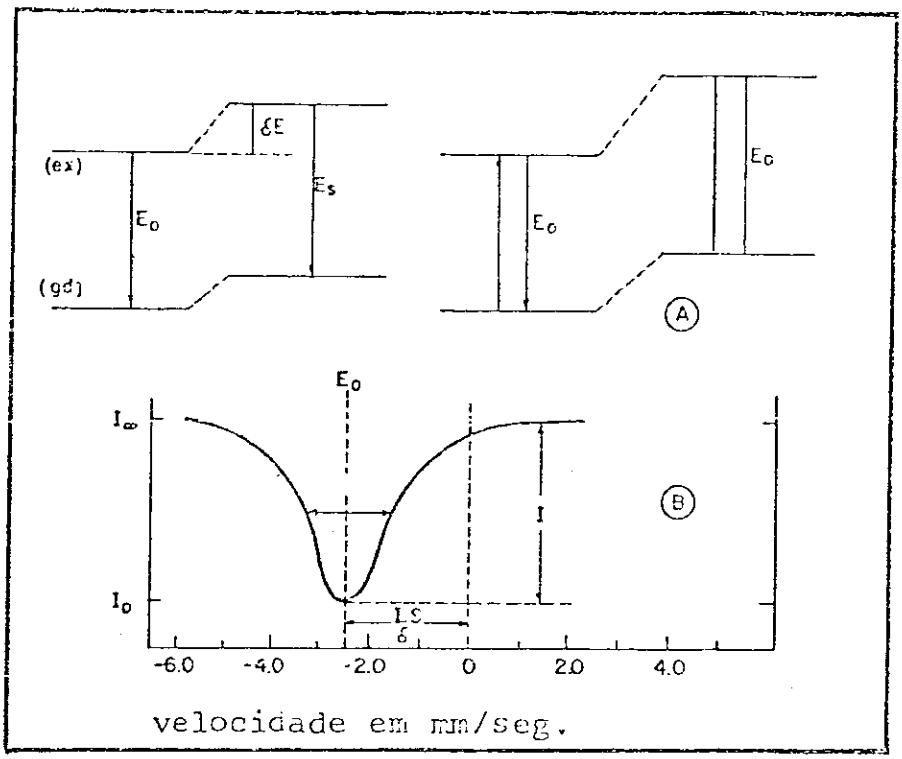

Fig. I-4:

A- Deslocamento de um nível nuclear sem degenerescencia de spin;

B- Medida de deslocamento isomérico (I.S.) em um espectro Mössbauer.

A equação de Poisson dará:

$$\sum_i V_{ii} \equiv \nabla^2 V = -4\pi\rho_{\text{eletrônico}} = -4\pi e \sum_n |\psi_{ns}(0)|^2 \qquad \text{(I-14)}$$

$-e\sum|\psi_{ns}(0)|^2$ dá a contribuição de todos os elétrons para a densidade de carga externa do núcleo.

Supondo o núcleo esférico e com distribuição uniforme de carga para o cálculo de δE, teremos:

$$\delta E = \frac{2}{5}\pi e^2 Z R^2 \sum|\psi|^2 \qquad \text{(I-15)}$$

A variação na energia da transição será:

$$\Delta\delta E = \frac{4\pi}{5} e^2 Z R^2 \frac{\delta R}{R} \sum|\psi|^2 \qquad \text{(I-16)}$$

onde usamos $\delta R = R_{est.excitado} + R_{est.fundamental}$

O desvio monopolar (I.S. - Fig. I-4) de um absorvedor em relação a uma fonte é definido por:

$$I.S. = \Delta\delta E_a - \Delta\delta E_f = \frac{4\pi}{5} e^2 Z R^2 \frac{\delta R}{R} \left(\Sigma |\psi_a|^2 - \Sigma |\psi_f|^2 \right) \qquad (I-17)$$

Kistner e Synyar[22] foram os primeiros a observar o deslocamento isomérico em um espectro Mössbauer.

Na eq.(I-17) aparecem dois fatores distintos em natureza, um atômico e da rêde e o outro nuclear; a densidade eletrônica na posição nuclear é especialmente sensível às ligações químicas do átomo; daí o desvio monopolar ser também chamado desvio químico. Em condições apropriadas é possível calcular a densidade eletrônica, podendo-se então medir $\frac{\delta R}{R}$.

Walker, Wertheim e Jacarino[23] em um trabalho histórico, determinaram este parâmetro nuclear para o Fe^{57} ($\frac{\delta R}{R} = -1,8 \times 10^{-3}$, valor muito grande em módulo e negativo, duas propriedades excepcionais), e calibraram o I.S. em termos da configuração eletrônica do Fe.

Danon[30] propos uma outra calibração corrigindo as aproximações feitas por Walker e colaboradores.

Experimentalmente o deslocamento isomérico é a distância do mínimo ao ponto de velocidade zero (Fig. I-4).

Se o material da fonte e do absorvedor forem exatamente o mesmo, não haverá deslocamento isomérico.

No caso do Fe^{57}, o núcleo no estado excitado possui raio menor que no estado fundamental. Logo[24], quanto maior a densidade de elétrons s no núcleo alvo, menor será o deslocamento isomérico.

O Fe^{2+} apresenta maior D.I. do que o Fe^{3+}, pois a presença de mais um eletron 3d no Fe^{2+} expande a nuvem de elétrons 3s, diminuindo assim a densidade eletrônica no núcleo.

Desta forma o D.I. nos dá informações sobre o estado de excitação dos átomos Mössbauer em diferentes compostos (Fig. I-6).

I-6-1b. DESDOBRAMENTO QUADRUPOLAR

Este tipo de desdobramento (representa a contribuição do termo ΔE, eq. I-13) é o resultado da interação do momento de quadrupolo Q do núcleo com o gradiente do campo elétrico, devido às outras cargas do cristal. O momento de quadrupolo nos dá a medida

do desvio do núcleo da forma esférica e é definido por[26]

$$eQ = \int (3z^2 - r^2)\rho dt \qquad \text{(I-18)}$$

onde e é a carga do próton, ρ é a densidade de carga em um elemento de volume dt a uma distância r do núcleo. Para Q = 0 o núcleo tem forma esférica, para Q > 0 tem forma alongada e para Q < 0 tem forma achatada[9].

O tensor T do gradiente do campo elétrico pode ser expresso num sistema de referência onde êle tenha uma forma diagonal:

$$T = \begin{vmatrix} V_{xx} & 0 & 0 \\ 0 & V_{yy} & 0 \\ 0 & 0 & V_{zz} \end{vmatrix}$$

Suas três componentes diagonais são ligadas pela equação de Laplace:

$$V_{xx} + V_{yy} + V_{zz} = 0 \qquad \text{(I-19)}$$

Esta relação pode ser considerada como uma aproximação, pois a densidade dos eletrons s não é nula, no núcleo. Mas no caso em que não há polarização desta nuvem de elétrons, (provocada pelas outras cargas), podemos afirmar que eles não contribuem para o gradiente e consequentemente é válida.

São necessários então somente dois parâmetros para especificar o gradiente de campo elétrico. Estes são a componente V_{zz} (também representada por eq) e o parâmetro de assimetria η definido como

$$\eta = \frac{V_{xx} - V_{yy}}{V_{zz}} \qquad \text{(I-20)}$$

As componentes são escolhidas tais que $|V_{zz}| \geq |V_{yy}| \geq |V_{xx}|$, o que faz com que $0 \leq \eta \leq 1$.

O gradiente de campo elétrico tem como principais fontes os elétrons das camadas incompletas e as cargas dos outros ions Mas o gradiente no núcleo não é a soma simples destas contribuições. Sternheimer[6,26] mostrou que a interação do gradiente externo com os elétrons das camadas incompletas e com as camadas internas, modifica o gradiente do núcleo. Escreveremos então o gradiente da seguinte maneira[26]:

$\frac{V_{zz}}{e} = q = (1 - R)q_{ion} + (1 - \gamma_\infty)q_{rede}$ onde R é o fator de blindagem e γ_∞ o de antiblindagem. Geralmente a interação representada

por R implica na indução de um gradiente de sinal contrário ao externo e γ_∞ em um gradiente de mesmo sinal.

Para um sistema em que o tensor gradiente seja diagonal, a Hamiltoniana Quadrupolar pode ser escrita como[8]

$$\mathcal{H} = \frac{e^2qQ}{4I(2I-1)}\left[3\hat{I}_z^2 - \hat{I}^2 + (\hat{I}_x^2 - \hat{I}_y^2)\right] \qquad \text{(I-21)}$$

onde $\hat{I} = (\hat{I}_x, \hat{I}_y, \hat{I}_z)$ é o operador de spin nuclear e I o número quântico de spin.

Para um gradiente de simetria axial, $\eta = 0$, e neste caso a Hamiltoniana comuta com $\hat{I}^2$ e $\hat{I}_z$ e os seus auto-valores serão:

$$E(m) = \frac{e^2qQ}{4I(2I-1)}\left[3m^2 - I(I+1)\right] \qquad \text{(I-22)}$$

Como o número quântico magnético m, aparece elevado ao quadrado, os estados cujos m diferem apenas em sinal permanecerão degenerados.

Tomando o caso particular do Fe^{57}, vemos que o estado fundamental (I = 1/2) não sofre desdobramento enquanto que o estado excitado (I = 3/2) dá origem a dois níveis (Fig. I-5A).

São possíveis duas transições e isto provoca o aparecimento de duas linhas de absorção (Fig. I-5B).

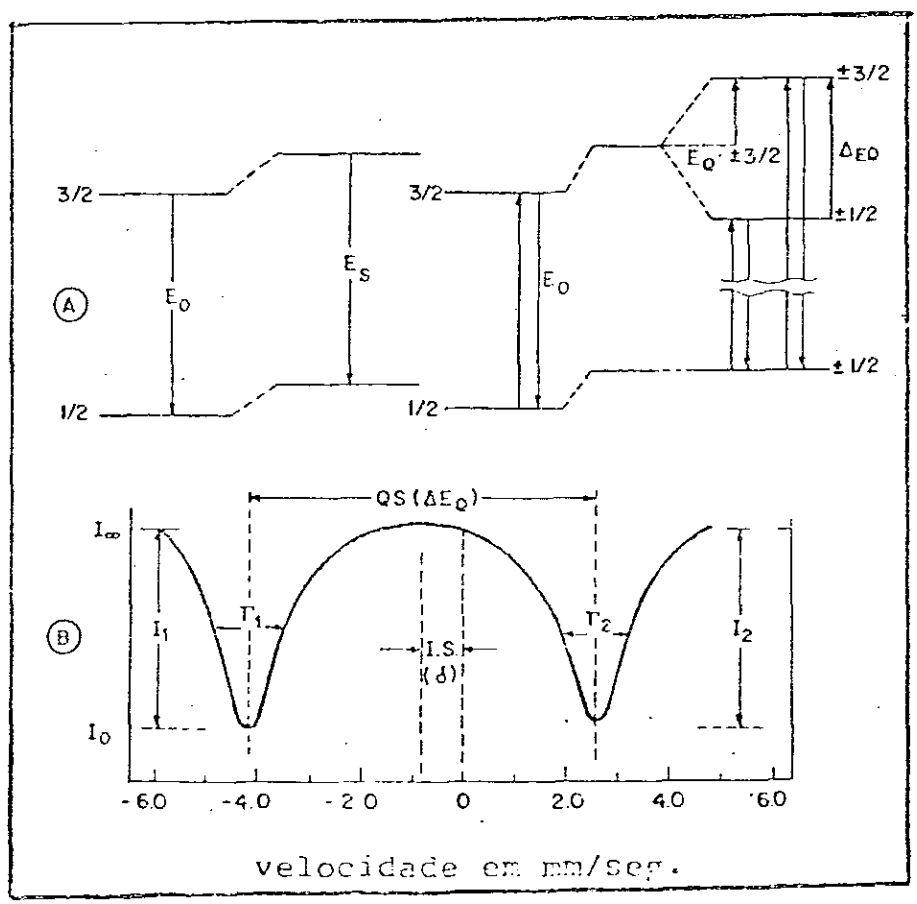

Fig. I-5

A- Desdobramento dos níveis nucleares na presença de campo elétrico.

B- Espectro Mössbauer apresentando desdobramento quadrupolar (D.Q.).

A distância entre os dois níveis do estado excitado é dada por $\Delta E_Q = 1/2 e^2qQ$. As transições possíveis indicadas na Fig I-5 têm as seguintes designações:

$$\pm \frac{3}{2} \longrightarrow \pm \frac{1}{2} \qquad \text{transições } \pi$$

$$\pm \frac{1}{2} \longrightarrow \pm \frac{1}{2} \qquad \text{transições } \sigma$$

Quando não temos simetria axial ou seja, quando $\eta \neq 0$, pode-se mostrar[27] que a separação entre os níveis é dada por

$$\Delta E_Q = \frac{1}{2} e^2 qQ \left[1 + \frac{\eta^2}{3}\right]^{1/2} \qquad \text{(I-23)}$$

Para calcular a intensidade das linhas π e σ devemos calcular primeiro a probabilidade relativa de cada transição. Estas probabilidades podem ser calculadas através dos coeficientes de Clebsh-Gordon[10].

Para a linha π da Fig. I-5 temos duas transições possíveis:

$$+ \frac{3}{2} \longrightarrow + \frac{1}{2}$$

$$- \frac{3}{2} \longrightarrow - \frac{1}{2}$$

A intensidade relativa e a distribuição angular desta linha é:

$$I_\pi(\theta) = 3F_1^1(\theta) + 3F_1^{-1}(\theta) = 3 + \cos^2\theta. \qquad \text{(I-24a)}$$

Para a linha σ temos quatro transições possíveis:

$$-1/2 \longrightarrow -1/2$$

$$+1/2 \longrightarrow +1/2$$

$$-1/2 \longrightarrow +1/2$$

$$+1/2 \longrightarrow -1/2$$

A intensidade relativa e a distribuição angular desta linha é:

$$I_\sigma(\theta) = 2F_1^0(\theta) + 2F_1^0(\theta) + F_1^1(\theta) + F_1^{-1}(\theta) = 5 - 3\cos^2\theta \qquad \text{(I-24b)}$$

Quando trabalhamos com sólidos policristalinos, devemos tomar uma média sobre θ para obter as intensidades das linhas. Se o fator -f não depende de θ, teremos

$$\frac{I_\pi}{I_\sigma} = \frac{\int_0^{\pi} f(3 + 3\cos^2\theta)\,\mathrm{sen}\theta\,d\theta}{\int_0^{\pi} f(5 - 3\cos^2\theta)\,\mathrm{sen}\theta\,d\theta} = 1 \qquad \text{(I-25)}$$

isto significa que as intensidades das duas linhas são iguais, não sendo possível diretamente identificar a linha π e a linha σ num alvo policristalino. Assim sendo, não poderemos também determinar o sinal de ΔE_Q num alvo deste tipo.

Acontece que dependendo da simetria do sólido, a probabilidade de emissão ou absorção sem recuo pode depender da direção de emissão do raio gama. Neste caso, como o fator -f depende de θ, a razão entre as intensidades, é agora dada por:

$$\frac{I_\pi}{I_\sigma} = \frac{\int_0^{\pi} f(\theta)(3 + 3\cos^2\theta)\,\mathrm{sen}\theta d\theta}{\int_0^{\pi} f(\theta)(5 - 3\cos^2\theta)\,\mathrm{sen}\theta d\theta} \neq 1 \qquad \text{(I-26)}$$

Quando esta assimetria na intensidade das linhas é devida a uma assimetria na amplitude de vibração do núcleo, é chamada de Efeito Karyazin-Goldanskii[27].

Foi observado que este efeito aumenta ou permanece o mesmo com o aumento da temperatura do absorvedor.

Se usarmos como alvo um monocristal, a razão entre as intensidades será:

$$\frac{I_\pi}{I_\sigma} = \frac{3 + 3\cos^2\theta}{5 - 3\cos^2\theta} \qquad \text{(I-27)}$$

Para $\theta = 0$, $I_\pi/I_\sigma = 3$ e para $\theta = \pi/2$, $I_\pi/I_\sigma = 3/5$.

Assim, medindo a quantidade I_π/I_σ em função do ângulo θ em um monocristal, é possível determinar quais das linhas correspondem à transição π e à transição σ. Determinamos então o sinal de ΔE_Q.

Podemos determinar o sinal do desdobramento quadrupolar em um alvo policristalino se o colocarmos em um campo magnético (B = 20.000 Gauss). Se a interação magnética entre o campo aplicado e o momento magnético do núcleo é comparável à interação quadrupolar, as linhas π e σ sofrerão um alongamento diferente, a linha π alargando-se mais que a linha σ. Identificando as duas transições, determinamos o sinal de ΔE_Q.

A Fig. I-6 mostra valores característicos do desdobramento quadrupolar para grupos diferentes de compostos de ferro.

O aparecimento do gradiente de campo elétrico na região do núcleo é devido a três fatores[9]:

1) cargas externas ao átomo. Por exemplo, as cargas iônicas da re

de produzem um gradiente de campo elétrico em uma dada posição atômica.

2) Eletrons pertencentes ao átomo. Por exemplo, nos ions de transição as camadas d não estão completamente cheias, e causam um gradiente de campo elétrico no núcleo.

3) Polarização das camadas mais internas do átomo. As camadas mais internas têm simetria esférica e normalmente não contribuem para o gradiente de campo elétrico. Entretanto, as cargas externas do átomo e mesmo seus próprios eletrons desemparelhados podem polarizar estas camadas mais internas que, então, darão uma contribuição para o gradiente de campo elétrico no núcleo.

As importâncias relativas destes três fatores dependem do tipo de sólido que estamos considerando.

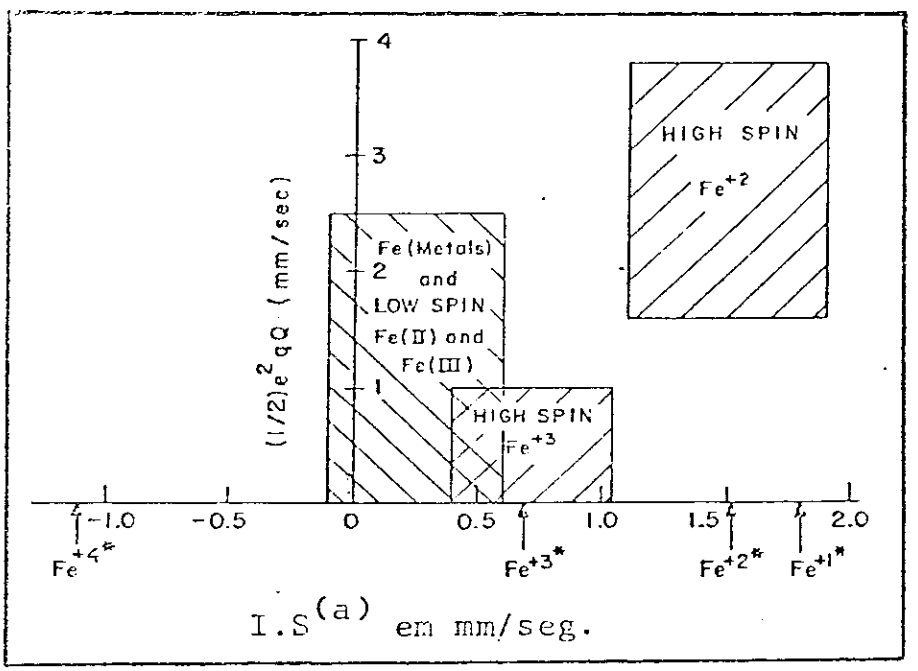

Fig. I-6 Valores característicos do deslocamento isomérico e desdobramento quadrupolar para diferentes estados do Fe^{57} (14.4 KeV).

(a) Relativo ao padrão:

$Na_2|Fe(CN)_5NO|.2H_2O$

* Ref. 23 - Pág. 22.

I-6-2 INTERAÇÃO MAGNÍTICA

Em vários casos o campo magnético, aplicado ao núcleo (campo externo ou interno) é capaz de dar aos níveis nucleares um desdobramento suficiente para ser detetado em Efeito Mössbauer.

Se um núcleo de momento magnético $\vec{\mu}$ e estado de energia E se encontra em um campo magnético $\vec{H}$, a Hamiltoniana da interação magnética será dada por[6]

$$\mathcal{H} = -\vec{\mu}.\vec{H} = -g\mu_n \vec{I}.\vec{H} \qquad (I-28)$$

onde μ_n é o magneton nuclear $\left(\mu_n = \frac{e\hbar}{2mc}\right)$, *g é a razão* giromagnética e $\vec{I}$ é o operador de spin do núcleo. Os auto-valores desta hamilto

niana são :

$$E_m = -g\mu_n Hm, \quad (m = I, I-1, \ldots, -I) \tag{I-29}$$

Assim, a degenerescência dos níveis nucleares de spin I é totalmente quebrada em (2I + 1) subníveis igualmente espaçados em separação $g\mu_n H$.

O número de linhas no espectro de emissão será determinado pelo número total de sub-níveis $(2I_f + 1)$ do estado fundamental e pelo número total de sub-níveis $(2I_e + 1)$ do estado excitado, como também pelas regras de seleção para o número quântico magnético m. Para transições dipolares, a regra de seleção para m é $\Delta m = 0, \pm 1$. Temos ainda que, para estas transições, a paridade deve ser conservada.

Para o núcleo de Fe^{57} ($I_f = 1/2$, $m = \pm 1/2$; $I_e = 3/2$, $m = \pm 3/2, \pm 1/2$ - ver Fig I-7) observamos seis transições quando o núcleo está colocado em um campo magnético.

Para podermos observar, pelo efeito Mössbauer, a diferença ΔE_m nas energias de sub-níveis nucleares de carater magnético , devemos ter[27]

$$\Delta E_m = \left| \frac{\mu_e H}{I_e} \right| > 2\Gamma_e \tag{I-30}$$

Para o núcleo do Fe^{57}, onde $\Gamma_e = 4{,}6 \times 10^{-9}$ e V, $I_e = 3/2$ e $\mu_e = -0{,}1547$ nm, esta condição só será satisfeita para $H \geq 30.000$ Oersted.

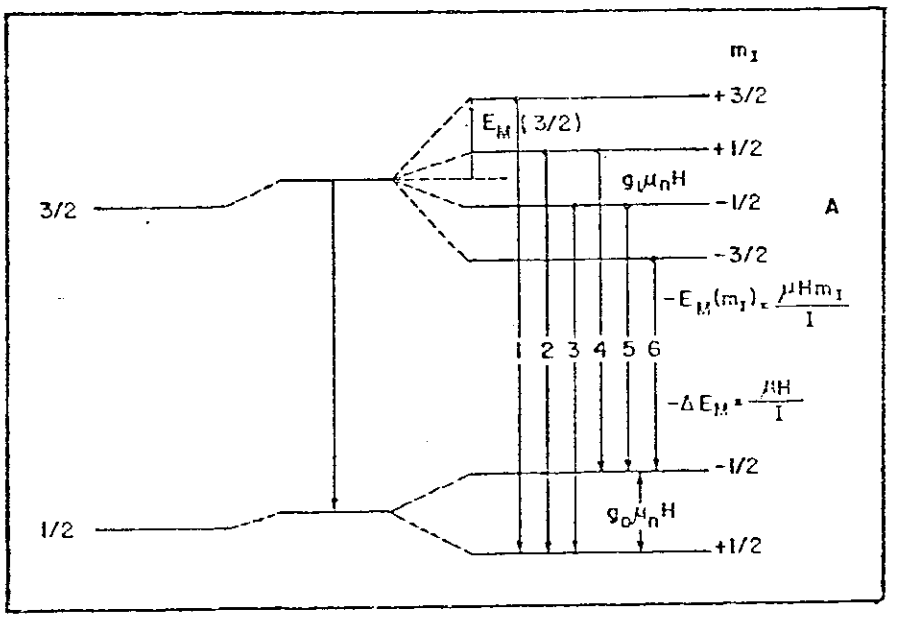

Fig. I-7 Desdobramento magnético hiperfino (efeito zeeman nuclear) com uma interação magnética pura.

A intensidade I_n (n = 1,2, ... 6) das linhas Mössbauer depende do ângulo θ entre a direção de H e a direção do raio gama e dos coeficientes de Clebsh-Gordon[28] correspondentes às transições.

Os resultados, que são encontrados em livros sobre o efeito Mössbauer[27,29] podem ser expressos da seguinte forma:

$$I_1 = I_6 \qquad I_2 = I_5 \qquad I_3 = I_4$$

$$I_1 : I_2 : I_3 = 3\frac{1}{2}(1 + \cos^2\theta) : 2\,\mathrm{sen}^2\theta : \frac{1}{2}(1 + \cos^2\theta) \qquad \text{(I-31)}$$

ou $I_1 : I_2 : I_3 = 3 : z : 1$ onde $z = \dfrac{4\,\mathrm{sen}^2\theta}{1+\cos^2\theta}$

Se o absorvedor é um material policristalino, devemos tomar a média de Z sobre todas as direções. Encontramos $\bar{Z} = 2$, o que significa que $I_1 : I_2 : I_3 = 3:2:1$.

Em materiais ferromagnéticos é fácil identificar as diferentes transições no espectro de seis linhas, e então encontrar: $\mu_e H$ e $\mu_f H$.

Para o Fe^{57} μ_f já conhecido de experiências de ressonância nuclear magnética e μ_e e H podem ser calculados[28]. Sendo μ_f = = + 0,0902 nm, encontraremos que μ_e = -0,1547 nm e H = 332 KGauss, à temperatura ambiente.

O aparecimento do campo magnético no núcleo pode ser explicado pela distribuição angular e radial da densidade eletrônica no átomo e pelo spin. A contribuição mais importante provém da interação de contato de Fermi, que consiste no acoplamento direto entre o núcleo e os elétrons s. No núcleo aparecem diferenças nas densidades de carga dos eletrons s↑ (spin-up) e eletrons s↓ (spin-down) se a carga eletrônica contiver uma camada magnética parcialmente cheia, por exemplo, a camada 3d do átomo de ferro. A interação entre a camada d polarizada e um eletron s é atrativa, enquanto que entre a camada d e um eletron s é repulsiva. As partes radiais das funções de onda dos eletrons s serão diferentes, sendo uma impelida na direção do núcleo, ao passo que a outra se afasta do núcleo. Consequentemente, a interação de contato de Fermi provoca um campo magnético local no núcleo, o qual pode ser da ordem de algumas centenas de KGauss.

I-6-3 INTERAÇÃO MAGNÉTICA E ELÉTRICA COMBINADAS

Se um núcleo estiver num campo elétrico e num campo magnético $\vec{H}$, as posições dos sub-níveis da estrutura hiperfina dependerão da razão entre as energias de interação magnética e elétrica, da simetria do gradiente de campo elétrico, do ângulo formado pelo

eixo principal do tensor do gradiente de campo elétrico e pela direção do campo magnético $\vec{H}$.

Se o tensor do gradiente de campo elétrico tiver simetria axial e seu eixo for paralelo a $\vec{H}$, a energia de interação hiperfina elétrica e magnética para $I_e = 3/2$ será[26,27]:

$$E_m = -g\mu_n H m_I + (-1)^{|m_I| \pm 1/2} e^2qQ/4 \qquad \text{(I-32)}$$

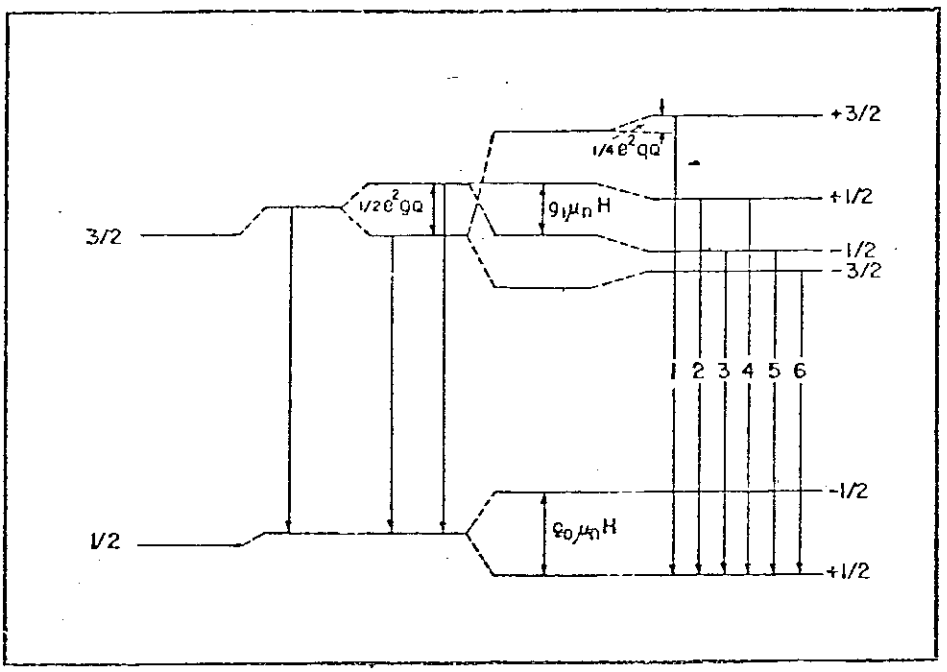

Fig. I-8 Desdobramento hiperfino do nível I=3/2 para V_{zz} paralelo a H.

Se o eixo de simetria de um tensor axialmente simétrico do gradiente de campo elétrico formar um ângulo $\theta \neq 0$ com a direção do campo magnético $\vec{H}$, para $I_e = 3/2$, a energia de interação hiperfina elétrica e magnética será[26,27]:

$$E_m = -g\mu_n H m_I + (-1)^{|m_I|+1/2}\left(\frac{e^2gQ}{4}\right)\left(\frac{3\cos^2\theta - 1}{2}\right) \qquad \text{(I-33)}$$

Em geral é bastante difícil determinar $e^2qQ/4$. Entretanto, se a determinação experimental da posição das linhas de absorção em relação ao seu centro de gravidade e consequentemente suas separações forem suficientemente precisas, esta quantidade em princípio pode ser obtida.

PARTE - II

INSTRUMENTAÇÃO MÖSSBAUER e TÉCNICAS EXPERIMENTAIS

II-1 INTRODUÇÃO

Em ótica, fenômenos ressonantes foram demonstrados no começo deste século. R.W.Wood em um experimento simples foi capaz, em 1904, de demonstrar a radiação ressonante, usando a familiar luz amarela (linhas D) emitida pelos átomos de sódio.

A possibilidade de fluorescência ressonante nuclear foi prevista por Kuhn[2] em 1929, mas somente em 1951 Moon[3], usando uma ultra centrífuga para compensar a energia de recuo, foi capaz de observar fluorescência ressonante nuclear.

As investigações clássicas em fluorescência ressonante ótica e nuclear, convencionais, foram todas executadas como experimentos de espalhamento.

Em trabalhos de efeito Mossbauer comumente observamos a transmissão. As razões principais são uma maior intensidade e uma geometria favorável.

Alguns experimentos de espalhamento[31, 32], contudo, têm sido executados por observação de raios X diretamente, medindo os raios X que seguem o processo de conversão interna, ou detetando os eletrons de conversão (Fig. II-1)

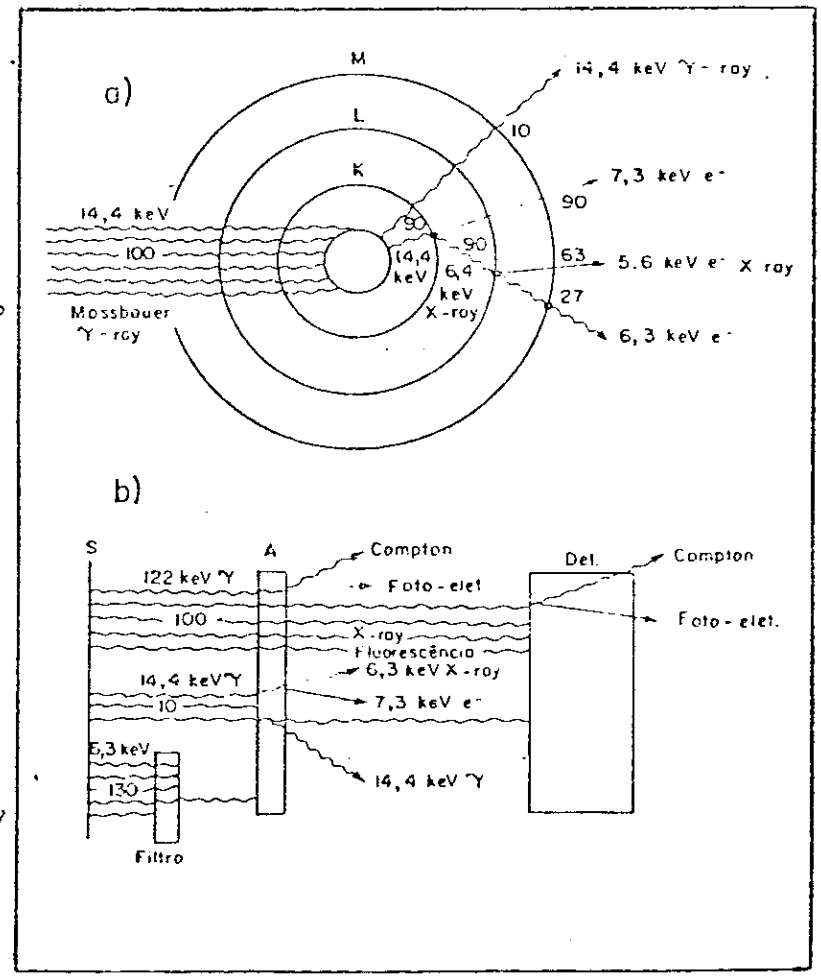

Fig. II-1

a) Esquema do processo de conversão interna para transição 14.4KeV do Co^{57}

b) Processos de degeneração da energia em uma fonte, absorvedor e detetor em um sistema de deteção Mössbauer.

Um esquema para um experimento de Mössbauer (transmissão) é esquematizado na Fig. II-2.

A fonte de gama é movimentada com uma velocidade v com respeito ao absorvedor. O raio gama então sofre um deslocamento Doppler $E = (v/c)E$ onde E é a energia do raio gama.

A intensidade I_{exp} no detetor é determinada como função da velocidade v. A velocidade v é definida como positiva se a fonte se move em direção ao absorvedor. Plota-se $I(v)/I(\infty)$, (eq. I-11) onde $I(v) = I_{exp} - B$ e B é o "background" (note-se que em velocidades grandes, nenhuma absorção ressonante ocorre).

II-2 ESPECTRÔMETRO MÖSSBAUER

Um espectrômetro Mössbauer[8,17,32,33] consiste de três partes:

a) Fonte Mössbauer

b) Absorvedor Mössbauer

c) Dispositivo e Controle de Velocidade

São usados basicamente dois modos diferentes de se obter um espectro Mössbauer. Em um, a fonte (absorvedor) se move com uma velocidade constante por um tempo pré-estabelecido e contagens durante esse período são registradas. A velocidade é então trocada por um novo valor e o procedimento é repetido até o espectro inteiro ser obtido.

O trabalho original de Mössbauer foi executado dessa maneira[1].

No segundo método, a fonte varre periodicamente um range de velocidade e a contagem em intervalos pré-estabelecidos de velocidade são armazenados em diferentes canais de um analisador multicanal.

Esses dois métodos juntam informações na mesma razão, mas cada um tem vantagens para certos tipos de investigações. Com um sistema de velocidade constante, pequena parte do espectro pode ser investigada com alta precisão.

Com o sistema de varredura de velocidade, o espectro inteiro é obtido simultâneamente e uma primeira impressão pode ser obtida rapidamente.

II-2-1 FONTE e ABSORVEDOR MÖSSBAUER

Ao observar o efeito Mössbauer podemos estar interessados no absorvedor (fonte); neste caso usaremos uma fonte (absorve

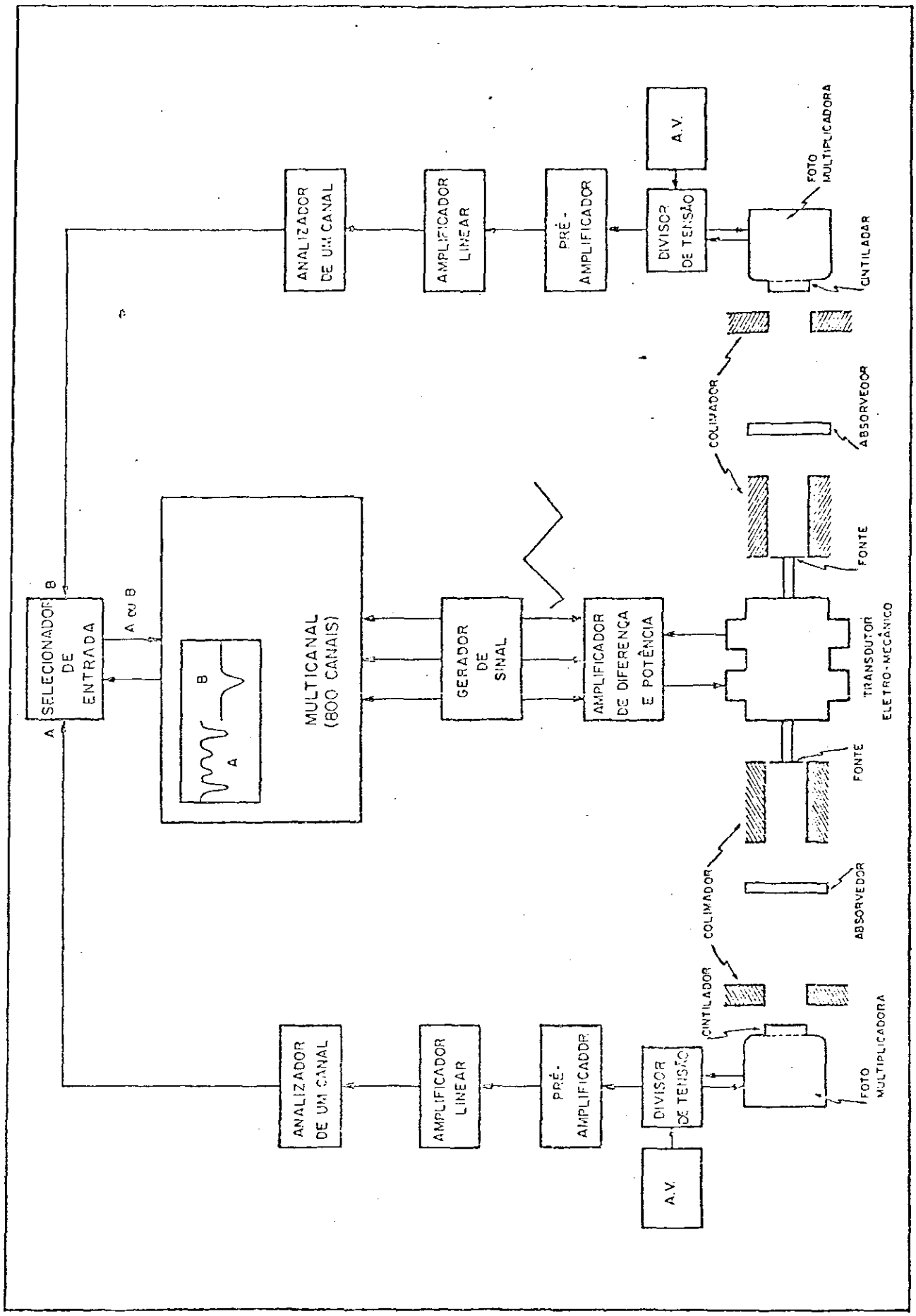

Fig. II-2 Diagrama em bloco de montagem do equipamento para um experimento Mössbauer

dor) que apresenta uma única linha de emissão (absorção), bem estreita, e uma alta fração sem recuo, f.

Não existe método bem provado, de acordo com o qual possa-se preparar fontes e absorvedores que forneçam linhas tão fortes quanto possível e tão finas quanto a largura de linha natural. Um procedimento levando ao melhor resultado tem que ser encontrado para cada isótopo, principalmente por tentativa.

Indicações de preparação de fontes e absorvedores podem ser encontradas em muitos artigos experimentais[22,23,34].

O material radioativo que constituirá a fonte é incorporado em uma matriz onde seus níveis nucleares permanecem inalterados. Qualquer metal diamagnético cúbico será uma boa escolha desde que o radioisótopo penetre na rede substancialmente.

A fonte usada por nós foi de Co^{57} com uma atividade inicial de 25 mC, em matriz de cobre, e os valores do deslocamento

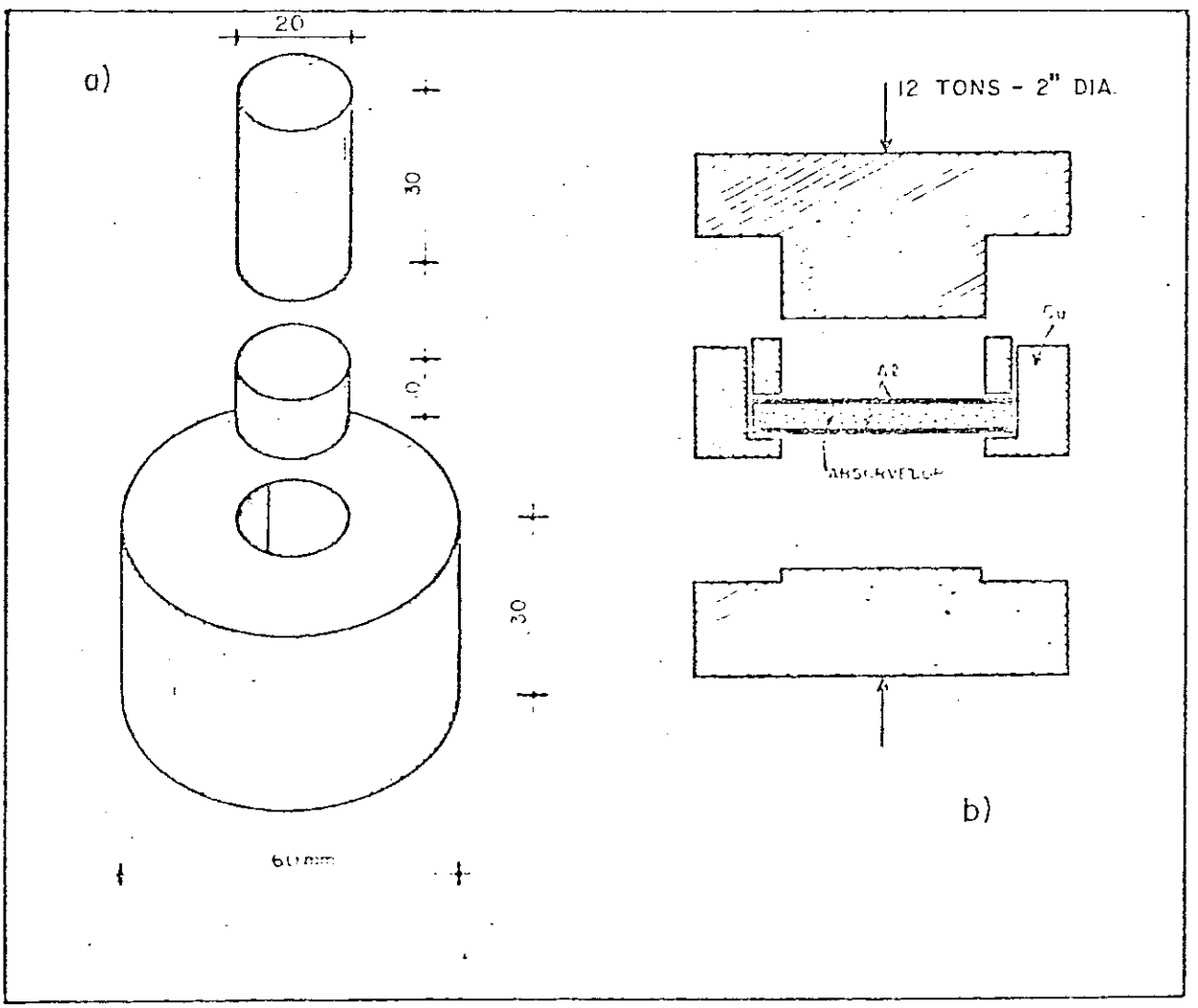

Fig. II-3 Sistema utilizado para compressão do material Mössbauer.
a - forma em aço
b - montagem da pastilha.

isomérico são dados relativos a essa fonte. A velocidade da fonte foi periodicamente calibrada com ferro metálico.

O material, ou o composto químico, que contém nuclídios no estado fundamental e que podem ser associados com o processo de absorção ressonante do raio gama é chamado absorvedor.

Um bom absorvedor deve satisfazer ("transição sem recuo") as seguintes condições experimentais:

1. O material deve ser uniformemente distribuido (gm/cm^2);
2. O diâmetro e a espessura do absorvedor deve ser tal que a intensidade (I_{exp}) seja significativa;
3. O material do absorvedor deve ser estável (mudança de estado físico ou reações químicas) durante as medidas;
4. Quando estudamos os parâmetros Mössbauer como função da temperatura, precauções devem ser tomadas para evitar gradiente de temperatura no absorvedor;
5. O absorvedor deve ser montado em um suporte rígido. Bolhas de nitrogênio líquido em "dewars", vibrações provocadas por acoplamentos de bombas de vácuo ao sistema, por exemplo, alargará as linhas consideravelmente, se precauções não forem tomadas.

Os absorvedores usados neste trabalho são policristalinos (125μm) e por compressão (Fig. II-3) entre folhas de alumínio (0,02 mm) formamos pastilhas (2cm de diâmetro) contendo ∿10mg Fe/$/cm^2$.

II-2-2 DISPOSITIVO e CONTROLE DE VELOCIDADE[33]

O sistema de varredura de velocidade, usando um analisador multicanal foi o utilizado neste trabalho (Fig. II-2).

A fonte é movimentada de tal modo que são computadas as velocidades de $-v_{max}$ a $+v_{max}$. A fonte está presa a um transdutor eletro-mecânico que mede a velocidade instantânea v(t). Esse sinal é usado para acumular o pulso de energia selecionado no contador em diferentes canais do multicanal, (Fig. II-4).

Os transdutores eletro-mecânicos de velocidade podem ser construidos de vários modos[17,33]. O mais simples é utilizar auto-falantes, usando uma bobina para comandar o cone e a outra para medir v(t) como podemos ver na Fig II-5.

Os cones estão presos por uma aste rígida e a esta prendemos a fonte de gama.

Extremo cuidado deve ser tomado no sentido de eliminar perturbações na forma de onda. O método para tal consiste em usar

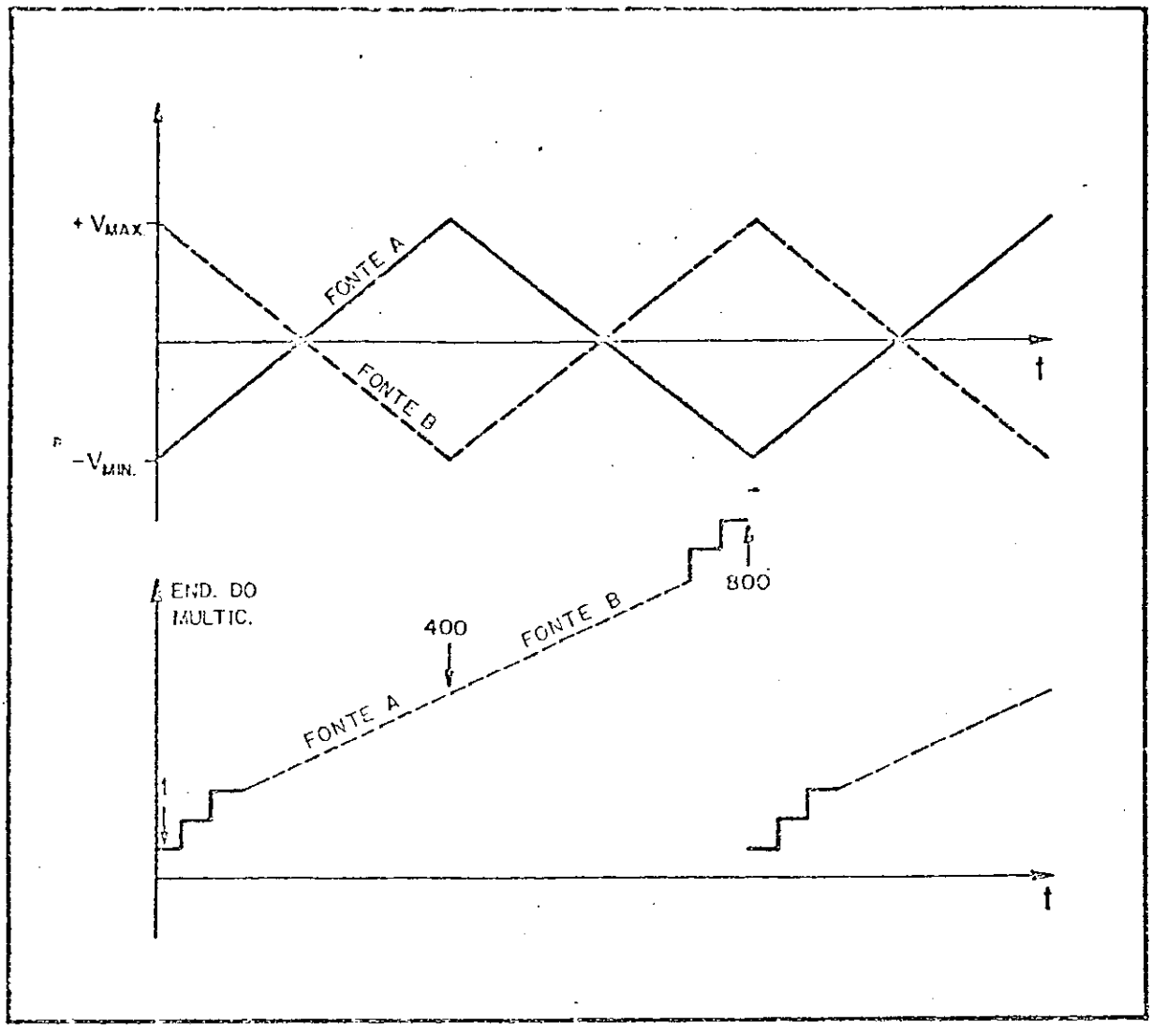

Fig. II-4 Sincronização entre o movimento das fontes e o avanço de endereço do multicanal.

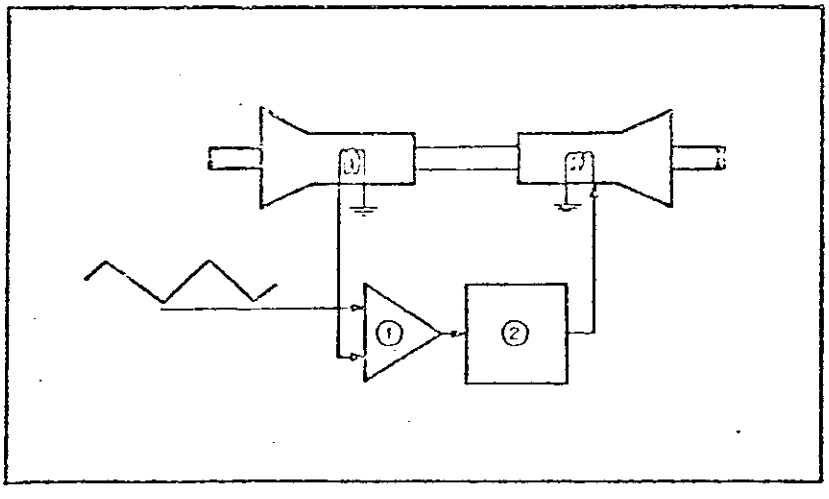

Fig. II-5 Transdutor eletro-mecânico e sistema de realimentação. ① Amplificador de diferença, ② Amplificador de potência.

um sistema de realimentação[33], (Fig. II-5).

Existem outras possibilidades de dispositivos de velocidade[33], tais como cristais piezoelétricos e variações na temperatura da fonte ou absorvedor.

II-3 DETEÇÃO DA RADIAÇÃO GAMA

O equipamento utilizado para detetar a radiação Mössbauer é o mesmo da espectroscopia nuclear.

Muitas substâncias cintilam quando bombardeadas por radiações nucleares, mas aquelas comumente usadas na prática caem em três classes: plásticos, líquidos e cristais orgânicos e inorgânicos.

Como detetor usamos um cristal de NaI(Tl), de pequena espessura, pois estamos interessados em detetar somente o nível 14.4 KeV.

Cristais de Iodeto de Sódio ativado com Tálio, são ótimos para detetar Raios-X e Gama. Eles podem ser feitos com uma alta eficiência e a quantidade de luz emitida pode ser relacionada à energia da radiação incidente.

A maioria dos detetores de radiação não podem funcionar satisfatoriamente sem o auxílio de equipamentos eletrônicos, tais como amplificadores, discriminadores e "scaler".

O pulso de luz emitida por um raio gama, ao passar através de um cristal de cintilação, pode ser detetado somente por uma fotomultiplicadora sensível. O pulso elétrico de uma fotomultiplicadora é então amplificado, discriminado em altura e levado ao "scaler" ou multicanal (Fig. II-2).

Outros detetores, tais como contadores proporcional e detetores usando semicondutores são também usados em espectroscopia Mössbauer.

II-4 SISTEMAS DE AQUECIMENTO e TRATAMENTO TÉRMICO

Os espectros Mössbauer do composto $FeSO_4.7H_2O$ e de seus subprodutos foram aqui estudados como função da temperatura no vácuo, ar e na atmosfera de nitrogênio.

Foram utilizados dois sistemas: um "cryostat" para temperaturas na faixa de -193 a +100°C e um forno na faixa de +25 a + 400°C.

O sistema "cryostat" é do tipo comercial e o forno é o

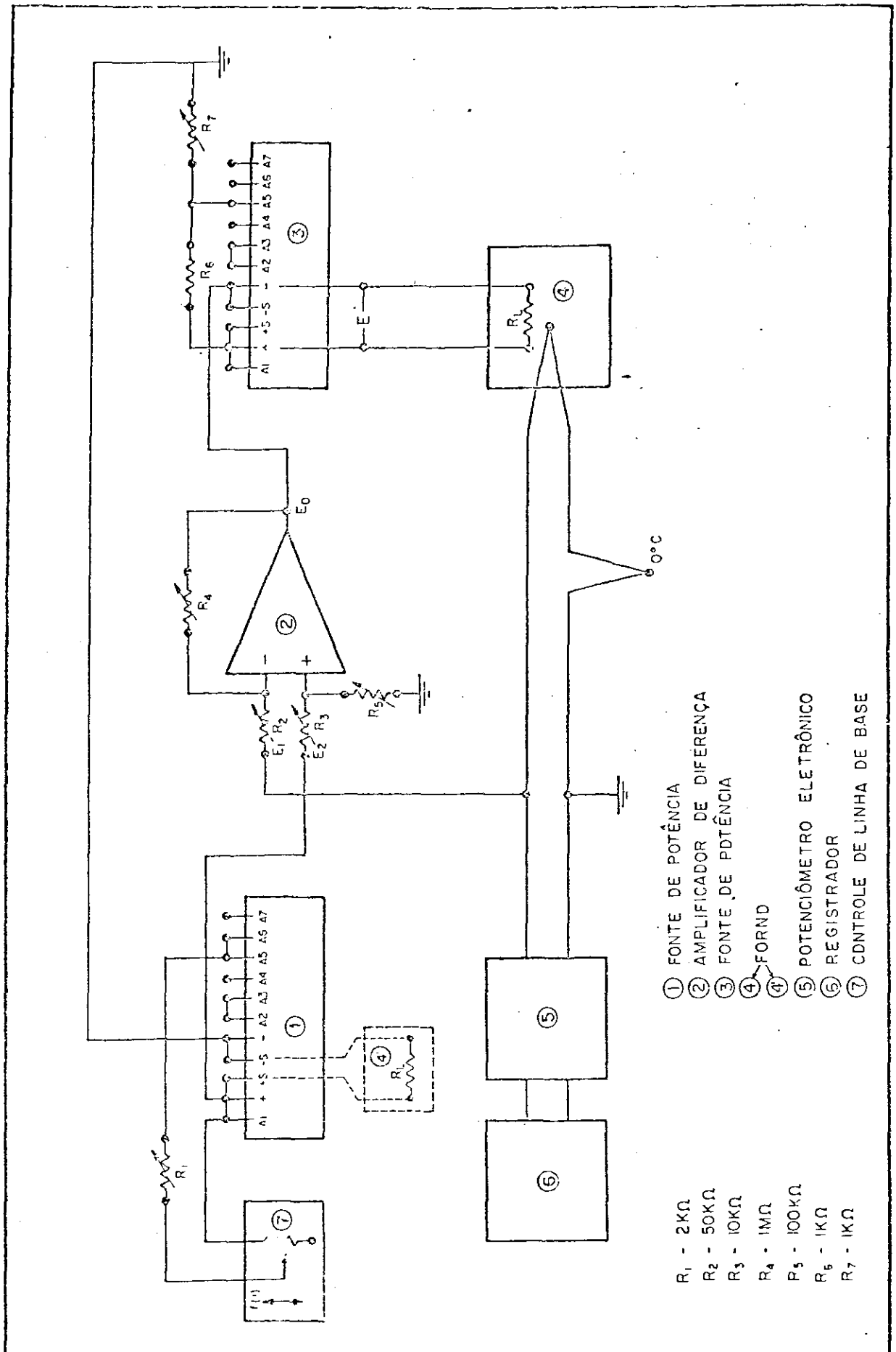

Fig. II-6 Esquema do controle de temperatura.

mostrado no esquema da Fig. II.7.

Para controlar a temperatura usamos o esquema da Fig. II-6.

A parte mais importante deste esquema é o estágio de entrada ②, que se constitue de um amplificador operacional.

A finalidade deste amplificador é executar a diferença entre os sinais do termopar (E_1) e o sinal de referência (E_2).

O sinal de referência fornecido pelo sistema ① é controlado pelo resistor R_1 e pelo resistor do sistema ⑦. Este último é programado por um motor, quando necessário, como uma função do tempo.

O sistema ③ alimenta a resistência de aquecimento R_L do sistema ④, com uma tensão E que é proporcional ao sinal E_o fornecido pelo sistema ②.

Uma opção sem realimentação é fornecida pelo sistema ① e muitas vezes usada para complementar o sistema ③ fornecendo uma maior potência ao sistema ④.

O sistema ⑤ possibilita uma leitura da temperatura (na região do absorvedor) como uma função da voltagem (mv) do termopar (cobre-constantan) e o sistema ⑥ registra em função do tempo esta leitura.

O ganho deste controle de temperatura é ajustado nos resistores R_2, R_3, R_4, R_5 e R_7.

Este controle de temperatura possibilita uma série de facilidades experimentais.

Por exemplo, o controle do sistema da Fig. II-8 e do sistema termo-gravimétrico esquematizado na Fig. II-9.

O sistema da Fig. II-8 foi utilizado para preparar os absorvedores Mössbauer, em atmosferas e temperaturas pré-estabelecidas.

Adaptando o sistema da Fig. II-7 a uma balança analítica (Fig. II-9), foi possível fazer estudos de perda de peso em função da temperatura do material Mössbauer.

A variação do peso, como função da voltagem medida na bobina da Fig. II-9 e da temperatura foram registradas em função do tempo no sistema ⑥, (Fig. II-6).

Alguns resultados de perda de peso são apresentados na Fig. III-4 e podem perfeitamente ser comparados com o resultado obtido por Gallagher e outros autores[36,37]

Fig. II-7 Forno Mössbauer

A - Desenho explodido

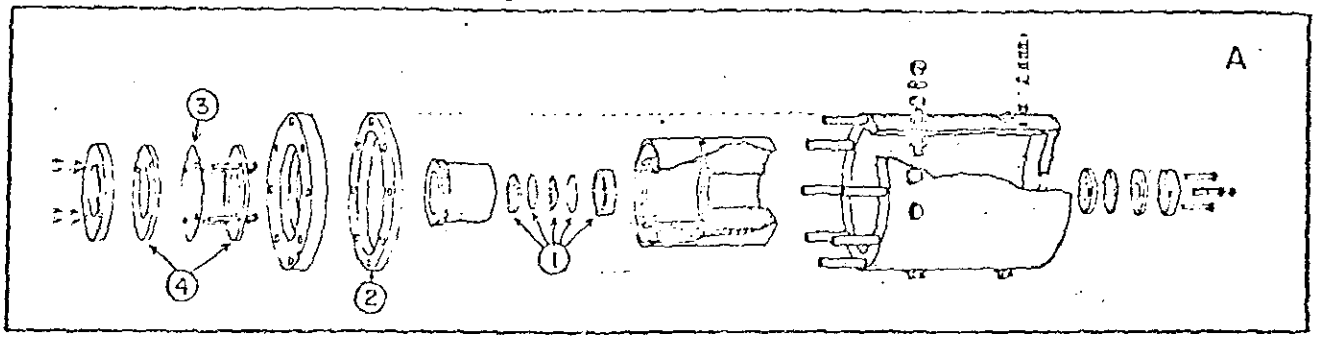

1. Montagem do absorvedor (veja Fig.II-3b)
2. junta de Teflon
3. janela de alumínio (0,02mm)
4. juntas de Teflon

B - 5. absorvedor
6. posição do termopar
7. resistência de aquecimento
8. entrada
9. saida } de gás

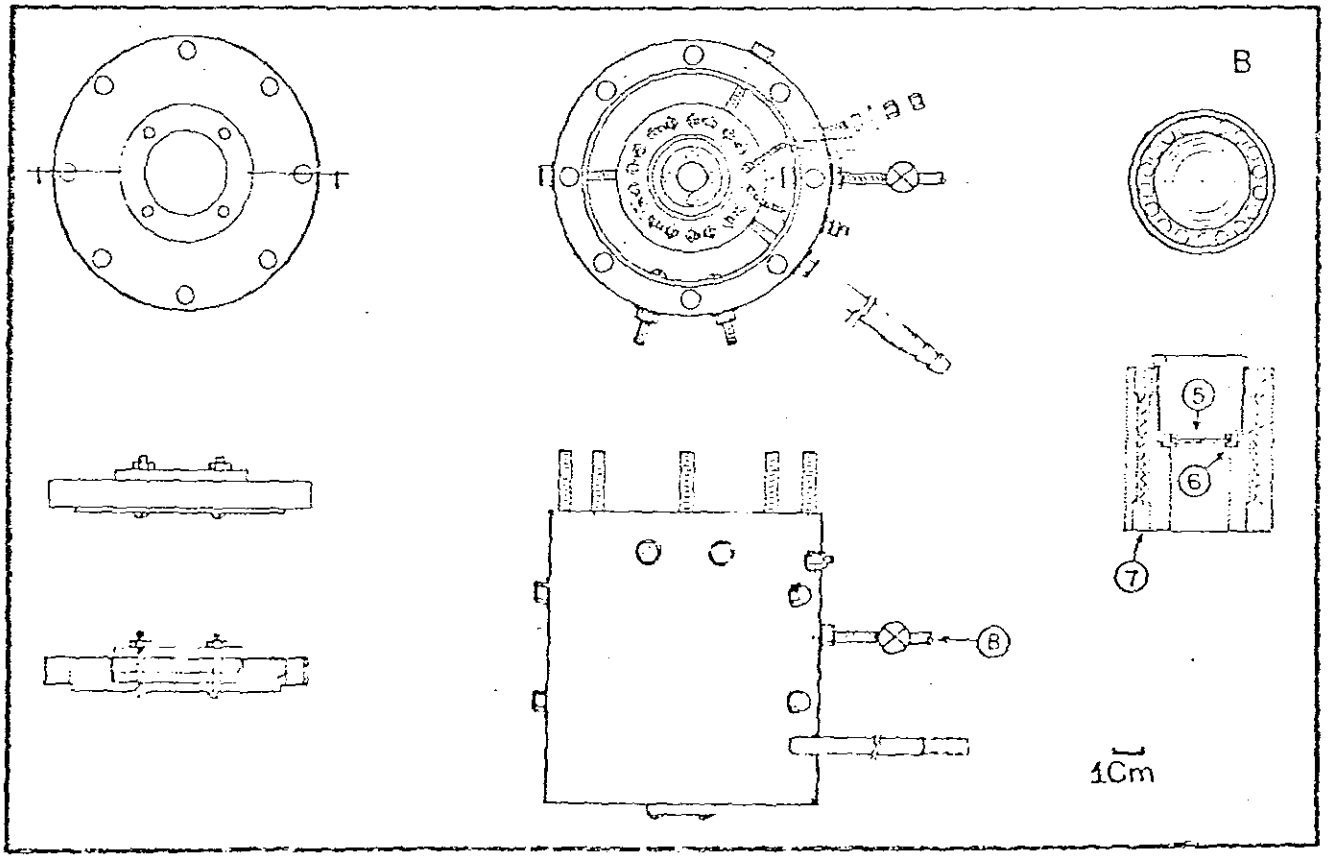

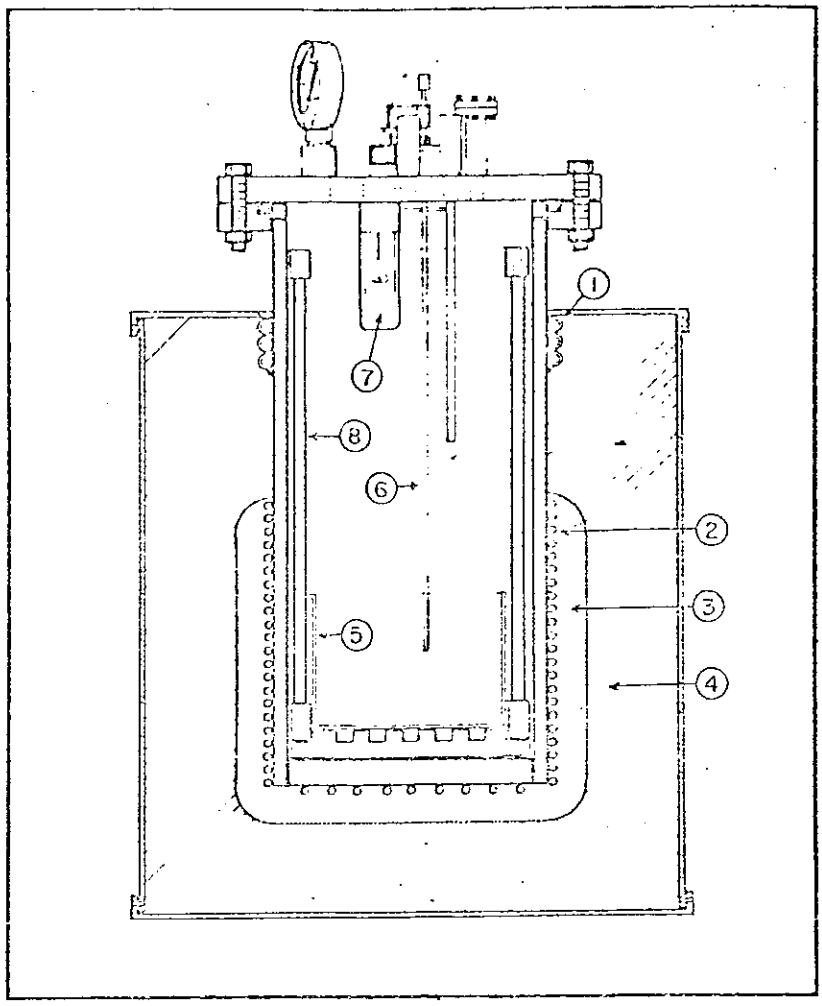

Fig. II-8a Forno utilizado para preparar o material Mössbauer

1. Circulação para água

2. resistência de aquecimento

3. cerâmica

4. isolante térmico

5. recipiente de vidro (pyrex)

6. termopar

7. lâmpada

8. suporte do recipiente 5

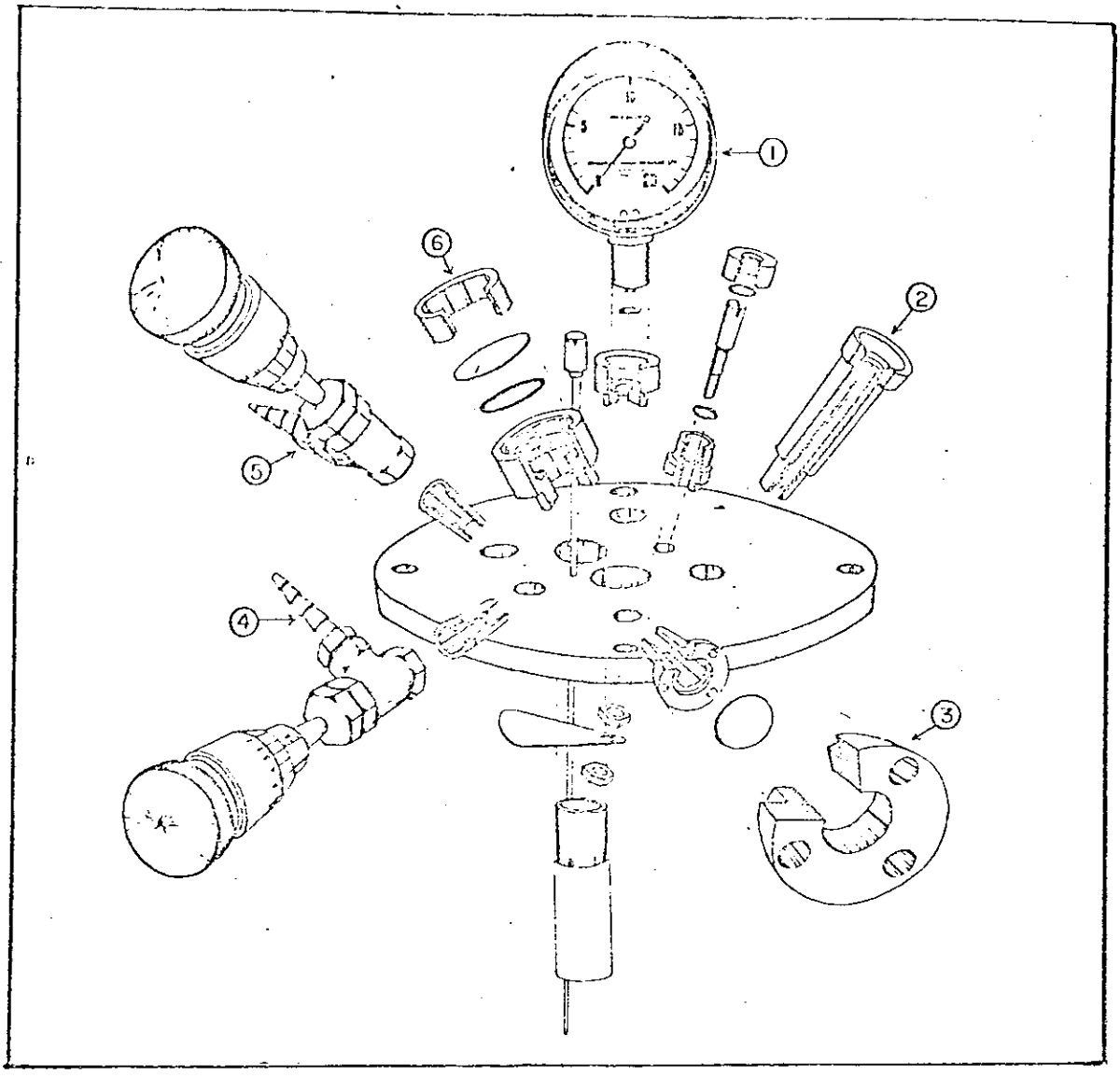

Fig. II-8b Desenho explodido da parte superior do sistema da Fig. II-8a.

1. Medidor de pressão

2. conexão do sistema de vácuo

3. válvula de proteção

4. entrada de gás

5. saida de gás (conectada a uma bomba de vácuo mecânica)

6. visor

7. conexão do terropar

Fig. II-9 Esquema em bloco do equipamento utilizado para preparar os absorvedores Mössbauer.

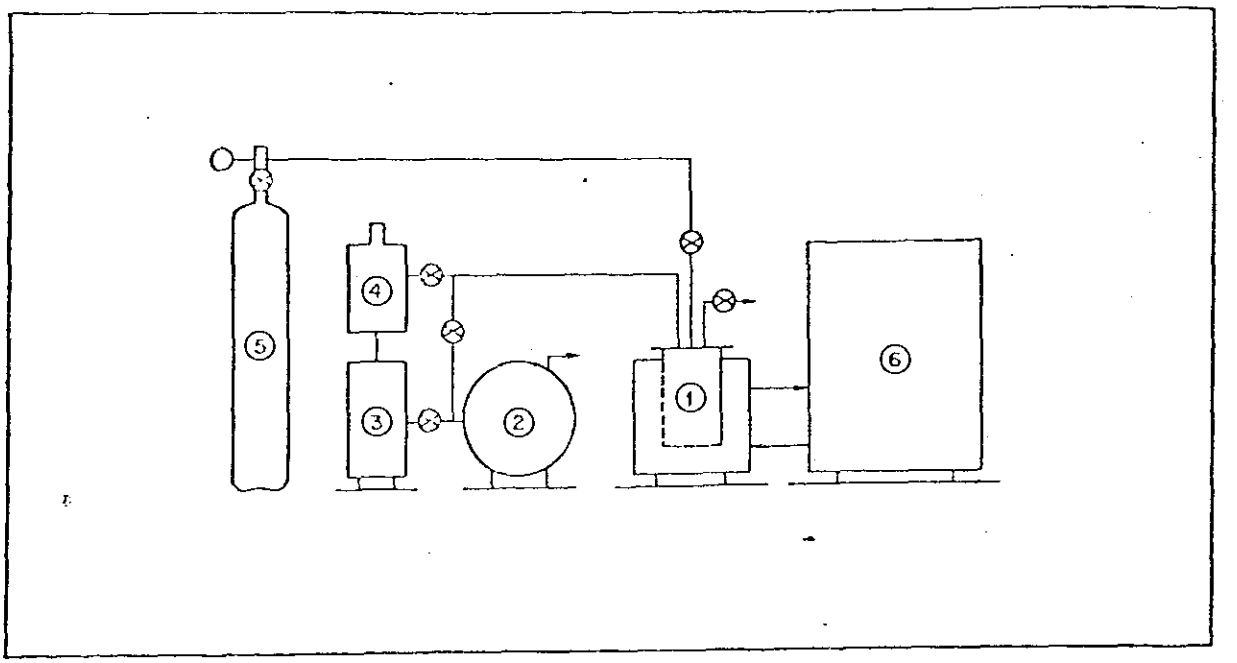

1) Sistema Fig. II-8a; 2) bomba mecânica; 3) bomba de difusão; 4) "trap"; 5) cilindro de gás (N_2); 6) sistema Fig. II-6.

Fig. II-10 Sistema termo-gravimétrico.

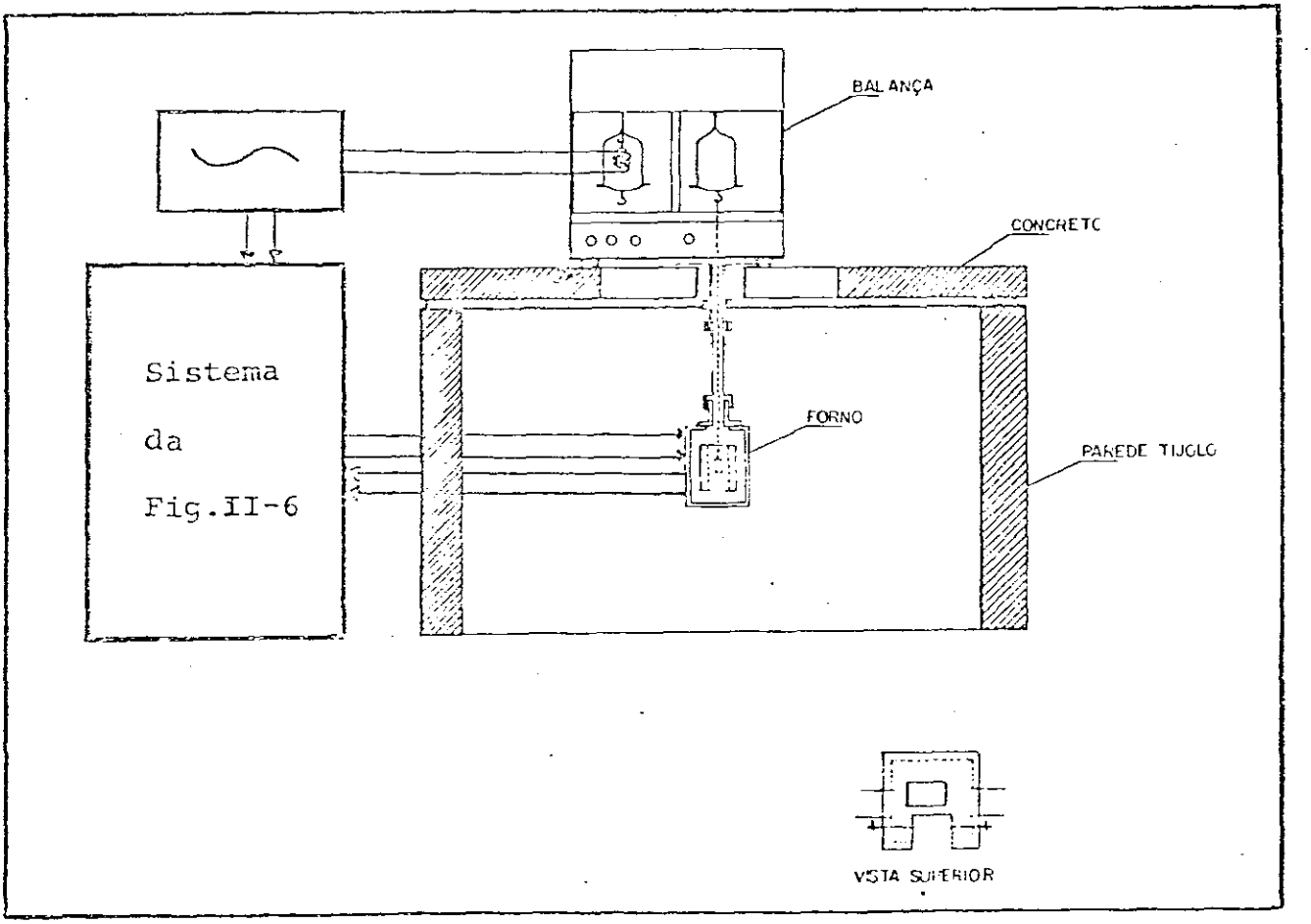

II-5 EQUIPAMENTO UTILIZADO e ESPECIFICAÇÕES

Os equipamentos mais importantes utilizados em nossos experimentos foram:

Fig. II-2 Multicanal DIDAC-800, no modo "Multicanal Scaling" (INTERTECHNIQUE)

Sistema "Drive-Transducer" (ELSCINT, AME-30)

As Larguras das Linhas do Espectro Mössbauer do Padrão $Na_2[Fe(CN)_5NO].2H_2O$ analizado neste sistema são:

$\Gamma_1 = 0,2380 \pm 0,0119$ mm/seg

$\Gamma_2 = 0,2383 \pm 0,0119$ mm/seg

$$\frac{v}{\text{canal}} = \frac{(1.7034 \pm 0.0014 \text{ mm/seg})^*}{231.379 \text{ canais} - 100.037 \text{ canais}}$$

Fig. II-6 Fonte de Potência (HEWLETT PACKARD - 6224A)

Amplificador de Diferença (OPERACIONAL NEXUS SD-5)

Controle de Linha de Base (ELSCINT ABA-1)

Fig. II-7 Forno Mössbauer (confeccionado em Alumínio, na UnB)

Intervalo de Temperatura	+ 25 a 400°C
Estabilização	± 0,04 a 300°C
Potência Requisitada	60W a 400°C
Diâmetro do Absorvedor	20 mm

Fig. II-10 Balança Analítica (VEB OSCHATZER WAAGENFABRIK - Tipo 705.21)

---

* Ref. 23.

REFERENCIAS

1. Mössbauer, R.L., Ref. 8, p. 101-120.
2. Kuhn, W. Phil, Mag. 8, 625 (1929).
3. Moon, P.B., Proc. Phys. Soc. (London) 64, 76 (1951).
4. Malmfors, K.G., "Resonance Scattering of γ-Rays". "Alpha-Beta and Gamma Ray Spectroscopy". Vol. 2, Edited by Kai Siegbahn. - North-Holland Publishing Company (1965).
5. Lamb, W.E., Phys. Rev. 55, 190 (1939).
6. Wertheim, G.K., "Mössbauer Effect: Principles and Applications" Academic Press (1964).
7. Debrunner, P.G. and Frauenfelder, H., "Introduction to the Mössbauer Effect" in "An Introduction to Mössbauer Spectroscopy", Edited by Leopold May (1971).
8. Frauenfelder, H., "The Mössbauer Effect", Benjamim, W.A. Inc, Publishers (1962).
9. Danon, J., "Lectures on the Mössbauer Effect", Gordon and Breach, Science Publishers, Inc (1968).
10. Mössbauer, R.L., in "Recoiless Nuclear Resonance Absorption and its Applications". "Alpha-Beta and Gamma Ray Spectroscopy" Vol. 2, Edited by Kai Siegbahn (1965).
11. Lipkin, H.J., Ann. Phys. (N.Y.) 9, 332 (1960); ibid 18, 182 (1962).
12. Lustig, H., Am. J. Phys. 22, 1 (1961).
13. Jackson, J.D., Classical Electrodynamics, John Wiley & Sons, Inc. (1963).
14. Boyle, B.A.J.F. and Hall, H.E., Rept., Progr. Phys. 25, 441 (1962).
15. Margulies, S. and Ehrmann, J.R., Nucl. Instr. Methods, 12, 131 (1961).
16. Heberle, J., Nucl. Instr. Methods, 58, 90 (1968).
17. Wertheim, G.K., Physics Today 20, 131 (1967).
18. Fluck E. in Advances in Inorganic Chemistry and Radio-Chem., Edited by Emeleus H.J. and Sharpe, A.G. - Acad. Press (N.Y.) Vol. 6, p. 278 (1964).
19. Muir, A.H. Jr; Ando, K.J. and Coogan, H.M., "Mössbauer Effect Data Index, 1958-65, Inter Science, N.Y., (1966).
20. Devoe, J.R., Spijkerman, J.J., And. Chem. 38, 382R (1966), ibid 40, 472R (1968).

21. Garg, V.K., Ph.D. Thesis, University of Roorkee, India (1971)
22. "Proceedings of the Second International Conference on the Mössbauer Effect", Edited by Compton, D.M.J. and Schoen, A.H. John Wiley and Sons, Inc., N.Y. (1962).
23. "Mössbauer Effecta Data Index", Edited by Stevens, J.G. and Stevens, V.E. (1970).
24. Bchugar, H.J., Rossman, G.R. and Gray, H.B., J.Am.Chem. Soc. 91, 4564 (1969).
25. "Mössbauer Effecta Data Index", Edited by Stevens, J.G. and Stevens, V.E., (1971).
26. Greenwood, N.N. and Gibb, T.C., "Mössbauer Spectroscopy" Chapman and Hall Ltd, London (1971).
27. Goldanskii, V.I. and Herber, R.H., "Chemical Applications of Mössbauer Spectroscopy", Acad. Press (1968).
28. Hanna, S.S., Heberle, J., Littlejohn, C. Perlow, G.J., Preston R.S. and Vincent, D.H., Phys. Rev. Lett., 4, 177 (1960).
29. Mössbauer, R.L. and Clauser, M.J., in "Hyperfine Interactions" Edited by Freeman, A.J., and Frankel, R.B., Acad. Press
30. Danon, J., in Applications of the Mössbauer Effect in Chemistry and Solid State Physics", International Atomic Energy Agency Thecnical Rep. Series, nº 50 (1966).
31. Spijkerman, J.J., "Conversion Electron Mössbauer Spectroscopy" American Lab. 3, 11 (1971).
32. DeVoe, J.R., NBS Technical Note 501 (july 1968 to june 1969).
33. Kalvius G.M. and Kankeleit E., "Mössbauer Spectroscopy and its Applications", Proceedings of a Panel Vienna 24-28 May 1971, International Atomic Energy Agency, Vienna, 1972.
34. Cranshaw T.E., Nucl. Inst. and Met., 30, 101-105 (1964).

REFERÊNCIAS

01 - W. C. Elmore, Phys. Rev. 54, 1092 (1938).

02 - E. Kneller, "Fine Particle Theory" in Magnetism and Metallurgy, Vol. 1, edited by A. E. Berkowitz and E. Kneller, Ac. Press, N. Y. (1969).

03 - L. Néel, Compt. Rend, 228, 664 (1949).

04 - A. M. Afanas'ev, I. P. Suzdalev, M. Ya. Gen, V. I. Goldanskii, V. P. Korneev and E. A. Manukim, Sov. Phys., JETP, 31, 65, (1970).

05 - T. Shinjo, J. Phys. Soc. Japan, 21, 917, (1966).

06 - Y. Ishikawa, J. Appl. Phys., 35, 1054 (1964).

07 - D. W. Collins, J. J. Dehn and L. N. Mulay, "Sueperparamagnetism and Mössbauer Spectroscopy ; a Review and New Results on Iron Dispersion" in Mössbauer Effect Methodology, Vol. 3, edited by I. J. Gruverman, Plenum Press. N. Y. (1967)

08 - I. S. Jacobs and C. P. Bean, "Fine Particles Thin Films and Exchange Anisotropy" in Magnetism, Vol. III, edited by G. T. Rado and H. Suhl, Ac. Press, N. Y. (1963).

09 - A. A. Van der Giessen, J. Phys. Chem Solids, 28, 343 (1967).

10 - G. N. Belozerski and Yu. Paulyukhin, Sov. Phys. Solid State, 19, 745 (1977)

11 - F. Van der Woude and A. J. Dekker, Phys. Stat. Sol., 9, 775 (1965).

12 - N. N. Greenwood and T. C. Gibb, "Mössbauer Spectroscopy" Chapman and Hall Ltd - London.

13 - W. Kunding, H. Bömmel, G. Constabaris and R. H. Lindquist, Phys. Rev., 142, 327 (1966).

14 - J. P. Suzdalev, Sov. Phys. JETP, 10, 775 (1970).

15 - F. E. Luborsky, J. Appl. Phys. 32, Suppl. 171S (1961).

16 - H. Trauble, "The influence of Crystal Defects on Magnetization Process in Ferromagnetic Single Crystal" in and Metallurgy, edited by A. E. Burowitz and E. Kneller, Vol. 2, Ac. Press, N. Y. (1969).

17 - G. A. Candela and R. A. Haines, Appl. Phys. Lett, 34, 868 (1979).

18 - P. Roggwiller and W. Kundig, Sol. State Comm., 10, 901 (1973).

19 - A. P. Amulyavichus and J. R. Suzdalev, Sov. Phys. JETP, 37, 859 (1973).

20 - Yu. S. Avraamov, V. M. Belova, V. I. Nikolaco and V. H. Stuchebuikov, Sov. Phys. Solid State, 16, 2071 (1975).

21 - S. Morup and H. Topsoe, Appl. Phys. 11, 63 (1976).

22 - C. C. Tsuei, G. Longworth and S. C. H. Lin, Phys. Rev. 170, 603 (1968).

23 - T. E. Sharon and C. C. Tsuei, Phys. Rev. B, 5, 1047 (1972).

24 - C. C. Tsuei and H. Lilienthal, Phys. Rev. B, 13, 4899 (1976).

25 - K. Skeff Neto and L. C. Miranda, Sol. State Comm. 28, 43 (1978).

26 - K. Skeff Neto, I. C. Cunha Lima, N. S. Almeida e L. C. Miranda, J. Phys., C, 11, 695 (1978).

27 - P. C. Morais and K. Skeff Neto, J. Appl. Phys. 54 (1), 307 (1983).

28 - S. M. Bhagat, M. L. Spano e J. N. Loyd, Solid State Comm. 38, 361 (1981).

29 - P. C. Morais, A. L. Tronconi and K. Skeff Neto, J. Appl. Phys. 55, 3744 (1984).

30 - N. M. L. Köch, P. C. Morais and K. Skeff Neto. Solid. State. Comm. 52, (9), 181 (1984).

31 - P. C. Morais and K. Skeff Neto, J. Appl. Phys. - aceito - (1984).

32 - A. Vértes and B. Zsolds, Acta Chimica, Acad. Scientiarum Hungaricae, Tomus 65, 3 (1970).

33 - A. Vértes, R. Szikely, T. Tarnáczy, Acta Chimica, Acad. Scientiarum Hungaricae, Tomus 63, 1 (1970).

34 - P. R. Gallagher, D. W. Johnson and F. Schrey, J. Amer. Ceram. Soc. 53, 566 (1970).

35 - K. Skeff Neto and V. K. Garg, Radiochem Radional. Lett., 15 (6), 357 (1973).

36 - K. Skeff Neto and V. K. Garg, J. Inorg. Nucl. Chim, 37, 2287 (1975).

37 - P. C. Morais and K. Skeff Neto, Polyhedron 2 (9), 875 (1983).

38 - M. C. L. Lara, N. M. L. Köche, P. C. Morais and K. Skeff Neto, Sol. Stat. Commun. - Submetido (1984)

39 - P. C. Morais, N. M. L. Köche, A. L. Tronconi and K. Skeff Neto, The Rev. Sci. Instrum. - aceito (1984).

40 - P. C. Morais and K. Skeff Neto, J. Appl. Phys. - submetido (1984).

41 - O. A. C. Nunes, A. M. M. Monteiro and K. Skeff Neto, The Rev. Sci. Instrum. 52(9), 1413 (1981).

42 - P. C. Morais and K. Skeff Neto, J. Appl. Phys., submetido (1984).

43 - P. C. Morais and K. Skeff Neto, J. Appl. Phys. - submetido (1984).

44 - O. A. C. Nunes, A. M. M. Monteiro and K. Skeff Neto, Appl. Phys. Lett. 35, 656 (1979).

45 - A. L. Tronconi, M. A. Amato, P. C. Morais and K. Skeff Neto, J. Appl. Phys. 56, 1462 (1984).

"EVIDÊNCIAS EXPERIMENTAIS DE UM SISTEMA MAGNÉTICO MULTIFÁSICO EM PEQUENOS AGREGADOS DE HIDROXISULFATO FÉRRICO"

KHALIL SKEFF NETO

Tese apresentada no Centro Brasileiro de Pesquisas Físicas, do Conselho Nacional de Desenvolvimento Científico e Tecnológico, fazendo parte da Banca Examinadora os seguintes Professores:

Jacques Abulafia Danon/CBPF

Richard B. Frankel/MIT/USA

Paulo Henrique Porcheto Domingues/UFRJ

Ramiro de Porto Algre Muniz/CBPF

Jader Benuzzi Martins/CBPF

Rio de Janeiro, 06 de dezembro de 1984